3D Structural Analysis of the Oman Ophiolite and the Lithosphere of the Eastern Arabian Continental Margin

Dissertation

zur Erlangung des Doktorgrades
an der Mathematisch-Naturwissenschaftlichen Fakultät
der Christian-Albrechts Universität zu Kiel

vorgelegt von
Lars Wiesenberg

Kiel, 2020

1. Gutachter: Prof. Dr. Thomas Meier
2. Gutachter: Prof. Dr. Frank Krüger

Tag der mündlichen Prüfung: 30.06.2020
Zum Druck genehmigt: 30.06.2020

Der Dekan

Erklärung

Hiermit erkläre ich, dass ich die vorliegende Doktorarbeit selbstständig und ohne Zuhilfenahme unerlaubter Hilfsmittel erstellt habe. Weder diese noch eine ähnliche Arbeit wurde an einer anderen Abteilung oder Hochschule im Rahmen eines Prüfungsverfahrens veröffentlicht oder zur Veröffentlichung vorgelegt. Ferner versichere ich, dass die Arbeit unter Einhaltung der Regeln guter wissenschaftlicher Praxis der Deutschen Forschungsgemeinschaft entstanden ist. Ich versichere das mir noch kein akademischer Titel entzogen wurde.

Ort, Datum Lars Wiesenberg

Abstract

The Oman Mountains along the eastern Arabian passive continental margin are geologically a highly complicated region. As part of the Peri-Arabic obduction along the convergence zone between the Arabian and Eurasien plate, oceanic crustal and mantle material were emplaced on the Arabian continent in Mid Cretaceous. The Semail ophiolite in the Oman Mountains covers an area of about $700x140km^2$. Additional tectonic processes lead to the circumstance that every geological strata of the ophiolite is exposed at the surface, which makes it one of the best preserved and studied ophiolite in the world in case of geological field investigations. However, the vertical extent of the Oman ophiolite as well as the structure and thickness of the underlying continental lithosphere has thus far been geophysically imaged by only a few local 2D studies, some of them dating back to the 1980s. To fully understand the obduction process and the formation of today's topography of the Oman Mountains, information on the present state of the Arabian continental lithosphere is needed.

In this work, a 3D model of the lithosphere beneath the eastern Arabian continental margin will be estimated. For that reason, we operated a temporary broadband seismic network with 40 instruments for continuous, passive seismic registration from October 2013 to February 2016. The dataset is complemented by data of 18 permanent broadband seismometers, operated by the Oman Earthquake Monitoring centre, the Dubai Seismic Network and the Global Seismographic Network. A newly implemented approach for inter-station phase velocity measurements was applied to compute Rayleigh and Love wave fundamental mode phase velocities in a period range of 2 – 40 s from ambient seismic noise cross correlations. This approach utilized the measured phases of the cross-correlation functions and performed a grid search to fit them to synthetic phases, calculated via the Bessel function of third kind. Azimuthal anisotropic Rayleigh and Love wave phase velocity maps are calculated, which show velocity anomalies across the eastern Arabian continental margin as a function of period. We then simultaneously inverted Rayleigh and Love wave local dispersion curves for shear wave velocity over depth by using a novel implementation of a radially anisotropic, probabilistic 1D inversion (Particle Swarm Optimization). The resulting 1D models are combined to construct the 3D model of isotropic shear wave velocity and radial anisotropy to a depth of 55 km beneath the eastern Arabian continental margin.

In addition, we calculated P- and S- receiver functions using our continuous Oman data and 286 teleseismic events from the ISC catalogue, which occurred during the time of the station deployment, to image different crustal and mantle discontinuities like the Moho and the mantle transition zone. A newly implemented migration approach led to depth information from P- and S- receiver functions.

We are able to present the first three-dimensional model of isotropic and radially anisotropic shear wave velocity of the eastern Arabian continental margin. It provides information on the lateral and vertical extent of the ophiolite and confirms previous works on 2D modelling of the ophiolite structure. Moreover, the 3D model clearly features the different properties of the strongly deformed crustal structure of the Oman Mountains, especially west- and eastwards of the Semail Gap. We present a map for the crustal thickness across the entire region, which is mostly consistent to the obtained results on receiver functions. The crustal thickness decreases from west to east and features a localized thickening beneath the Oman Mountains which is most prominent in the Jebel Akhdar window. In combination with azimuthal anisotropy, the 3D model substantiate previous works on post- obductional extension leading to the exhumation of once subducted and partly metamorphosed rocks in the Saih Hatat and Jebel Akhdar window. Azimuthal anisotropy in the upper crust would support a compressional regime, causative for the uplift of the Oman Mountains, whereas azimuthal anisotropy in the lower crust points to the importance of an extensional phase in the area of the Oman Mountains. Despite that the timing of this extensional phase has still to be identified, a reinvestigation of the question about the formation of the Oman Mountains seems to be required. By evaluating our results on the present state structure of the continental lithosphere, clear differences between the areas west- and eastwards of the Semail Gap are observable. In combination with differences in the lateral thrusting of the ophiolite onto the Arabian continent, we are able to propose properties of the continental crust which are beneficial for an obduction, namely a relatively large deformability and crustal thickness in combination with a rather flat subduction during obduction. In summary, the new model provides considerable insight in the lithospheric structure of the eastern Arabian continental margin and can serve as a starting point for revisiting its geodynamic evolution.

Zusammenfassung

Entlang des östlichen arabischen Kontinentalrandes erstreckt sich mit dem Al-Hajar Gebirge ein geologisch höchst komplexes Gebiet. Dieses ist Teil der Peri-Arabischen Obduktion, welche entlang der Konvergenzzone zwischen der arabischen und eurasischen Platte verläuft. In der mittleren Kreide schob sich ozeanisches Krusten- und Mantelmaterial auf den arabischen Kontinent. Der Semail Ophiolit erstreckt sich über eine Fläche von $700x140km^2$ und ist damit einer der größten zusammenhängenden Ophiolitkomplexe der Welt. Zusätzliche tektonische Prozesse führten dazu, dass jede geologische Einheit des Ophioliten an der Oberfläche des Gebirges aufgeschlossen ist. Dadurch ist das Al-Hajar Gebirge und speziell der Oman Ophiolit Ziel vieler geologischer Studien. Es fanden allerdings nur wenige geophysikalische Projekte statt, weshalb nicht viele Informationen zur Geometrie und allgemeinen Struktur des Ophioliten und der darunterliegenden kontinentalen Lithosphäre existieren. Vor allem Letztere sind notwendig, um den Obduktionsprozess und die Entstehung des Al-Hajar Gebirges zu verstehen.

Das Ziel dieser Arbeit besteht darin, ein 3D Modell der Lithosphäre des östlichen arabischen Kontinentalrandes zu erstellen. Dazu betrieben wir von Oktober 2013 bis Februar 2016 ein temporäres seismisches Netzwerk, welches aus 40 Seismometern bestand, zur kontinuierlichen Aufnahme seismischer Daten. Der Datensatz wurde durch Permanentstationen der Erdbebendienste des Omans und Dubais sowie des Global Seismographic Networks vervollständigt. Phasengeschwindigkeiten für Rayleigh- und Lovewellen können mithilfe eines neuen Ansatzes zur Berechnung von Dispersionskurven unter Nutzung von Ambient Noise Kreuzkorrelationen berechnet werden. Für diesen Ansatz wird die frequenzabhängige Phase der berechneten Kreuzkorrelationen bestimmt. Durch ein Gitter aus theoretischen Phasen ist es möglich, Geschwindigkeiten für jede berechnete Phase zu bestimmen. Das Gitter aus theoretischen Phasen basiert auf der Besselfunktion 3. Art. Im nächsten Schritt können Phasengeschwindigkeitskarten für Rayleigh- und Lovewellen berechnet werden. Sie zeigen Geschwindigkeitsanomalien und azimuthale Anisotropie als Funktion der Periode entlang des östlichen arabischen Kontinentalrandes. Eine Inversion von lokalen Dispersionskurven führt zu 1D-Geschwindigkeitsmodellen über die Tiefe. Diese auf Zufall basierende Inversionsmethode beruht auf der Partikelschwarmoptimierung. Da die Inversion simultan für Rayleigh- und Lovewellen erfolgte, kann neben der isotropen Scherwellengeschwindigkeit auch die radiale Anisotropie bestimmt werden. Durch die Kombination aller 1D Modelle innerhalb unseres Arbeitsgebietes, konnte ein 3D Geschwindigkeitsmodell inklusive radialer Anisotropy über die Tiefe bestimmt werden.

Zusätzlich wurden P- und S- Receiver Funktionen berechnet, um Diskontinuitäten innerhalb der Lithosphäre wie z.B. der Moho oder der Mantelübergangszone darzustellen. Dazu wurden neben dem erhobenen Datensatz 286 Erdbeben aus dem ISC Katalog genutzt. Ein neuer Migrationsansatz führt zu tiefenabhängigen Ergebnissen.

Schließlich können wir das erste dreidimensionale Strukturmodell des östlichen arabischen Kontinentalrandes vorstellen. Es zeigt die 3D Geometrie des Ophioliten und bestätigt dabei bekannte 2D Modelle früherer Arbeiten. Zudem zeigt es Unterschiede innerhalb der deformierten Kruste unterhalb des Al-Hajar Gebirges. Diese sind vor allem westlich und östlich des Semail Gap zu beobachten. Das 3D Model beinhaltet eine Darstellung der Krustenmächtigkeit der gesamten Region. Diese stimmt größtenteils mit den Ergebnissen der Receiver Funktionen überein. Die Mächtigkeit der kontinentalen Kruste nimmt nach Osten hin stetig ab. Im Al-Hajar Gebirge ist eine Zunahme der kontinentalen Krustenmächtigkeit zu beobachten. Am deutlichsten ist dies unterhalb des Jebel Akhdar zu erkennen. Eine gemeinsame Betrachtung von isotroper Scherwellengeschwindigkeit, radialer und azimuthaler Anisotropie liefert zusätzliche Informationen zu vergangenen tektonischen Ereignissen. Dass die tektonischen Fenster im Saih Hatat und Jebel Akhdar durch eine Extionsphase direkt nach der Obduktion entstanden sind, lässt sich durch unsere Ergebnisse bestätigen. Azimuthale Anisotropie in der oberen Kruste würde vorherige Arbeiten bestätigen, welche die Entstehung des Gebirges durch Kompression erklären. Allerdings zeigt die azimuthale Anisoptropie in größeren Tiefen, dass es eine relativ starke Extensionsphase gegeben haben muss, welche durch bisherige Modelle nicht erklärt werden kann. Der Zeitpunkt dieser Extensionsphase muss noch bestimmt werden. Sie würde allerdings zu einer neuen Diskussion zur Entstehung des Al-Hajar Gebirges führen. Westlich und östlich des Semail Gap sind deutliche Unterschiede in der Struktur der kontinentalen Lithosphäre zu erkennen. Zudem ist die Obduktion westlich des Semail Gap weiter vorangeschritten als östlich. Daraus lässt sich schlussfolgern, dass die Eigenschaften der kontinentalen Kruste des westlichen Bereiches wie hohe Verformbarkeit, hohe Krustenmächtigkeit und eine flache Subduktion eher für das Stattfinden einer Obduktion geeignet sind. Somit lässt sich zeigen, dass unsere Ergebnisse, insbesondere das 3D Modell, wichtige Einblicke in die Struktur der Lithosphäre des östlichen arabischen Kontinentalrands liefert. Zudem könnte es dazu führen, dass bisherige Interpretationen zur geodynamischen Entwicklung überdacht werden müssen.

Contents

List of Figures

List of Tables

Chapter 1

Introduction

The Oman Mountains or Al-Hajar Mountains along the eastern passive continental margin of the Arabian plate are since decades of high geological interest. In the past, the entire area was involved in various deformational processes causative for todays shape. One of the most prominent occasions was the emplacement of oceanic crustal and mantle material on the Arabian continent in Mid- Cretaceous resulting in the worlds largest and best preserved ophiolite in northeastern Oman. Additional tectonic processes led to today's topography and the circumstance that every geological strata, either crustal or mantle material of the Oman ophiolite is exposed at the surface [Nicolas et al., 2000; Nicolas and Boudier, 2011]. This is contrasted by a mostly undisturbed Arabian continent. It is known that the Arabian plate is an accretion of single terranes which occured in Precambrium [Stoeser and Camp, 1985; Husseini, 1988; Allen, 2007]. Since then, it was most of the time a stable passive continental margin with almost continuous sedimentation. The Arabian platform partly features very old sediments which can be predated to late Precambrium or middle Cambrium [Gorin et al., 1982; Qidwai et al., 1988; Amthor et al., 2003; Allen et al., 2004; Rieu et al., 2007; Rieu and Allen, 2008]. In this work, we will present a 3D structural model of the lithosphere beneath the eastern Arabian continental margin featuring the different properties of the highly deformed region of the Oman Mountains. It will certainly contribute to the understanding of the obduction process and the formation of today's topography of the Oman Mountains.

1.1 Geological setting

Obduction is one of plate tectonics oddities, where a dense oceanic plate is thrust on top of a light continental one [Coleman, 1971]. The obduction of the Oman ophiolite is part of the Peri-Arabic obduction [Ricou, 1971] which corresponds to an almost synchronous thrust movement from Turkey to Oman, along the convergence zone between Arabia and Eurasia in upper Cretaceous. However, the obduction process itself is still not fully understood and debates ranging from local to large scale thrusting. While local scale thrusting includes e.g. underplating during subduction [Parkinson, 1998], large scale thrusts are associated with intraoceanic subduction [Ricou, 1971; Breton et al., 2004]. Agard et al. (2007) proposed a mechanism in which large scale obduction is triggered by intraplate instabilities as a result of sharp plate acceleration.

The Semail ophiolite in the Oman Mountains stretches over $\approx 700km$ length with a width of up to $\approx 140km$ across the eastern passive continental margin of the Arabian plate. It exhibits its maximum thickness of up to 12 km in the Wadi Andam area, east of the Semail Gap and south of Saih Hatat [Manghnani and Coleman, 1981; Coleman, 1981]. From top to bottom, the Oman ophiolite contains the following sequences: pillow lavas, sheeted dykes, plutonic gabbros and mantle peridodites [Rabu et al., 1993; Hacker and Gnos, 1997]. Beneath the ophiolite, allochthonous deep- ocean sediments (Hawasina) are located which were thrust over the continental margin contemporaneously with the ophiolite. In addition, they are covering parts of the Arabian continental plate south of the Oman Mountains and are exposed in the Hawasina Window (Fig.1.1) within the Oman Mountains. The allochthonous rocks were transported at least 300 km laterally from northeast direction [Searle and Cox, 1999]. Their lateral extent towards southwest is indicated by the Hawasina Frontal Thrust in figure 1.1. Autochthonous middle Permian to late Cretaceous continental shelf sediments (Hajar Supergroup) are located beneath the allochthonous strata of the Oman ophiolite and the Hawasina sediments. Further down, the pre Permian sediments of the Huqf Supergroup are located. The Hajar and Huqf supergroup are exposed in the Jebel Akhdar and Saih Hatat windows (Fig.1.1). In these regions within the Al-Hajar Mountains, the ophiolite got probably eroded. Their formation is related to a post- obductional extension regime in late Maastrichtian to early Paleocene [Michard et al., 1994; Fournier et al., 2006]. Especially in the Saih Hatat window, the exhumed rocks of the Arabian continental margin were partly subducted to depths of more than 60 km [Michard et al., 1991; Michard et al., 1994; Searle et al., 2004] leading to a transformation to high pressure metamorphic rocks like blueshist and eclogite. In contrast, the exhumed rocks in the Jebel Akhdar window are mostly unmetamorphosed. Between the Jebel Akhdar and Saih Hatat dome, the Semail Gap Fault zone is located. It is one of the most prominent tectonic features in the Oman Mountains and extents mostly in northeast direction [Scharf et al., 2019].

The formation of todays topography of the Al- Hajar Mountains is related to a major uplift phase which started in early Oligocene, often referred to a compressional deformation regime. This is documented for example by apatite fission track data [Mount et al., 1998], evaluation of strike-slip and reverse faults [Fournier et al., 2006] or thermochronological data [Hansman et al., 2017]. Further east at the Salmah Plateau towards the Qalhat Fault, the compressional deformation started in Burdigalian (early Miocene) [Wyns et al., 1992]. The cause of the uplift is a still ongoing debate. While a Cenozoic compression in the Musandam area in the northernmost Oman Mountains can clearly be related to the Zagros collision belt in Iran [Ricateau and Riche, 1980; Searle et al., 1983; Searle, 1988; Regard et al., 2005], it is not very clear for the central and eastern Oman Mountains. Besides the proposition of an uplift in the central Oman Mountains due to the Zagros collision [Fournier et al., 2006], Hansman et al. (2017) proposed that the uplift is caused by a slowdown of the Makran subduction in late Eocene, based on their thermal modelling.

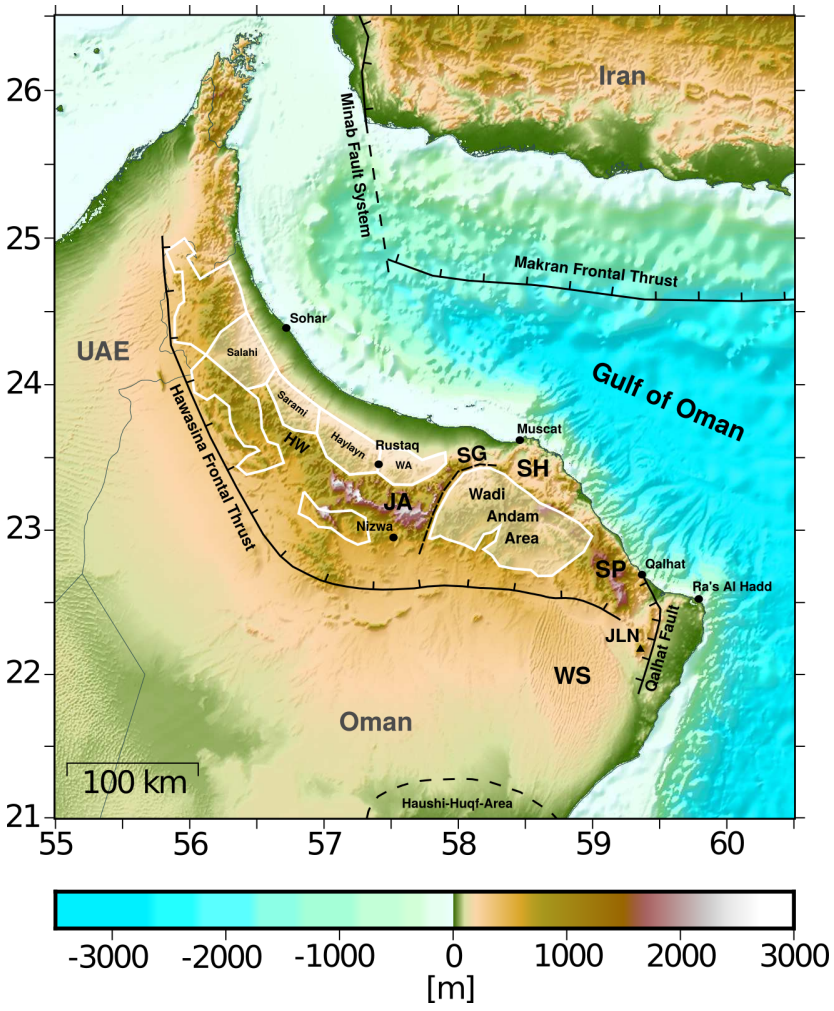

Figure 1.1: Map of the eastern Arabian continental margin showing the most prominent geological features of the area; White areas indicate where the ophiolite is exposed at the surface; SG: Semail Gap; JA: Jebel Akhdar; SH: Saih Hatat; HW: Hawasina Window; WA: Wadi Abiyyad; SP: Salmah Plateau; WS: Wahiba Sands; JLN: Jebel Ja'alan

Besides the Semail ophiolite in the Al-Hajar Mountains, there are different ophiolite occurrences along the southeastern passive continental margin which are mainly existent on Masirah Island. Therefore, it is called Masirah ophiolite. The Masirah oceanic crust was formed in upper Jurassic [Gnos and Perrin, 1996; Gnos et al., 1997] which is earlier than the Semail oceanic crust in the Al-Hajar Mountains. The obduction of the Masirah ophiolite occured later than the Semail ophiolite during late Maastrichtian to Paleocene times [Shackleton and Ries, 1990; Smewing et al., 1991; Schreurs and Immenhauser, 1999] and can be related to the northward drift of the Indian plate along the southeastern Arabian continental margin. In addition to the obduction of the Masirah ophiolite, the southeastern Arabian continental margin was affected by various episodes of faulting which are related to the breakup of Gondwana and the Tethyan rifting [Montenat et al., 2003; Béchennec et al., 1993; Pratt and Smewing, 1993]. The area features a NNE- trending paleohigh extending from the easternmost part of Arabia (Ra's Al Hadd) across the Wahiba Sands to Salalah in Dhofar. The Haushi-Huqf area (see location in Fig.1.1) is probably the most prominent part of that paleohigh since it features onces uplifted old Paleozoic sediments [Dubreuilh et al., 1992]. The uplift began in Paleozoic (probably pre- Ordovician) which is shown by local open folds and continued intermittently until late Cretaceous where the major uplift by faulting occured [Ries and Shackleton, 1990].

1.2 Motivation

Despite of being the best preserved and probably best studied ophiolite in the world in case of geological field and laboratory investigations, only a few geophysical studies took place in the past. For that reason, the internal structure of the Oman Mountains and the 3D geometry of the ophiolite is fairly unknown. Most of the geophysical studies to estimate ophiolite thicknesses are based on gravity data [Shelton, 1990; Manghnani and Coleman, 1981] or a joint interpretation of gravity data and different geophysical methods [Ravaut et al., 1997; Al-Lazki et al., 2002]. Their results revealed a distinct negative Bouguer anomaly in the mountain area which they modelled with a crustal thickness of up to $47km$ beneath Jebel Akhdar and further northwest. In addition, they showed positive Bouguer anomalies of the ophiolite section with a modelled contrast of $\approx 400-500g/cm^3$ to the surrounding crust. This corresponds to one of the first laboratory measurements of seismic velocities and densities on rock samples of the Oman ophiolite in that region [Christensen and Smewing, 1981]. The ophiolite thickness has been interpreted to reach $3-4km$ in the Sarami region north of the Hawasina window [Shelton, 1990], $4-9km$ in the Haylayn region northwest of Jebel Akhdar [Shelton, 1990; Ravaut et al., 1997] and up to 12 km in the Wadi Andam area east of the Semail gap [Manghnani and Coleman, 1981] (see Fig.1.1 for locations). Al-Lazki et al. (2002) provided a cross section of the crust through the central part of the Al-Hajar Mountains, including the Jebel Akhdar window by using a variety of geophysical methods (gravity

data, receiver functions and well data). They proposed an ophiolite thickness of $\approx 4-5km$ north of Jebel Akhdar in the Wadi Abiyyad area. Seismic refraction studies in the northern UAE revealed a similar thickness [Naville et al., 2013]. Since these studies were only locally in form of 2D profiles, they are not suitable to image possible lateral variations of the thickness of the Oman ophiolite which is necessary to understand the processes leading to the ophiolite emplacement. Lateral variations in ophiolite thickness might occur in case of strong deformational processes during the obduction process.

Oceanic lithosphere is strongly anisotropic [Hess, 1964] and different geological units show varying paleomagnetic directions [Godard et al., 2003]. Therefore, information on azimuthal anisotropy of the Oman ophiolite might also contribute to the determination of its vertical and lateral extent. In addition, information on azimuthal anisotropy for the entire crust can be used to identify deformational processes in the past like extension or compression and therefore contribute to the understanding of the formation and shape of the Oman Mountains.

The structure and thickness of the continental lithosphere beneath the Al-Hajar Mountains is of high interest, since the extent and dynamics of the obduction process is strongly depending on it [Duretz et al., 2016]. Models of the crustal thickness are again mostly based on gravity data [Ravaut et al., 1997; Al-Lazki et al., 2002; Jiménez-Munt et al., 2012]. The 2D profiles from Ravaut et al. (1997) show a localized crustal thickening beneath the Al-Hajar Mountains. The same counts for the model from Al-Lazki et al. (2002). They proposed a crustal thickening of up to $\approx 49km$ beneath Jebel Akhdar based on their gravity data and receiver functions. The gravity based model of the region from Jimenez-Munt et al. (2012) shows a thinning of the crust towards southeast. This is comparable to the Crust1.0 model [Laske et al., 2013] in that region. However, both models do not show local features like the crustal thickening beneath the Oman Mountains. Al-Hashmi et al. (2011) performed a joint inversion of receiver functions and Rayleigh wave group velocities to obtain information regarding the lithospheric structure in Oman by using the instruments of the Oman Seismic Network. They proposed a relatively constant crustal thickness of 36 to 48 km with only small, local variations across the eastern Arabian continental margin. However, their results are varying to Crust1.0, especially in the eastern part of the eastern Arabian continental margin. Less than 30 km of crustal thickness in the Crust1.0 model are in contrast to more than 40 km in the results from Al-Hashmi et al. (2011). The previous information on the crustal thickness is not sufficient enough to contribute to the overall understanding of the crust and its influence on geodynamical processes. Mapping of the entire crust is necessary to understand the overall formation of the Oman Mountains, especially the emplacement of the Oman ophiolite, but later deformational processes as well.

In this work, we will estimate a 3D model of shear wave velocity over depth by using a probabilistic 1D inversion method (Particle Swarm Optimization) to provide information on the lateral and vertical extent of the Oman ophiolite. In addition, the model will feature velocity

distributions for the entire crust, including a map of the crustal thickness beneath the eastern Arabian continental margin. Since the estimation of the 3D model is performed by inverting Rayleigh and Love wave phase velocity dispersion curves, we are able to calculate radial anisotropy for the entire 3D model. Radial anisotropy can be related to deformational processes in the past and provides infortmation regarding the deformability of the lithospheric structure. Rayleigh and Love wave dispersion curves are calculated via surface wave tomography using the vertical and horizontal components of ambient seismic noise cross correlations. By implementing a new approach for estimating phase velocity dispersion curves at low periods, we are able to sufficiently resolve the structure of the upper crust of the Oman Mountains. Besides Rayleigh and Love wave phase velocities as a function of period, the resulting phase velocity maps will provide information on azimuthal anisotropy for the entire region of the Oman Mountains and therefore indications on former deformational processes like extension and compression which have highly affected the todays shape of the Al- Hajar Mountains. In addition, P- and S- receiver functions will be calculated to confirm our results on the crustal thickness beneath the Al-Hajar Mountains and provide additional information on deeper discontinuities in the Earth mantle. The key questions of this work are the following:

Are we able to resolve the vertical and lateral extent of the Oman ophiolite from our 3D model and is it confirming previous results on the ophiolite thickness? Can we relate variations in the ophiolite thickness to lateral variations of the obduction process? What information can be provided regarding the present state of the continental plate, whose properties are from high interest since they control the extent and dynamics of the obduction process?

How do our obtained information from the 3D model including radial anisotropy in combination with azimuthal anisotropy contribute to the understanding of the formation of the Al-Hajar Mountains? What is the driving force of the Mountain building? Why are the Jebel Akhdar and Saih Hatat windows so localized? Are there any relations to the Semail Gap? What is the origin of the lokalized crustal thickening beneath the Oman Mountains? When did the thickening occur?

What informatios can we obtain for the crustal thickness from P- and S- receiver functions? Are they consistent with previous works? Are there any information regarding the lithosphere- asthenosphere boundary and deeper discontinuities like the mantle transition zone?

Besides of geodynamic questions, this work also deals with new methodical approaches to calculate the 3D model. Therefore, their reliabilities are also from interest. This includes a new apporach to calculate Rayleigh and Love wave phase velocity curves at low periods (<10 s). What is the minimum period for which we still receive a reliable result in the following surface wave tomography? What are the advantages to other common methods for calculating phase velocity dispersion curves? What is the resolution of the calculated phase

velocity maps? The calculation of the 3D model is based on a probabilistic 1D inversion method (Particle Swarm Optimization) which inverts for Rayleigh and Love wave dipsersion curves simultaneously to include radial anisotropy. What are the uncertainties and limitations of the inversion?

1.3 Data

From October 2013 to February 2016, we operated a temporary seismic network consisting of 40 broadband seismometers which were provided by the GIPP- Pool of the GFZ Potsdam (Fig. 1.2). They are covering mostly the Al- Hajar Mountains in northern Oman and parts of the Arabian continent south of the mountain range with an average spacing of around 20 km. The seismometers recorded continuously over these 2.5 years with a sampling of 100 Hz. The amount of data loss due to e.g. mechanical failure is minor and more then 90 percent of the data is available for processing. The dataset was completed by data of 13 permanent broadband seismometers, operated by the Earthquake Monitoring centre Oman and one GSN Station in UAE. Later, we got additional data from four station from the Dubai seismic network.

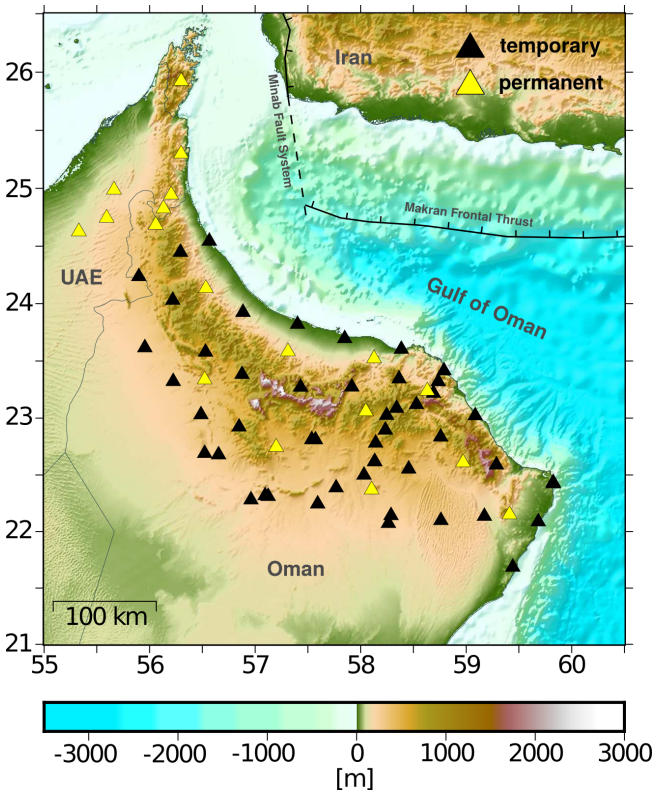

Figure 1.2: Stationmap, showing the location of all the stations used in this work; black triangles: temporary seismic network; yellow triangles: permanent stations operated by the Earthquake Monitoring Centre Oman (13), Dubai Seismic Network (4) and GSN (1)

Chapter 2

Ambient noise surface wave tomography

The second chapter of the thesis deals with surface wave tomography to estimate Rayleigh and Love wave phase velocity maps capable for imaging the lithospheric structure of the eastern Arabian continental margin. For that reason, we use the continuously recorded data to calculate ambient seismic noise cross correlations for the vertical and transverse component and each path within our array of temporary and permanent stations. Afterwards, a newly implemented approach for calculating surface wave phase velocity dispersion curves will be introduced. Details about this new approach will be provided including synthetic tests which will substantiate its advantages and robustness in our case compared to more common approaches for estimating phase velocity dispersion curves. An automated picking process leads to smooth and realistic phase velocity dispersion curves for each inter-station path. The resulting phase velocity curves are used to estimate phase velocity maps for Rayleigh and Love waves at periods ranging from 2 to 40 s. The last part of the chapter also deals with the effects of regularization on the tomographic inversion. A checkerboard test provide information on the quality of the resulting phase velocity maps at certain periods. Finally, results of different features, either from isotropic or azimuthal anisotropic phase velocity maps will be presented.

2.1 Seismic waves

2.1.1 Body waves

Body waves can be divided into longitudinal or compressional waves (P- waves) and transverse or shear waves (S- waves). They traverse through the interior of the medium. P- waves are the fastest type of all waves and arrive mainly at first after an event. They oscillate in the direction of travel, cause volumetric changes of the medium and can progate through fluids as well. In contrast, S- waves are slower than P- waves and oscillate in transverse direction of the direction of propagation without any kind of volume change of the medium. For that reason, S- waves can not propagate through fluids [Lay and Wallace, 1995].

2.1.2 Surface waves

Next to body waves, there is a second main type of seismic waves, surface waves. They propagate along the free surface. Normaly, surface waves have the strongest amplitudes in seismograms. However, they are slow compared to body waves and their velocity is strongly frequency dependent. Due to geometrical spreading the energy of surface waves disperse in just two dimensions, with a decay of $1/r$ with increasing distance r from the source. In contrast, body waves are dissipating in three dimensions with an energy loss of $1/r^2$. There are two types of surface waves: Rayleigh and Love waves.

Rayleigh waves

Rayleigh waves are named after Lord Rayleigh, who first mathematically proofed their existence in 1885 [Rayleigh, 1885] before they were first observed. They arise due to interference between multiple reflected P- waves and vertically orientated S- waves (SV) with the free surface. That results in a retrograde, elliptical particle motion along the free surface [Kennett, 1976; Shearer, 2009]. It is possible to derive the equation for Rayleigh waves from the wave equation of plane P- waves by introducing a free surface. The derivation mainly follows Shearer (2009):
The wave equation of a plane P- wave, propagating in $+x$ direction is given by

$$u = Ae^{-i\omega(t-ps-\eta z)}, \tag{2.1}$$

with p : horizontal slowness; $\eta = \sqrt{\frac{1}{c^2} - p^2}$: vertical slowness; c: P- wave velocity.
It is possible to express the wave equation in form of a scalar potential ϕ for a P- wave and a vector potential Ψ for a S- wave, like:

$$u = \nabla\phi + \nabla \times \Psi \tag{2.2}$$

Ψ_y is the only part of Ψ which excites SV motion for plane wave propagation in x direction. Solutions for ϕ and Ψ_y are given by:

$$\phi = Ae^{-i\omega(t-px-\eta_\alpha z)}, \tag{2.3}$$
$$\Psi_y = Be^{-i\omega(t-px-\eta_\beta z)}, \tag{2.4}$$

with A and B as the amplitudes of the P- and SV- waves, respectively. The vertical slownesses η_α and η_β are given by

$$\eta_\alpha = \sqrt{\frac{1}{\alpha^2} - p^2}, \tag{2.5}$$
$$\eta_\beta = \sqrt{\frac{1}{\beta^2} - p^2} \tag{2.6}$$

By assuming that P and SV have the same horizontal slowness, the ray parameter p is constant. In addition, the y component of the displacement and its partial derivatives are zero for P and SV plane wave, due to the propagation in $+x$ direction. Therefore, the P- and SV-wave displacements can be expressed as:

$$u_x^P = \partial_x\phi = pAi\omega e^{-i\omega(t-px-\eta_\alpha z)}, \tag{2.7}$$
$$u_z^P = \partial_z\phi = \eta_\alpha Ai\omega e^{-i\omega(t-px-\eta_\alpha z)}, \tag{2.8}$$
$$u_x^S = -\partial_z\Psi_y = -\eta_\beta Bi\omega e^{-i\omega(t-px-\eta_\beta z)}, \tag{2.9}$$
$$u_z^S = \partial_x\Psi_y = pBi\omega e^{-i\omega(t-px-\eta_\alpha z)}. \tag{2.10}$$

For the next step, we introduce the boundary condition of a free surface $z = 0$. Thus, the normal and shear tractions must vanish: $\tau_{xz} = \tau_{zz} = 0$.

$$\tau_{xz} = \mu(\partial_z u_x + \partial_x u_z), \tag{2.11}$$
$$\tau_{zz} = \lambda(\partial_x u_x + \partial_z u_z) + 2\mu\partial_z u_z. \tag{2.12}$$

By substituting (2.7) - (2.10) into (2.11) and (2.12), we obtain:

$$\tau_{xz}^P = -A(2\mu p\eta_\alpha)\omega^2 e^{-i\omega(t-px-\eta_\alpha z)}, \tag{2.13}$$
$$\tau_{zz}^P = -A[(\lambda+2\mu)\eta_\alpha^2 + \lambda p^2]\omega^2 e^{-i\omega(t-px-\eta_\alpha z)}, \tag{2.14}$$
$$\tau_{xz}^S = -B\mu(p^2-\eta_\beta^2)\omega^2 e^{-i\omega(t-px-\eta_\beta z)}, \tag{2.15}$$
$$\tau_{zz}^S = -B(2\mu p\eta_\beta)\omega^2 e^{-i\omega(t-px-\eta_\beta z)}. \tag{2.16}$$

For the free surface, we require:

$$\tau_{xz} = \tau_{xz}^P + \tau_{xz}^S, \tag{2.17}$$
$$\tau_{zz} = \tau_{zz}^P + \tau_{zz}^S. \tag{2.18}$$

Now, it is possible to substitute (2.13) - (2.16) into (2.17) and (2.18). After simplifications, we get:

$$A(2p\eta_\alpha) + B(p^2 - \eta_\beta^2) = 0, \tag{2.19}$$
$$A[(\lambda + 2\mu)\eta_\alpha^2 + \lambda p^2] + B(2\mu\eta_\beta p) = 0. \tag{2.20}$$

By substituting $\lambda + 2\mu = \rho\alpha^2$, $\mu = \rho\beta^2$ and $\lambda = \rho(\alpha^2 - 2\beta^2)$, the equations for τ_{zz} can be written in terms of P and S velocities.

$$A[2p\eta_\alpha] + B[p^2 - \eta_\beta^2] = 0, \tag{2.21}$$
$$A[\alpha^2(\eta_\alpha^2 + p^2) - 2\beta^2 p^2] + B[2\beta^2\eta_\beta p] = 0. \tag{2.22}$$

These two equations describe the free surface boundary conditions for P- and SV- waves, where p is the horizontal slowness. The vertical slownesses η_α and η_β were defined in (2.5) and (2.6) and are imaginary in case of $p > \beta^{-1} > \alpha^{-1}$. By excluding the depth dependence from (2.1), we obtain

$$u = Ae^{i\omega\eta z}e^{-i\omega(t-px)}. \tag{2.23}$$

Imaginary values for η will lead to real values in the exponent and so- called evanescent waves. Evanescent waves are inhomogeneous waves and their amplitudes grow or decay exponentially as a function of depth. The equations (2.19) and (2.20) can be written in matrix form, to produce a linear system of equations for A and B.

$$\begin{bmatrix} (2p\eta_\alpha) & (p^2 - \eta_\beta^2) \\ \alpha^2(\eta_\alpha^2 + p^2) - 2\beta^2 p^2 & B(2\beta^2\eta_\beta p) \end{bmatrix} \quad \begin{bmatrix} A \\ B \end{bmatrix} = 0$$

We achieve the non- trivial solution only when the determinant equals zero.

$$(p^2 - \eta_\beta^2)[\alpha^2(\eta_\alpha^2 + p^2) - 2\beta^2 p^2] - 4\beta^2 p^2 \eta_\alpha \eta_\beta = 0 \tag{2.24}$$

Resubstituting for η_α and η_β, lead to an equation in terms of p and P- and S- wave velocities:

$$\left(2p^2 - \frac{1}{\beta^2}\right)^2 + 4p^2\left(\frac{1}{\alpha^2} - p^2\right)^{\frac{1}{2}}\left(\frac{1}{\beta^2} - p^2\right)^{\frac{1}{2}} = 0 \tag{2.25}$$

By assuming η_α and η_β as imaginary values ($p > \beta^{-1} > \alpha^{-1}$), this can be rewritten as:

$$\left(2p^2 - \frac{1}{\beta^2}\right)^2 - 4p^2 \left(p^2 - \frac{1}{\alpha^2}\right)^{\frac{1}{2}} \left(p^2 - \frac{1}{\beta^2}\right)^{\frac{1}{2}} = 0 \tag{2.26}$$

This is the Rayleigh function. It depends on P- wave velocity (α) and S- wave velocity (β). The terms of the equations which yield the roots give the Rayleigh wave velocity. It propagates along an isotropic and elastic surface of a half space $(y > 0)$. The corresponding phase velocity is $c = \frac{1}{p}$ and is always slightly smaller than β.

Love waves

Love waves are formed by constructive interference of horizontal polarized shear waves at the free surface. They are transversely polarized. Unlike Rayleigh waves, Love waves require an increase in velocity with depth [Shearer, 2009]. Therefore, with increasing shear wave velocity with depth, a waveguide can be formed, in which rays are multiply reflected between the surface and reflection points. The energy is trapped, if the ray strikes the reflection point at postcritical angles [Lay and Wallace, 1995]. By assuming that Love waves are trapped within a layer (β_1) over a halfspace (β_2), the dispersion equation for Love waves can be written as [Lay and Wallace, 1995]:

$$\tan\left(\omega \eta_\beta 1 H\right) = \frac{\mu_2 \eta_\beta 2}{i \mu_1 \eta_\beta 1} = \frac{\mu_2 \hat{\eta}_\beta 2}{\mu_1 \eta_\beta 1}, \tag{2.27}$$

with H as the thickness of the layer and ω as the frequency. A postcritical situation, where the phase velocity $c = \frac{1}{p} < \beta_2$ will yield $\eta_\beta 2 = i\hat{\eta}_\beta 2$ and $\hat{\eta}_\beta 2$ is real. Equation (2.27) gives a condition which is related to ω and c and must be satisfied. Rewriting equation (2.27) yields:

$$\tan\left(H\omega \sqrt{\frac{1}{\beta_1^2} - \frac{1}{c^2}}\right) = \frac{\mu_2 \sqrt{\frac{1}{c^2} - \frac{1}{\beta_2^2}}}{\mu_1 \sqrt{\frac{1}{\beta_1^2} - \frac{1}{c^2}}}. \tag{2.28}$$

This equation depends only on the material parameters μ_1, μ_2, β_1 and β_2 and the variables c and ω. If the condition $\beta_1 < c < \beta_2$ is ensured, then the solution is real.

Dispersion of surface waves

Surface waves are dispersive which means that their velocity changes as a function of frequency as they are propagating away from the source. Individual components of surface waves (modes) propagate with different velocities. Since the velocity is the product of frequency and wavelength, lower frequencies possess longer wavelengths and penetrate deeper into the Earth. Furthermore, lower frequencies pass through the Earth with higher velocities, because in general the velocity increases with depth.

When different frequency components travel with different phase velocities, pulse shapes will not stay the same as they travel but will become dispersed as the frequencies separate [Shearer, 2009]. This results in interferences of wave disturbances with constructive and destructive patterns. Constructive interference patterns behave like wave packets, which propagate along the surface with their group velocity $U(\omega)$. The effect of dispersion can be illustrated by considering two harmonic waves with slightly different frequencies and wavenumbers. Following Shearer (2009), the sum of of the two waves can be written as:

$$u(x,t) \;=\; \cos(\omega_1 t - k_1 x) + \cos(\omega_2 t - k_2 x). \tag{2.29}$$

Here, $\omega_{1,2}$ are the specific frequencies and $k_{1,2}$ are the different wavenumbers for both harmonic waves. They can be written as a function of their average values ω and k:

$$\omega_1 \;=\; \omega - \delta\omega, k_1 = k - \delta k, \tag{2.30}$$

$$\omega_2 \;=\; \omega + \delta\omega, k_2 = k + \delta k, \tag{2.31}$$

By substituting these equations into (2.29), we obtain

$$u(x,t) \;=\; \cos(\omega t - \delta\omega t - kx + \delta kx) + \cos(\omega t + \delta\omega t - kx - \delta kx) \tag{2.32}$$

$$=\; \cos[(\omega t - kx) - (\delta\omega t - \delta kx) + \cos[(\omega t - kx) + (\delta\omega t - \delta kx)] \tag{2.33}$$

$$=\; 2\cos(\omega t - kx)\cos(\delta kx - \delta\omega t), \tag{2.34}$$

by using the trigonometric identity $2\cos(A)\cos(B) = \cos(A+B) + cos(A-B)$. This results in a signal with an average frequency and wavenumber. The values for $\delta\omega$ and δk are smaller than their corresponding average values ω and k. For that reason, the second term of (2.34) varies less in time and space than the first one. The velocities of both terms are different. The velocity of the short period term is called phase velocity (ω/k), whereas the long period term is called group velocity, which can be written as:

$$U(\omega) = \frac{d\omega}{dk}. \tag{2.35}$$

By using the relationship of harmonic wave parameters, the frequency is also the product of velocity and wavenumber $(\omega = ck)$. Therefore, group velocities can be expressed as

$$U = \frac{d\omega}{dk} = \frac{dck}{dk} = c + k\frac{dc}{dk} = \left(1 - k\frac{dc}{d\omega}\right)^{-1}. \tag{2.36}$$

In general, the phase velocities of Rayleigh and Love waves increase with period. Due to (2.36) and the fact that $\frac{dc}{d\omega}$ is negative, group velocities do not only depend upon phase velocities but are smaller as well $(U < c)$ [Shearer, 2009]. If phase velocities are constant over frequency, group- and phase velocities would be the same.

2.1.3 Ambient noise tomography

Surface wave tomography by using ambient seismic noise from continuous seismic records is still a relative new method for imaging the subsurface compared to the ones using teleseismic data. First investigations started around the beginning of the century. Since then, it became a common method to provide structural information of the lithosphere [Sabra et al., 2005; Shapiro et al., 2005; Yao et al., 2006; Lin et al., 2008; Yang et al., 2007; Bensen et al., 2008; Stehly et al., 2009]. In contrast to Surface wave tomography of teleseismic data, the period range of cross correlated ambient seismic noise allows for estimations of surface wave velocities at periods smaller than 50s [Stehly et al., 2006] and thus better imaging of the lithosphere- asthenosphere system [Kästle et al., 2016].

The cross correlation of ambient seimic noise between two station allows us to calculate the Green's function. This can be associated with a point source at the location of one station and the receiver at the location of the second one [Shapiro and Campillo, 2004]. If we assume only one source, the Fourier transform of the cross correlation can be written as [Sheriff and Geldart, 1995]:

$$\mathscr{F}\{\rho_{u_1u_2}(t)\} = u_1(\omega)u_2^*(\omega) \tag{2.37}$$

By assuming a single force $f(\omega)$ and looking just at the vertical component of the seismogram $u_i(\omega)$, it can be written as:

$$u_i(\omega) = G_i(\omega)f(\omega) \tag{2.38}$$

with $G_i(\omega)$ as the Green's function. Therefore, (2.37) can be expressed as:

$$\mathscr{F}\{\rho_{u_1u_2}(t)\} = G_1(\omega)G_2^*(\omega)|f(\omega)|^2 \tag{2.39}$$

$$\mathscr{F}\{\rho_{u_1u_2}(t)\} = |G_1(\omega)||G_2(\omega)|e^{i\Delta\phi(\omega)}|f(\omega)|^2|f(\omega)|^2 \tag{2.40}$$

For ambient seismic noise, it is necessary to assume that there is a uniform distribution of sources in space like it is shown in Fig. 2.1 and (2.40) needs to be written as:

$$\mathscr{F}\{\rho_{u_1u_2}(t)\} = \iint |G_1(\omega)||G_2(\omega)|e^{i\Delta\phi(\omega)}|f(\omega)|^2|f(\omega)|^2 dxdy \tag{2.41}$$

This can be simplified by applying the stationary phase effect which can be used for dispersive surface waves [Aki and Richards, 2002]. The integration is performed along paths for which the phase remains constant and the amplitude possesses the highest gradients. In general, this can be expressed as:

$$\int A(y)e^{i\phi(y)}dy \Rightarrow \frac{d\phi}{dy} = 0 \tag{2.42}$$

According to this, there is a self- canceling effect on the integral along the y- axis and only the integral along the x- axis is remaining, which represents the path of the two stations. This means that only sources on the great circle along the path of the two stations are contributing to the cross correlation, except the ones between these two. This is also shown in Fig. 2.1. In addition, it is possible to differ between the causal and acausal part of the cross correlation, by considering Huygen's principle. It describes the principle of propagating waves and states that any point on a wavefront can be a point source for a new spherical wave. In addition, it allows to forecast the future position of a wavefront if its present position is known [Lowrie and Fichtner, 2007]. In general, we obtain:

$$\int A(y)e^{i\phi(y)}dy = \sqrt{\frac{2\pi}{\phi''(0)}}A_0 e^{i(\phi(0)\pm\frac{\pi}{4})} \tag{2.43}$$

Together with the method of stationary phase, (2.41) can be rewritten:

$$\mathscr{F}\{\rho_{u_1u_2}(t)\} = \int A(\omega)dx\sqrt{\frac{2\pi}{\phi''(0)}}e^{i(\phi(\omega)\pm\frac{\pi}{4})} \tag{2.44}$$

In addition, it is necessary to consider that the waves can travel from both directions. Either they are propagating from station 1 to station 2 or vice versa. Therefore, the phase difference $\Delta\phi(\omega)$ differ like:

$$\Delta\phi(\omega) = -kR \qquad (Station1 \Rightarrow Station2) \tag{2.45}$$

$$\Delta\phi(\omega) = kR \qquad (Station2 \Rightarrow Station1) \tag{2.46}$$

with R as the inter-station distance. This can be inserted in (2.44):

$$\mathscr{F}\{\rho_{u_1u_2}(t)\} = \sqrt{\frac{2\pi}{\phi''(0)}}e^{-i(kR+\frac{\pi}{4})}\int_{-\infty}^{0} A(\omega)dx + \sqrt{\frac{2\pi}{\phi''(0)}}e^{i(kR+\frac{\pi}{4})}\int_{R}^{\infty} A(\omega)dx \tag{2.47}$$

The first summand represents the causal and the second one the acausal part of the double sided cross correlation function. The calculation of the single sided cross correlation $\bar{\rho}_{u_1u_2}(t)$ leads to the symmetric part of the cross correlation :

$$\bar{\rho}_{u_1u_2}(t) = \frac{1}{2}(\rho_{u_1u_2}(t) + \rho_{u_1u_2}(-t)) \tag{2.48}$$

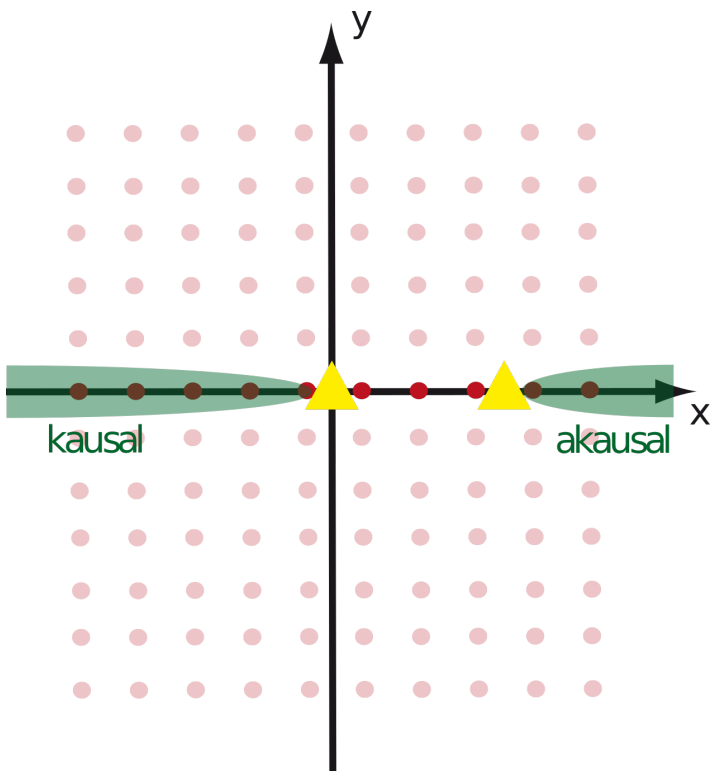

Figure 2.1: Distribution of noise sources (red dots) in two dimensions; Sources, which contribute to the cross correlation of the two stations (yellow triangles) are highlighted (green)

A phaseshift of $-\frac{\pi}{4}$ of the cross correlation function leads to the frequency depending Green's function. The Green's function can be used to estimate the structure of the subsurface at various depths in different ways. The common approaches are to calculate either group velocities [Shapiro et al., 2005; Yang et al., 2007; Stehly et al., 2009] or phase velocities [Lin et al., 2008; Ekström et al., 2009]. Tromp et al. (2010) were the first who introduced the inversion of the entire ambient noise waveform. However, for the ambient seismic noise method, we assume an equal distribution of sources, which is only valid in theory. In practice, we might have to deal with predominent directions of local noise sources. This will probably lead to errors in the results and needs to be corrected.

Boschi et al. (2012) derived different approaches to calculate surface wave phase velocities, by following the approach of Tsai and Moschetti (2010). The first one is based on calculations using the far- field approximation in time domain, while the second approach is dealing with the real part of the spectrum in frequency domain. Later, Kästle et al. (2016) improved the second approach of Boschi et al. (2012). He calculated phase velocities by using the zero crossings of the real part of the spectrum of the cross correlation and the Bessel function. The basic idea to that approach goes back to Aki (1957). In this work, we develope a different approach for calculating phase velocities. This will be discussed in Chapter 2.3.1.

2.2 Ambient noise cross correlation

As mentioned before in section 2.1.3, we are aiming for the frequency depending Green's function to calculate phase velocity dispersion curves for Rayleigh and Love waves. Methods using ambient seismic noise are based on long term correlations of passive seismic data in combination with a necessary amount of stacking for stabilization. The data processing, to achieve the cross correlation functions, mainly follows the procedure described by Bensen et al. (2007). After cutting the waveforms of two stations to common times, apply a resampling and a filtering (exact values are listed in Tab. 2.1), a normalization in time domain is performed for each station individually. Afterwards we calculate the cross correlation function, before a whitening in the frequency domain is applied on the result. In case of calculating Love wave dispersion curves, it is necessary to rotate the north and east component of the raw data into the direction of the path between the two stations, to evaluate the transverse component.

In general, ambient seismic noise is characterized by weak amplitudes compared to earthquakes and other temporary or local sources. By applying a time domain normalization, we homogenize the amplitudes gradually to the ones of the noise and remove the influence of temporary sources like earthquakes in our measurements. For that reason, we apply multiple bandpass filtered envelopes as inverse weights to the data, to treat parts of the wave seperatly. The corner frequencies for each bandpass filter are also listed in Tab. 2.1. In addition, we introduce a water level onto the weight functions to prevent the waveforms to be weighted below a certain value or even to zero. In our case, we use a water level of ten percent of the root mean square of the amplitude.

After calculating the cross correlation, a whitening of the spectrum needs to be done to reduce the influence of permanent sources like microseism in the ocean. This is performed in frequency domain, in which we normalize the spectrum by its own weighted amplitude spectrum. It is weighted by an exponent in a range of [0,1]. This results in a normalization of the spectrum and a reduction of the influence of permanent sources like microseism in the oceans. Inverse Fourier transformation yields the cross correlation function in time domain.

We performed the noise correlation on daily data with a criterion, that 20h of a day need to be existent. The resulting cross correlation function is in a frequency range of 0.01 Hz to 1Hz.

Table 2.1: List of parameters for noise correlation

Parameter	Value
data segmentation for one correlation	24h
criteria for minimum amount of data	20h
Resampling	5Hz
Filter	0.01 - 1Hz
Bandpassfilter for weight functions in time domain normalization	0.01 - 0.1Hz 0.1 - 0.2Hz 0.2Hz - 1Hz
Weight exponent for Whitening	0.7

We calculated the cross correlations for the vertical and transverse component and each possible combinations of station pairs. Overall, it resulted in 2113 cross correlations for the vertical component and 1805 for the transverse component with an average amount of around 600 stacks per path.

At this point it is already possible to obtain information from the Green's functions, without calculating phase velocity dispersion curves. Fig.2.2 shows the daily cross correlation functions of one path for vertical and transverse component. Here, a bandpassfilter from 0.01 Hz to 0.143 Hz is applied. Looking at the vertical component, a clear signal can be identified at $\pm 50s$ which is the Rayleigh wave fundamental mode. However, the amplitudes are higher in the acausal part of the cross correlation functions, most likely due to uneven distributed noise sources and predominent directions of the noise. In addition, variations in the amplitudes, such as in the time from May to September, can be refered to seasonal variations of noise source, possibly due to local climate changes or even monsoon periods in Asia. Compared to the vertical component, the transverse component shows a much lower signal to noise ratio. However, it is possible to detect the Love wave fundamental mode, again with higher amplitudes in the acausal part. Seasonal variations are observable, but not as clear as in the vertical component.

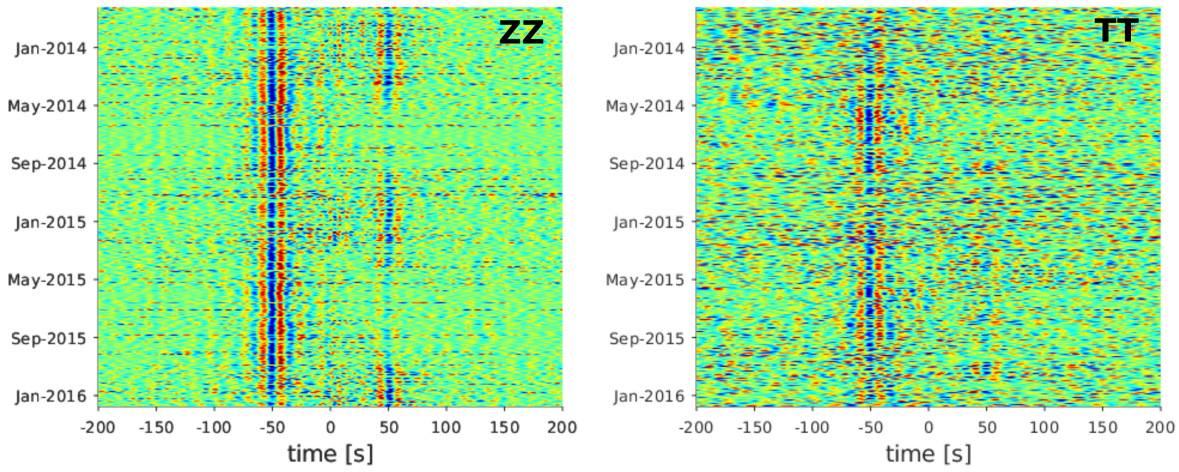

Figure 2.2: Daily cross correlation functions of one path for the vertical and transverse component; filtered between 0.01 Hz an 0.143 Hz

Moreover, it is possible to calculate group velocities of the cross correlation functions by using the Multiple Filter Technique (MFT) [Dziewonski et al., 1969]. Filtering for every period and calculating the enveloppe enables us to analyze the frequency dependent cross correlation function (Fig.2.3). This allows us to evaluate the cross correlation regarding dispersion, propagation with depth or influence from higher modes. The amplitude spectra is located on the right side. For the vertical component, a clear amplitude maximum of the fundamental mode can be observed at periods between 4 and 50 s. The corresponding lag time is then the group traveltime which can be used to estimate group velocities. At periods smaller than 4s, there might be an influence of higher modes or different interfering wave packages which makes a clear identification of the fundamental mode difficult. For the horizontal component, the fundamental mode is clearly observable to a minimum period of around 10 s. Again, a lower signal to noise ratio prevents us to evaluate smaller periods. This can also be seen in the stacked cross correlation function on top of the spectrograms, where only for the vertical component a clear Green's function is present. The one for the horizontal might be superposed by high frequency noise.

At last, Fig.2.4 shows the cross correlation functions, again for the vertical and transverse component and each path, sorted by inter-station distance. They are filtered between 0.01 and 0.1 Hz. For both, vertical and transverse component, a clear fundamental mode can be observed. With increasing inter-station distance, the amplitudes of the acausal part remain stronger, compared to the ones in the causal part. This kind of result also reflects the quality of the ambient noise cross correlations. For the vertical component, an almost lineraly propagating fundamental mode can be observed up to around 450 km inter-station distance. In contrast, the transverse component features again a relatively low signal to noise ratio. The fundamental mode can be observed up to 350 km inter-station distance.

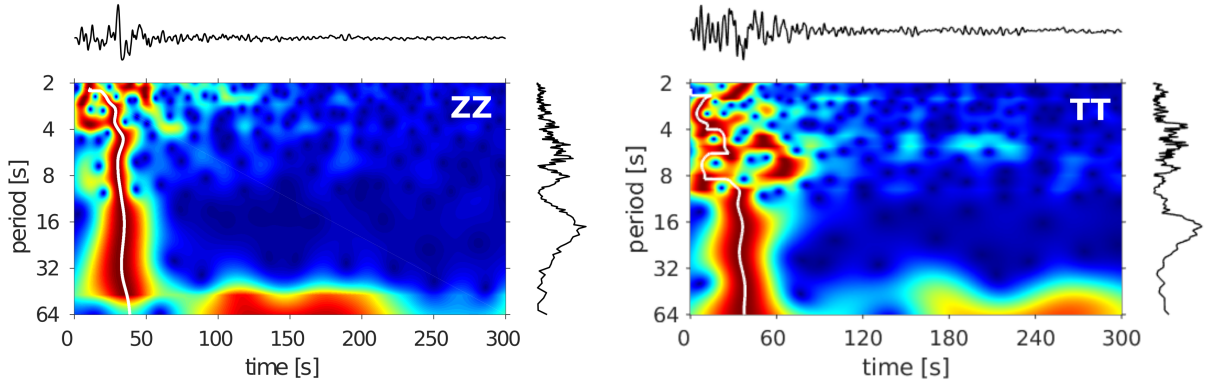

Figure 2.3: Spectrograms of a stacked single sided cross correlation function for the vertical and transverse component; top: stacked cross correlation function; right: amplitude spectrum

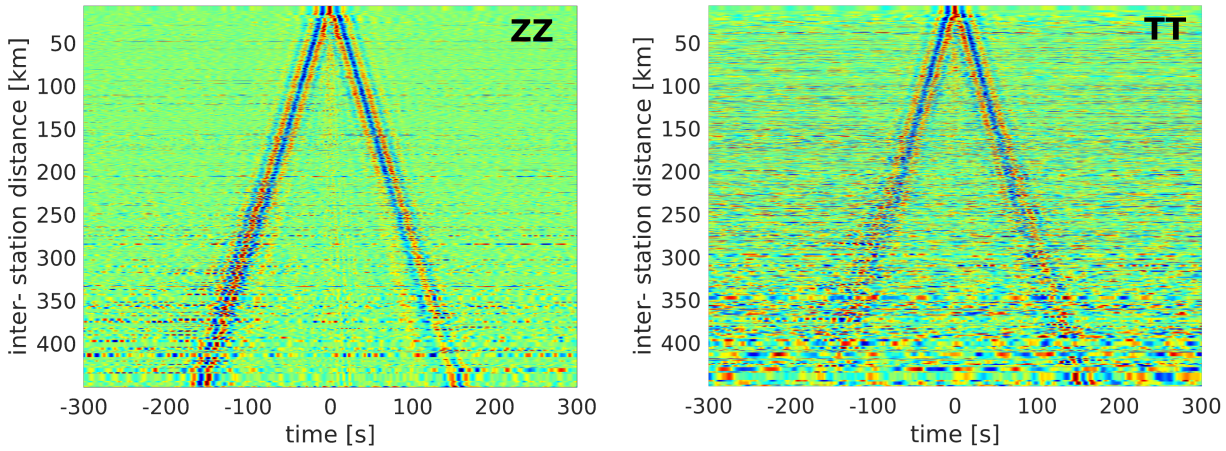

Figure 2.4: Double sided cross correlation functions for each combination of stations, sorted by inter-station distance for the vertical and transverse component; filtered between 0.01 Hz and 0.1 Hz

2.3 Phase velocity dispersion curves

Up to now, the results contain only information on group velocities from ambient seismic noise. The main goal of this chapter is to estimate phase velocities from ambient noise cross correlations and perform a tomographic inversion.

There are two possibilities to calculate inter-station phase velocities from surface waves, either in time- or frequency domain. Boschi et al. (2012) derived these two different approaches based on the theoretical formulation of Tsai and Moschetti (2010). The approach based on time domain cross correlations utilizes the far- field approximation of the wavefield equation, while the frequency domain uses the real part of the cross correlation spectrum and estimate their roots (zero crossings). Latter approach was later improved by Kaestle et al. (2016). It is based on the work of Ekström et al. (2009) and Aki (1957). Aki already showed

in 1957, that the normalized and averaged cross spectrum is varying like the Bessel function of first kind (J_0), depending on frequency (ω_0), inter-station distance (r) and velocity ($c(\omega_0)$).

$$\bar{\rho}(r,\omega_0) = J_0\left(\frac{\omega_0 r}{c(\omega_0)}\right) \tag{2.49}$$

Since the zero crossings of the Bessel functions (z_n) are well known, it is possible to derive phase velocities at these distinct frequencies (ω_n) [Ekström et al., 2009]:

$$c(\omega_n) = \frac{\omega_n r}{z_n} \tag{2.50}$$

However, additional noise in the spectrum might lead to additional and unwanted or missed zero crossings [Ekström et al., 2009]. One solution for identifying the correct zero crossings is a comparison with a realistic background model [Kästle et al., 2016]. This is sufficient enough for lower frequencies, where the zero crossings show some diffusive behaviour. For higher frequencies Ekström et al. (2009) proposed an implementation of criterias regarding smoothness and continuity of dispersion curves. Therefore, it is not necessary to reconstruct the amplitude of the Green's function which is the case for analyzing time domain cross correlations [Bensen et al., 2007; Lin et al., 2008].

2.3.1 Grid search approach

In this work, we introduce a different approach, which also uses the spectrum of the cross correlation. Instead of using the zero crossings of the real part of the cross spectrum, we measure the phase directly from our cross correlation functions and fit them into a grid of synthetic phases calculated via the Bessel function of third kind. For calculating the phases, we follow Meier et al. (2004) and Soomro et al. (2016). Their algorithm is developed for teleseismic data and allows to measure the fundamental mode Rayleigh and Love wave phase velocities from the phase difference of the fundamental modes between two stations. Using that, we are able to estimate the phase of our cross correlations as a function of frequency. Since the cross correlations of our ambient noise data already provide phase differences, we only use this approach for smoothing the spectrum and to isolate the contribution of the fundamental mode. Correlations between the fundamental mode and higher modes or uncorrelated noise are influencing the spectrum which could result in rough phases. For that reason, the cross correlation function is filtered by using a frequency dependent Gaussian bandpass filter. Afterwards, it is windowed in time domain by a Gaussian window, which is centred around the amplitude maximum of the cross correlation. The window is applied to enhance the signal to noise ratio of the fundamental mode. Transformation in the frequency domain leads to an overall smoother phase as a function of frequency. In addition, the 2π ambiguities, up to $\pm 12\pi$, from the measured phases are calculated as well.

In order to perform the grid search, it is necessary to calculate a grid of synthetic phases, for which we use the Bessel function of third kind. It is a linear combination of the Bessel function of first kind and the Bessel function of second kind (Y_0) as the imaginary part (2.51).

$$H(\omega) = J_0\left(\frac{\omega r}{c(\omega)}\right) - iY_0\left(\frac{\omega r}{c(\omega)}\right). \tag{2.51}$$

This allows to calculate synthetic phases as a grid, depending on frequency and velocity, which will be sufficient for the calculation of Rayleigh wave phase velocity dispersion curves. The calculation of Love wave phase velocity dispersion curves would induce an error at lowest frequencies [Kästle et al., 2016]. For that reason, the known equation for the vertical component is corrected by the Bessel function of first kind and second order [Aki, 1957; Haney et al., 2012; Kästle et al., 2016; Ekström, 2017] like:

$$\bar{\rho}(r,\omega_0) = \frac{1}{2}J_0\left(\frac{\omega_0 r}{c(\omega_0)}\right) - \frac{1}{2}J_2\left(\frac{\omega_0 r}{c(\omega_0)}\right). \tag{2.52}$$

This can also be used for the Hankel function, which can be written as:

$$H(\omega) = \frac{1}{2}H_0(\omega) - \frac{1}{2}H_2(\omega). \tag{2.53}$$

$$H(\omega) = \frac{1}{2}\left(J_0\left(\frac{\omega r}{c(\omega)}\right) - iY_0\left(\frac{\omega r}{c(\omega)}\right)\right) - \frac{1}{2}\left(J_2\left(\frac{\omega r}{c(\omega)}\right) - iY_2\left(\frac{\omega r}{c(\omega)}\right)\right). \tag{2.54}$$

By calculating the unwrapped phase $\phi_{th}(\omega)$ of $H(\omega)$, we are able to perform the grid search with our measured phases $\phi_{obs}(\omega)$ at each frequency and estimate phase velocities. This can be expressed like:

$$c_{obs}(\omega) = c_{th}(\omega) \Leftrightarrow min(\mid \phi_{obs}(\omega) - \phi_{th}(\omega) \mid) \tag{2.55}$$

Fig.2.5 illustrates Eq. (2.55) for one path of our data with an inter-station distance of around 100 km. The black and white striped line represents the dispersion curve from our measured phases, while all the black lines show their 2π ambiguities, up to $\pm 12\pi$. The grid of the unwrapped, theoretical phases is shown in the background. The dispersion curves are smooth and converge towards higher frequencies. For comparison, the figure shows the result for the "zero crossing" method as well. The real part of the spectrum and its zero crossings are shown on top of the grid. Their resulting phase velocity values are plotted as red dots into the grid. There is qualitatively no difference between the results of both methods in this case.

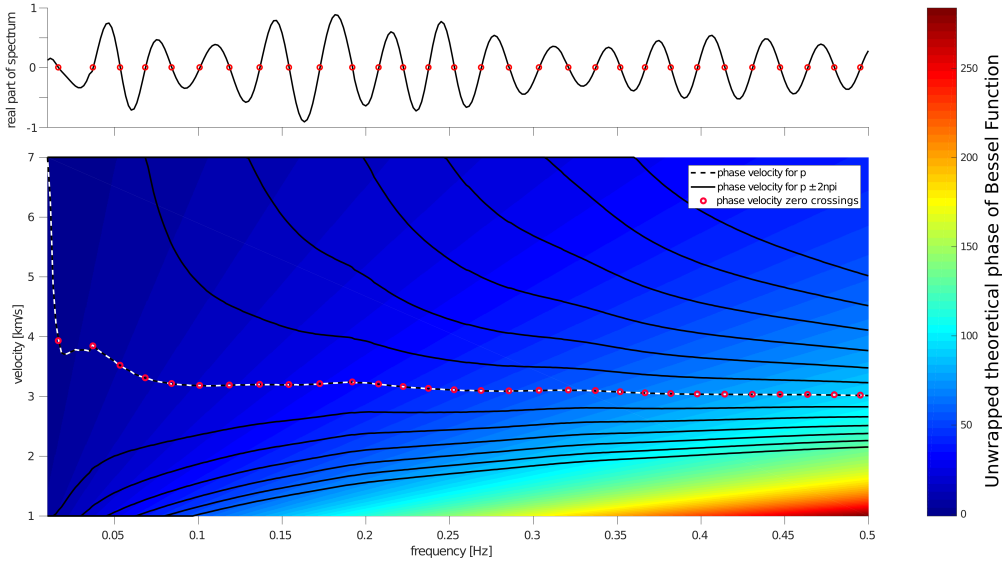

Figure 2.5: Calculation of phase velocities by performing a grid search between measured phases from ambient noise cross correlations and a grid of synthetic phases, calculated via the Bessel function of third kind; top: real part of the spectrum and its zero crossings

2.3.2 Grid search vs zero crossings

In section 2.3.1, we described a different approach to calculate phase velocity dispersion curves from ambient seismic noise cross correlations, besides of the more common one using the zero crossings of the real part cross spectrum. However, the results are qualitatively the same and still, we used our approach. The next part explains, why we are doing though and why our approach is in our case the better choise instead of the one using the zero crossings.

We are aiming for phase velocity dispersion curves at high frequencies to provide information for the uppermost part of the crust. Due to strong lateral heterogeneities in the upper crust, the cross correlation functions might contain a poor signal to noise ratio and are superposed by high frequency noise. For that reason, it needs to be clarified that the approaches for calculating phase velocites, are still providing reliable results at high frequencies of up to 0.5 Hz. Fig.2.6 shows a synthetic test for which we calculated a synthetic Green's function from a synthetic dispersion curve, before we re- calculated the disperion curve again, using both described methods. We added two percent of random noise on the synthetic Green's function. In addition to the described features in Fig.2.5, Fig.2.6 also shows the synthetic dispersion curve (orange), which we used for this test. It is calculated for an inter-station distance of 100 km, in a frequency range of 0.01 - 0.5 Hz.

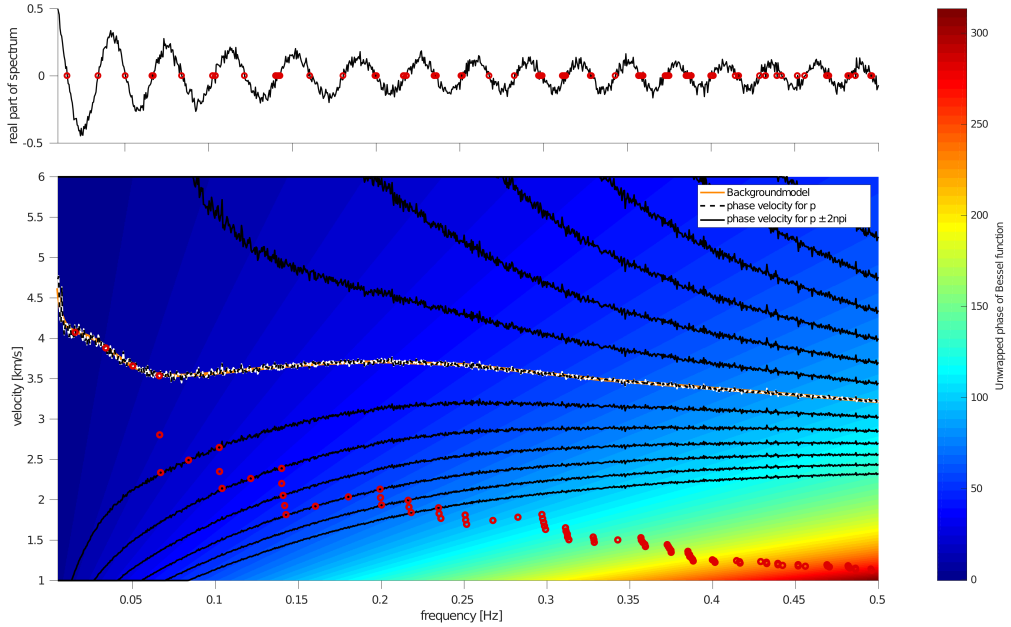

Figure 2.6: Synthetic test for a calculation of phase velocities by performing a grid search between measured phases from ambient noise cross correlations and a grid of synthetic phases; top: real part of the spectrum and its zero crossings

The results are slightly rougher, due to the random noise. Following the black and white striped dispersion curve, it is, regardless of minor scale roughness, still following the trend of the synthetic dispersion curve. In contrast, the phase velocities calculated from the zero crossings are starting to differ from the synthetic dispersion curve at around 0.07 Hz. This difference is increasing towards higher frequencies. This effect occurs due to the roughness in the real part of the cross spectrum which leads to additional zero crossings. Everytime an additional zero crossing occurs, the velocity values seem to be shifted by 2π.

Another aspect for which we prefer the grid search approach is the amount of samples of the calculated phase velocity dispersion curve. While it is arbitrary in case of the grid search, it is not for the zero crossing method and depends highly on the wavelength and thus on inter-station distance. Fig.2.7 shows the summary of a series of synthetic tests regarding the dependency of the number of zero crossings and the inter-station distance for different amounts of random noise which were added to the synthetic Green's function. In case of no random noise, the number of zero crossings are linearly increasing with inter-station distance. Dispersion measurements of paths with an inter-station distance smaller than 30 km contain less than 10 zero crossings. Especially at smallest distances, the number of zero crossings is highly increasing, if random noise is added. Towards larger distances, the number of zero crossings are converging towards the values without noise. In addition, Fig.2.7 shows the number of zero crossings from all paths within our dataset for Rayleigh and Love waves. They are almost linearly increasing up to 300 km inter-station distance. Since the phase velocity dispersion curves are converging towards higher frequencies, it will become

difficult to select the correct branche. Therefore, a sufficient amount of samples is important. Especially for paths with small inter-station distances, this might lead to problems for the zero crossing method, due to an insufficient amount of samples in that frequency range. By using the grid search approach, we are able to observe irregularities, like higher modes or structural heterogeneity, which lead to discontinuities or phase shifts in the dispersion curves.

Since we seek for information in the upper crust, phase velocity dispersion curves at high frequencies are necessary. Due to structural heterogeneities, we might have to deal with rough cross correlation functions. Therefore, our method using the grid search and the Bessel function of third kind might be more suitable, because it seems more robust at higher frequencies and contains an arbitrary amount of samples.

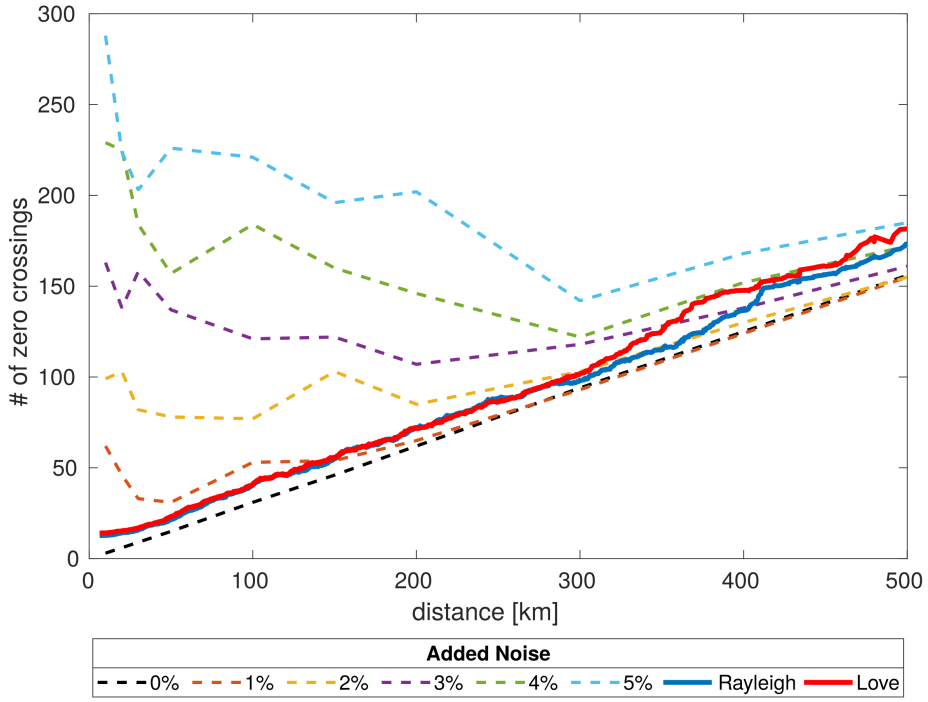

Figure 2.7: Synthetic test to show the number of zero crossings in the real part of the spectrum as a function of inter-station distance and the applied additional random noise, compared to the number of zero crossings in our measured data

2.3.3 Automated picking of phase velocity dispersion curves

We calculated phase velocity dispersion curves for the entire frequency band and 2π ambiguities, up to $\pm 12\pi$. In the next step, it is necessary to evaluate these phase velocities and only use the most realistic and smooth parts for further processing. For that reason, we use an automated picking process for dispersion curves, introduced by Soomro et al. (2016). This selection contains three main criteria, a background model, the smoothness criterion and the length criterion, shown in Fig. 2.8. Since, we are working on a different frequency range the criteria were slightly adapted for our purposes which will be described.

Background model criterion

At first the correct 2π branch has to be identified, by using a suitable background model. As seen before, the different 2π branches are getting very close to each other at higher frequencies which makes a correct identification of the correct dispersion curve difficult. With decreasing frequency, the dispersion curves are more divergent. This allows for an easier idenfication of the correct branch. We use a local Crust1.0 model of that area for this criterion [Laske et al., 2013]. Fig. 2.8 (left) shows the procedure of the criterion. After selecting the correct branch, a threshold is defined to reject portions of the dispersion curves, which differ to much from the background model. This can be written as [Soomro et al., 2016]:

$$\left| \frac{c(\omega_i) - c_0(\omega_i)}{c_0(\omega_i)} \right| x100 < th_{\Delta C}, \tag{2.56}$$

where $th_{\Delta C}$ is the maximum deviation from the background model in percent, $c_0(\omega_i)$ is the phase velocity for the background model and $c(\omega_i)$ is the observed phase velocity for each frequency ω_i. For small frequencies, we allow for a constant threshold of 15 percent difference from the background model. Towards higher frequencies ($> 0.08Hz$), the threshold is linearly increasing up to 50 percent. This is necessary because of the structural heterogeneities in the uppermost parts of the crust which is difficult to explain by only one background model. We expect high velocities in the subsurface below the Al- Hajar Mountains where the ophiolite is emplaced and smaller values across the Arabian platform.

Smoothness criterion

In order to select only smooth parts of the dispersion curve, its roughness is calculated by using the smoothed first derivative with respect to frequency. At low frequencies, we follow the approach from Soomro et al. (2016) by comparing the smoothed first derivative from the measured phase velocity disperion curve to the one of the backgroundmodel as absolute

values. This can be expressed as:

$$S(\omega_i) = \sum_{\omega_j=\omega_i-d(\omega_i)}^{\omega_i+d(\omega_i)} \left| \frac{c^{'}(\omega_j) - c_0^{'}(\omega_j)}{c_0(\omega_j)} \right| < th_S, \tag{2.57}$$

with $c(\omega)^{'}$ as the first derivative of the phase velocity and $c_0(\omega)^{'}$ as the corresponding first derivative of the background model. If this value exceeds a defined threshold th_S, it will be rejected. According to the background model criterion, we choose a different approach at higher frequencies. Here, we only consider the first smoothed derivative of the measured dispersion curve itself and remove the backgroundmodel. In addition, we define two different thresholds and treat negative perturbations differently from positive ones, since we allow for rather negative changes of the dispersion curves at high frequencies.

Length criterion

This criterion rejects very short portions of the so far selected dispersion curves, which may lead to an error, especially at high frequencies. The length criterion defines a threshold which depends on the length of the segment (Δf) and its mean frequency. Fig. 2.8 shows, that this threshold relaxes at low frequencies and is more strict at higher frequencies. The segment has to be longer than the required length (red dot), otherwise it will be rejected (beige dot).

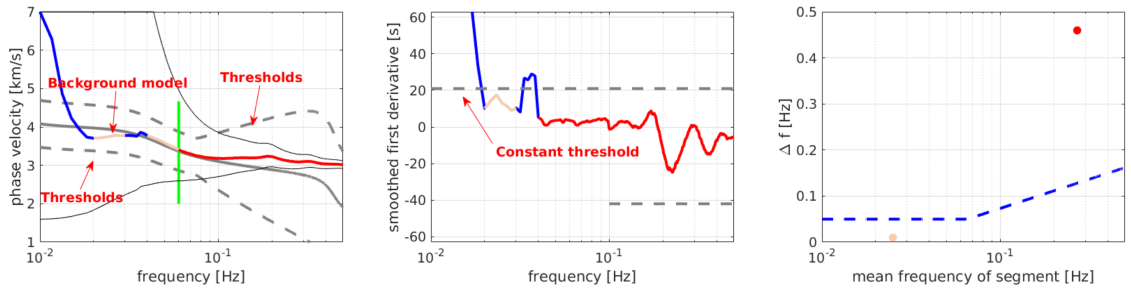

Figure 2.8: Criteria for the automated picking process; left: Background model criterion; centre: Smoothness criterion; right: Length criterion; The red portion of the dispersion curve is accepted for further processing and evaluation, whereas the beige one is rejected, because it only satisfies single criteria

2.3.4 Results

We calculated Rayleigh and Love wave phase velocity dispersion curves for each path and performed the automated picking process to select only the smooth portions or even reject the entire path. This resulted in 1072 remaining paths for Rayleigh wave phase velocity dispersion curves, which is slightly more than 50 percent of the calculated ambient noise cross correlations. For Love wave phase velocity dispersion curves, only 672 remained which is

roughly 37 percent of the once calculated cross correlation functions and again an indication for the higher data quality of the Rayleigh wave data.

The dispersion measurements are plotted on top of each other for both Rayleigh and Love waves (Fig. 2.9). The respective 2D histograms are shown below. The measurements have been obtained in a broad frequency range (2 - 40 s). The 2D histograms show that the dispersion curves are converging towards higher periods. Most of the measurements are in a frequency range of 8 - 15 s for both, Rayleigh and Love waves. Towards lowest periods, the amount of dispersion curves is decreasing. In addition, they are diverging due to the structural complexity of the upper crust.

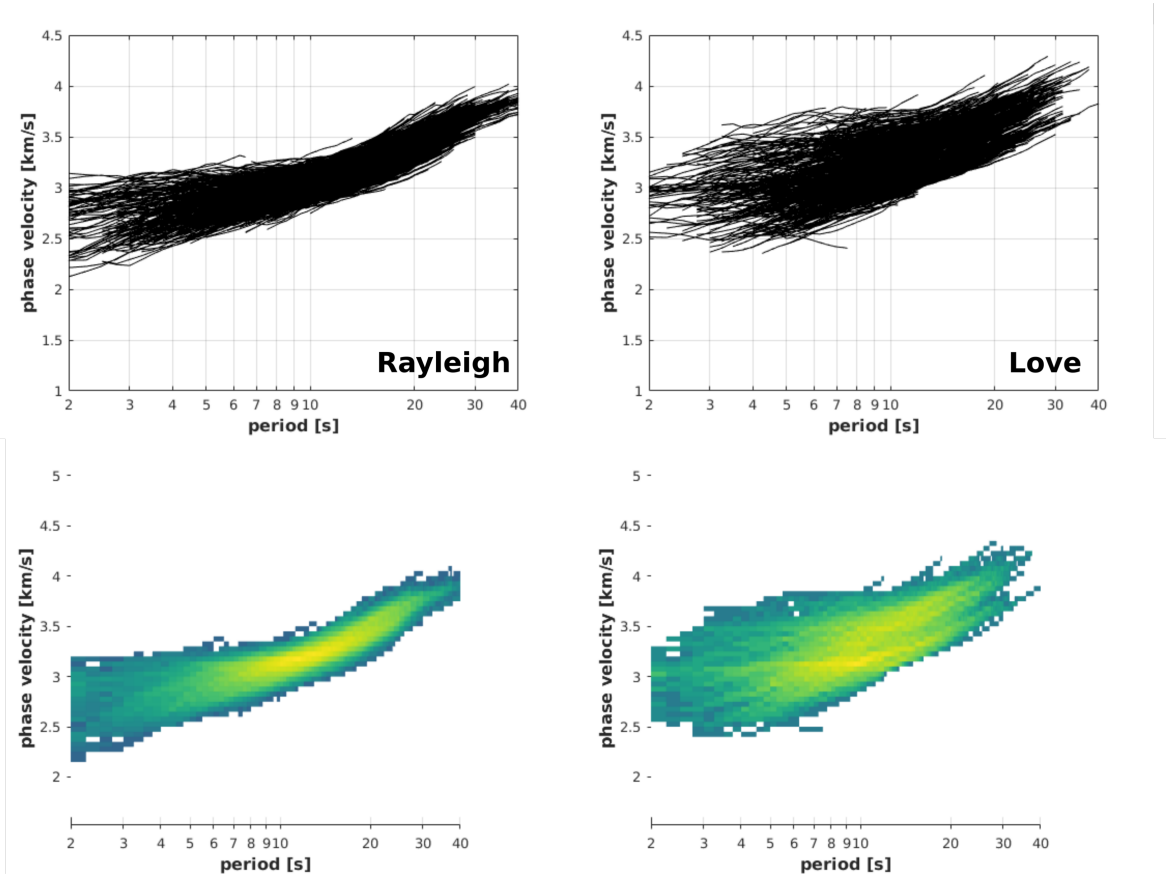

Figure 2.9: Dispersion curves plotted on top of each other (top) and the corresponding 2D histograms for Rayleigh (left) and Love (right) wave phase velocity curves of the entire data set

To illustrate the structural differences in the uppermost part of the crust of the study area, we defined three regions which strongly differ in their structure (Fig.2.10). The corresponding dispersion curves for Rayleigh waves are highlighted. The blue curves represent paths within Area I. It is mostly located across the Al- Hajar Mountains, which are strongly deformed by the obduction process and later tectonical events. They mostly consist of oceanic lithosphere and old, once subducted and partly metamorphosed continental sedimentary rocks. For that reason, they show distinct higher velocities at lowest periods than the curves insight area II

(red) and III (green), which are paths crossing mostly minor consolidated young sediments south of the Al-Hajar Mountains. At higher periods, the dispersion curves are converging towards each other. In addition, there are clear differences between the paths crossing area II and III. The velocities of the red dispersion curves are consistently higher than the green ones. At high periods, this indicates a thinning of the crust towards eastern direction.

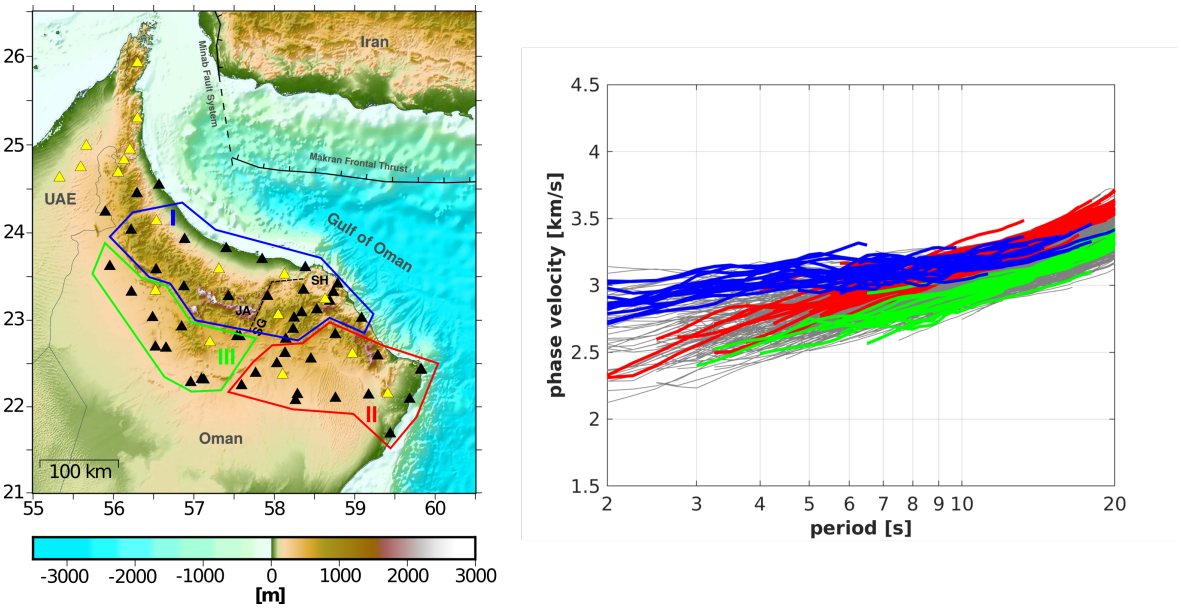

Figure 2.10: Highlighted dispersion curves for three defined areas from Rayleigh wave measurements; Blue area: Al- Hajar Mountains; Red area: Southeast of Al- Hajar Mountains; Green area: Southwest of Al- Hajar Mountains

For the following calculation of ambient noise phase velocity maps, standard deviations from the dispersion curves are needed. Unfortunately, we obtained only one dispersion curve per path by using the symmetric part of the ambient noise cross correlation function. By exerting the discussed processing for calculating dispersion curves on the causal and acausal part of the cross correlation function as well, we are able to estimate a standard deviation. Figure 2.11 shows three paths for which we were able to calculate dispersion curves for the causal, acausal and symmetric part. However, there are portions of the dispersion curves or even entire paths, where only the symmetric part exists. In this case, we use the average standard deviation of all paths which have at least one additional curve besides the symmetric one. The standard deviations for the Rayleigh and Love wave dispersion measurements are shown in figure 2.12. Overall, it seems that the standard deviations for Rayleigh wave dispersion curves are slightly smaller. The mean standard deviation is around $\approx 2.5\%$ for Rayleigh and $\approx 3.3\%$ for Love wave dispersion curves.

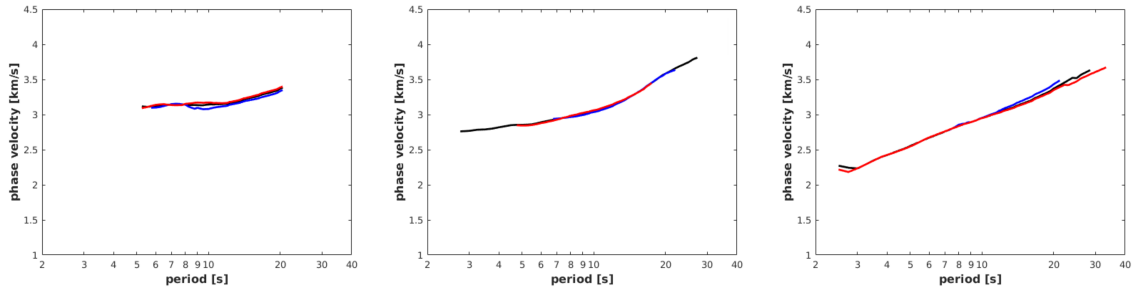

Figure 2.11: Rayleigh wave phase velocity dispersion curves for the symmetric (black), causal (blue) and acausal (red) part of the cross correlation function

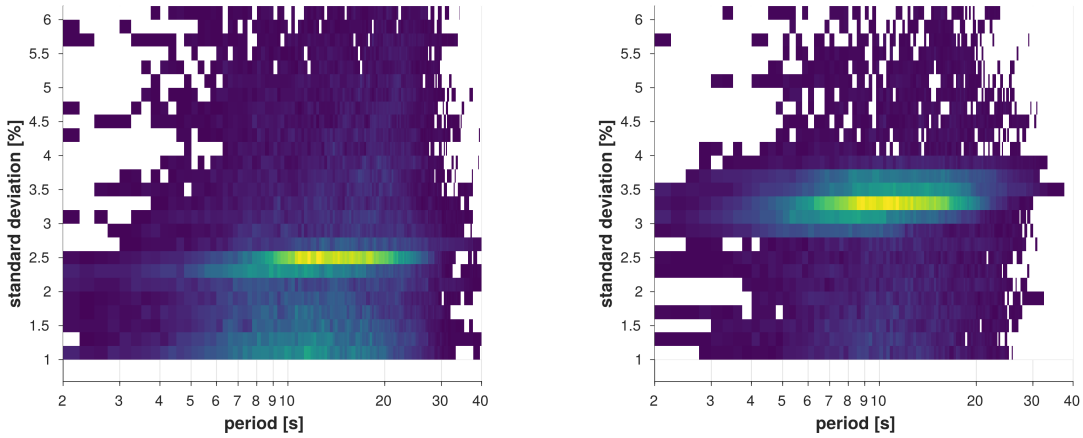

Figure 2.12: 2D histogram showing the standard deviation as a function of period; left: Rayleigh; right: Love

2.4 Determination of phase velocity maps

The next part contains the calculation of phase velocity maps by inverting the surface wave phase velocity dispersion curves from our ambient seismic noise data. Surface wave inversion problems are existent for decades. The relationship between seismic waveforms and the Earth model is not linear and thus using surface wave data to determine Earth structure is nonlinear as well. The inversion consists of a linear and a nonlinear part [Barmin et al., 2001]. A linear part deals with the calculation of 2D dispersion maps, while the nonlinear part deals with the estimation of Earth stucture from the dispersion maps. The nearly linear part is called surface wave tomography. However, there are some surface wave inversion methods which linearize the relation between the seismic waveform and an Earth model, by estimating the Earth model iteratively without estimating dispersion maps [Nolet, 1987; Snieder, 1988; Marquering et al., 1996].

Several surface wave tomographic techniques are currently in use [Li and Romanowicz, 1995; Marquering et al., 1996; Meier et al., 1997; Yoshizawa and Kennett, 2002]. They vary in theoretical assumptions, the parametrization and geometry of the model, application of regularization and damping and the possibility to estimate azimuthal anisotropy besides

isotropic velocities. The results can further be used to estimate shear wave velocity structures of the subsurface or to perform a joint inversion with different geophysical datasets [Levshin et al., 2001]. In this work, we use the approach of Deschamps et al. (2008) which is based on ray theory to invert surface wave velocity dispersion curves for Rayleigh and Love waves in a frequency range of 2 - 40 s. The resulting 2D phase velocity maps show the spatial distribution of phase velocities at each grid point. Dispersion curves depend on the sensitivity of Earths structure along the inter-station path. Therefore, phase velocity anomalies can be estimated with respect to an average value. Figure 2.13 shows the number of paths per period for Rayleigh and Love waves. At lowest periods of 2 seconds, the number of paths is around 50 and 30 for Rayleigh and Love waves, respectively. The maximum amount of paths are within 10 to 12 seconds with roughly 870 and 540 paths for Rayleigh and Love waves. Overall, there are approximately half of the measurements for Love than for Rayleigh waves. With increasing period the number of paths are again decreasing. At 30 s, they are below 100 and 30 for Rayleigh and Love waves, respectively.

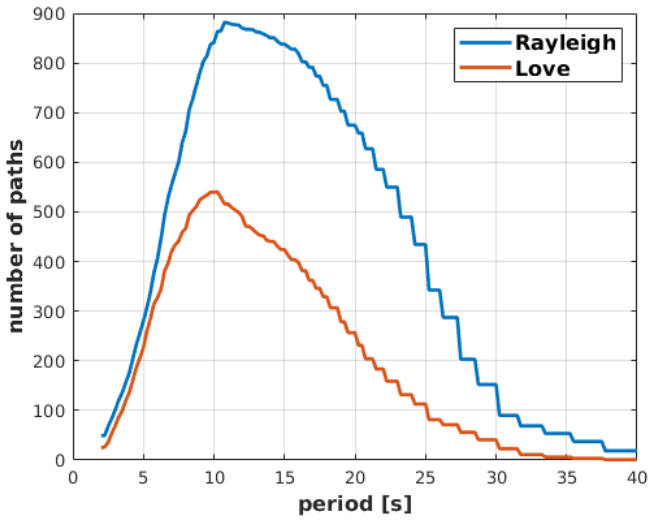

Figure 2.13: Histogram showing the number of paths for Rayleigh and Love waves at each period

Each inter-station dispersion curve $C_i(\omega)$ can be used to image the structure of the subsurface. They can be expressed as the perturbations of phase velocities $\delta C_i(\omega,\theta,\phi)$ from an average value and their errors $\Delta C_i(\omega,\theta,\phi)$ at each gridpoint with coordinates θ,ϕ. This can be expressed for each path i as:

$$\int_\theta \int_\phi K_i(\omega,\theta,\phi)\,\delta C(\omega,\theta,\phi)\,d\phi\,d\theta = \delta C_i(\omega) \pm \Delta C_i(\omega) \tag{2.58}$$

with frequency ω and sensitivity kernel $K_i(\omega,\theta,\phi)$. If the medium is anisotropic, group- and phase velocities vary with azimuth. This is called azimuthal anisotropy and the mathematical argument for the azimuthal dependence of Rayleigh and Love waves goes back to Smith

and Dahlen (1973). One of the first applications for imaging azimuthal anisotropy was done by Tanimoto and Anderson (1984), where they showed an relation between the fast propagation direction and the direction of mantle flow. Following Smith and Dahlen (1973), the anisotropic part can be defined by the 2Ψ- and 4Ψ- terms of the phase velocity variation, where Ψ represents the azimuth of the wave propagation. In principle, they account for the π and $\pi/2$ periodic variations of the phase velocities. The contribution of the 4Ψ anisotropy is small. However the effect should not be neglected, which was shown in several works [Montagner and Nataf, 1986; Trampert and Woodhouse, 2003; Beucler and Montagner, 2006; Darbyshire and Lebedev, 2009]. The phase velocity anomaly can be written as:

$$\delta C(\theta,\phi) = \delta C_{iso}(\theta,\phi) + \delta C_{2\Psi}(\theta,\phi) + \delta C_{4\Psi}(\theta,\phi) \tag{2.59}$$

with the isotropic variation $\delta C_{iso}(\theta,\phi)$ and anisotropic variations $\delta C_{2\Psi}(\theta,\phi)$ and $\delta C_{4\Psi}(\theta,\phi)$. This allows for the isolation of the isotropic contribution from the anisotropic ones. The 2Ψ and 4Ψ anisotropy are defined as:

$$\delta C_{2\Psi}(\theta,\phi) = A_{2\Psi} cos(2\Psi) + B_{2\Psi} sin(2\Psi) \tag{2.60}$$

$$\delta C_{4\Psi}(\theta,\phi) = A_{4\Psi} cos(4\Psi) + B_{4\Psi} sin(4\Psi). \tag{2.61}$$

$A_{2\Psi}$,$A_{4\Psi}$,$B_{2\Psi}$,$B_{4\Psi}$ are the four unknown anisotropic coefficients at each grid point (θ,ϕ). Together with the isotropic phase velocity anomaly, we invert for five unknowns per grid point. The amplitude Λ and the fast propagation direction Θ are given by

$$\Lambda_{2\Psi} = \sqrt{A_{2\Psi}^2 + B_{2\Psi}^2} \tag{2.62}$$

$$\Theta_{2\Psi} = \frac{1}{2} arctan\left(\frac{B_{2\Psi}}{A_{2\Psi}}\right) \tag{2.63}$$

$$\Lambda_{4\Psi} = \sqrt{A_{4\Psi}^2 + B_{4\Psi}^2} \tag{2.64}$$

$$\Theta_{4\Psi} = \frac{1}{4} arctan\left(\frac{B_{4\Psi}}{A_{4\Psi}}\right). \tag{2.65}$$

Chevrot and Zhao (2007) stated that the sensitivity areas of the inter-station measurements are complex. By including all inter-station combinations, the sensitivity can be improved at intermediate and long wavelengths. Smoothing of the sensitivity areas leads to a more robust result. The sensitivity areas $K(\theta,\phi)$ are estimated at knots of a dense integration grid, following Lebedev and van der Hilst (2008) and Wang and Dahlen (1995). This results in a triangular grid of knots with equal interknot spacing. Our final models are calculated with a knot spacing of 3 km. This value is considerably smaller than the one e.g. Darbyshire and Lebedev (2009) used (30km). Since we are dealing with smaller periods to resolve small scale features in the uppermost crust, a smaller knot spacing, which still performs accurate integration over the sensitivity kernels might be necessary. The grid knot surrounding each

knot points form a hexagon shape which needs to be calculated at each grid knot. Afterwards, the sensitivity areas $K(\theta,\phi)$ are estimated at each grid knot and multiplied with the respective surrounding hexagon area. This yields the weight of the knot in the integral over the sensitivity area. The sensitivity kernels are adapted by a finite ray path width. Variations of the ray path width result in differences in shape and power of the anomalies. This will be further illustrated and discussed in section 2.4.2. In addition, a model grid is defined. It is also triangular like the integration grid, but contains a larger knot spacing. Here we used a knot spacing of 10 km which is based on the station coverage of our array. The same arrangement of knots is used for each period. The isotropic and azimuthal anisotropic phase velocity perturbations are unknown. They are calculated at each model grid knot by integrating over the area which includes the neighbouring grid knots. To calculate the isotropic and anisotropic phase velocity anomalies, this system of linear equations needs to be solved. Following Deschamps et al. (2008), Eq.(2.56) can be solved like:

$$d = Gm \tag{2.66}$$

with d representing the data vector which contains the path averaged phase velocity at a certain period. The model vector m contains the five unknown isotropic and anisotropic coefficients. G is the sensitivity matrix. If N is the number of available paths at each period and M is the number of knots, the transposed data- and model vector can be stated as:

$$d^T = (\overline{\delta C_1} \cdots \overline{\delta C_N}) \tag{2.67}$$

$$m^T = (\delta C_{iso,1} \cdots \delta C_{iso,M} A_{2\Psi,1} \cdots A_{2\Psi,M} B_{2\Psi,1} \cdots B_{2\Psi,M} A_{4\Psi,1} \cdots A_{4\Psi,M} B_{2\Psi,1} \cdots B_{4\Psi,M}) \tag{2.68}$$

The sensitivity matrix consists of five sub matrices:

$$G = (\ G_{iso}\ G_{C2\Psi}\ G_{S2\Psi}\ G_{C4\Psi}\ G_{S4\Psi}\ ) \tag{2.69}$$

$$G_{iso} = \begin{pmatrix} K_{11} & \cdots & K_{1M} \\ \cdots & \cdots & \cdots \\ K_{N1} & \cdots & K_{NM} \end{pmatrix},$$

$$G_{C2\Psi} = \begin{pmatrix} a_1K_{11} & \cdots & a_1K_{1M} \\ \cdots & \cdots & \cdots \\ a_NK_{N1} & \cdots & a_NK_{NM} \end{pmatrix}, G_{S2\Psi} = \begin{pmatrix} b_1K_{11} & \cdots & b_1K_{1M} \\ \cdots & \cdots & \cdots \\ b_NK_{N1} & \cdots & b_NK_{NM} \end{pmatrix},$$

$$G_{C4\Psi} = \begin{pmatrix} c_1K_{11} & \cdots & c_1K_{1M} \\ \cdots & \cdots & \cdots \\ c_NK_{N1} & \cdots & c_NK_{NM} \end{pmatrix}, G_{S4\Psi} = \begin{pmatrix} d_1K_{11} & \cdots & d_1K_{1M} \\ \cdots & \cdots & \cdots \\ d_NK_{N1} & \cdots & d_NK_{NM} \end{pmatrix},$$

K_{ij} are the weights of each path i and knot j. The azimuthal dependence is included by $a_i = cos(2\Psi_i)$, $b_i = sin(2\Psi_i)$, $c_i = cos(4\Psi_i)$ and $d_i = sin(4\Psi_i)$, with Ψ_i as the azimuth of the path i.

2.4.1 Regularization

The result of the tomographic inversion depends highly on the regularization. In general, a regularization means to apply some constraints on the model amplitude and the velocity perturbations, in order to increase the robustness of the inversion. It is necessary to select a proper regularization which is a compromise between a smooth model and the ability to explain the measured data (variance reduction) [Deschamps et al., 2008]. This is always subjective. The effect of regularization and its success depends on the data quality and -quantity and the study area itself. The isotropic and anisotropic parts are treated independently. In this work, we evaluate the effects of regularization only visually to find an optimal one for our final model.

Smoothing and damping are the common parameters of regularization. They have a strong effect on the entire tomographic map which might lead to problems for evaluating the results. Darbyshire and Lebedev (2009) mentioned, that oversmoothing results in a smooth tomographic map, but with a loss of resolution. On the other hand, undersmoothing might introduce artifacts. The effect of norm damping is minor. Therefore, it remains constant for most periods. We applied two types of smoothing. The first one is a lateral smoothing, which penalizes the second lateral derivatives of the velocity distribution [Deschamps et al., 2008]. It reduces the perturbation difference at each knot with the average value of the surrounding knots. It is suitable to determine the regular gradients, while small scale anomalies will be averaged out. In addition, we use a second kind of smoothing, called gradient damping [Darbyshire and Lebedev, 2009]. The difference between two neighbouring knots is penalized, which is similar to using the first derivative of the anomaly distribution.

The quality of the resulting tomographic maps depends on the remaining variance. This value needs to be sufficiently small. This is not the case if the variance reduction is too small, which might be due to noisy or rough dispersion curves. To enhance the quality of the measurements, we performed an outlier rejection. It selects the most consistent data. Here, we tested outlier rejections of 0%, 5%, 10%, 15%, 20%, 25% and 30%. In the end, we used 20% as a compromise between a smooth result with a respectively low remaining variance and still enough paths per period. It is worth to mention that the regularization tests were performed with a model grid of 30 km and an integration grid of 10 km spacing, whereas for the final model we used 10 and 3 km, respectively. The reason, for which we increased the grid densities of the final models, will be part of the upcoming resolution test in section 2.4.3. After testing several sets of regularization, it became clear that only one set is not sufficient enough to obtain small scale features for each period. Especially at lowest periods,

less smoothing is necessary to resolve local lateral variations of the structure. In this work, the smoothness values are linear increasing with period. In addition, the smoothness of the isotropic term is smaller than the ones for the anisotropic terms, which was also mentioned by Darbyshire and Lebedev (2009). Figure 2.14 shows phase velocity maps for 5 s period and different smoothing for the isotropic term. The anisotropic terms remain constant. It seems that a change of the isotropic damping is effecting the anisotropic part as well. By introducing a high isotropic damping, the isotropic signal leaks to the anisotropic part.

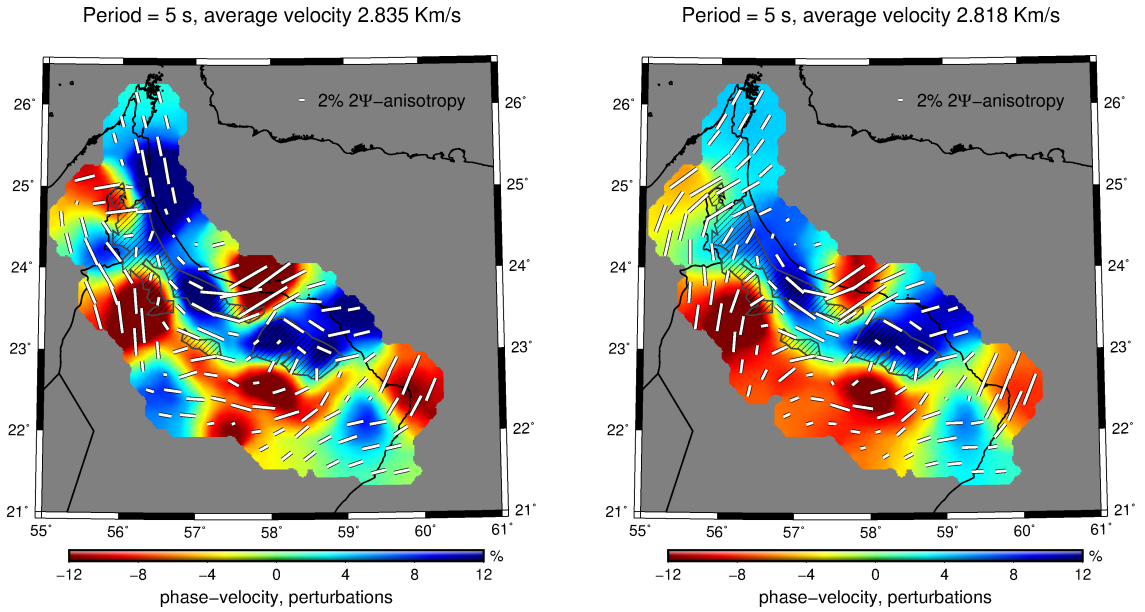

(a) isotropic damping: 0.05

(b) isotropic damping: 0.1

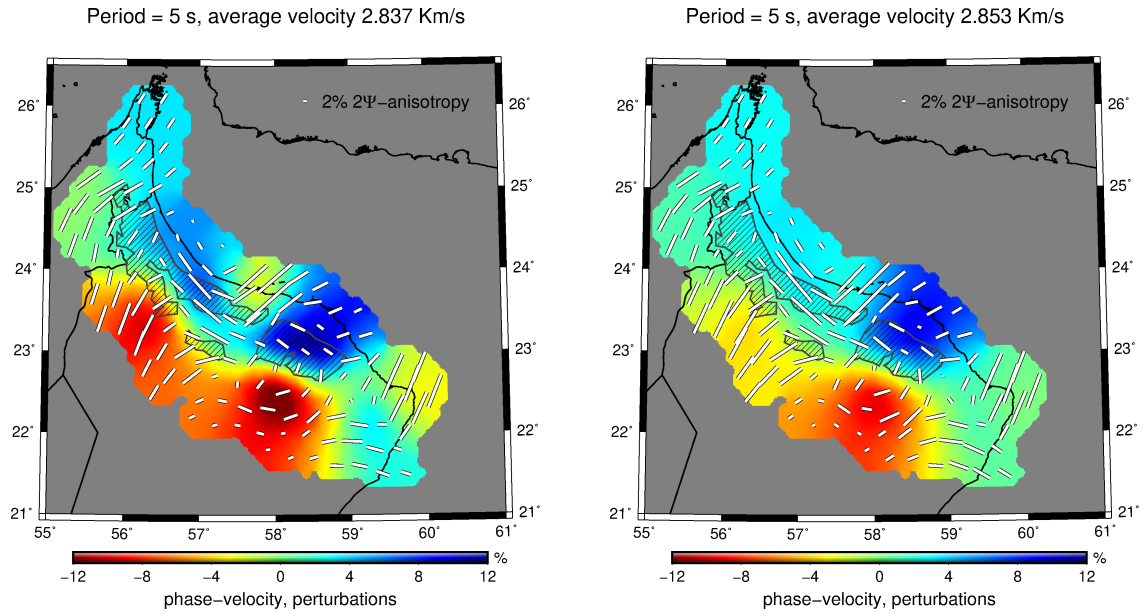

(c) isotropic damping: 0.2

(d) isotropic damping: 0.4

Figure 2.14: Isotropic damping of Rayleigh wave phase velocity maps; Anisotropic damping is fix: 0.2

In contrast, figure 2.15 shows phase velocity maps with different smoothing for the anisotropic terms, while the isotropic term remains constant. We observe the same effect, only reversed. An overdamping of the anisotropic part leads to a leakage of the anisotropic signal to the isotropic part. High damping values might decrease the resolution, which is clearly observable in figure 2.14 and 2.15, but also provide a dominent feature for a particular region. On the other hand, low damping values show a higher resolution with a certain risk of artifacts due to errors in the phase velocity dispersion curves.

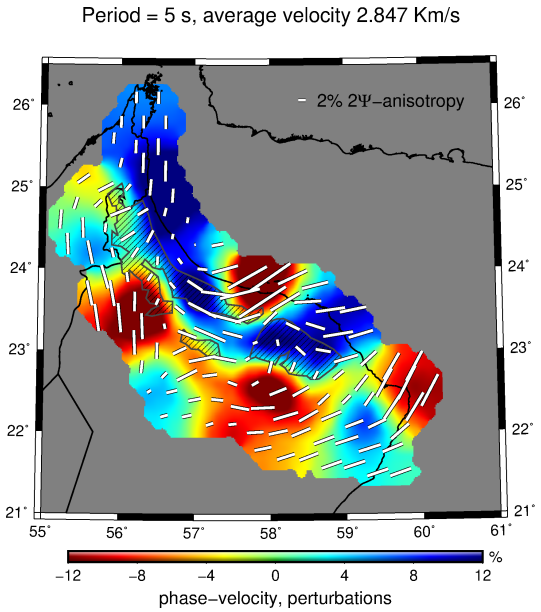

(a) anisotropic damping: 0.2

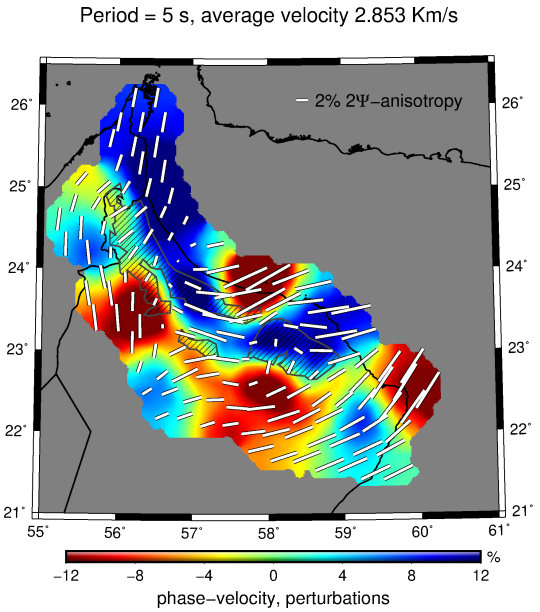

(b) anisotropic damping: 0.3

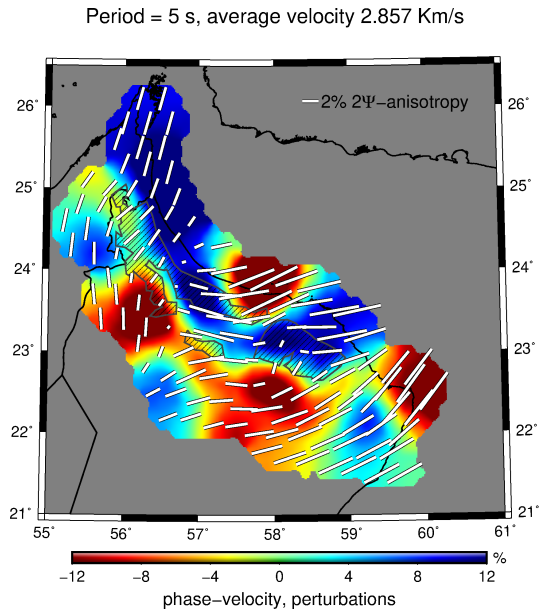

(c) anisotropic damping: 0.4

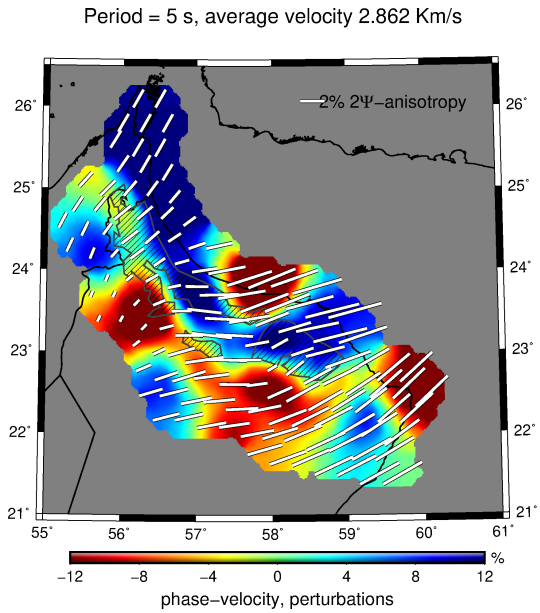

(d) anisotropic damping: 0.7

Figure 2.15: Anisotropic damping of Rayleigh wave phase velocity maps; Isotropic damping is fix: 0.1

2.4.2 Ray path width

Besides a sufficient path coverage of the area and a reasonable regularization of the inversion, a finite path width of surface wave ray paths enhances the sensitivity areas of the inversion. Especially by assuming a relatively strong lateral heterogeneity, this might be necessary to be done. The ray theory approximation could fail if the scale length of lateral heterogeneity is smaller than the wavelength of the waves. Wang and Dahlen (1995) formulated a condition which validates the ray theory approximation by using the Jordan-Wenzel-Kramer-Brillouin (JWKB) approximation. They assume that the Fresnel zone, which defines the path width of the ray path, should be much smaller than the scale length of lateral heterogeneity. Yoshizawa and Kennett (2002) stated, that the influence area of a surface wave path looks like a delta function in geometrical ray theory, based on the high frequency approximation. In reality, the path width should cover a finite region around the ray path. They showed that the influence area of surface wave ray paths and thus the path width could be up to hundreds of kilometers.

In this work, we tested path widths from 0 to 50 km. The results are shown in figure 2.16 for 5 s period and 0, 10, 30 and 50 km path width. The effect of using different ray path widths is only on smaller scale. Basically, the results are showing the same features. The pattern of the isotropic part is slightly changing towards higher ray path widths, while the amplitude and direction of the azimuthal anisotropy remain mostly the same. The correct ray path width for the inversion needs to be selected with caution. A too large ray path width might affect the amplitudes of the anomalies in a way that small scale variations will be dimmished or even overlain by more regional variations. However, we observe slightly different average velocities and a slight decrease of the remaining variance with increasing path width. Therefore, the usage of finite path widths result in more robust and reliable phase velocity maps. For our final models, we used a constant path width of 50 km for each period.

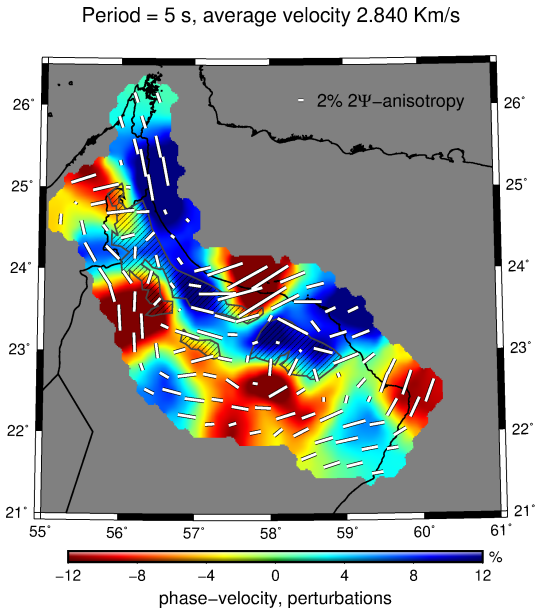

(a) Ray path width: 0km

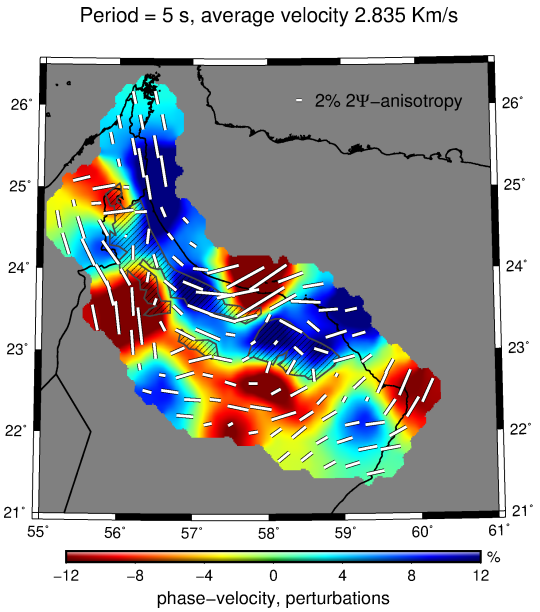

(b) Ray path width: 10km

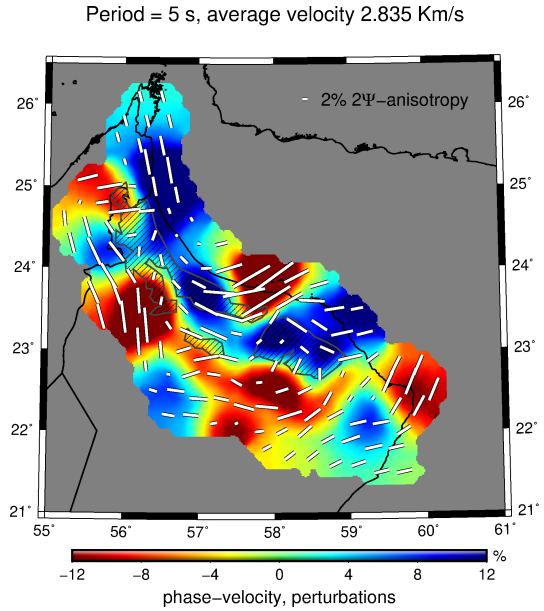

(c) Ray path width: 30km

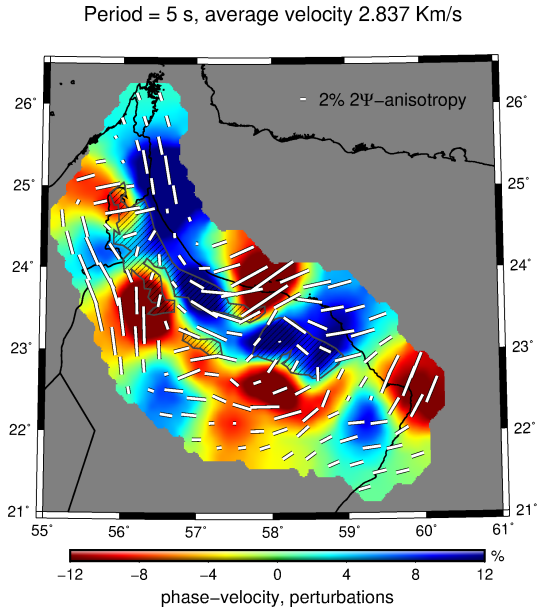

(d) Ray path width: 50km

Figure 2.16: Phase velocity maps with increasing ray path width

2.4.3 Resolution tests

In order to verify the reliability of the tomographic maps, we perform a checkerboard test. This is the most common resolution test, which was introduced by Spakman and Nolet (1988). We define a simple regular pattern of synthetic positive and negative anomalies in the model space, which we try to invert with our path distribution for each period. The evaluation of the results provides information about the resolution of the tomographic maps. We performed checkerboardtests with a size and spacing of checkers of 30 km. Figure 2.17 and 2.18 show the results for different model grids (10 and 30 km) used for the calculation of the phase velocity maps, exemplary for the periods 2, 7 and 15 s. We observe lateral smearing effects in all tests. This is slightly more pronounced for the 10 km grid, whereas the results from the 30 km grid feature a higher amplitude damping. However, the inversion results show a sufficient resolution for all periods in the centre part of our area, including the main part of the Al- Hajar Mountains, Jebel Akhdar, Saih Hatat and south of the mountain range. Despite the lateral smearing at 2 s, the resolution in the easternmost part of study area is higher for the 10 km grid. The best resolution is obtained at 7 s with the least amplitude damping. Here, the inverted anomalies are again slightly better recovered for the 10 km grid compared to the 30 km grid. With increasing periods, the resolution increases as well, especially in the eastern part of the study area. In the western part, the inversion results for the 30 km grid show strong lateral smearing and the anomalies are not well recovered, even at highest periods. For the 10 km grid the resolution in the western part is slightly higher at 7 s and 15 s. Smearing occurs in areas with a small amount of crossing paths, which is the case in the western part. For that reason, the results obtained from that area need to be interpreted with caution.

Especially at intermediate and high periods, the resolution tests for the 10 km grid show better results compared to the 30 km grid. At lowest periods, better recovered anomalies for the 10 km grid are contradicted by a stronger lateral smearing. However, the calculation of the final phase velocity maps will be performed by using the 10 km model grid which in fact shows the overall higher resolution compared to the 30 km model grid.

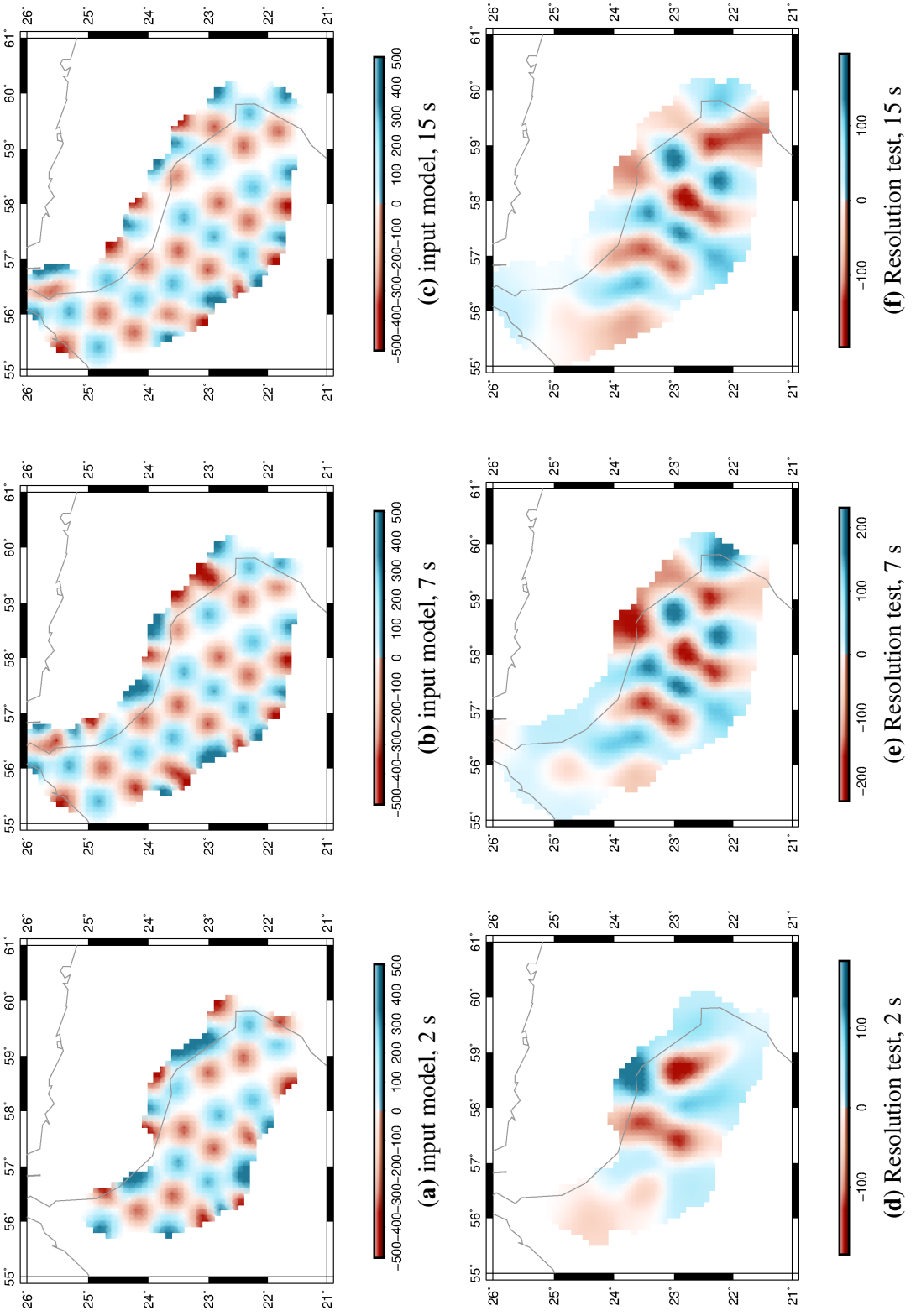

Figure 2.17: Checkerboardtest for phase velocity maps using the 30 km model grid with anomalies of 30 km size and spacing. Figures a-c show the input models for 2, 7 and 15 s period. Figures d-f show the corresponding results.

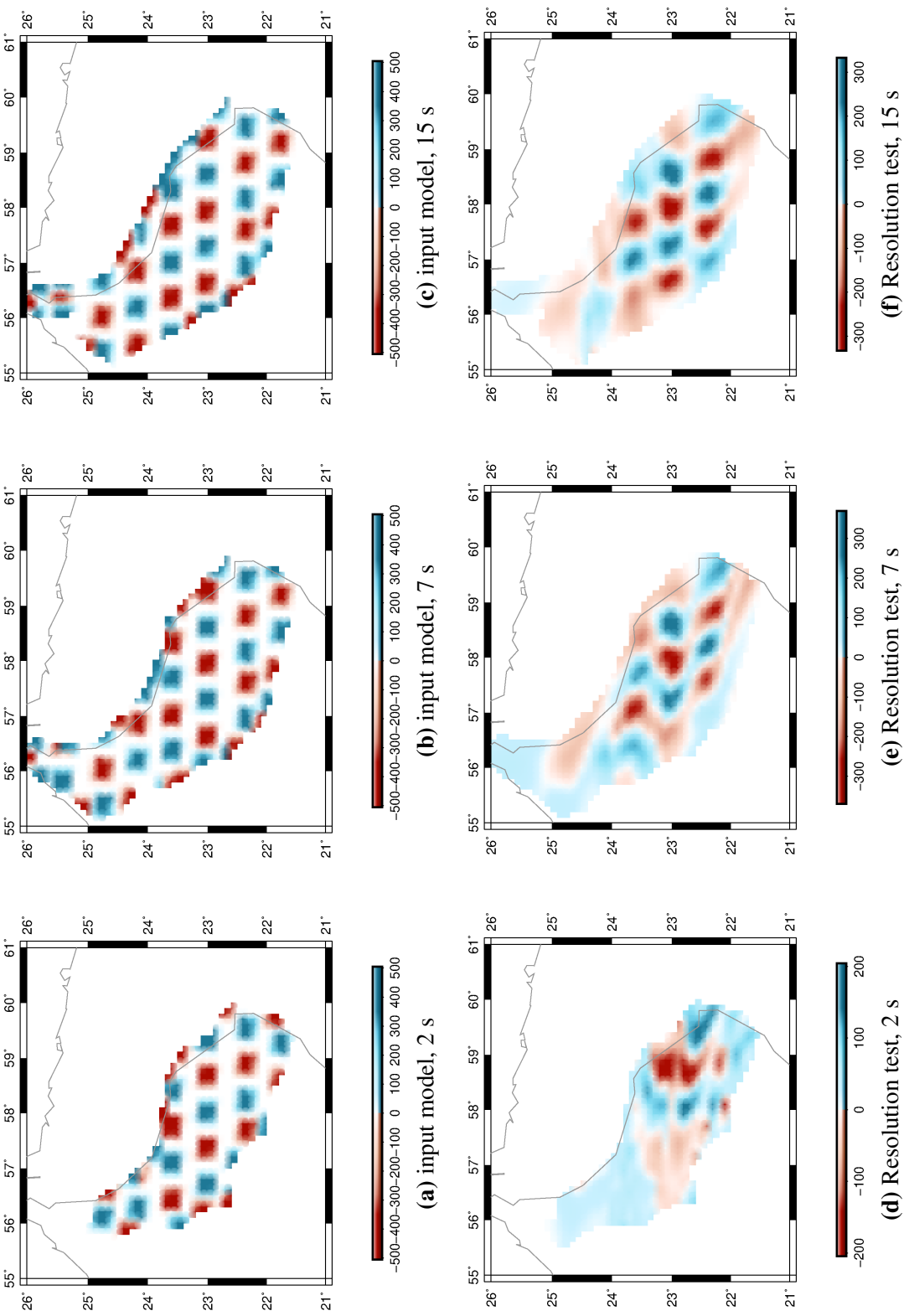

Figure 2.18: Checkerboardtest for phase velocity maps using the 10 km model grid with anomalies of 30 km size and spacing. Figures a-c show the input models for 2, 7 and 15 s period. Figures d-f show the corresponding results.

2.5 Results

The inversion of our data resulted in isotropic and azimuthal anisotropic tomographic phase velocity maps for Rayleigh and Love waves in a period range from 2 to 40 s. Lateral velocity variations enable us to evaluate structural features in the lithosphere. The sensitivity of phase velocities depends on the period. While shorter periods contain information regarding the subsurface and upper crust (e.g. the existence of the ophiolite), longer periods are more sensitive to the lower crust or even upper mantle [Boschi and Ekström, 2002]. After performing some tests regarding the regularization, ray path width and outlier rejection, the final parametrization of the inversion is as follows: The smoothing is linear increasing with period. For Love waves, the smoothing is overall slightly higher than for Rayleigh waves, just as it is for the anisotropic terms compared to the isotropic one. The ray path width is 50 km. We performed the inversions on a model grid with 10 km spacing, an integration grid of 3 km spacing and the outlier rejection removes 20 % of the data which are least mututal consistent. It is worth to point out that the remaining variances for the Rayleigh wave phase velocity maps were always slightly smaller than for the Love wave phase velocity maps.

2.5.1 Isotropic phase velocity maps

Figure 2.19 and 2.20 show isotropic phase velocity maps exemplary for 3, 5, 7, 10, 12 and 20 s period of the study area for Rayleigh and Love waves, respectively. Additional isotropic Rayleigh and Love wave phase velocitiy maps between 2 and 30 s period can be found in appendix A. Phase velocities are imaged as perturbations around an average value. Striped areas highlight the exposed obducted material, which is mostly across the flanks of the Al-Hajar Mountains.

A first thing to mention is, that the average velocities are higher for Love waves than for Rayleigh waves for all periods. In addition, Love waves are normally more sensitive to shallower structures than Rayleigh waves at the same period. At lowest periods the phase velocity maps indicate a high consistency with surface topography. High velocity anomalies are located across the Al- Hajar Mountains and the locations of the emplaced ophiolite, while there are considerably lower velocities further south and south east on the Arabian platform which are mostly covered by younger sediments. This contrast is more pronounced for Rayleigh than for Love waves. It is well known that the Al- Hajar Mountains are disrupted by regions, where the ophiolite got eroded and once subducted and partly metamorphosed, old continental sediments were exhumed on top of the surface. This include the Jebel Akhdar- and Saih Hatat window [Hanna, 1990; Coleman, 1981; Searle and Cox, 1999; Al-Lazki et al., 2002]. For that reason, lower phase velocities are assumed for these regions, compared to the ones covered by the ophiolite. However, we observe only minor variations within the high velocity anomaly and distinct variations towards the named tectonic windows are not observable.

Towards higher periods, the high velocity anomaly is decreasing, but is still slightly observable at 12 s period for both, Rayleigh and Love phase velocity maps. This period is sensitive to a depth range of 16- 20 km. Therefore, the high velocity anomaly can not be explained by the obduction process and the ophiolite solely. Additional tectonic processes might have contributed to the anomalous high velocity across the Al- Hajar Mountains. At 7 s period, the Jebel Akhdar and Saih Hatat region are better observable due to slower velocities. This is slightly more pronounced in the Rayleigh wave phase velocity map. In addition, we observe a high velocity anomaly in the eastern part of the area in the Wahiba Sands. This is also more pronounced in the Rayleigh wave phase velocity maps. The overall change in pattern with increasing period lead to an almost bimodal distribution of velocity anomalies at 20 s period. Higher velocities in the east are contrasted by lower velocities in the west. This period is sensitive to lower crustal level and might indicate a thinning of the crust towards the east. Unfortunately, the phase velocity maps are only capable to provide information as a function of period which corresponds to a certain depth range. This is of course not sufficient enough to assign velocity anomalies exactly to certain crustal structures or tectonic processes. For exact depth estimations, an additional inversion is needed. This is the subject of Chapter 4.

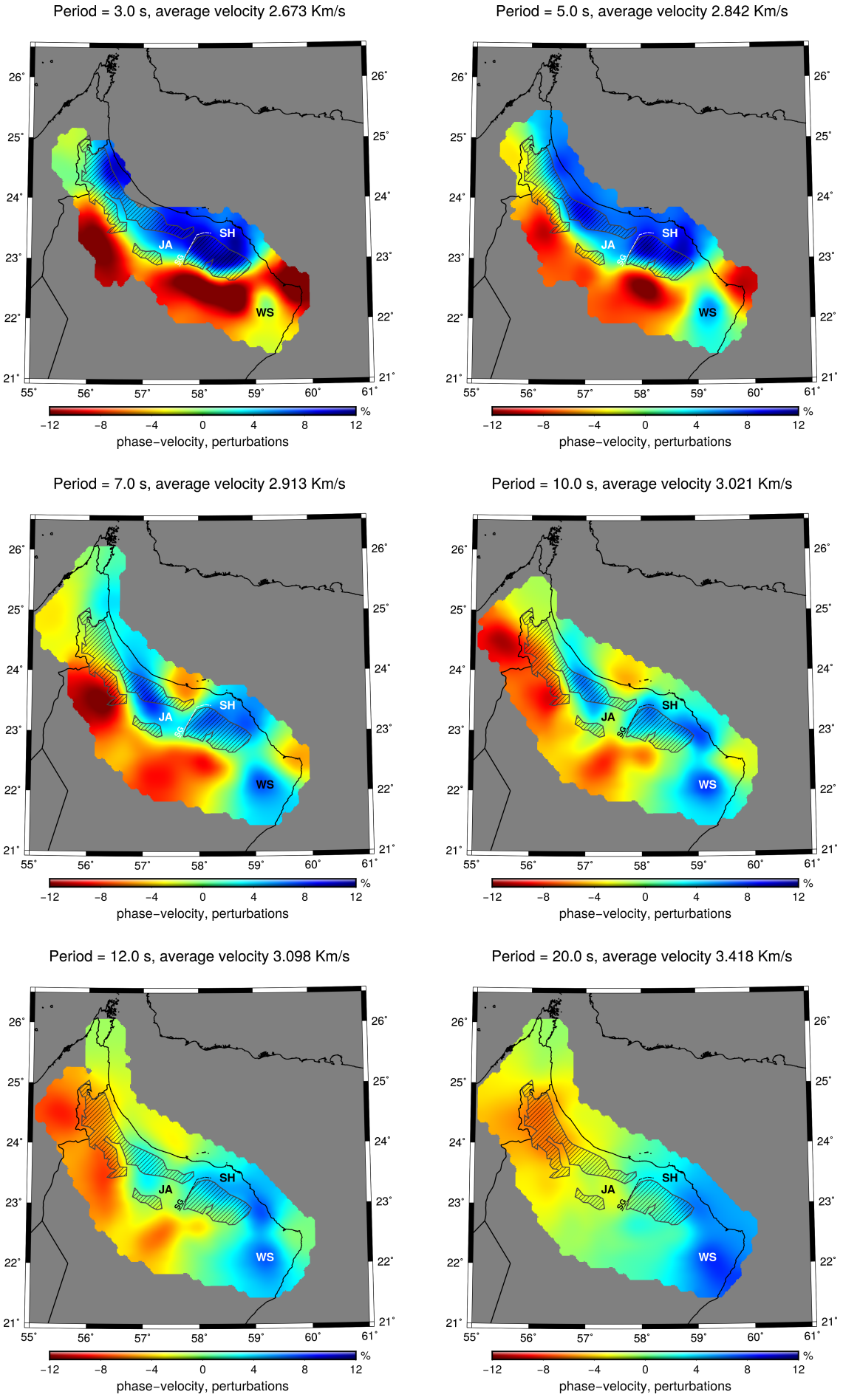

Figure 2.19: Isotropic Rayleigh wave phase velocity maps for 3, 5, 7, 10, 12, 20 s

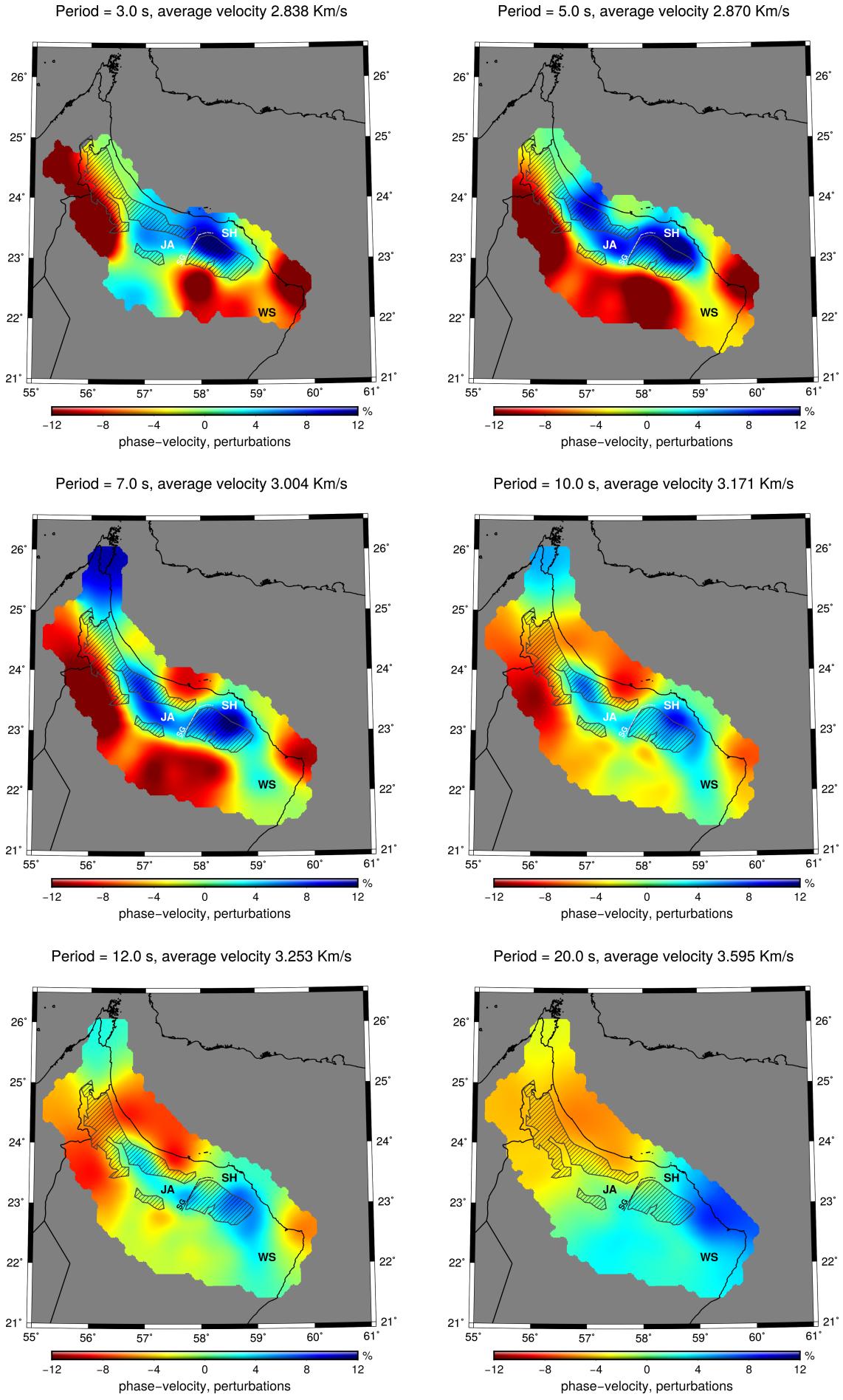

Figure 2.20: Isotropic Love wave phase velocity maps for 3, 5, 7, 10, 12, 20 s

2.5.2 Azimuthal anisotropic phase velocity maps

The directional dependence of seismic wave velocities is called azimuthal anisotropy. In most cases, variations in seismic wave velocities are caused by minerals which are aligned towards a preferred direction under a stress or strain regime. Azimuthal anisotropy is present in the Earths crust and mantle. However, the cause of azimuthal anisotropy might be a different one for the crust than for the mantle. While anisotropy in the mantle is controlled by temperature and flow, anisotropy in the crust often correlates with geological provinces [Lin et al., 2011]. For that reason, azimuthal anisotropy on crustal level might be explained as frozen-in anisotropy, resulting from deformational events in the past, like compression or extension, while in the mantle, especially in the asthenosphere, azimuthal anisotropy can be related to present day flow pattern [Debayle and Ricard, 2013].

Figure 2.21 and 2.22 show results for azimuthal anisotropic Rayleigh and Love wave phase velocity maps for the same periods as the isotropic maps. More anisotropic Rayleigh and Love wave phase velocitiy maps between 2 and 30 s period can be found in appendix A. At lower periods, NW-SE directed azimuthal anisotropy is observable across the high velocity area of the Al- Hajar Mountains, west of the Semail Gap. East of the Semail Gap, it is turning towards W-E direction. In contrast, we observe mostly SW-NE directed azimuthal anisotropy further south on the Arabian platform. The pattern is still visible at 7 s period. At higher periods, the tomographic maps of Rayleigh waves show a change of azimuthal anisotropy towards SW-NE direction beneath the Al-Hajar Mountains. In contrast, NW-SE directed azimuthal anisotropy is still observable at 12 s in the Love wave tomographic maps in the same area. The eastern part of the study area features mostly consistent azimuthal anisotropy in Rayleigh and Love wave phase velocity maps. While overall SW-NE directed azimuthal anisotropy is observable at lower periods with the highest amplitudes in the Salmah Plateau, it is NW-SE at high periods. Overall, the azimuthal anisotropy shows almost the same bi-modal distribution at highest periods as the isotropic velocity. The azimuthal anisotropy is changing from SW-NE in the western part to NW-SE in the easternmost part of the study area.

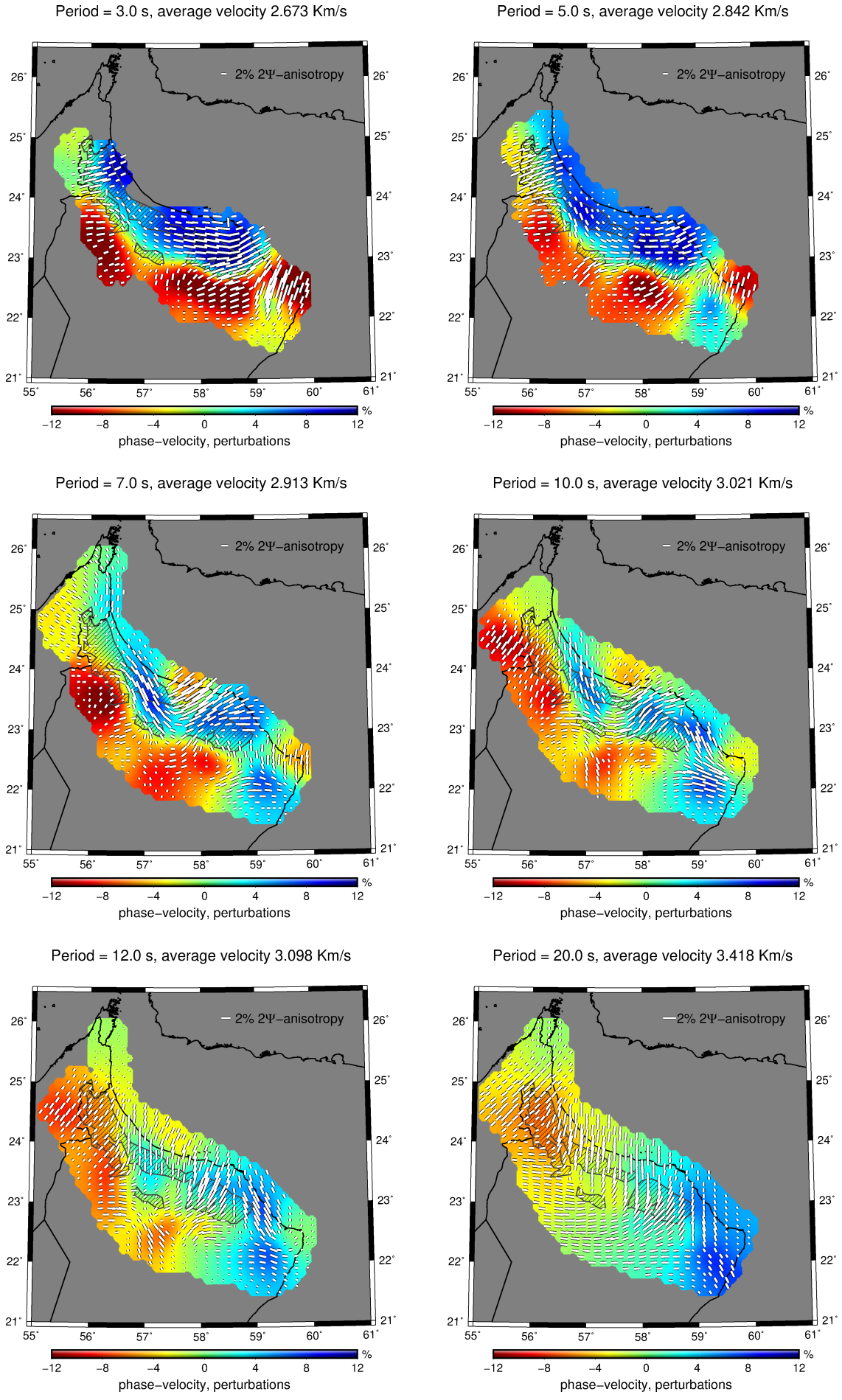

Figure 2.21: Anisotropic Rayleigh wave phase velocity maps for 3, 5, 7, 10, 12, 20 s

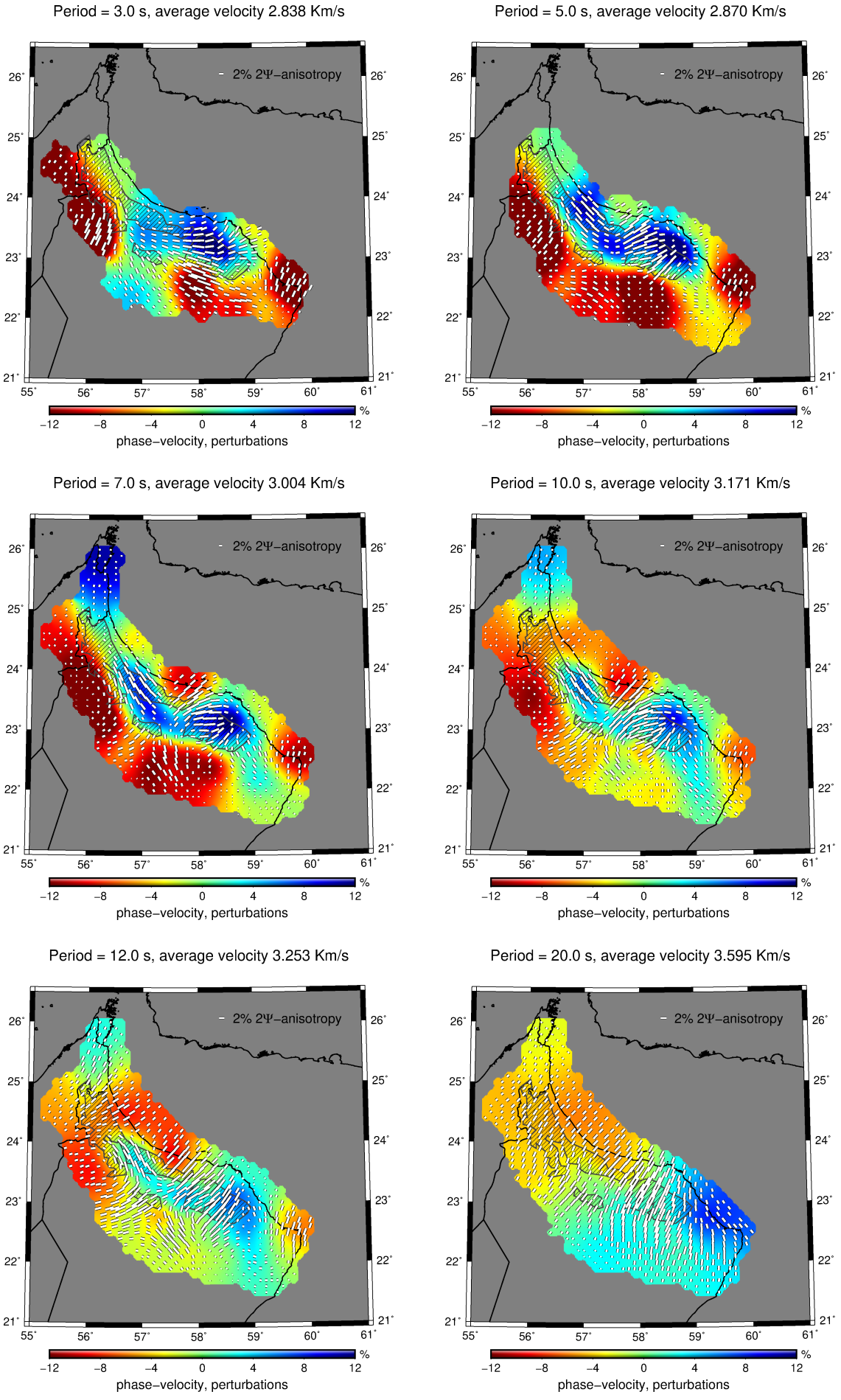

Figure 2.22: Anisotropic Love wave phase velocity maps for 3, 5, 7, 10, 12, 20 s

Chapter 3

Receiver functions

The third chapter of the thesis deals with the calculation of receiver functions by using our continuous Oman data to image different crustal and mantle discontinuities like the Moho, lithosphere-asthenosphere- boundary and mantle transition zone. Imaging the Moho by using receiver functions has already been done for some stations in northern Oman [Al-Lazki et al., 2002; Al-Hashmi et al., 2011]. They combined their results with different geophysical or geological methods to estimate 1D or 2D structures in the subsurface. Al- Hashmi et al. (2011) performed a joint inversion of receiver functions and Rayleigh wave group velocities to determine pointwise the lithospheric structure in Oman. In addition, they calculated v_p/v_s ratios.

In this work we will calculate P- and S- receiver functions, using teleseismic events from October 2013 until February 2016 with magnitude 6 or higher from the ISC catalogue. The first part includes a detailled introduction to different processing steps for calculating receiver functions. Receiver function results in time domain for different lithospheric discontinuities will be discussed and compared to existing work. Afterwards, a migration technique is applied to estimate receiver functions as a function of depth. The obtained results will be discussed in the next chapter, together with our 3D model of shear wave velocity over depth and azimuthal anisotropy from ambient seismic noise tomography.

3.1 Receiver function method

The receiver function method is one of the most common seismological methods to investigate the lithospheric structure with only one three- component station. It uses the fact that incoming teleseismic waves produce conversions (P-to-S or S-to-P) at crustal boundaries or multiple reverberations in the shallow layering [Lay and Wallace, 1995]. First observations of P-to-S or S-to-P conversions were made several years ago [Phinney, 1964; Bath and Stefánsson, 1966]. Nowadays, the receiver function method is a standard tool for investigating lithospheric structures [Al-Lazki et al., 2002; Kind et al., 2002; Al-Hashmi et al., 2011; Knapmeyer-Endrun et al., 2013; Kind et al., 2017].

3.1.1 P- receiver functions

Most of the studies regarding receiver functions are analysing P-to-S conversions of the P-arrival of teleseismic data. This is due to the fact that P- waves are the first arrival of a teleseismic event, with usually the highest amplitude. For that reason, they are easier to identify, compared to the S- wave arrivals. The P-to-S conversion is generated at sharp discontinuities below the receiver and its amplitude is stronger on the radial component [Lay and Wallace, 1995]. Thus, this SV- polarized wave is called Ps- phase (Fig.3.1). It is arriving after the direct P- phase. The time delay is increasing with the depth of the interface. In principle, it should be possible to calculate the depths of discontinuities by calculating the time delay between the Ps- and P- phase. However, the Ps- phase is rarely observed in seismograms because it is overlain by the coda of the P- phase [Shearer, 2009]. The process of calculating

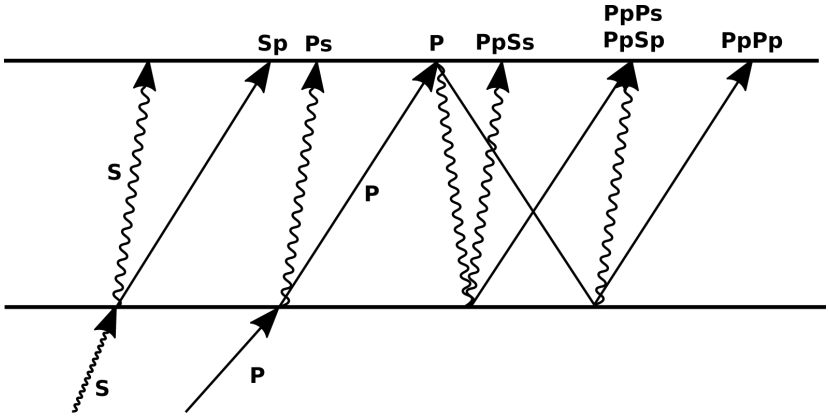

Figure 3.1: Upcoming P- and S- waves will generate converted or reflected phases on a velocity discontinuity. Notice the different incidence angles for Ps and Sp conversions.

P- receiver functions includes two steps. At first a coordinate rotation is necessary to isolate the Ps- phase from the P- phase which has its highest amplitudes on the vertical component. For that reason, it seems to be sufficient to transform our ZNE orientated data into the ZRT coordinate system, with R as the radial component and T as the transverse component [Kennett, 1991; Bostock, 1998]. However, this is only valid for very steep incidence angles. For

P- receiver functions, it is more suitable to perform a rotation into the LQT system. This transformation can be written as [Plesinger et al., 1986]:

$$\begin{bmatrix} L \\ Q \\ T \end{bmatrix} = \begin{bmatrix} \cos(i) & -\sin(i)\sin(baz) & -\sin(i)\cos(baz) \\ \sin(i) & \cos(i)\sin(baz) & \cos(i)\cos(baz) \\ 0 & -\cos(baz) & \sin(baz) \end{bmatrix} \begin{bmatrix} Z \\ E \\ N \end{bmatrix} \tag{3.1}$$

with i the incidence angle and baz as the backazimuth, measured clockwise from northern direction. The L- component is aligned in direction of P- wave propagation, the Q- component into SV- phase direction and T- component into SH- phase direction. This leads to an isolation of the P- and Ps- phase into different components. A deconvolution of the vertical component from the radial component removes the obscuring effects of the source function and the instrument response [Lay and Wallace, 1995]. It can be performed in time- or frequency domain. In this work, spiking deconvolution in time domain has been used which is described by Kind et al. (1995). They used the deconvolution method introduced by Berkhout (1977). This method generates an inverse filter in time domain, by minimizing the least square differences between the observed seismogram and the desired delta spike function. The displacement $u(\omega)$ for each component (L,Q,T) can be written as:

$$u_L(\omega) = S(\omega)G_L(\omega)I(\omega) \tag{3.2}$$

$$u_Q(\omega) = S(\omega)G_Q(\omega)I(\omega) \tag{3.3}$$

$$u_T(\omega) = S(\omega)G_T(\omega)I(\omega), \tag{3.4}$$

with $S(\omega)$ as the source time function, $G_L(\omega)$, $G_Q(\omega)$ and $G_T(\omega)$ as the Green's function for each component and $I(\omega)$ as the instrument response. The P- wave on the L- component is used for this deconvolution filter and can be approximated as a delta function $(G_L(t) \approx \delta(t))$. Therefore, the L- component can be expressed as:

$$u_L(\omega) \approx S(\omega)I(\omega) \tag{3.5}$$

Therefore, the deconvolution process of the SV- and SH- component can be written as:

$$G_Q(\omega) = \frac{u_Q(\omega)}{u_L(\omega)} \tag{3.6}$$

$$G_T(\omega) = \frac{u_T(\omega)}{u_L(\omega)} \tag{3.7}$$

Afterwards, all components are normalized to the maximum amplitude of the L- component. The deconvolved Q- component is then called receiver function. The T- component provides information on the dipping of a certain discontinuity and anisotropy of the structure by a change of polarity of the receiver function over azimuth. A change of polarity with a 90° symmetry indicates the pressence of anisotropy, whereas 180° symmetry indicates a dipping of a discontinuity [Frederiksen and Bostock, 2000].

In this work, we use 286 teleseismic events from the ISC catalogue with magnitudes of 6 or higher which took place during our station deployment from October 2013 to February 2016. They are mostly from northeast to east direction, which can be seen in figure 3.2. The radius represents the epicentral distance according to one reference station within our array. Since there is large gap of almost no teleseismic events between 120 ° and 300 ° azimuth, we increased the number of events to a minimum magnitude of 5.5. Unfortunately, there is only a minor amount of additional teleseismic events in the mentioned gap. In addition, the resulting receiver functions possess a poor signal to noise ratio.

We calculated receiver functions for incoming P- and PKP- waves. For the P- phase, we selected events with an epicentral distance of 30° - 100°, while the accepted epicentral distance for PKP- waves is larger then 150°. However, the number of receiver functions from PKP- waves is less than five for each station. Moreover, most of them possess a poor signal to noise ratio and thus a bad quality. For that reason, PKP- phases will be removed from the upcoming evalutation of P- receiver functions.

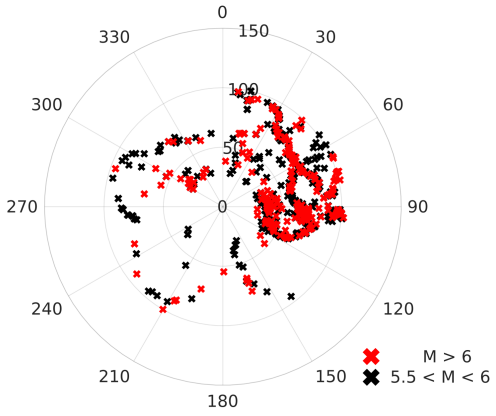

Figure 3.2: Teleseismic events from October 2013 to February 2016 with magnitudes larger than 6 (red) and magnitudes from 5.5 to 6 (black) as a function of azimuth. The azimuths [°] are calculated for one reference station within our array (COO16); radius = epicentral distance [°]

3.1.2 S- receiver functions

In contrast of analysing P-to-S conversions by the P- receiver function method, the study of S-to-P conversions is still relatively new. Overall it is more difficult to calculate S- receiver functions, because S- waves are arriving after the P- wave with smaller amplitudes. They might even be superposed by the coda of the P- wave. Overall, S- waves are characterized by lower frequencies than P- waves, resulting in a lower spatial resolution [Yuan et al., 2006]. First studies were performed to distinguish S-to-P conversions from S- waves by using polarity analysis [Bath and Stefánsson, 1966; Smith, 1970; Burdick and Langston, 1977; Sacks and Snoke, 1977; Faber and Müller, 1980; Bock and Kind, 1991]. Later, the common approach of P- receiver function analysis, including coordinate transformation and deconvolution was applied to S- waves [Farra and Vinnik, 2000; Vinnik and Farra, 2002; Vinnik et al., 2004]. Due to the ray geometry, S-to-P conversions are limited to a certain range of epicentral distances and their incidence angle is usually larger than that of the direct S- wave (Fig.3.1). It might even be the case that they occur at critical incident angles [Yuan et al., 2006]. However, in contrast to P- receiver functions, the S-to-P conversions arrive prior to the direct S- wave and thus at negative times, whereas multiple reflection arrive after the direct S- wave. This allows for studies on the lithosphere- asthenosphere- boundary using the S-to-P conversions because there are only minor effects from multiple reflections, expecially for deeper discontinuities.

The processing of S- receiver functions is mostly the same as for P- receiver function. Receiver functions are calculated for S- and SKSac- waves. The different S- phases are rotated into the LQT ray coordinate system as well. We use the same teleseismic events from the ISC catalogue. Since S-to-P conversions have negative arrival times, the time axis will be reversed for the evaluation of the results. Due to the fact that beyond 85° epicentral distance, SKS- waves arrive prior to S- waves [Yuan et al., 2006], we selected events within 55° to 85° for the calculation of S- receiver functions and 85° to 120° for SKS- receiver functions. Unlike PKP- receiver functions, SKS- receiver functions will be included into the results.

3.1.3 Post processing

The calculation of receiver functions, either for P- or S- waves, are based on the following parameters: The raw waveforms are lowpass filtered at 5 Hz and resampled to 20 Hz. Theoretical backazimuths and incidence angles were used for the rotation of the traces into the LQT ray coordinate system. The window length for the deconvolution is 100 s. Before constructing receiver function profiles to identify discontinuities, further processing steps of the measurements are required. At first, we perform a manual quality control on the raw receiver functions. Receiver functions, which show a low signal to noise ratio are either repicked or simply removed. A good indicator for estimating the signal to noise ratio is the quality of the P- or S- onset in the L- or Q- component, respectively.

Stacking of single receiver functions, either station wise or over a geographical region, is an unavoidable step for imaging discontinuities. Differential times depend on epicentral distances. For that reason, only receiver functions with similar epicentral distances can be stacked. Especially, converted phases from large depths are effected by their different slownesses. The moveout correction is a solution for that problem. It requires ray tracing within a suitable velocity model and has the effect that the time axis is compressed or stretched, to align the same type of converted phases. For that reason, a reference epicentral distance of 67°, which corresponds to a slowness of $6.4 s/^\circ$ is used at which the receiver function remains unchanged. For smaller epicentral distances, the time axis is compressed and stretched for larger epicentral distances. In addition, a 1D velocity model is required. Usually, the IASP91 is sufficient enough for that purpose. Figure 3.3 shows P- receiver functions for two different stations after the moveout correction was applied. They are lowpass filtered at 3 s. The top, black receiver function is the stacked one over each single receiver function of the station, respectively. At both stations, we observe a clear peak at 3 or 5 s which is consistent in each receiver function and probably coming from the Ps- Moho conversion. At later delay times, stable peaks of Ps- Moho- multiples (PpPs and PpSs) are present. Figure 3.4 shows the T- component of the receiver functions for the same stations. They are sorted by azimuth and binned over 2°. Since the distribution of our events is mostly limited to azimuths of 20° and 110°, an evaluation regarding dipping and anisotropy of discontinuities, e.g the Moho, becomes difficult. Slight indications for a change in polarity might be present for a peak at $\approx 5s$ between 20° and 100° at station COO16. However, this is not consistent. For that reason, the upcoming evaluation of receiver functions will not include a discussion of a potential pressence of dipping discontinuities and anisotropy within the crustal and mantle lithosphere.

Stacking over single stations is suitable for shallow discontinuities like the Moho. However, a stacking over a certain geographical region might be more meaningful at greater depths. By calculating the piercing point location for conversions at a certain depth, all traces within a defined area are stacked [Dueker and Sheehan, 1997].

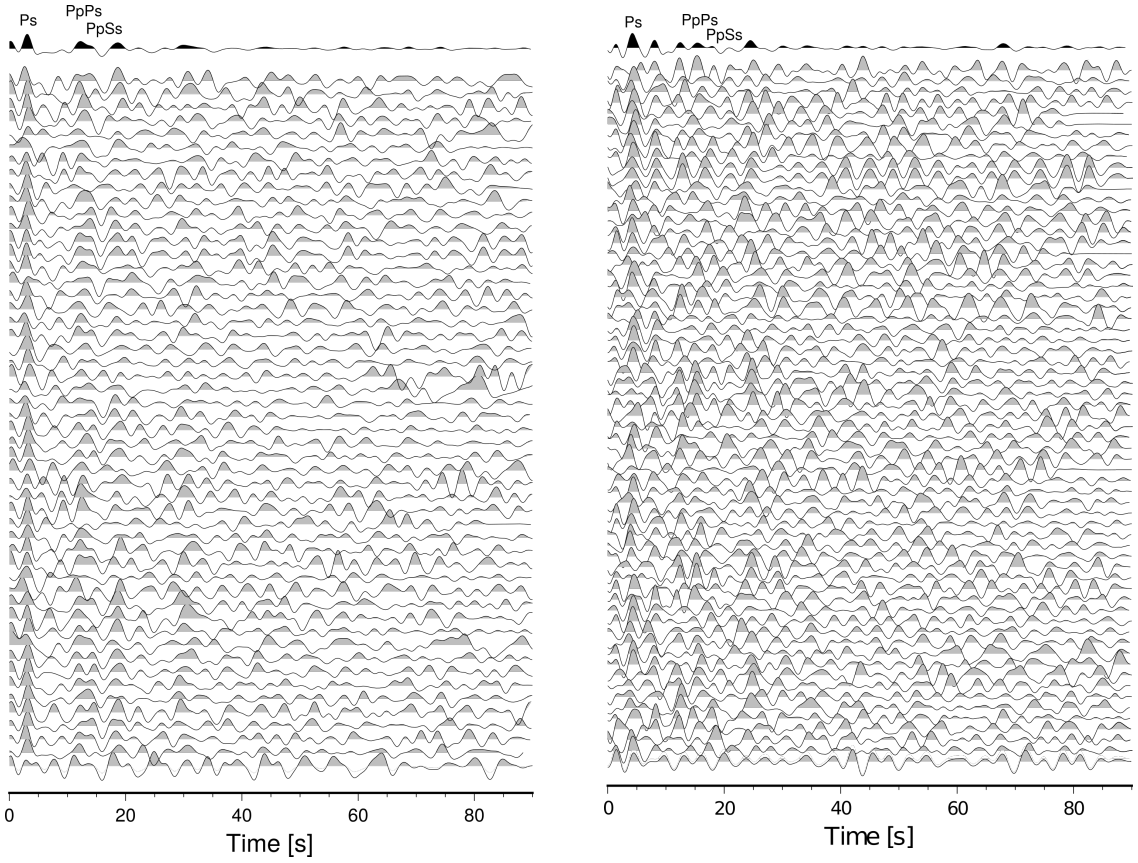

Figure 3.3: Q- component of P- receiver functions for stations COO02 (left) and COO16 (right) after moveout correction, sorted by occurence of the respective teleseismic event; top: stacked receiver function (black) and highlighted Ps-, PpPs- and PpSs- conversion

3.2 Results

We calculated P- and S- receiver functions for each event and station within their selected ranges of epicentral distances. This resulted in 2293 P- receiver functions, which is roughly 35 receiver functions per station. The number of single receiver functions per station ranges from 15 to 95. The total number of S- receiver functions is with 736 considerably lower. This already includes SKS receiver functions. Overall, this leads to an average number of 12 S- and SKS- receiver functions per station. There are even stations without any obtained S- receiver functions.

P-to-S and S-to-P conversions are clearly observable in our data. Figure 3.5 shows all P- and S- receiver functions, sorted by slowness and lowpass filtered at $2s$ and $4s$, respectively. In addition, they are slightly binned in steps over $0.1s/^\circ$ for P and $0.15s/^\circ$ for S. A moveout correction is not applied in this case. For P- receiver functions, we observe a clear Moho conversion at $4-6s$ which is followed by a negative peak. This might be an indication for the LAB. However, it might also be interpreted as the side lobe of the previous Moho peak. In addition, indications for the mantle transition zone can be seen. The 410 km discontinuity

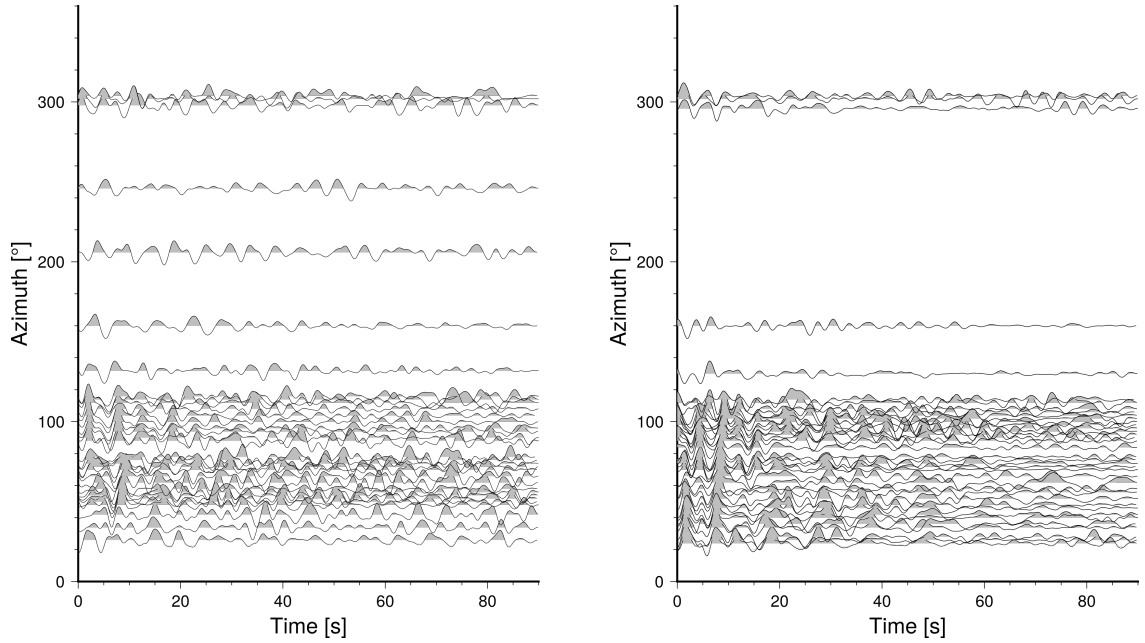

Figure 3.4: T- component of P- receiver functions for stations COO02 (left) and COO16 (right) after moveout correction, sorted by azimuth

is located at around $40-45s$ and the 660 km discontinuity at around $65-70s$. Indications for the 520 km discontinuity are not present. With increasing slowness, indications for a slight moveout of the conversions from the mantle transition zone are observable. For S- receiver functions, the figure is divided into two parts. The traces with low slowness values are from SKS- receiver functions, while the traces with a slowness of $9.8s/°$ or higher are from S- receiver functions. They show the Moho conversion at $4-6s$, like P- receiver functions. This is again directly followed by a negative peak which could be interpreted as the LAB or as the side lobe of the previous Moho peak. Unfortunately, there is no evidence for both discontinuities in SKS- receiver function.

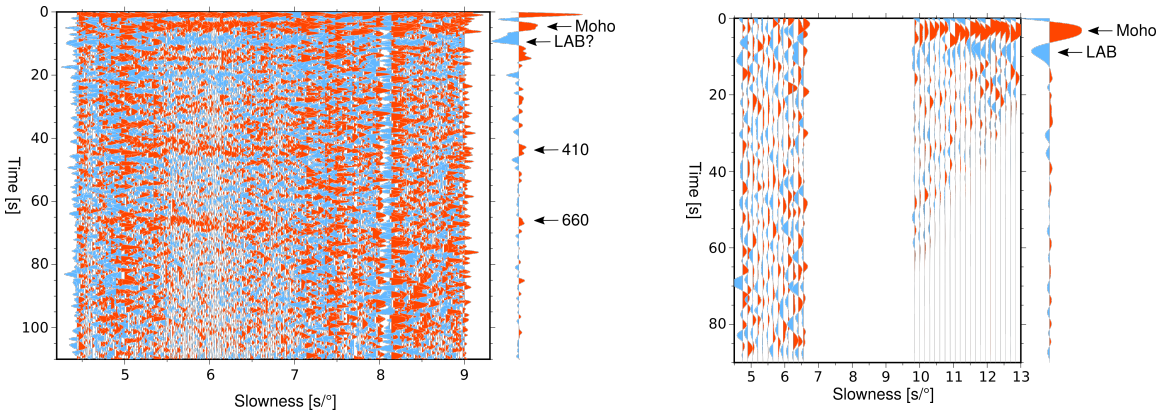

Figure 3.5: Receiver functions plotted as a function of slowness $[s/°]$; Left: P- receiver functions sorted and binned ($0.1\ s/°$) over slowness and lowpass filtered at 2s; Right: S- receiver functions sorted and binned ($0.15\ s/°$) over slowness and lowpass filtered at 4s

3.2.1 Moho from stacked receiver functions

Station wise evaluation of moveout corrected receiver functions is a common way to evaluate lithospheric discontinuities like the Moho. Here, we show stacked Moho conversions for P- and S- receiver functions (Fig.3.6). The size of the triangles represents the number of stacks for each station. For both, P- and S- receiver functions, we observe a relatively stable distribution of smaller delay times in the eastern part of the network and higher delay times in the central part around Jebel Akhdar and further northwest. This suggests a thinning of the crust from west to east, which is comparable to the global Crust1.0 model [Laske et al., 2013]. In addition to P-to-S conversion time, a corresponding Moho depth range is estimated in the same color scale. We assume that the crust consists of one single layer with a constant P- and S- wave velocity. Then, the travel time of the P-to-S conversion (t_{ps}) is the difference between the S- and P- travel time. This can be written as [Zhu and Kanamori, 2000]:

$$d = \frac{t_{Ps}}{\sqrt{\frac{1}{v_s^2} - p^2} - \sqrt{\frac{1}{v_p^2} - p^2}} \tag{3.8}$$

where d is the Moho depth and p the ray parameter. We used average velocities from the IASP91 model for P- and S- waves ($v_p = 6.1 km/s; v_s = 3.5 km/s$). Despite some scatter in the measurements, the Moho ranges from 32 km in the eastern part to 47 km in the westernmost part. This is contradictory to the results of Al-Hashmi et al. (2011). They proposed a crustal thickness of $\approx 45 km$ in the eastern part as well.

This approach of estimating crustal thicknesses from Ps- conversions has the advantage of being less affected by lateral velocity variations because P-to-S conversion points are usually close to the station. However, a problem occurs due to a trade-off between the thickness and the v_p/v_s ratio of the crust [Zhu and Kanamori, 2000]. This can be solved by including additional P- phases which will be discussed in section 3.2.4.

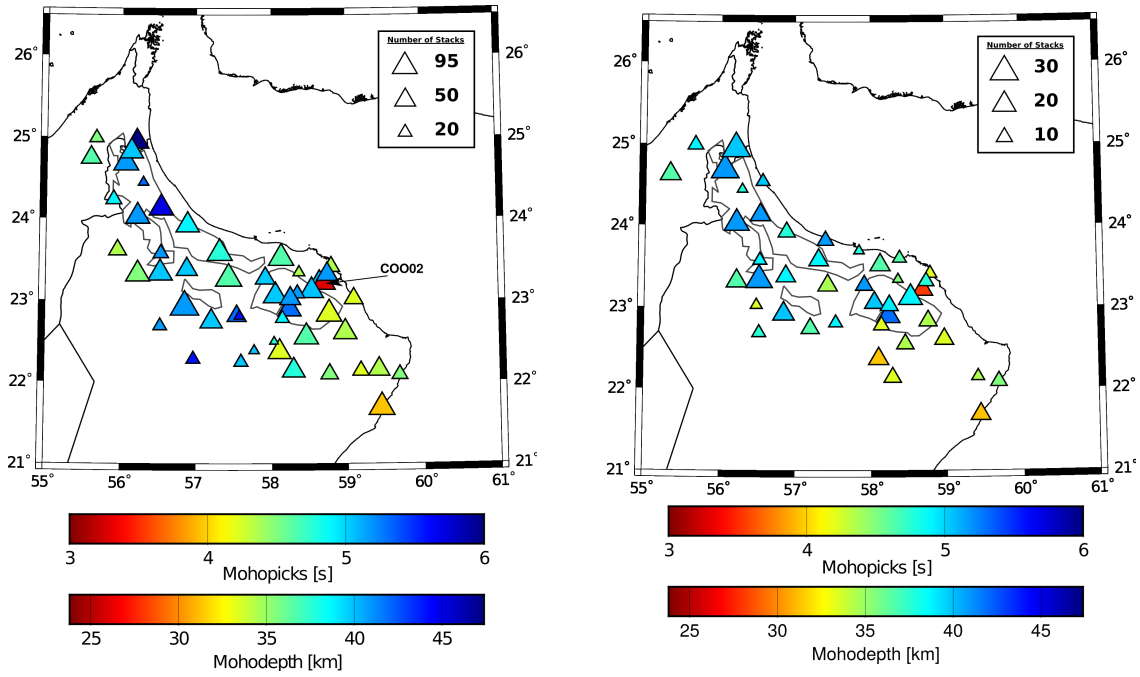

Figure 3.6: Mohopicks [s] and converted depth [km] for stacked receiver functions at each station; P (left) and S (right)

The result of station COO02 is worth to point out. It is highlighted in figure 3.6 (left) and shows a distinct smaller Ps- conversion than the surrounding stations. The single receiver functions of station COO02 show a highly consistent Ps- conversion at $\approx 3.2s$ (see Fig.3.3(left)). Therefore it might not be referred to a systematic error in the processing or an insufficient signal to noise ratio in individual receiver functions which superposes the stacked one. However, the question remains what the Ps- conversion of station COO02 represents. Figure 3.7 shows the results for the stacked and moveout corrected P- receiver functions for the stations COO51 and WSAR which are $\approx 12km$ and $\approx 6km$ away from station COO02, respectively. Both stations show a Ps- conversion from the Moho at $\approx 5.1s$ which corresponds to a Moho depth of $\approx 40km$ which is distinct different to station COO02. All three stations are located in the Saih Hatat window which is characterized by exhumed and partly metamorphosed rocks in the subsurface with a thickness of up to 20 km [Michard et al., 1991]. This might locally affect the receiver functions from COO02 and leads to an assumption that the Ps- conversion represents a shallower discontinuity like the basement of the exhumed metamorphic rocks.

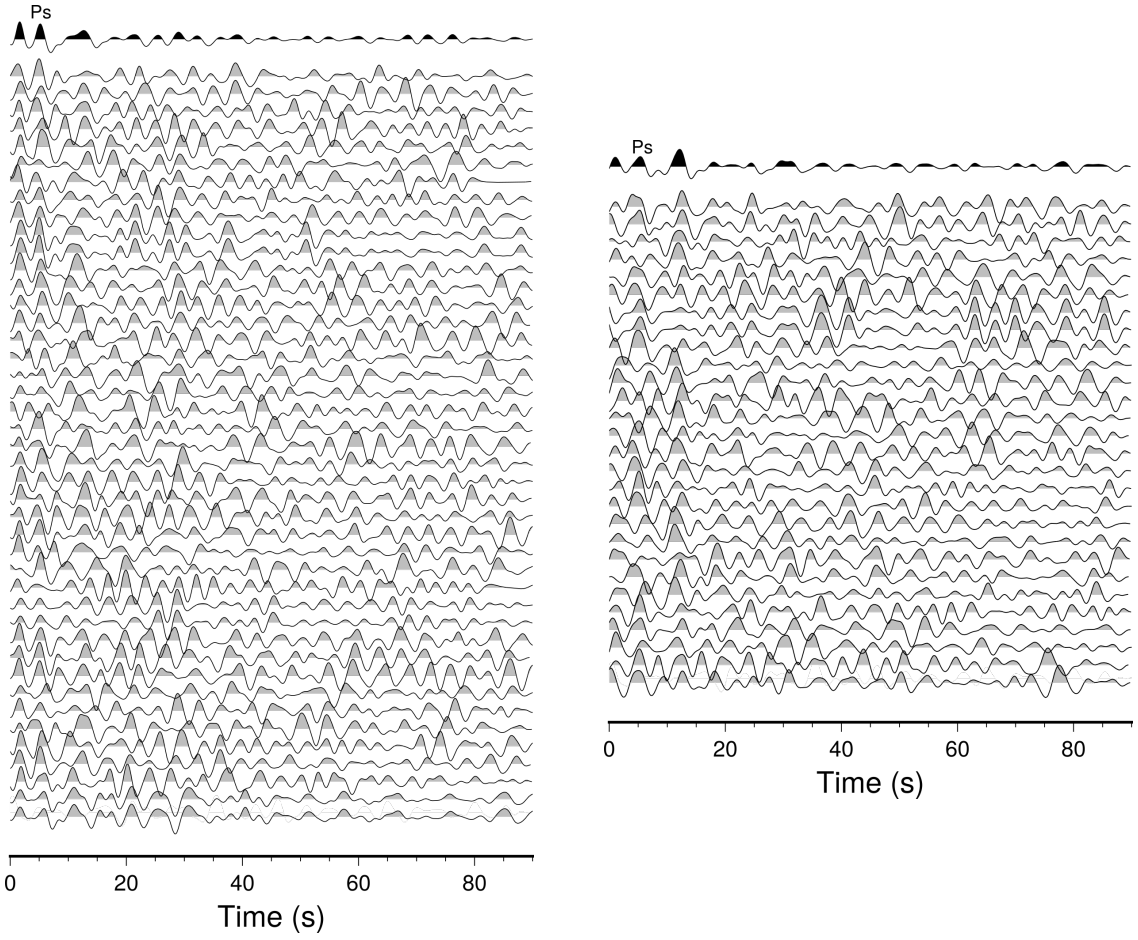

Figure 3.7: Q- component of P- receiver functions for stations COO51 (left) and WSAR (right) after moveout correction, sorted by azimuth; top: station wise stacked receiver function (black)

3.2.2 Lithosphere- asthenosphere- boundary

Information on the lithosphere- asthenosphere boundary are required to fully understand the kinematic and geodynamic evolution of the Al- Hajar Mountains. Unfortunately, there is only little information about the lithosphere- asthenosphere boundary in northern Oman. Previous studies are more focused on the Arabian shield and the Red sea [Hansen et al., 2007; Stern and Johnson, 2010].

For investigating the lithosphere- asthenosphere boundary, we use S- receiver functions, since they are minor effected by multiple reflections. They are stacked geographically over piercing points in 120 km depth. This might enhance the results regarding spatial variations of the discontinuity. Figure 3.8a shows locations of the piercing points which are slightely moved to northeast direction. In addition, the figure shows the location of three profils for which S- receiver functions have been evaluated (Fig.3.8b-d). Each receiver function is a result of geographically stacked bins of $0.5x0.5^{\circ}$ size. The number of stacks is written next to each trace. The top receiver function represents the stacked one for the entire profile.

They are lowpass filtered at 5 s. The main negative peak is related to the lithosphere- asthenosphere boundary. We can identify negative peaks which might represent the thickness of the lithosphere. Unfortunately, they might be effected by side lobes of the previous Moho peak. Therefore, an interpretation of lateral variations of the lithospheric thickness needs to be treated with caution. Overall, the lithosphere- asthenosphere boundary travel times range from 9 to 12 s which correspond to a lithospheric thickness of $\approx 80 - 110km$ based on IASP91. The thickness of the lithosphere of the centre part of the Arabian shield is up to 160 km [Hansen et al., 2007; Stern and Johnson, 2010] and thus thicker than below the Al-Hajar Mountains. In addition, Stern and Johnson (2010) proposes a lithospheric of $< 80km$ at the Red Sea coast which would be more comparable to our results.

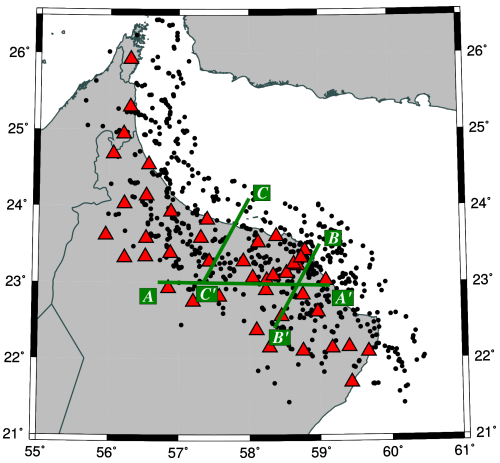

(a) Stationmap with piercing points at 120 km depth

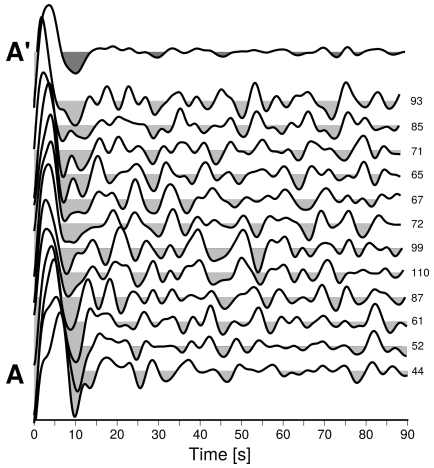

(b) Stacked S- Receiver functions for Profil AA'; binned over 0.5x0.5°

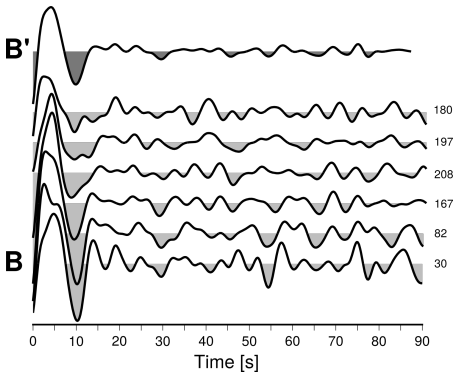

(c) Stacked S- Receiver functions for Profil BB'; binned over 0.5x0.5°

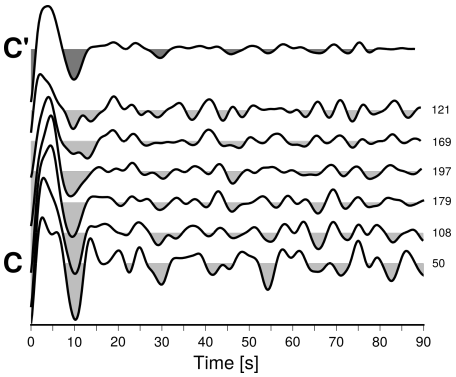

(d) Stacked S- Receiver functions for Profil CC'; binned over 0.5x0.5°

Figure 3.8: Profiles of stacked S- Receiver functions with piercing points at 120 km depth; lowpass filtered at 5 s

3.2.3 Mantle transition zone

The mantle transition zone divides the upper and lower mantle and is located in a depth range of 410 to 660 km. The upper and lower boundary of the transition zone are clearly observable in seismological data, due to an increase of seismic velocities in these depths. The 410 km discontinuity occurs as a result of a phase transformation from olivine to spinel (wadsleyite) due to certain pressure and temperature conditions. At 660 km, a phase transformation from spinel to perovskite occurs. The pressure and temperature conditions for the phase transformations and thus the depth of these discontinuities are linked to the Clapeyron slope [Bina and Helffrich, 1994]. The phase transformation for the 410 km discontinuity has a positive Clapeyron slope. For that reason, it is expected to be shallower in colder regions like subducting slabs and deeper in regions with higher temperatures like mantle plumes. The phase transformation for the 660 km discontinuity has a negative Clapeyron slope which results in a shallower depth at higher temperatures and vice versa. Besides the 410 and 660 km discontinuities, there is an additional one at $\approx 520km$ whose appearance in seismological observations as a global feature is not compelling [Bock, 1994; Egorkin, 1997]. It is assumed that it occurs due to a phase transformation of wadsleyite to ringwoodite [Deuss and Woodhouse, 2001].

In order to resolve conversions from discontinuities of the mantle transition zone, the P- receiver functions were stacked geographically. For that reason, we calculated piercing points at 550 km depth and applied a lowpass filter at 6 s. The receiver functions were binned over $0.5x0.5^\circ$ for the profils AA' and BB' and $0.25x0.25^\circ$ for CC'. The results are shown in figure 3.9. The Ps- conversions at the 410 and 660 km discontinuity are marked with blue and red lines. In addition, they are compared to the theoretical arrival times of the IASP91 model. The conversion for the 410 km discontinuity shows only minor variations and ranges from 43 to 45 s. This is close to the global average of the IASP91 model. In contrast, the conversions for the 660 km discontinuity show stronger variations and differ up to 2.5 s from IASP91. Especially towards the Arabian shield, the 660 km conversion times seem to increase, compared to IASP91. Overall, both discontinuities seem to shallow below the Gulf of Oman. Here, the conversion times are lower than IASP91. Unfortunately, there are no clear indications for the 520 km discontinuity.

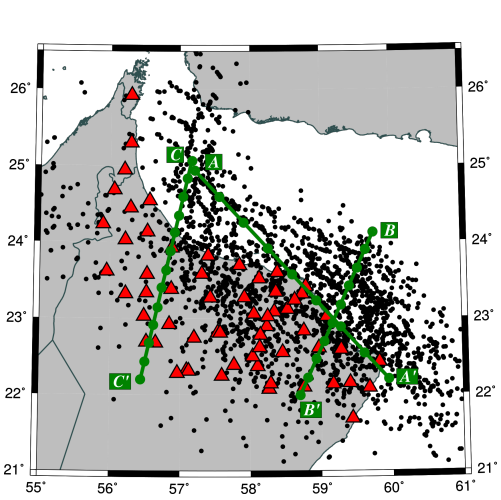

(a) Stationmap with piercing points at 550 km depth

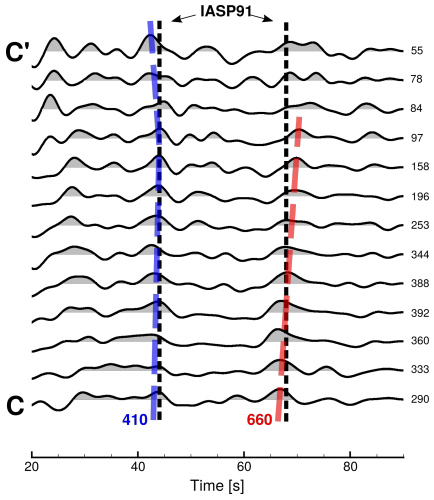

(b) Stacked P- Receiver functions for Profil CC'; binned over 0.25x0.25°

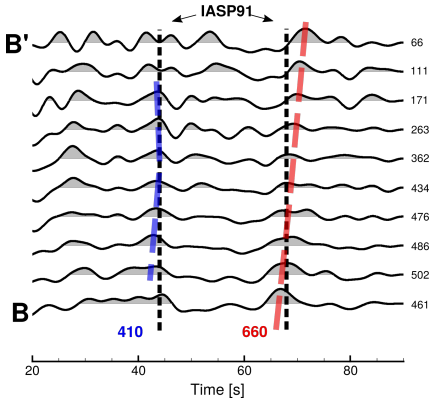

(c) Stacked P- Receiver functions for Profil BB'; binned over 0.5x0.5°

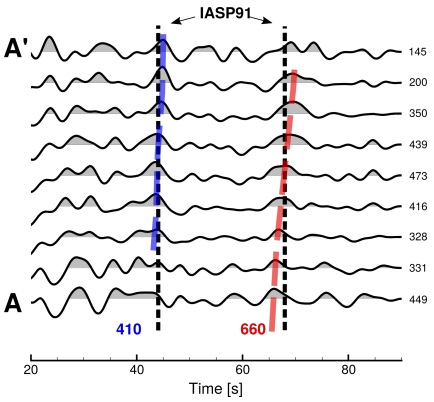

(d) Stacked P- Receiver functions for Profil AA'; binned over 0.5x0.5°

Figure 3.9: Profiles of stacked P- Receiver functions with piercing points at 550 km depth; lowpass filtered at 6 s

Another approach to investigate the mantle transition zone deals with the differential time between the 410 and 660 km conversion. It is independent of the shallow mantle structure and thus provide indications on the thickness of the transition zone [Li et al., 2003]. Figure 3.10 shows the differential times along the profils AA', BB' and CC' as a function of latitude. The error bars are calculated by using the width of each peak at 90 % amplitude, relative to the maximum. The resulting uncertainties for the 410 and 660 km conversions are summated for each receiver function separately. The result is used as the uncertainty of the differential time. They are compared to the reference value from IASP91 which allows us to estimate variations in thickness of the mantle transition zone and maybe even give assumptions regarding temperature variations in the mantle. Overall, most of the differential times are differing less than 1 s from IASP91 with an uncertainty of $\pm 0.3 - 0.8s$ which indicates that the mantle transition zone features a rather uniform thickness. A variation of 1

s corresponds roughly to 10 km variation in thickness or to $70 - 100°C$ variation in temperature according to the phase transformation hypothesis [Li et al., 2003]. Minor differences are still observable. While the differential times in the northwestern part of the area (Profil AA' and CC') are smaller than IASP91, the ones from the entire profil BB' are above the reference value. Towards southeast, they are increasing to even higher values which differ more than 1 s from IASP91. This would indicate that the mantle transition zone features a slight thinning in the northwestern part of the Oman Mountains and the Gulf of Oman and a minor thickening towards south and southeast. Unfortunately, it will be difficult to provide information on temperature variations. Since the 410 and 660 km discontinuities are linked to phase transformations and the Clapeyron slope, they should converge or diverge in different temperature regimes, respectively. This can not be observed in Fig.3.9. They are mostly varying in the same direction, either towards smaller or larger conversion times.

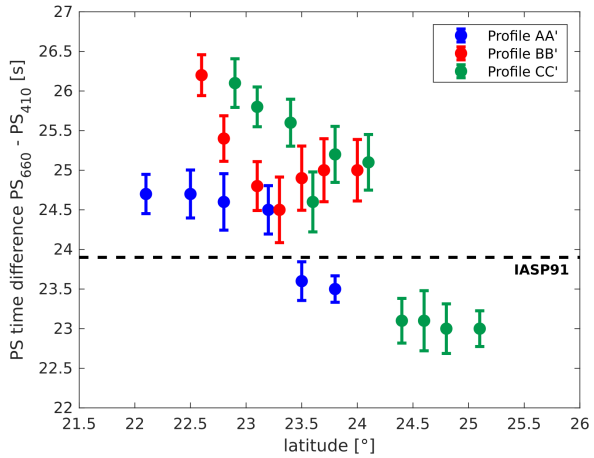

Figure 3.10: Differential time between the 410 and 660 km conversion for the profiles AA', BB' and CC', compared to the one from IASP91

3.2.4 Migration to depth

Evaluations of receiver functions as a function of conversion time are not sufficient enough to clearly pinpoint discontinuities. They need to be converted to depths which can be done in form of an inversion or migration. The inversion of receiver functions requires synthetic L- and Q- components of teleseismic P- waves and the assumption that the Earth's crust can be modelled by layers with constant velocities over a homogeneous half space [Kind et al., 1995]. An iterative comparison of synthetic and observed seismograms leads to an 1D S-wave velocity model over depth. Typically, the results are strongly non-unique [Kind et al., 1995], which is why a joint inversions of receiver functions in combination with different geophysical methods is often performed. A common method is a joint inversion of receiver functions and surface wave group velocity measurements to receive depth related information [Julià et al., 2000; Julià et al., 2003; Pasyanos et al., 2007; Gök et al., 2008; Al-Hashmi et al.,

2011].

Zhu and Kanamori (2000) introduced a different approach which is not based on an inversion. They performed a grid search which compares the Moho conversions of the different Ps-phases as a function of Moho depth and v_p/v_s ratio. Remembering section 3.2.1, we already estimated Moho depths by just evaluating Ps- conversions, for which we had to deal with a trade-off between the Moho depth and v_p/v_s ratio. A change in the v_p/v_s ratio of 0.1 leads to a difference of $4km$ in crustal thickness [Zhu and Kanamori, 2000]. Different phases, such as $PpPs$ or $PpSs$ show similar trade-offs. They can be written as [Zhu and Kanamori, 2000]:

$$d = \frac{t_{PpPs}}{\sqrt{\frac{1}{v_s^2} - p^2} + \sqrt{\frac{1}{v_p^2} - p^2}} \tag{3.9}$$

$$d = \frac{t_{PpSs}}{2\sqrt{\frac{1}{v_s^2} - p^2}} \tag{3.10}$$

with t_{PpPs} and t_{PpSs} as their respective conversion times. However, their maximum semblance leads to the most likely Moho depth and a corresponding v_p/v_s ratio. Unfortunately, this approach was not succesful in our case because most stations do not feature consistent peaks from the different P- phases besides Ps. Figure 3.11 shows two examples (COO02 and COO32) to illustrate the problem of the multiples. There are two additional examples (COO42 and UOSS) in appendix B. Each figure features the single receiver functions, sorted

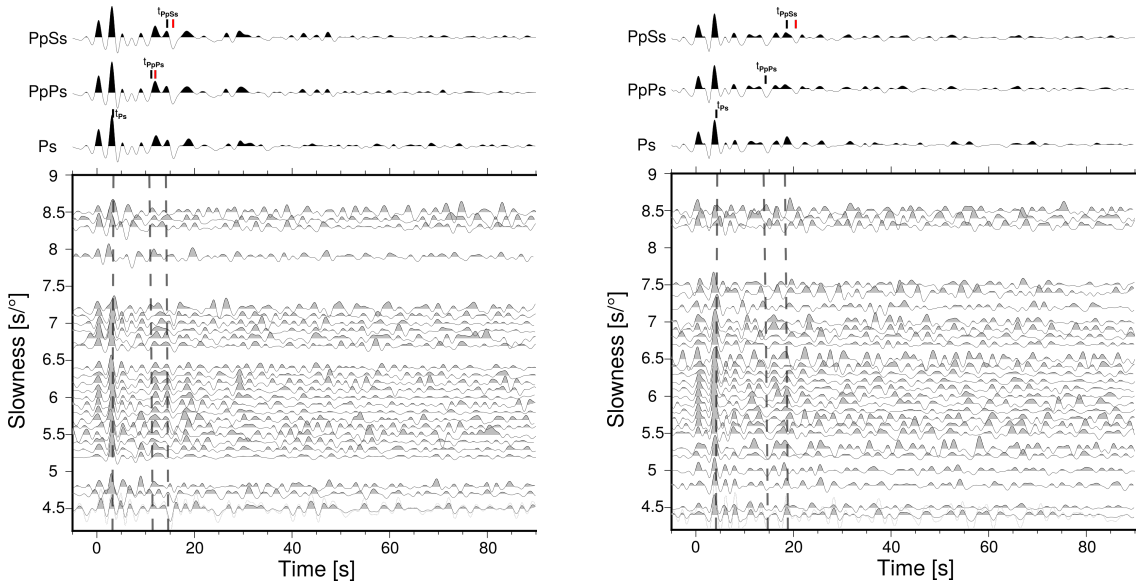

Figure 3.11: Detection of different P- phases for station COO02 (left) and COO32 (right). centre: single receiver functions, sorted by slowness. Dashed lines: theoretical arrival times for Ps, PpPs and PpSs based on velocities from IASP91 as a function of slowness; top: stacked receiver functions, moveout corrected for the different phases Ps, PpPs and PpSs. Black line: theoretical arrival times of the respective phase; Red line: observed arrival time of the respective phase.

and binned by slowness. The three receiver functions on top represent the stacked ones which are moveout corrected for the different P- phases (Ps, PpPs and PpSs). By using the picked Ps- conversion time and the corresponding Moho depth after Eq.(3.2), we are able to estimate theoretical arrival times for PpPs and PpSs by using Eq.(3.3) and Eq.(3.4) and the information from the IASP91 model. The results are plotted as a function of slowness (striped lines). They exhibit a slight moveout towards higher slowness values. The arrival times in the moveout corrected receiver functions on top are based on the reference slowness of $6.4 s/^{\circ}$. The results for station COO02 and COO42 feature two of the rare good results for which all three phases are observable (red lines). They are close to the theoretical ones which are based on the picked Ps- conversion. By calculating the depths of the discontinuities (Eq.(3.3) and Eq.(3.4)), using the observed arrival times t_{PpPs} and t_{PpSs}, they can directly be related to the multiples of the previously observed and picked Ps- conversion. For example, the Ps- conversion time of COO02 corresponds to a depth of $25.7 km$, whereas the ones for PpPs and PpSs resulted in $27.2 km$ and $27.8 km$, respectively. In contrast, there is no PpPs- conversion observable for COO32 (Fig.3.11), whereas PpSs is again present. It can be assigned to the picked Ps- conversion. For station UOSS, there are even no multiples observable (appendix B). Overall, there are many stations for which we were not able to observe multiple P phases, either due to a low signal to noise ratio or a strong oscillation of the receiver functions as a function of slowness. Table B.1 in appendix B summarizes the results for all stations and shows which P- phase is observable in the moveout corrected, stacked receiver functions. This clearly indicates that the approach after Zhu and Kanamori (2000) will not provide sufficient results for our data.

We use a semblance based approach to migrate the information from receiver functions into depth. For that reason, the receiver functions are binned over a certain lateral range and piercing points down to 800 km in steps of 5 km. Each trace of one bin is shifted by the travel time difference of the Ps- conversion which depends on the conversion depth and the slowness. Afterwards, the peak of the stacked receiver function at the theoretical Ps- delay time is compared to the mean peak of every single trace inside the bin. The theoretical Ps- delay time is based on the IASP91 model and the given depth. A minimum amount of 15 single traces is required for one bin to be accepted for the migration. This results in 3D semblance models for P- and S- receiver functions over depth which we evaluate in form of 2D vertical cross sections. Figure 3.12 shows vertical cross sections for P- receiver functions. Yellowish colors indicate a high semblance. Their locations are shown in the top panel of figure 3.12. Profil AA' was binned over the width of the entire profile. We still observe a shallowing Moho towards southeast direction. Towards nortwest, it is dimishing which might be due to stronger lateral variations of the Moho topography. At roughly 100 km, a strong semblance can be observed. This could be referred to the lithosphere- asthenosphere-boundary and interpreted as a relatively stable lithosphere thickness. The profiles BB', CC' and DD' are binned over $0.5 \text{x} 0.5^{\circ}$. They also show a clear Moho and indications for the

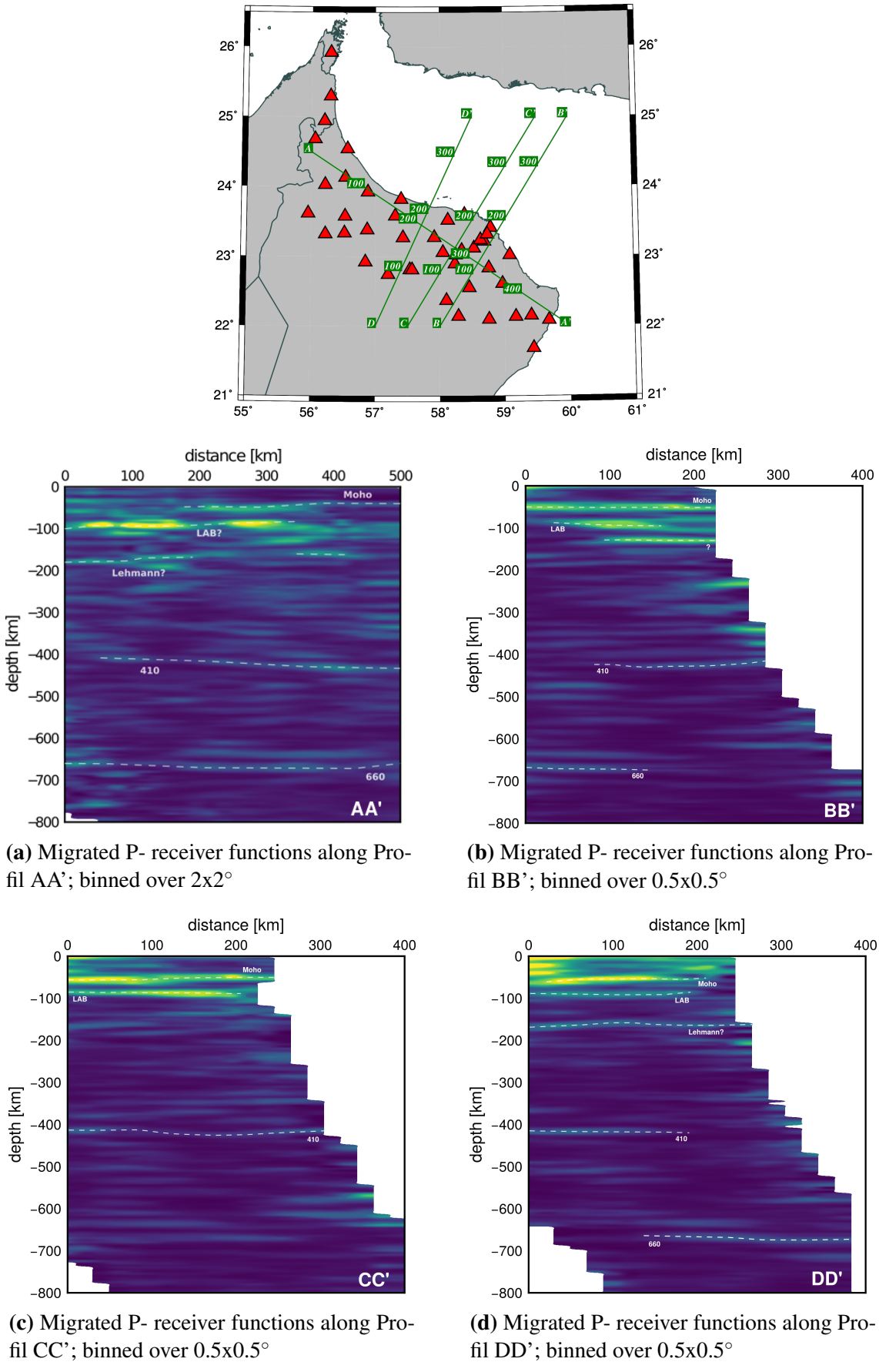

(a) Migrated P- receiver functions along Profil AA'; binned over 2x2°

(b) Migrated P- receiver functions along Profil BB'; binned over 0.5x0.5°

(c) Migrated P- receiver functions along Profil CC'; binned over 0.5x0.5°

(d) Migrated P- receiver functions along Profil DD'; binned over 0.5x0.5°

Figure 3.12: Depth migration for P- receiver functions. The color represents the semblance; top: Location of vertical cross sections

lithosphere- asthenosphere- boundary at roughly 100 km. However, the interpretation of the lithospheric thickness needs to be treated with caution, due to effects of multiples in P-receiver functions. To enhance the quality of the results and reduce the effects of multiples, a similar approach like the one by Zhu and Kanamori (2000) might be useful to apply. Stacking of migration results for different P- phases might dimmish multiples and improve the quality of the Ps- conversion of the desired discontinuity. The cross sections also provide indications of deeper seismic discontinuities. The mantle transition zone can clearly be observed in almost every profile. In addition, high semblance values can be seen at $180 - 200km$ depth in Profil AA' and DD' which could be interpreted as the Lehmann discontinuity.

Figure 3.13 shows the migration results of S- receiver functions for the same profiles. Since we require a minimum amount of 15 traces inside one bin, the results are rougher and reliable to a maximum depth of only 300 km. Surprisingly, the cross sections show a very clear Moho which is comparable to all previous results. They also reflect a thinning crust toeards eastern direction. However, there is no evidence of the lithosphere- asthenosphere- boundary at all. Since indications for the lithosphere- asthenosphere boundary should be rather observable in S- receiver functions, the obtained results are highly inconsistent and need to be treated with caution.

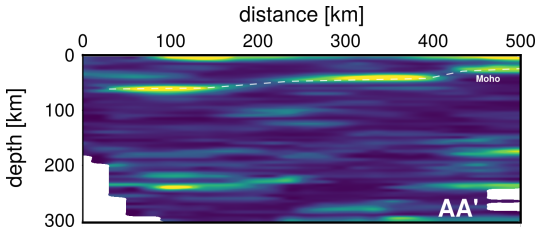

(a) Migrated S- receiver functions along Profil AA'; binned over 0.5x0.5°

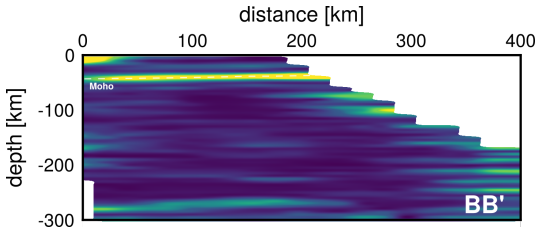

(b) Migrated S- receiver functions along Profil BB'; binned over 0.5x0.5°

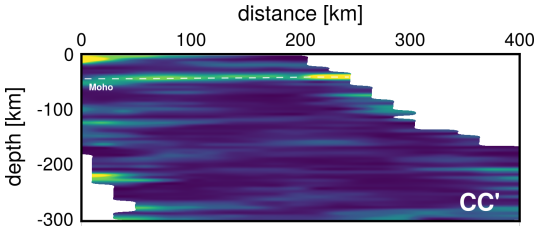

(c) Migrated S- receiver functions along Profil CC'; binned over 0.5x0.5°

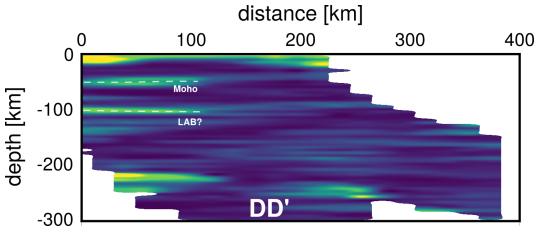

(d) Migrated S- receiver functions along Profil DD'; binned over 0.5x0.5°

Figure 3.13: Depth migration for S- receiver functions. The color represents the semblance

Chapter 4

3D Structure of the lithosphere of the eastern Arabian continental margin

The following chapter aims to determine the 3D model of shear wave velocity over depth by inverting the obtained results of ambient seismic noise surface wave tomography. For that reason, we use a probabilistic 1D inversion method, the Particle Swarm Optimization. It is applied to 1D local dispersion curves which were constructed from the phase velocity maps. The resulting 1D models of shear wave velocity over depth are used to construct the 3D velocity model. Since the inversion is performed for Rayleigh and Love waves simultaneously, we are able to obtain information on radial anisotropy within the crustal structure of the study area. Details about the Particle Swarm Optimization including a suitable parametrization and regularization to sucessfully invert our data are given in this chapter. The selection of inversion parameters and a priori information are also based on the obtained results from our receiver functions in the previous chapter. The resulting 3D model is presented in form of horizontal map views and vertical cross sections of isotropic shear wave velocity perturbations and radial anisotropy.

In the end, we are able to combine the obtained information from isotropic shear wave velocity over depth, radial and azimuthal anisotropy and receiver functions to discuss the 3D structure of the Oman ophiolite and the underlying continental lithosphere. In addition, we will discuss observations leading to a better understanding of the obduction process and the formation of the Al- Hajar Mountains.

4.1 1D inversion for shear wave velocity over depth

For appropriate evaluations of our frequency dependent phase velocities, an inversion to shear wave velocities over depth is necessary. The relation between surface wave dispersion measurements and the seismic velocity structure of the Earth is nonlinear [Shapiro and Ritzwoller, 2002]. There are two common approaches to solve this nonlinear problem, either a waveform fitting by linearizing the relation between the model and seismic waveforms and then iteratively calculating the model [Snieder, 1988; Nolet, 1990] or by inverting the surface wave dispersion measurements individually for 1D shear wave velocity over depth like it was performed by e.g. Meier et al. (2004) and Lebedev et al. (2006). In this work, we use the latter approach by applying the Partical Swarm Optimization, which is a probabilistic algorithm to invert phase velocitiy dispersion curves to shear wave velocity over depth. We seek to invert Rayleigh and Love wave phase velocities simultaneously to provide additional information on radial anisotropy.

4.1.1 Particle Swarm Optimization

The algorithm for optimizing nonlinear functions was already introduced in 1995 by Eberhart and Kennedy. The Particle Swarm Optimization is a stochastic global optimization algorithm which is related to actual swarming theory like it can be seen in fish schooling or bird flocking [Eberhart and Kennedy, 1995]. The basis of this approach is a swarm of particles which are vectors in the parameter space. The particle movement is realized by adding a velocity vector to the position of the particle which consists of three components: a cognitive-, a social- and a dynamic component [Engelbrecht, 2005]. The cognitive component contains the individual experience of each particle, which means that every particle remembers the position at which they reached their best objective function value. The social component yields shared information of the entire swarm. In other words, every particle knows the global best position, reached by another one. The dynamic component contains information about previous movement of the particles. Overall, they try to move in two directions, defined by the cognitive and social component, having an inertial momentum, which is the dynamic component [Wilken and Rabbel, 2012]. The displacement vector can be written as [Wilken and Rabbel, 2012]:

$$v_{ij}(t+1) = \omega v_{ij}(t) + c_1 r_{1j}(y_{Cij}(t) - x_{ij}(t)) + c_2 r_{2j}(y_{Gj}(t) - x_{ij}(t)), \tag{4.1}$$

with $x_{ij}(t)$ and $v_{ij}(t)$ as the position and the displacement of a particle i, in dimension j and at iteration t. The parameter space is defined by n_x dimensions ($j = [1, n_x]$). c_1, c_2 and ω are positive constants which contain information about exploration and convergence of the swarm. r_1 and r_2 are uniformly distributed random numbers from $[0, 1]$ for each n_x dimension. The first term of 4.1 represents the momentum from the previous displacement.

The second term is the cognitive component which yields the direction of the best local position $y_{Ci}(t)$. It will change if the particle reaches a better position [Engelbrecht, 2005]. The last term is the social component. It contains the movement of the swarm towards the direction of the global best position $y_G(t)$ and triggers the local convergence of the entire swarm. By following Wilken and Rabbel (2012), the algorithm of the PSO is implemented as follows:

(i) Randomly initialize a population of particles and evaluate the misfit.
(ii) Calculation of the local best position of each particle for the first iteration.
(iii) Determination of the global best position.
(iv) Adjusting all particles according to Eq.4.1
(v) Check stopping- criterion and restart from (ii).

By inverting local dispersion curves to shear wave velocity, models will be chosen randomly to find certain ones which fit our selection criteria. Local dispersion curves can be obtained from the calculated phase velocity maps which will be part of the next section. The selection criteria include the definition of a reasonable final model, a priori information and a sufficient misfit. Latter one is estimated by taking the rms value of the relative difference between the measured and synthetic data. The inversion aims to get a good fit between the observed local dispersion curve and a theoretical dispersion curves by iteratively improve the model parameters. The theoretical phase velocity dispersion curves for Rayleigh and Love waves for an elastic and isotropic 1D model are calculated with the Knopoff method which is based on the Thomson-Haskell matrix method and an Earth flattening approximation [Knopoff, 1964; Schwab and Knopoff, 1972]. The Thomson-Haskell method constructs layer matrices to relate the component of motion from one layer to the next one. The product of all layers yields the relation of motion between the free surface and the deepest considered layer. This is used to calculate the synthetic dispersion curve for the 1D inversion. For each iteration, repeated forward calculations are performed to search for the global best position. During the first iterations, the global misfit is decreasing fast until no better model can be found. The process reaches the stagnation phase. In this case, the particles will get reinitialized randomly in the parameter space [Wilken and Rabbel, 2012]. The inversion ends if the stopping criterion or the maximum number of considered iterations is reached. The results contain many acceptable and not- acceptable models. The variability enables us to estimate uncertainties of the results.

4.1.2 Local dispersion curves

Ambient noise surface wave tomography has been used to calculate period- depending phase velocity maps in a period range of $2-40s$. They provide information regarding the spatial distribution and predominent directions of isotropic and azimuthal anisotropic phase velocity perturbations with a lateral resolution of ≈ 30 km. Local dispersion curves can be extracted

from these phase velocity maps for Rayleigh and Love waves and a grid spacing of 10 km. They will be used for the 1D inversion. Since each phase velocity map was calculated with its own regularization, the local dispersion curves might show a relatively strong roughness, especially at lowest periods. For that reason, the roughness of each dispersion curve needs to be evaluated to remove portions of dispersion curves which exceeds a given threshold. The approach for estimating the roughness of local dispersion curves is mostly the same as the smoothness criterion in section 2.3.3. Even the same local Crust1.0 background models for Rayleigh and Love waves are used [Laske et al., 2013]. The smoothed first derivative of the local dispersion curve as a function of frequency is estimated and compared to the corresponding value of the backgroundmodel. By taking its absolute value, positive and negative variations are treated equally. This is sufficient for lower frequencies. According to the smoothness criterion in section 2.3.3, we treat higher frequencies differently, by just evaluating the first derivative of the local dispersion curve without taking the background model into account. This is due to strong lateral heterogeneities in the upper crust. Figure 4.1 shows two examples of this process. On the left side, the roughness of the dispersion curve is below the constant threshold of $0.6s$. In contrast, the roughness of the dispersion curve on the right side exceeds the threshold at highest frequencies which leads to a rejection of this portion of the local dispersion curve. The roughness of each accepted local dispersion curve is then used to calculate the standard deviation at each frequency.

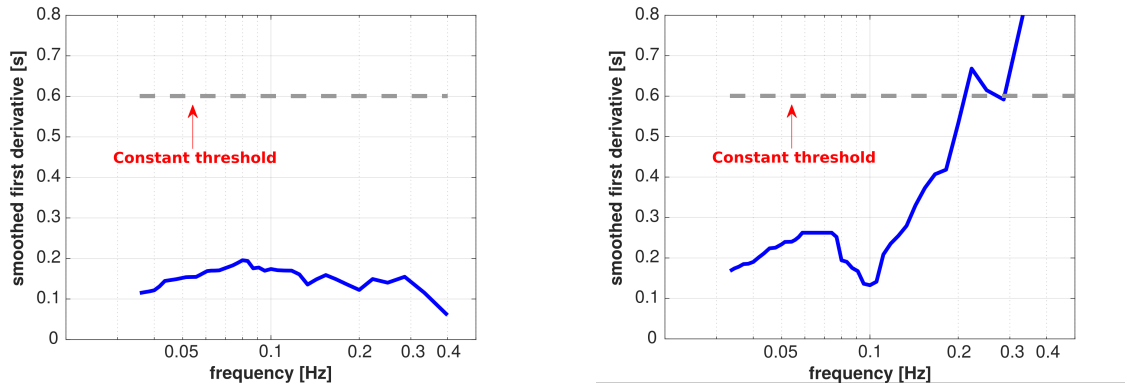

Figure 4.1: Illustration of the smoothness criterion. The smoothed first derivatives of the phase velocities are plotted over frequency. Left: A smooth example where the roughness of the local dispersion curve is overall below the threshold. Right: An example with strong roughness at highest frequencies which exceeds the threshold. The gray dashed line represents the constant threshold of 0.6 s.

Since ambient seismic noise surface wave tomography was performed with a model grid of 10 km knot spacing, we were able to estimate a dense grid of local dispersion curves with a sampling of 10x10km as well. This results in 1122 local Rayleigh wave dispersion curves with an average standard deviation of $0.136km/s$ and 1105 local Love wave dispersion curves with an average standard deviation of $0.193km/s$. Figure 4.2 shows the remaining

local dispersion curves for Rayleigh and Love as 2D histograms. They show the already mentioned convergence of the dispersion curves towards higher periods and strong lateral heterogeneity at lowest periods. Overall, most of the dispersion curves are in a frequency range of 2 to 20 s. Especially for Love waves, phase velocity maps of longer periods consist of less than 30 paths which makes a reliable interpretation difficult.

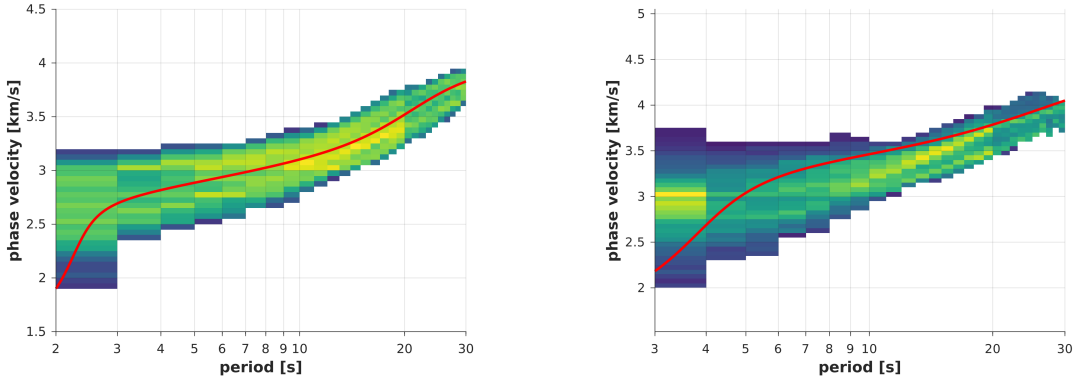

(a) Rayleigh **(b)** Love

Figure 4.2: Local Rayleigh and Love wave phase velocitiy dispersion curves as 2D histograms; Red: Local 1D model from Crust1.0 [Laske et al., 2013]

4.1.3 Parametrization

The inversion results, the amount of acceptable results and its uncertainties depend highly on the parametrization of the model space. It includes the number of layers, the range of allowed velocity perturbations, the thickness of layers, the inclusion of radial anisotropy and the perturbation order. The quality of the final model and the uncertainties depend on the width of the search space considered in the inversion [Shapiro and Ritzwoller, 2002]. The parametrization needs to be chosen with caution. A weakly constrained inversion results in a huge amount of models which fit the observed data, but also leads to large uncertainties. Much tighter constraints will reduce the uncertainties. However, the resulting models tend to be affected by systematic errors in the data.

The strategy to parametrize our inversion mainly follows the work of El-Sharkawy (2019). He was constraining each model parameter individually. The parameter space is defined by the ($\pm$) maximum allowed perturbation of shear wave velocity from the background model at each layer. Therefore, the background model defines only the boundaries of the parameter space. However, an appropriate background model is still highly useful for obtaining robust results. Inappropriate background models might lead to trade- offs between the individual parameters. For our inversion, we decided to take a simple backgroundmodel with a constant shear wave velocity ($2.9 km/s$) in the entire crust. In addition, a Moho depth is defined for each local dispersion curve which is based on the Moho depth of the closest Crust1.0

Model [Laske et al., 2013]. The models are characterized by a large number of layers. Each layer contains information about P- wave velocity, S- wave velocity, density and layer thickness. The parametrization of the crust is the same for every 1D grid point. Above the Moho, we consider cubic perturbations of shear wave velocity, whereas it is kept constant beneath the Moho. Figure 4.3 shows three different model parametrizations for different regions within our study area. They are only differing in terms of assumed Moho depth. The dots are indications for the location of the defined layers, while its color represents the kind of perturbations. Red represents cubic perturbation and black constant perturbation. Since we are inverting for shear wave velocity and depth, the additional horizontal line in the same color indicates that the layer can vary with depth. The parametrization of each depth

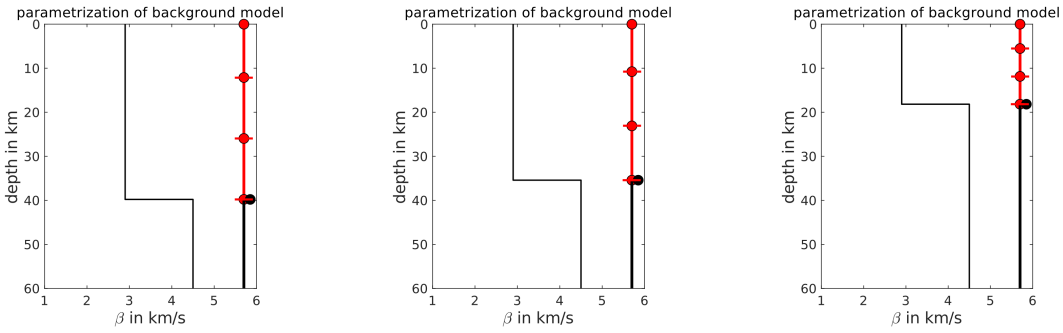

(a) West **(b)** Center **(c)** East

Figure 4.3: Parametrization of the background model examplary for three different local grid points within the area. They differ in terms of Moho depth. The parametrization in the crust is the same for every background model in the entire area.

layer consists of several single parameters, namely the dimension of the parameter space, regularizations and order and kind of perturbations. The definition of each parameter follows El-Sharkawy (2019) and can be seen in table 4.1. Table 4.2 shows the final parametrization which we used for the inversion of every local dispersion curve to construct the 3D model. It allows for relative large isotropic shear wave velocity perturbations in the crust. They can differ with $\pm 1.2 km/s$ and $\pm 1.6 km/s$ from the reference model. In addition, we do not allow for any damping of the absolute values of shear wave velocity perturbations (*pwvabs*). The same is considered for the damping of the absolute values of perturbations in depth (*pwdabs*). The node which represents the Moho (node: 24) and the one above (node: 16) receive a certain damping to the differences of the shear wave velocity perturbations between different nodes ($pwvdiff$). This will be further discussed in the next section. The depths of the nodes ($pdepth$) in the crust can vary within ± 3 km, except the first one which is kept fix. The Moho depth can vary within ± 5 km. This seems to be unreasonable for the eastern part of our study area where we already noticed inconsistencies between the results from Al-Hashmi et al. (2011), Crust1.0 [Laske et al., 2013] and our obtained results on receiver

Table 4.1: Definition of the different parameters for the inversion of dispersion curves

nodes	layer indices which is located at the top of the layer
pmax.iso	maximum isotropic perturbations in shear wave velocity at each depth node [km/s]
pmax.aniso	maximum anisotropic perturbations in shear wave velocity at each depth node [km/s]
pdis	defines the shear wave velocity to be continuous or discontinuous
pwvabs	model regularization (damping) applied to absolute values of isotropic or anisotropic shear wave velocity perturbations
pwvdiff	model regularization (damping) applied to differences of the shear wave velocity perturbations between different nodes
pdepth	maximum absolute value of perturbations in depth [km]; node is kept fix if pdepth = 0
pwdabs	model regularization (damping) applied to absolute values of the perturbation in depth
porder	order of perturbations; constant (0), linear (1), quadratic (2), cubic (3)
paniso	flag to allow for anisotropy, either radial or azimuthal, in shear wave velocity between current and next deeper node
pcoup	coupling perturbations in v_p and ρ to perturbations in v_s

functions. In contrast, they are mostly consistent in the central and western part of the study area. Since it was already mentioned that we are using the Moho depth from Crust1.0 for the background models, it needs to be varified that this is also valid for the eastern part. For that reason, a first test was performed to show which information on the crustal thickness fit our local dispersion curves in the eastern part of the study area the best. Figure 4.4 shows an example for one local grid point near Jebel Ja'alan. The 1D inversion is performed by using the final parametrization of table 4.2 and the Moho depth information from (a) Crust1.0, (b) our results on receiver functions and (c) the results from Al-Hasmi et al. (2011) as a priori information in the reference model. During the inversion, the Moho depth can vary within $\pm$5 km. The upper panel of figure 4.4(a,b,c) shows the observed dispersion curves with their standard deviation (blue), the corresponding synthetic dispersion curves of the model with the minimum misfit (red) and their misfit. Beneath each dispersion curve, the second figure shows the best 5000 depth models of the entire inversion, respectively. They are color-coded by the misfit. Blue models indicate low misfits, while grey models are rejected due to high misfits. The black and yellow striped model represents the best fitting model. The 1D inversion for the Moho from Crust1.0 as a priori information features the lowest misfit of the dispersion curve. With increasing crustal thickness, the misfit is steadily increasing. The best fitting model the Crust1.0- inversion shows a distinct increase in shear wave velocity

Table 4.2: Final parametrization of the 1D inversion

node	pmax. iso	pmax. aniso	pdis	pwvabs	pwvdiff	pdepth	pwdabs	porder	paniso	pcoup
1	1.2	0.5	1	0	0	0	0	3	1	0
8	1.2	0.5	0	0	0	3	0	-3	1	0
16	1.6	0.5	0	0	0.2	3	0	-3	1	0
24	0.2	0.5	1	0	3	5	0	0	0	0
42	0	0.5	0	0	0	0	0			

at $\approx 19km$ which is the Moho. In contrast, the best fitting models of the two inversions which contain the respective information on receiver functions show only minor increases of shear wave velocity at the Moho depth. In addition, they already show velocities of more than $4.2km/s$ in depths of $\approx 20km$. Therefore, using the Moho depths from Crust1.0 as a priori information for the reference model and a variation in depth ($pdepth$) of $\pm 5km$ for the inversion seem to be suitable to fit the local dispersion curves even in the eastern part of our study area.

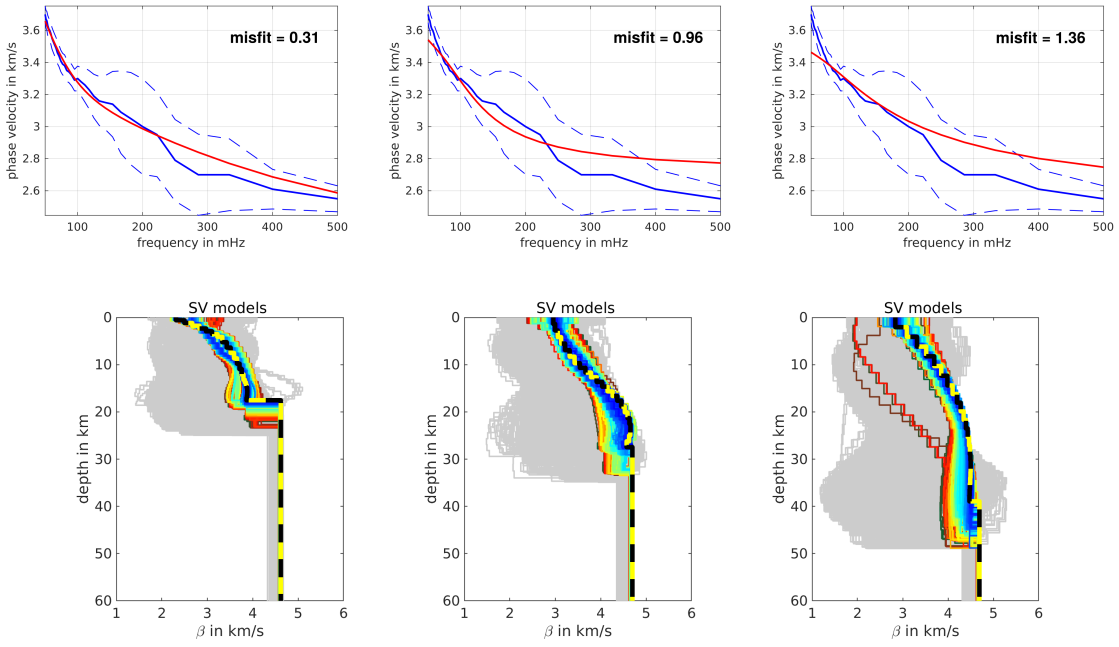

(a) Crust1.0 **(b)** RF **(c)** Al-Hashmi

Figure 4.4: 1D inversions for the different Moho information from (a) Crust 1.0: 20 km, (b) Receiver functions from our data: 32 km and (c) Receiver functions from Al-Hashmi et al. (2011): 42 km on one local dispersion curve in the eastern part of the study area near Jebel Ja'alan

4.1.4 Radial anisotropy

In contrast to azimuthal anisotropy, radial anisotropy defines the difference between Rayleigh and Love wave dispersion curves. In geological terms, radial anisotropy can be interpreted as arrangements of anisotropic minerals caused by former tectonical episodes of deformation. In case of an undisturbed stratification with horizontal layering, the horizontally polarized shear wave velocity V_{SH} is larger than the vertically polarized shear wave velocity V_{SV}. Radial anisotropy provides important information on crustal and mantle dynamics. Generally, Rayleigh and Love wave dispersion curves are inconsistent in terms of that they can not be fit at once using a simple isotropic model [Shapiro and Ritzwoller, 2002]. That problem can be solved by introducing radial anisotropy which was already a topic in many researches [McEvilly, 1964; Dziewonski and Anderson, 1981; Gaherty and Jordan, 1995; Montagner and Jobert, 1988; Montagner and Tanimoto, 1991; Ekström and Dziewonski, 1998; Villasenor et al., 2001; Shapiro and Ritzwoller, 2002]. Radial anisotropy in the crust can be explained by geological deformation processes, like extension or compression.

To ensure that a simultaneous inversion of Rayleigh and Love wave dispersion curves by introducing radial anisotropy will enhance the results, it is necessary to test all different combination of inversions. This includes inversions for Rayleigh waves, Love waves, isotropic Rayleigh and Love waves simultaneously and anisotropic Rayleigh and Love waves simultaneously. For that reason, the 1D inversions are performed at first for one single grid point. The results are shown in figure 4.5. The upper parts of Fig.4.5(a,b,c,d) show the observed Rayleigh (blue) and Love (cyan) wave dispersion curves with their standard deviation. The parametrization from table 4.2 is used in all cases. A new parameter is defined for the anisotropic Rayleigh and Love wave inversion (*pmax.aniso*). This parameter determines the maximum allowed anisotropic perturbations in shear wave velocity at each depth node. It can vary within $\pm 0.5 km/s$ at each node.

The inversion for Rayleigh waves show overall the best fitting of the dispersion curve (misfit: 0.22). The figure below shows a good resolution and a well defined model. The Love wave inversion features a large amount of acceptable models which results in relatively large uncertainties. The misfit between the observed and synthetic dispersion curve is with 0.4 worse than the one for the Rayleigh wave inversion. The simultaneous inversions of Rayleigh and Love wave dispersion curves show distinct discrepancies between each other. The isotropic inversion shows a large amount of acceptable models. The dispersions curves are poorly fitted and feature a large misfit of 0.97, compared to the one including radial anisotropy (misfit: 0.3). During the parameter tests, this was observed very often. In fact, by performing the isotropic inversion of Rayleigh and Love wave dispersion simultaneously, one of the observed curves was fitted relatively well, whereas the other one was not. This agrees with the fact that it is difficult to explain Rayleigh and Love wave dispersion curves with just one isotropic model [Shapiro and Ritzwoller, 2002]. By introducing a maximum al-

lowed anisotropic perturbation in shear wave velocity, the results are improving distinctly. The dispersion curves for Rayleigh and Love waves are fitted well. The depth models are well resolved and comparable to the result of the Rayleigh wave inversion. It is worth to mention that the anisotropic Rayleigh and Love wave inversion features the least amount of rejected models. This is probably due to the much higher amount of forward calculations in the inversion which is necessary to do and part of the next section.

This test was repeated for every local dispersion curve within our study area. Figure 4.6 shows the minimum misfits for every 1D inversion and any kind of inversion by using Rayleigh and/or Love wave dispersion curves. The lowest misfits are obtained by inverting only one dispersion curve, either Rayleigh or Love (a,b). The average misfit is 0.27 for both sets of inversion. The isotropic inversions of Rayleigh and Love waves show the largest misfits (average misfit: 0.61). The maximum values are obtained in the area of the Al- Hajar Mountains. This again reflects the weakness of a combined isotropic inversion of Rayleigh and Love wave dispersion curves. By introducing radial anisotropy, the misfits are again lower (average misfit: 0.35). However, the tests have shown that a simultaneous inversion of Rayleigh and Love wave dispersion curves by introducing radial anisotropy is suitable to estimate the 3D structural model of our study area. The misfits are comparable to the ones obtained from Rayleigh or Love wave inversion. The introduction of radial anisotropy enhances the results for a combined inversion of Rayleigh and Love wave dispersion curves significantly.

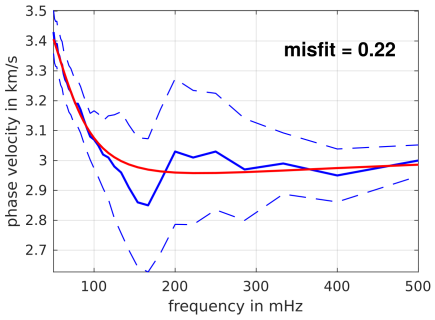

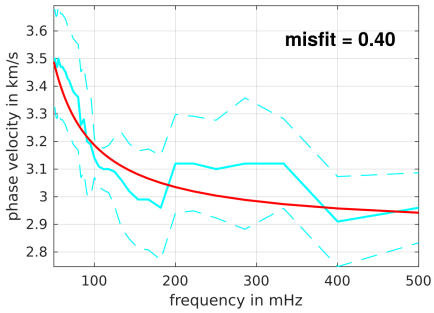

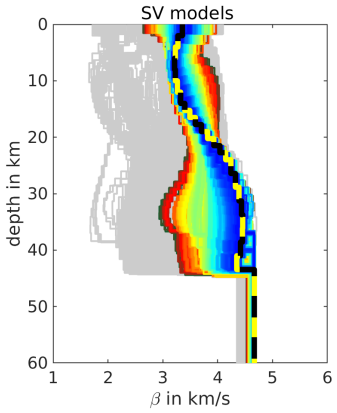

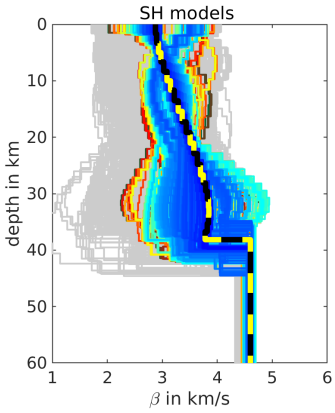

(a) Rayleigh **(b)** Love

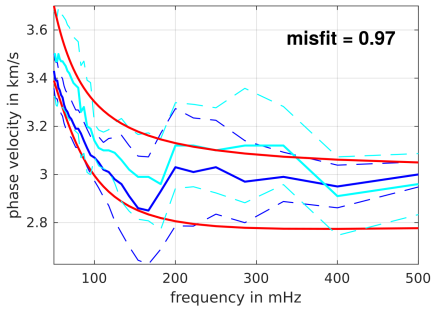

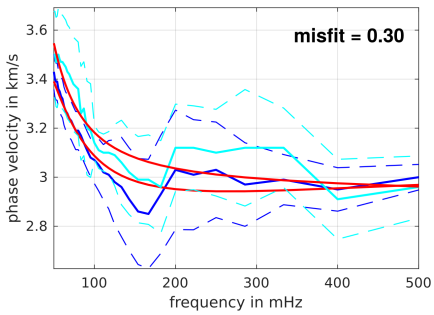

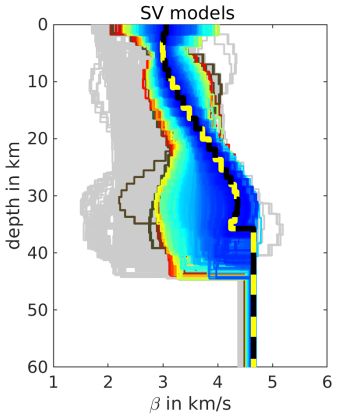

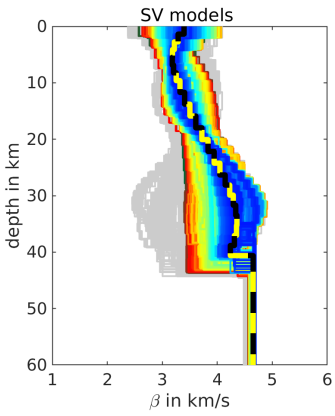

(c) Rayleigh + Love isotropic **(d)** Rayleigh + Love anisotropic

Figure 4.5: Inversion results for one local point by using the different combinations for inverting Rayleigh and Love wave dispersion curves

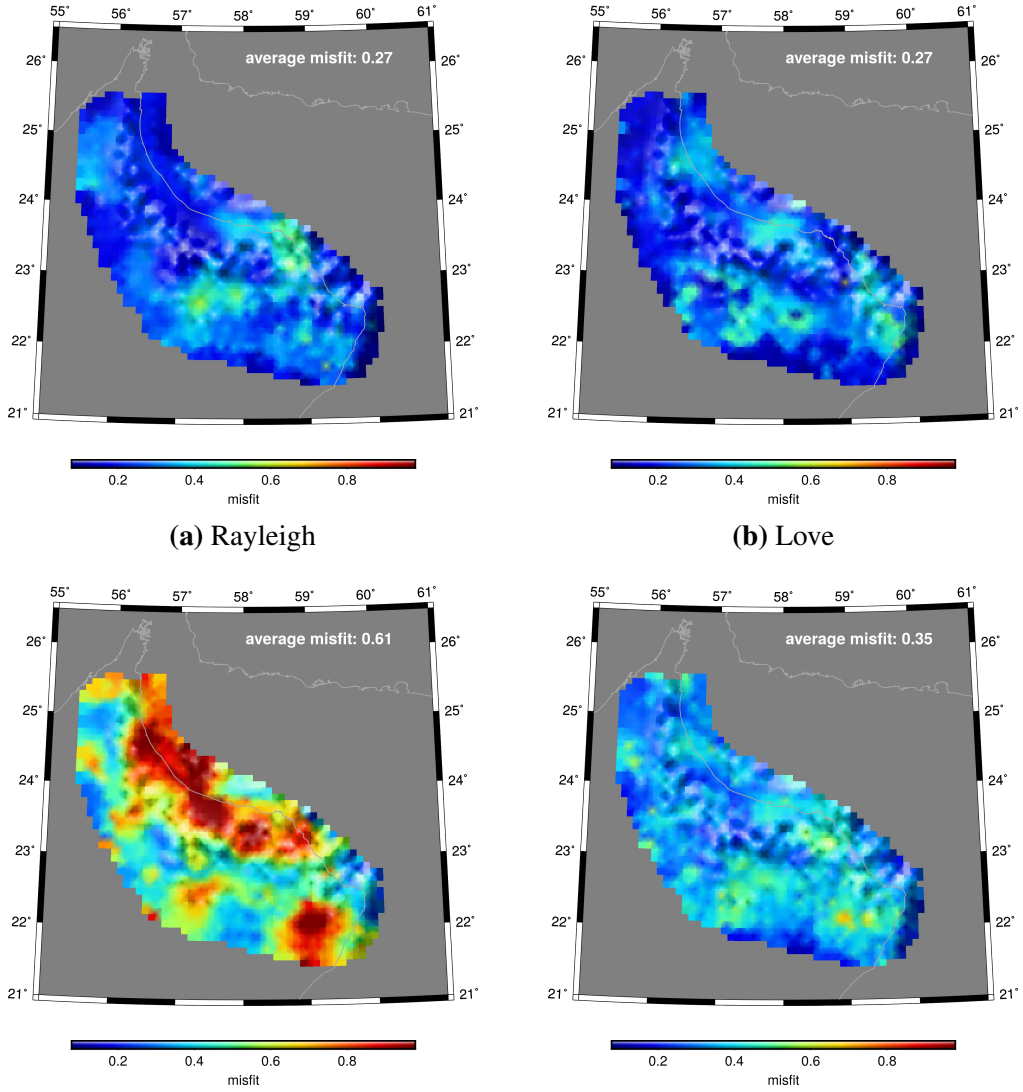

(a) Rayleigh

(b) Love

(c) Rayleigh + Love isotropic

(d) Rayleigh + Love anisotropic

Figure 4.6: Map of the lowest misfit of each 1D inversion and each combination for inverting Rayleigh and/or Love wave dispersion curves

4.1.5 Regularization and uncertainties

The regularization of the depth inversion has huge effects on the results in terms of model amplitude, -roughness and the magnitude of the perturbations from the background model. This leads to the fact, that the robustness of the inversion relies on the data quality and a priori information. The regularization of the inversion is controlled by three model parameters. *pwvabs* represents the damping of the absolute velocities at each node, while *pwdabs* damps the absolute depths, if the node allows for variability. At last, $pwvdiff$ damps the difference in velocity perturbations between different nodes. Following El-Sharkawy (2019), the parameter with the strongest effect on Rayleigh wave inversion is $pwvdiff$. Especially at nodes which are at the ends of different perturbation orders, a relatively strong damping to the differences of shear wave velocity perturbations should be applied. Since we are using a

background model with constant velocities in the entire crust, *pwvabs* and *pwdabs* are set to zero for all nodes. At this point the question arises, how does $pwvdiff$ affect the inversion for radial anisotropy and what amount of damping is necessary? Some tests showed that besides a strong damping of the node which represents the Moho ($pwvdiff = 3$), a slight damping of the node above the Moho is required. This is shown in figure 4.7 for $pwvdiff$ = 0; 0.2; 0.5. The dispersion curves are located in the top panel, the corresponding 1D depth models for radial anisotropic perturbations beneath. The lower panel represents trade-offs between radial anisotropy at the Moho and at the node above, here referred as lower crust. Without any damping, the inversion result shows very poor resolution (Fig.4.7a). While the dispersion curves are fitted well, many acceptable results are obtained across the entire parameter space. On the other hand, high damping (Fig.4.7c) leads to smooth models and a minor trade-off between the radial anisotropy of the lower crust and the Moho. However, the dispersion curves are poorly fitted. Slight damping (Fig.4.7b) results in a smooth result and a good fitting of the dispersion curves.

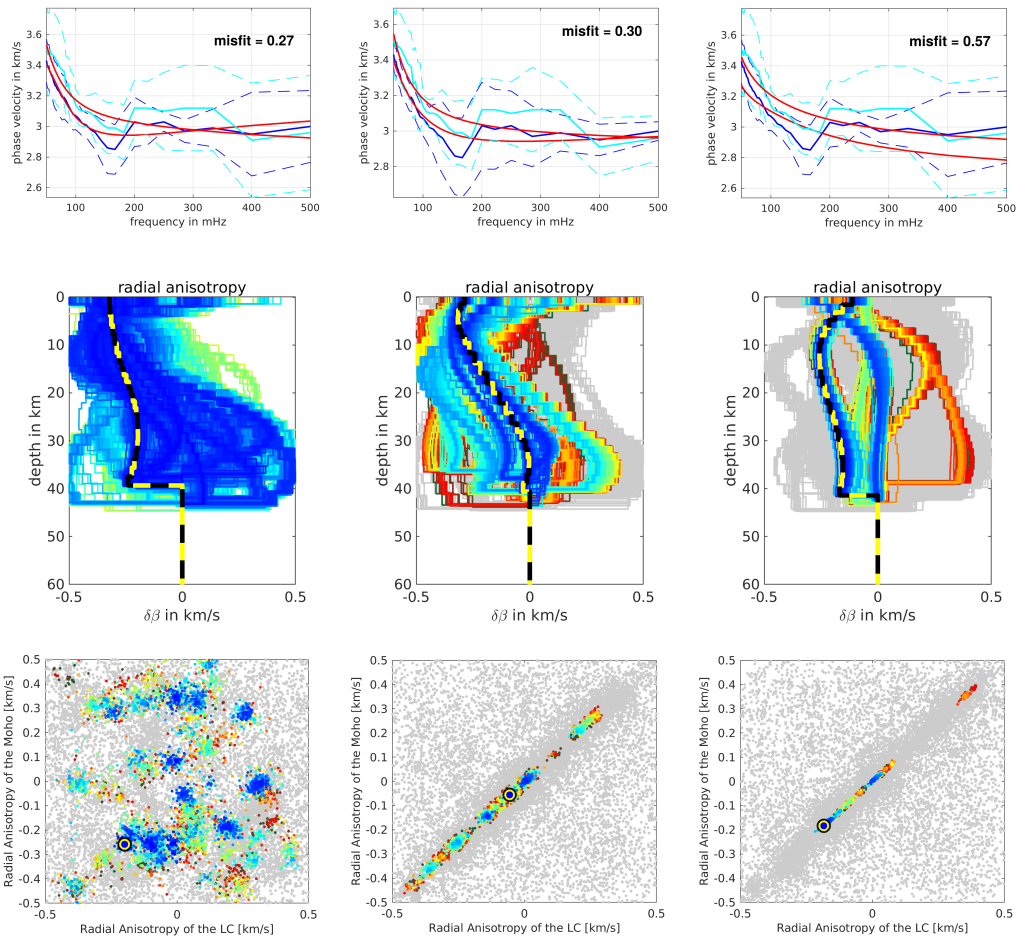

(a) pwvdiff = 0 **(b)** pwvdiff = 0.2 **(c)** pwvdiff = 0.5

Figure 4.7: Regularization effect of $pwvdiff$ on the inversion results. The fit of the dispersion curve and their corresponding 1D models are shown in the upper and middle panel. The lower panel show trade-offs between radial anisotropy in the lower crust and at the Moho

The robustness and resolution of the inversion also depends on the number of forward calculations to fully explore the parameter space. El-Sharkawy (2019) performed the depth inversion for Rayleigh waves with 8000 forward calculations. Since we do not invert only for velocity and depth, but for radial anisotropy as well, more forward calculations are needed. Figure 4.8 shows tests with increasing numbers of forward calculations. In all cases, the dispersion curves are well fitted and the best fitting model is nearly the same for 10000 and 20000 forward calculations. However, the inversion for 40000 forward calculations resulted in a considerably different best fitting model and a smaller misfit. The trade-off plots also indicate that a higher amount of forward calculations is necessary, because the parameter space is not well explored in case of 10000 forward calculations. Therefore, the final 1D inversions for Rayleigh and Love wave dispersion curves including radial anisotropy utilize 40000 forward calculations.

Since the inversion is performed for Rayleigh and Love waves simultaneously, they can be weighted to control their influence on the final result. Due to lower data quality in the horizontal components which is caused by a lower signal to noise ratio or high frequency noise, the results for Love wave dispersion measurements are mostly rougher than the ones for Rayleigh wave dispersion measurement. This leads to an asumption, that Rayleigh wave dispersion curves should have a higher influence on the inversion result than Love wave dispersion curves. This is realized in the misfit which is the weighted average of the relative difference between the synthetic and observed Rayleigh and Love wave dispersion curves. Figure 4.9 shows inversion results for the following cases: twice the weight for Rayleigh waves (a); equal weights (b); quadruple the weight for Rayleigh waves (c). The results are strongly varying regarding the best fitting model. At the same time, the amount of acceptable models seem to increase with stronger weighting, whereas the misfit shows only minor variations. The trade- off plot for the equal weighting whows the best resolution. Major problems can be seen in the fits of the dispersion curves. Figure 4.9c features the strongest weighting, which results in a poorly fitted Love wave dispersion curve, whereas the best fitting model still contain an acceptable misfit. The weighting of Rayleigh and Love wave dispersion curves for a simultaneous inversion need to be used with caution. It shows some potential to increase the quality of the results, but further testing and a different parametrizaiton seems to be required. Therefore, we now consider Rayleigh and Love wave dispersion curves as equal for the final 1D inversions.

Another important aspect is the uncertainty of the inversion which has strong influence on the quality of the results. We are able to estimate uncertainties of every parameter which was inverted. This include shear wave velocity, depth and radial anisotropy at each node. The inversion is performed with dispersion curves up to a maximum period of 20 s which leads to the assumption that the resolution decreases towards the Moho. At the same time, we expect small uncertainties and high resolution in the subsurface. Figure 4.10 shows

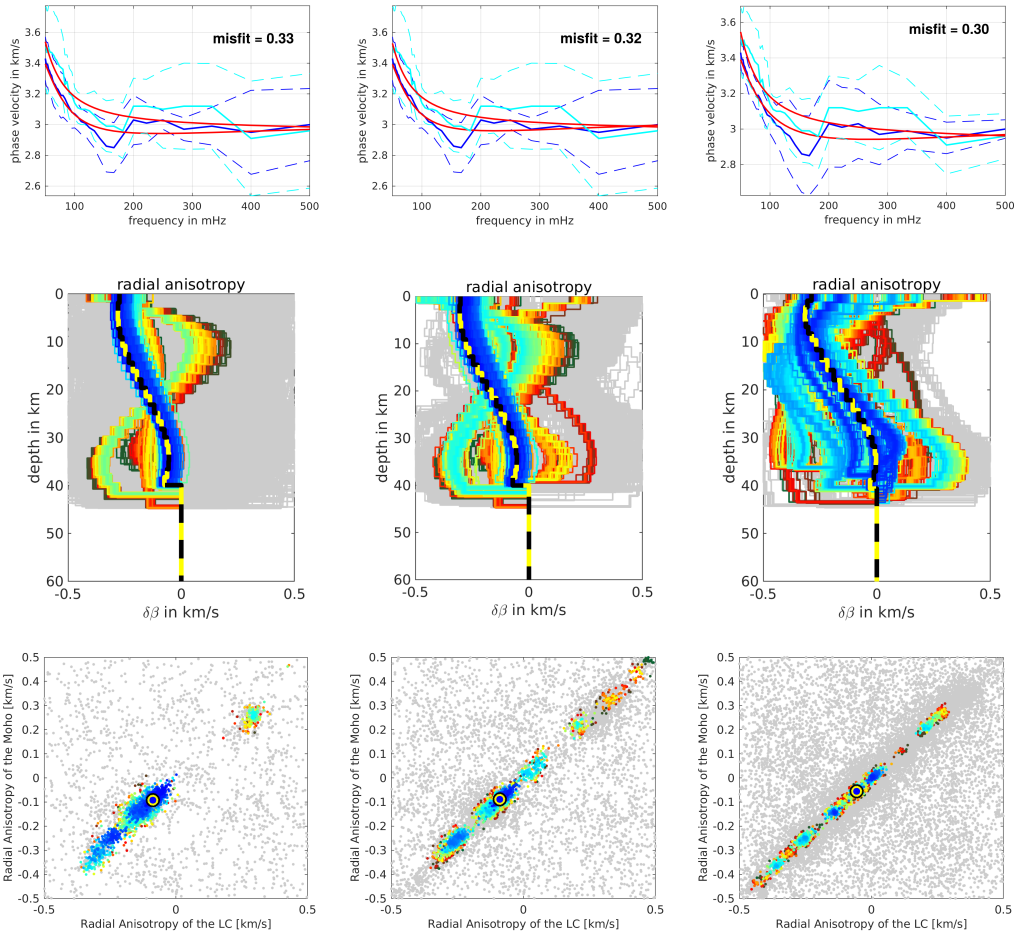

(a) Number of FC: 10000 **(b)** Number of FC: 20000 **(c)** Number of FC: 40000

Figure 4.8: Effects of different numbers of Forward calculations (FC) on the inversion results. The fit of the dispersion curve and their corresponding 1D models are shown in the upper and middle panel. The lower panel show trade-offs between radial anisotropy in the lower crust and at the Moho

uncertainties for two exemplary grid points, one in the western and eastern part of the study area which are distinct different regarding their crustal structure. From top to bottom, figure 4.10 features the uncertainties of shear wave velocity and radial anisotropy in the middle crust and the Moho depth. They contain the rms misfit values of all resulted models as a function of one parameter. The rms misfit value is shown as envelope. The maximum allowed misfit value (red line) is empirically defined and needs to be considered when evaluating the uncertainties. The yellow dot shows the perturbation of the model parameter with the minimum misfit (most likely), while the red triangle features the expected perturbation (centroid) based on the average over all models which are below the maximum allowed misfit. The shear wave velocities of the middle crust in the western and eastern part are overall well defined with uncertainties of $-0.09-0.20\,km/s$ and $-0.27-0.09\,km/s$, respectively. The same applies for the uncertainties of the radial anisotropy in the middle crust. They are with $-0.12-0.08\,km/s$ for the western part and $-0.07-0.12\,km/s$ for the eastern part well de-

fined. The uncertainties in the Moho depth in the western and eastern part are $-0.5-0.16\,km$ and $-0.4-0.3\,km$. Overall, the inversion of Rayleigh and Love wave dispersion curves by introducing radial anisotropy and in combination with an appropriate parametrization lead to small uncertainties and even allows for Moho depth estimations. For constructing the final 3D model, we use the centroid models instead of the best fitting models to counteract possible high uncertainties, e.g. Moho depth or radial anisotropy in larger depths. In this case, the centroid model leads to a more robust result, because it represents the average perturbation of a variety of models below the maximum allowed misfit. If the models contain small uncertainties, the differences between the most likely and centroid perturbations are minor which is the case for the examples in figure 4.10.

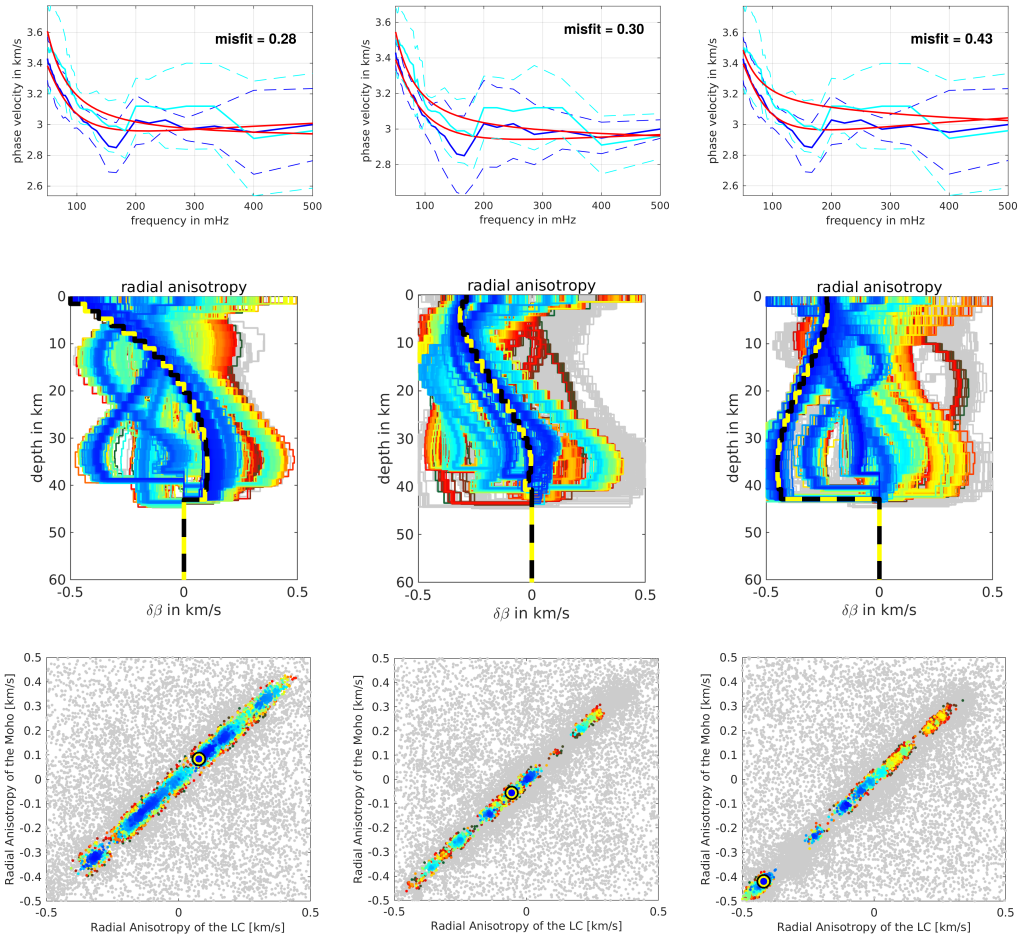

(a) Rayleigh:Love = 1:0.5 **(b)** Rayleigh:Love = 1:1 **(c)** Rayleigh:Love = 2:0.5

Figure 4.9: Effect of different weights for Rayleigh and Love on the inversion results. The fit of the dispersion curve and their corresponding 1D models are shown in the upper and middle panel. The lower panel show trade-offs between radial anisotropy in the lower crust and at the Moho

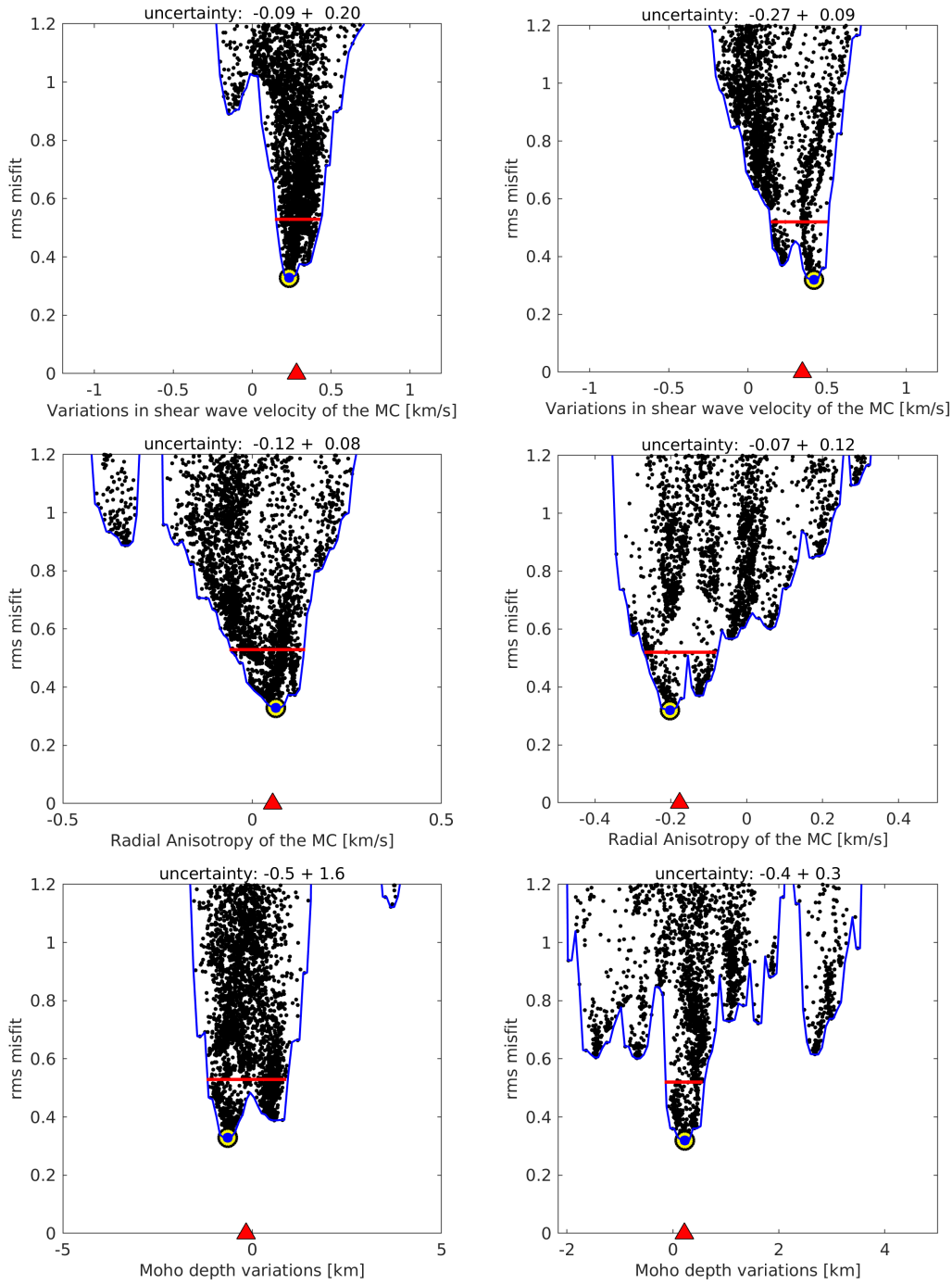

(a) West **(b)** East

Figure 4.10: Uncertainties of shear wave velocity of the MC, radial anisotropy of the MC and Moho depth for two different locations across the area (West, East)

4.2 Results

We applied the method of 1D inversion using Particle Swarm Optimization and the obtained information regarding the parametrization and regularization to our local dispersion curves from ambient seismic noise surface wave tomography. The 1D inversion is performed for each single grid point by using the final parametrization from table 4.2. Tests on the effects of regularization have shown that a slight damping to differences of shear wave velocity perturbations at the node above the Moho is required, to obtain reliable results. For that reason, $pwvdiff$ is set to 0.2 at this certain node. In addition, each 1D inversion is performed with 40000 forward calculations. Rayleigh and Love wave dispersion curves are contributing equally to the resulting model. The results for shear wave velocities are presented as isotropic shear wave velocities. They have been calculated from V_{SV} and V_{SH} by using a Voigt average. This can be written as [Babuska and Cara, 1991]:

$$V_s = \frac{2}{3}V_{SV} + \frac{1}{3}V_{SH}. \tag{4.2}$$

with V_s as the isotropic shear wave velocity. This resulted in 1D shear wave velocity models as a function of depth down to 55 km. They show the overall structure of the crust. It must be pointed out, that there is no resolution below the Moho. Here, we defined a half space with a constant velocity and only allow for minor shear wave velocity perturbations ($\pm 0.2 km/s$).

Figure 4.11 and 4.13 show 1D shear wave velocity models from different areas across the study area. Their locations can be seen in figure 4.14. The 1D models in figure 4.11 are very close to the 2D profile of Al-Lazki et al. (2002). The 1D model of Nizwa, south of Jebel Akhdar is located in the Hawasina Formation and features with $2.5\,km/s$ the lowest shear wave velocity in the subsurface, whereas the velocity in the subsurface of Wadi Abiyyad, which contains ophiolite strata is considerably higher ($3.3\,km/s$). The shear wave velocity below Jebel Akhdar shows an intermediate value of $2.97\,km/s$ which is reasonable due to the fact that once buried, pre- Permian sediments are located on top of the surface. The velocities of the Jebel Akhdar- and Nizwa model are steadily increasing with depth. The Wadi Abiyyad model shows a low velocity zone between $\approx 5-8 km$ before the velocities are again increasing in the middle crust. Furthermore, we observe a local crustal thickening below Jebel Akhdar towards $\approx 43\,km$.

Figure 4.12 compares the result of the three 1D models to the results of Al-Lazki et al. (2002). The geological interpretation, shear wave velocities from the upper crust and the crustal thickness are obtained from their results and shown as black lines. In addition, the velocity of the ophiolite is based on the work of Christensen and Smewing (1981) which Al-Lazki et al. used in their reference model to estimate a crustal thickness from receiver functions. The depths of the layers in figure 4.12 were slightly adapted in personal communication with Andreas Scharf (Sultan Qaboos University Muskat, Oman) to fit geological

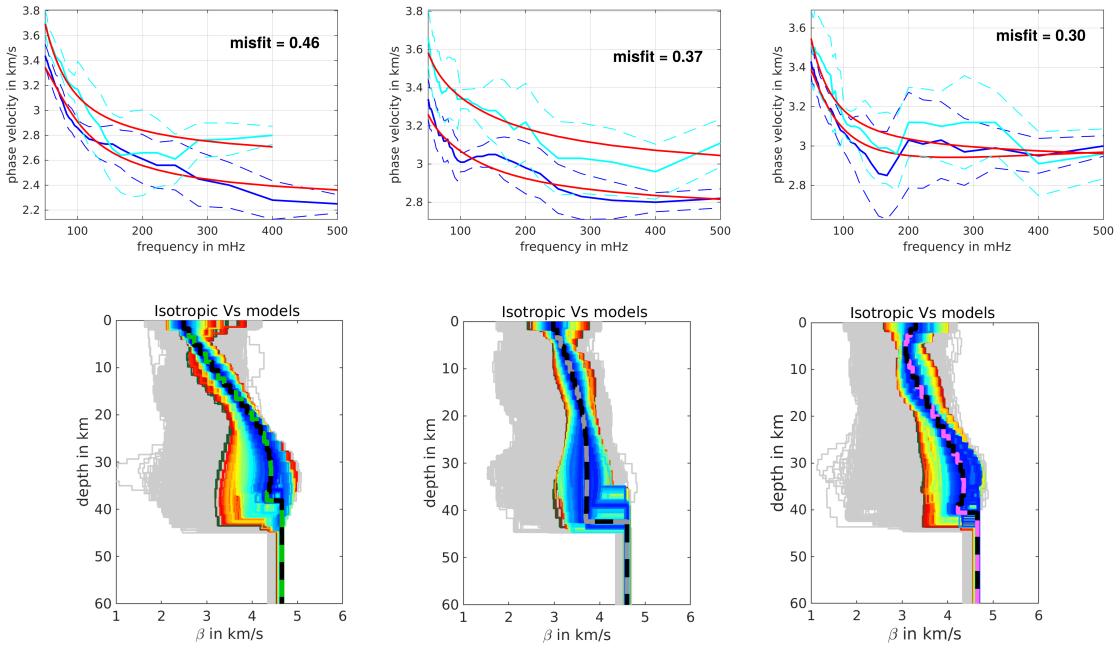

(a) Nizwa **(b)** Jebel Akhdar **(c)** Wadi Abiyyad

Figure 4.11: 1D shear wave velocity models from the final 3D model and their corresponding dispersion curves: a) Nizwa, b) Jebel Akhdar, c) Wadi Abiyyad

field mapping. The information for the middle and lower crust is based on average values from local Crust1.0 models [Laske et al., 2013]. The Moho depth from the Al-Lazki model is based on gravity data modelling in combination with local 1D information from receiver functions. The results are strongly comparable in the upper crust. The isotropic shear wave velocities from our 1D models are highly consistent with the ones from previous works which are interpreted as the ophiolite, pre Permian sediments and Hawasina/Aruma sediments. Even indications for a low velocity zone below the ophiolite in Wadi Abiyyad are observable. Slight discrepancies are observable for the crustal thickness. While both models feature a crustal thickening beneath Jebel Akhdar, the Moho is overall $3-4km$ deeper in the Al-Lazki model.

Figure 4.13 shows three additional 1D shear wave velocity models. The model of Al-Amirat in Saih Hatat is comparable to the one of Jebel Akhdar. The velocity in the subsurface is almost the same ($2.96\,km/s$) and the velocity increase in the upper and middle crust seems to be slightly stronger in the Al-Amirat model. Its crustal thickness is with $38\,km$ thinner than beneath Jebel Akhdar. The 1D model in figure 4.13b is located in Wadi Andam, south of Saih Hatat and east of the Semail Gap and contains ophiolite strata like the one in Wadi Abiyyad. While the velocity in the subsurface is similar ($3.25\,km/s$), the model shows distinct differences in $5-10km$ depth. A low velocity zone beneath the high velocities in the

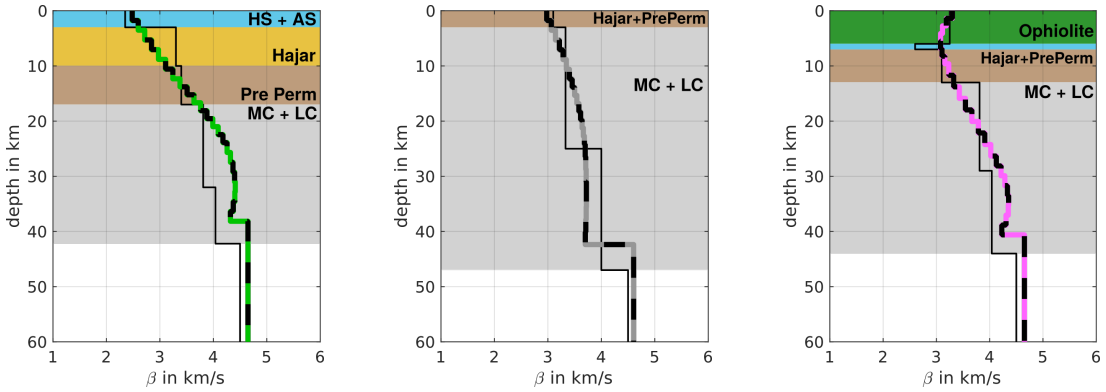

(a) Nizwa **(b)** Jebel Akhdar **(c)** Wadi Abiyyad

Figure 4.12: 1D shear velocity best fitting model (dashed line) in comparison to a corresponding 1D reference model (black line) based on information from previous models; HS + AS: Hawasina Sediments + Aruma Sediments;Hajar: Sediments of the Hajar Supergroup; Pre Perm: Pre Permian sediments (Huqf + Haima); MC + LC: Middle and lower Crust

subsurface is not observable. Instead, the velocity is steadily increasing with depth, while the Moho is at roughly 40 km. The last model (Fig.4.13c) is located in the eastern part of our area, near Jebel Ja'alan in the Wahiba Sands. It shows low velocities in the subsurface, which coincides with the existing quarternary sediments in that region. In contrast to the other presented 1D models, it features a shallow Moho depth of roughly 19 km.

4.2.1 3D anisotropic shear wave velocity model

The 3D model of shear wave velocity and radial anisotropy down to 55 km is constructed by combining all 1D inversions at each grid node. Figures 4.14 - 4.19 illustrate the resulted model as representative horizontal map views and vertical cross sections. Isotropic shear wave velocity perturbations, calculated by using SV- and SH- velocities and Eq. 4.2, are shown relatively to the average value in that certain depth. The color scheme is the same as the one used for the surface wave phase velocity maps. Blue colors represent higher velocities than the average, while red colors indicate lower velocities. The radial anisotropy is shown as the absolute difference between V_{SH} and V_{SV}. Here, blue represents areas in which V_{SV} is larger than V_{SH}, while red indicates that V_{SH} is larger than V_{SV}. The same applies to the vertical cross sections for radial anisotropy. The isotropic velocity perturbations in the vertical cross sections are calculated by using a linearly increasing reference model with depth, down to 30 km. From 30 km downwards, the reference velocity remains constant to enhance lateral variations in lower crustal velocities and Moho depth.

Figure 4.14 shows selected horizontal maps of isotropic shear wave velocity at depths of 2, 7, 10, 15, 25 and 30 km. Appendix C contains more horizontal map views of isotropic shear wave velocity at depths between 2 and 40 km. They show different tectonic features from the subsurface down to the Moho. They are quite similar to the maps of surface wave tomo-

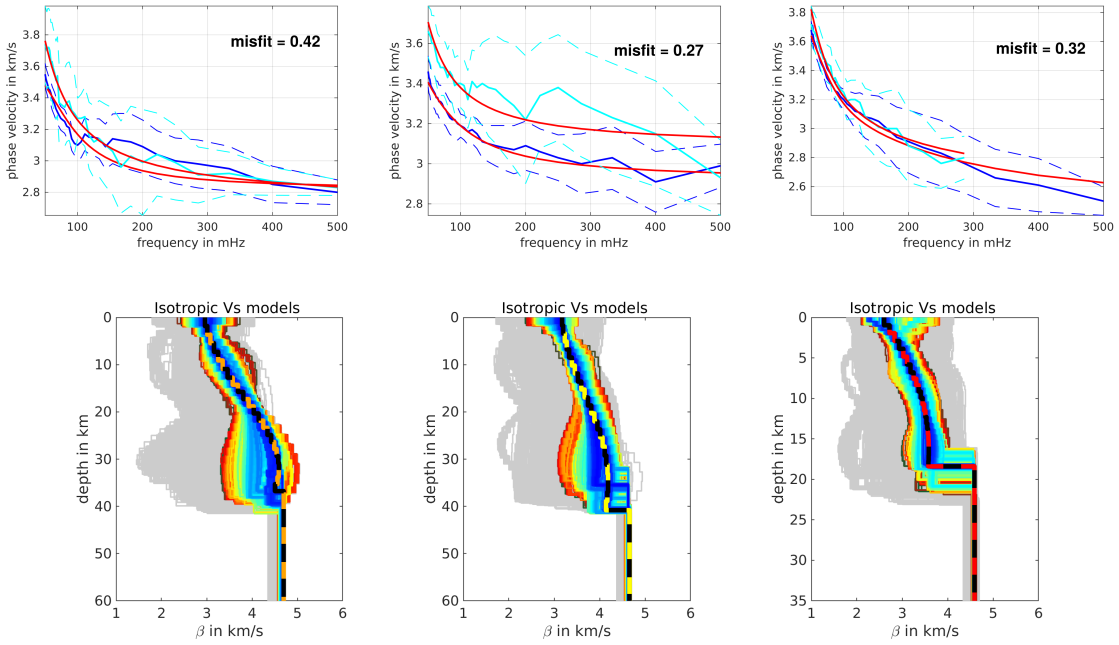

(a) Al-Amirat **(b)** Wadi Andam **(c)** Jebel Ja'alan

Figure 4.13: 1D shear wave velocity models from the final 3D model and their corresponding dispersion curves: a) Al-Amirat (Saih Hatat), b) Wadi Andam, c) Jebel Ja'alan

graphy (Fig. 2.19 and 2.20). The main features at 2 km are the high velocities across the Al-Hajar Mountains, originating from the obducted oceanic crustal and mantle material. This is contrasted by distinct lower velocities further south and southwest on the Arabian platform. Differences between the opholite covered areas and the tectonic windows in Jebel Akhdar and Saih Hatat can not be observed at 2 km. Towards intermediate depths of 7 and 10 km, the high velocity anomalies across the Al- Hajar Mountains are steadily decreasing but are still observable. At 15 km, they are almost vanished. Since the high velocity anomalies across the Al- Hajar Mountains are observable to these depths, they might not be explained by the presence of oceanic crustal and mantle rocks solely. Additional tectonic processes seem to contribute to the existence of relatively high velocities in the upper and middle crust. At 7 and 10 km, the Jebel Akhdar and Saih Hatat windows are better observable due to lower velocities. At 10 km and deeper, the highest velocities are located below the Wahiba Sands in the eastern part of the study area. Towards larger depths (25 and 30 km), very high velocities are observable in the eastern part which seem to move towards western direction with increasing depth. They are reflecting mantle velocities and a Moho depth in the eastern part of 25 km or less. Overall, the maps of 25 and 30 km can be divided into three sections with different velocities. While the velocities in the eastern part are the highest ($\approx 4.6 km/s$), we observe intermediate velocities in the central part ($\approx 4.1 km/s$) and low velocities in the western part ($\approx 3.8 km/s$). The central part is locally disturbed by lower velocities beneath Jebel Akhdar indicating a localized crustal thickening in this area.

Figure 4.15 shows horizontal maps of radial anisotropy at the same depths than the ones for isotropic shear wave velocity. Appendix C contains more horizontal map views of radial anisotropy at depths between 2 and 40 km. At 2 km, radial anisotropy is smaller than $\pm 0.1 km/s$ in most parts of the study area, except the northern flank of the Al-Hajar Mountains where slightly stronger negative radial anisotropy is observable. Towards larger depths, radial anisotropy increases. Strong negative anomalies can be observed all over the northern flanks of the Al- Hajar Mountains and partly across Jebel Akhdar down to 15 km. Negative anomalies can be observed further east in the Wahiba Sands on the same maps. Towards greater depths of $\approx 20 km$, the negative anomalies vanish. In contrast, positive anomalies are observable on the Arabian platform which conincide with a tectonically undisturbed crustual structure and horizontal layering. The positive anomalies even increase down to 15 km. They are dimishing at 25 km depth, but are still observable. The transition between the positive radial anisotropy of the Arabian platform and the mostly negative one further northeast collocates with the Hawasina Frontal Thrust which marks the maximum lateral extent of the obduction onto the continent. (Fig.4.15, 15 km). This transition is clearly observable down to $\approx 26 km$. Note the effect of the incoming Moho at 25 and 30 km. The inversion do not allow for radial anisotropy beneath the Moho. Therefore, it is zero which can be seen in the eastern part at 25 and 30 km.

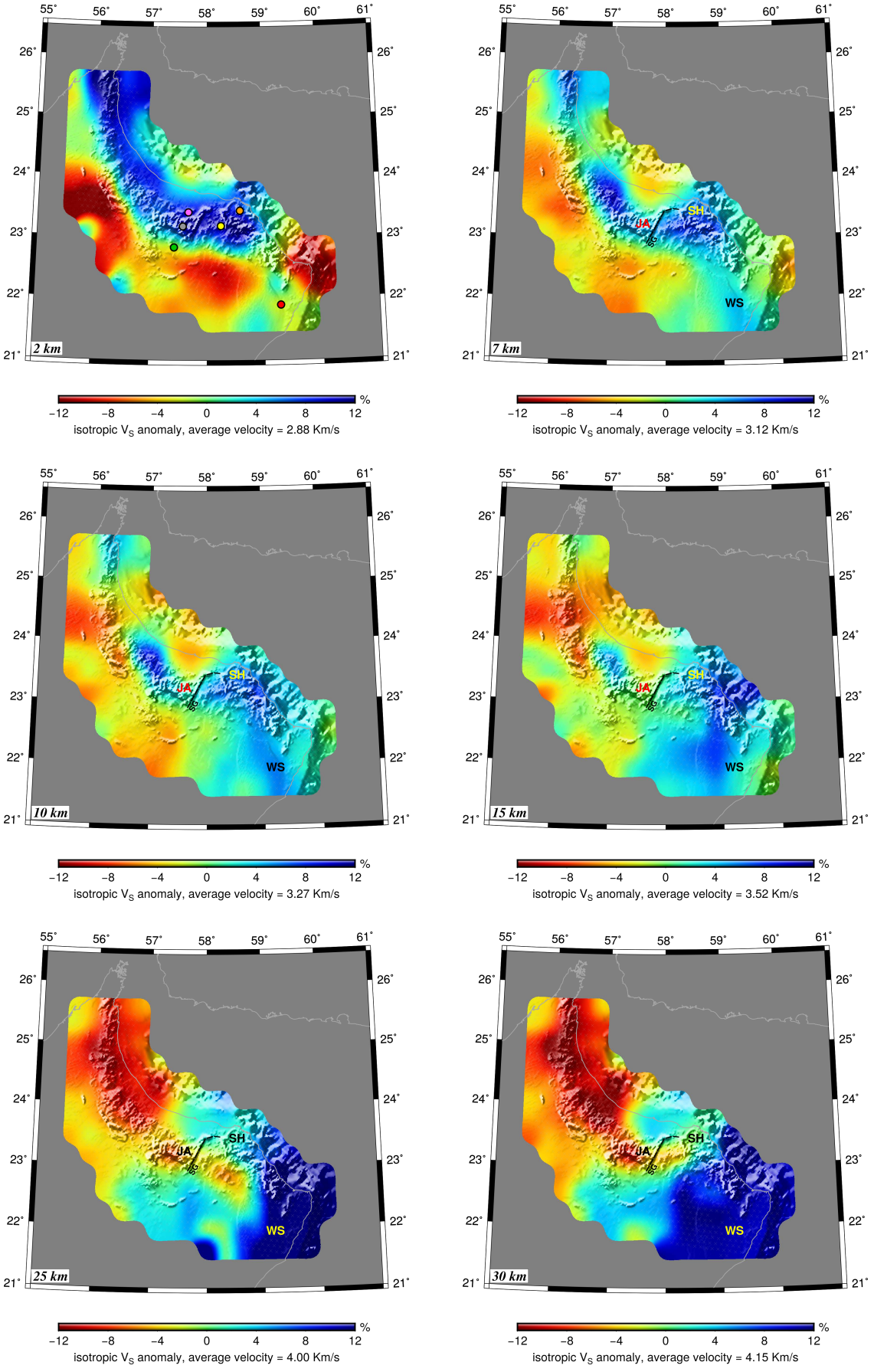

Figure 4.14: Horizontal maps of the 3D shear wave velocity model at depths of 2, 7, 10, 15, 25 and 30 km. The isotropic shear wave velocity is shown as perturbations with respect to the average value of each respective depth.

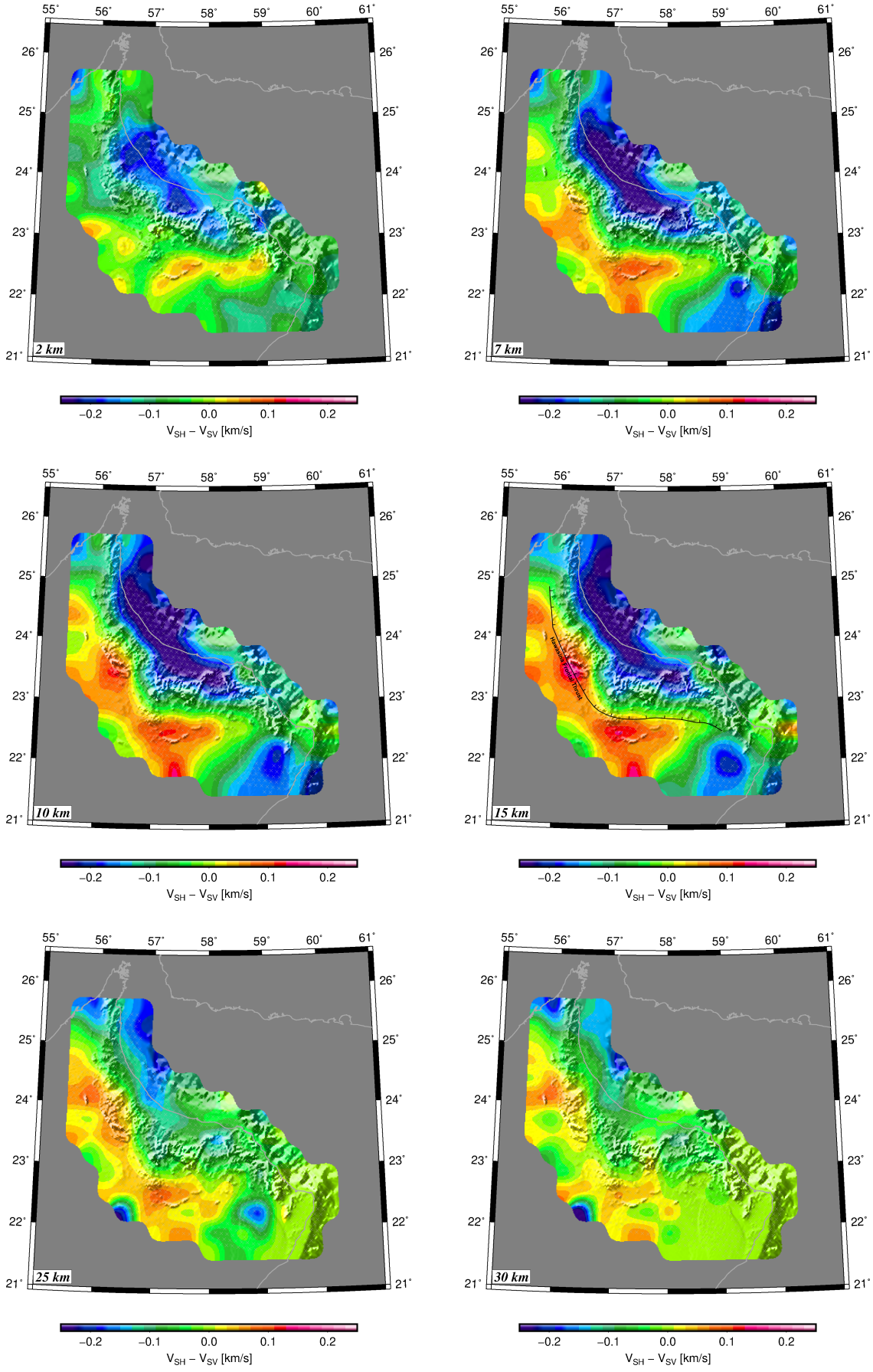

Figure 4.15: Horizontal maps of the radial anisotropy at depths of 2, 7, 10, 15, 25 and 30 km. The radial anisotropy is shown as absolute difference between V_{SH} and V_{SV}.

In addition to horizontal maps, we show vertical cross sections through the 3D model. A first set of four cross sections is shown in figure 4.16 for isotropic shear wave velocity perturbations and figure 4.17 for radial anisotropy. The location of each profile can be seen in the horizontal map in the top panel of figure 4.16. The white dashed line represents the Moho in each profile of isotropic shear wave velocity.

Profile AA' extends across the entire study area from northwest to southeast, crossing the Al- Hajar Mountains, including the Jebel Akhdar and continues further southeast towards the Wahiba Sands. High velocity anomalies are observable at 90 - 120 km and 190 - 240 km along the profile in the first kilometers of the subsurface. They are related to the ophiolite. In addition, they show a negative anomaly for radial anisotropy. Between these velocity anomalies, at the intercept point with profile DD', lower velocities are observable, which are underlain by a high velocity anomaly down to $\approx 20km$. The lower crust between 90 - 120 km is characterized by lower velocities and positive radial anisotropy. Overall, below the western part of the Al- Hajar Mountains, we observe a relatively stable and thick crust with Moho depths of $\approx 43km$ on average. The first kilometers of the subsurface beneath Jebel Akhdar show slightly lower velocities than further northwest beneath the ophiolite. The Moho is located at $\approx 43km$ as well. Further southeast, east of the Semail Gap, the overall structure is changing considerably. The main feature is the distinct decrease in crustal thickness. The Moho shallows to roughly 20 km. The first kilometers of the subsurface show overall lower velocities, compared to the Al- Hajar Mountains. Beneath the Wahiba Sands in the easternmost part of the profile, we observe again higher velocities and negative radial anisotropy in the entire crust.

The profiles BB', CC' and DD' are perpendicularly intercepting profile AA'. Profile BB' crosses the mountain range of Wadi Andam, which is covered by obducted oceanic crustal and mantle material. The profile can be divided in roughly two parts. The southern part, which is on the Arabian platform is characterized by low velocities in the first kilometers of the subsurface. The velocities are steadily increasing with depth. In addition, this part of the profile shows positive radial anisotropy down to 25 - 30 km. In the northern part of the profile, a high velocity anomaly is observable in the first kilometers of the subsurface. The thickness seems to be larger, compared to the mentioned ophiolite regions in Profil AA'. At the same time, negative radial anisotropy can be seen in this area, which is smaller in amplitude than in Profile AA' at 90 - 120 km and 190 - 240 km. Beneath Saih Hatat, we observe lower velocities in the subsurface. Towards the middle crust they are increasing. Between 10 and 20 km, the velocities beneath Saih Hatat are larger than the ones beneath the Ophiolite further south and beneath Jebel Akhdar. The entire crust beneath Saih Hatat features only minor negative radial anisotropy in the upper crust. The crustal thickness is with $\approx 35 - 38km$ relatively stable beneath Saih Hatat and Wadi Andam. It decreases to $\approx 28km$ towards the Arabian platform.

Profile CC' follows the 2D profile of Al-Lazki et al. (2002). It crosses the Hawasina formation, Jebel Akhdar, and the ophiolite covered mountains north of Jebel Akhdar. Again, we observe a high velocity anomaly at 120 - 180 km along the profile in the first $3-4km$ of the subsurface, which can be related to the ophiolite. The Hawasina formation south of Jebel Akhdar is characterized by lower velocities in the upper crust, compared to the ones beneath Jebel Akhdar and the mountain range further north. Over the entire profile, the velocities are steadily increasing down to $\approx 25km$. In the lower crust, we observe distinct differences in the velocity distribution. A low velocity anomaly is located beneath Jebel Akhdar, in combination with a slightly thicker crust. This is comparable to Al- Lazki et al. (2002). They also show a locally thicker crust beneath Jebel Akhdar. The radial anisotropy divides the profile into two parts. We observe a positive anomaly in the Hawasina formation and on the Arabian platform down to $\approx 25-30km$, whereas the anomaly is negative in the mountain range north of Jebel Akhdar.

Profil DD' is further northwest and crosses the high velocity anomaly, which was already meantioned in Profile AA'. It is located in a depth range of 4 to 20 km beneath the Al-Hajar Mountains and extends in north or northeast direction. Further south, the velocity perturbations are mostly similar to profil BB' and CC'. Low velocities are observable in the subsurface. They are steadily increasing with depth. The crustal thickness is with $\approx 42km$ relatively stable over the entire profile. Again, we observe positive radial anisotropy within the crust of the Arabian platform and negative radial anisotropy beneath the northern flanks of the Oman Mountains.

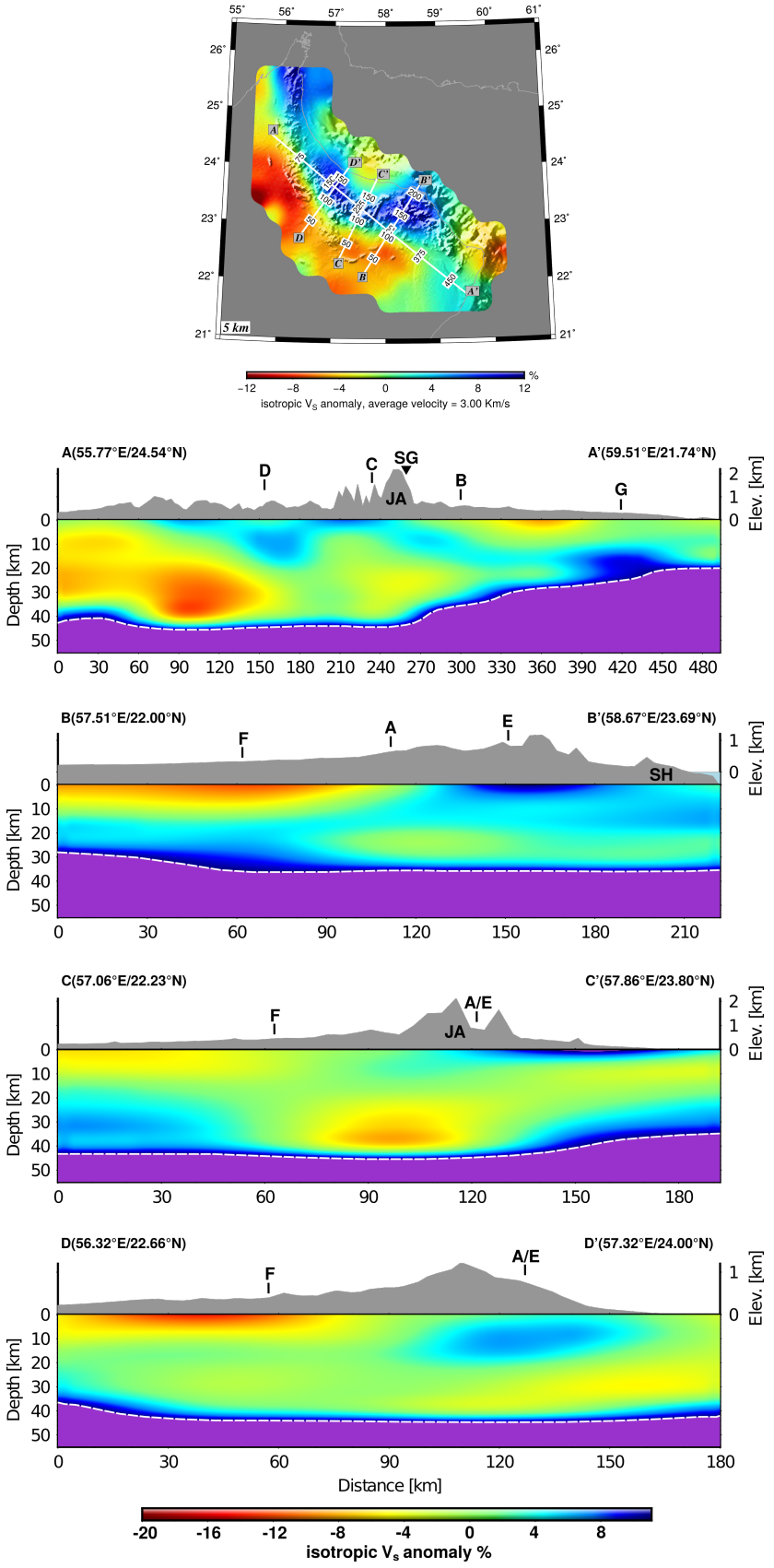

Figure 4.16: Vertical cross sections through the 3D model in northeastern Oman. Perturbations in isotropic shear wave velocity are shown down to 55 km. The topography of each profile is plotted on top of each section. The location of each profile is shown on the horizontal man on top; JA: Jebel Akhdar, SH: Saih Hatat, SG: Semail Gap

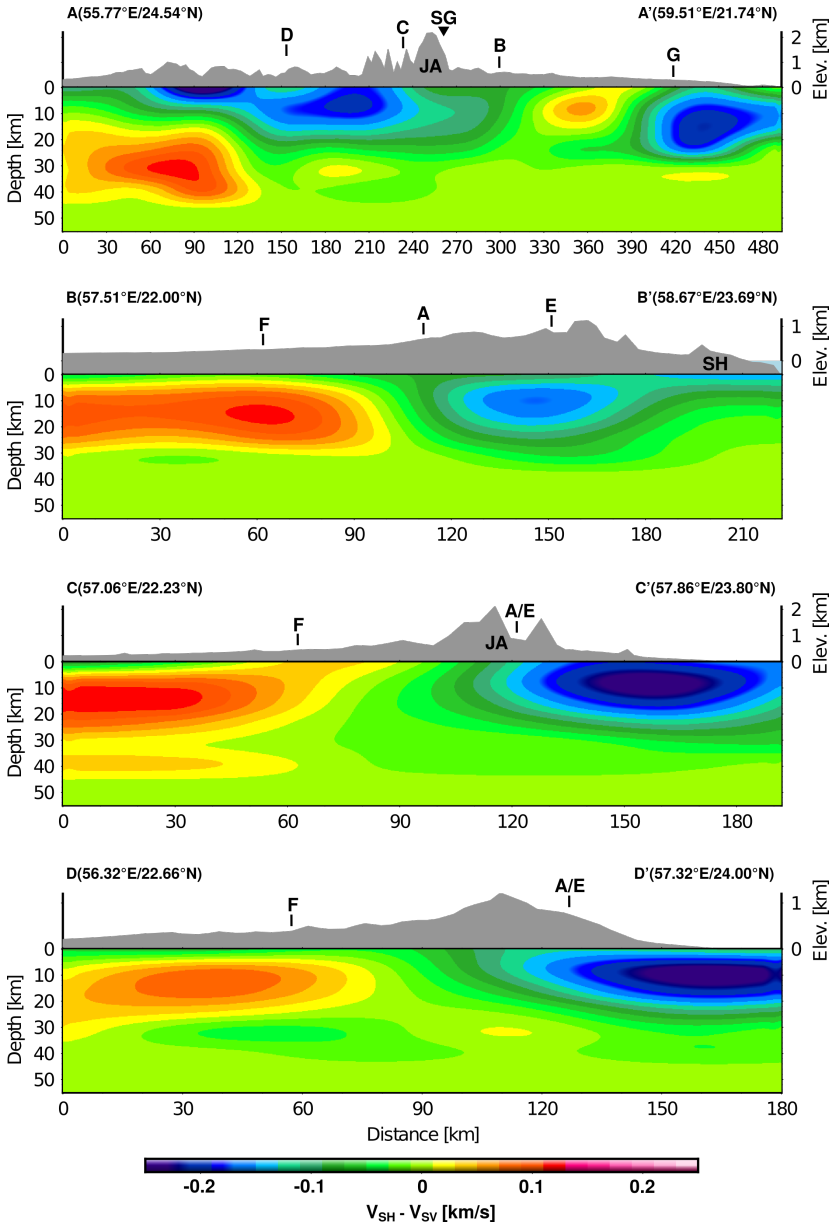

Figure 4.17: Vertical cross sections through the 3D model in northeastern Oman. Radial anisotropy is shown down to 55 km. The topography of each profile is plotted on top of each section; JA: Jebel Akhdar, SH: Saih Hatat, SG: Semail Gap

A second set of vertical cross sections is shown in Figure 4.18 an 4.19. Their locations can be seen on the horizontal map in the top panel of figure 4.18.

Profil EE' extends across the Al- Hajar Mountains and Jebel Akhdar. East of the Semail Gap, it turns to northeast direction and extends across the Wadi Andam area. It summarizes the information regarding the ophiolite emplacement. It seems that the obducted oceanic crustal and mantle material in the eastern part ($\approx 220-290km$) of the profile show a higher thickness than the ones in the western part of the Al- Hajar Mountains ($\approx 20-60km$ and $\approx 120-180km$) with $6-8km$ and $3-4km$, respectively. In addition, these areas feature negative radial anisotropy. In between, lower velocities beneath Jebel Akhdar are partly

observed at the same depths, with minor radial anisotropy. At the Semail Gap, a step of the Moho of $\approx 10km$ is observable. While it is at around 43 km west of the Semail Gap, it is with 35 km east of the Semail Gap considerably shallower.

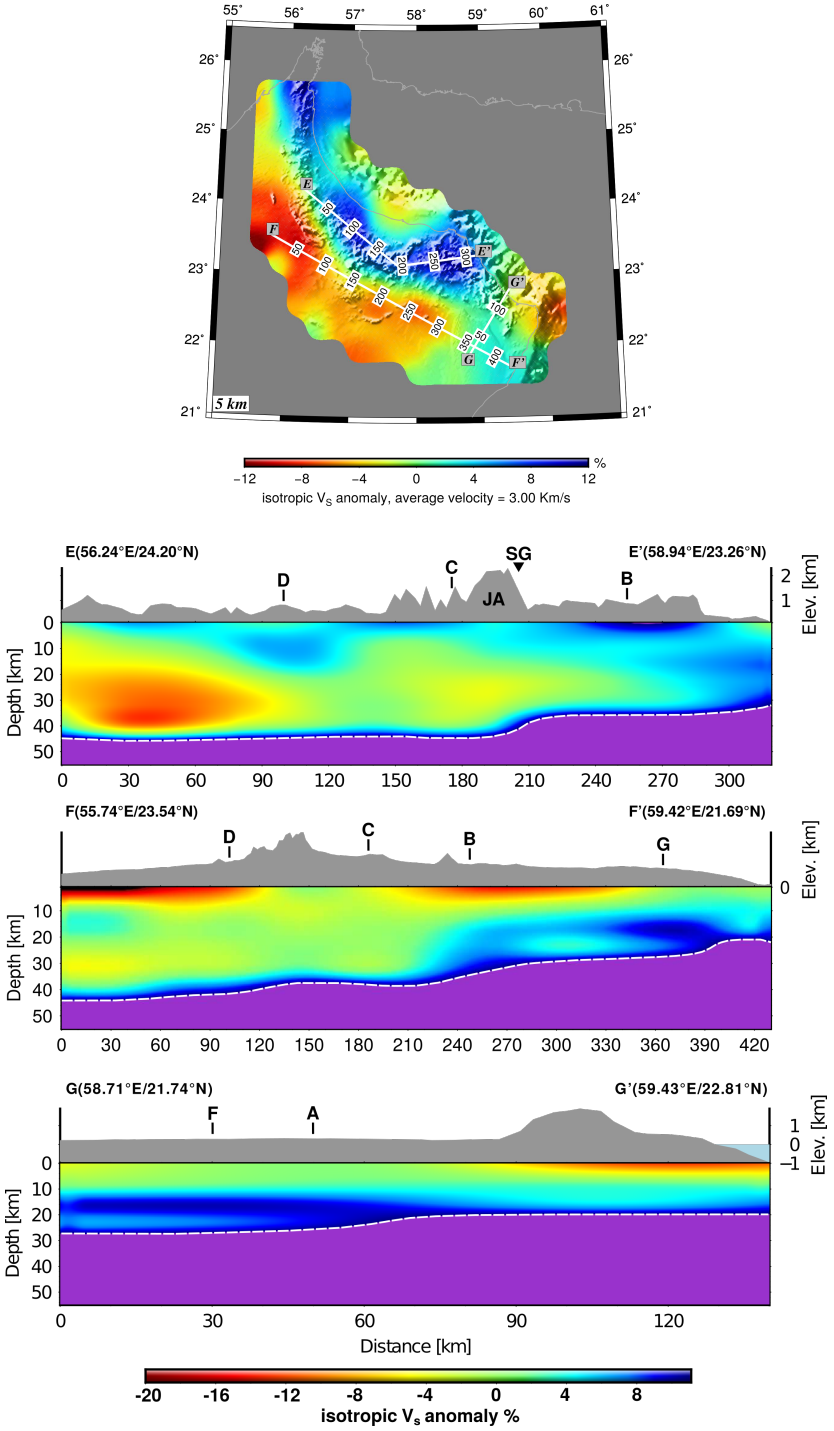

Figure 4.18: Vertical cross sections through the 3D model in northeastern Oman. Perturbations in isotropic shear wave velocity are shown down to 55 km. The topography of each profile is plotted on top of each section. The location of each profile is shown on the horizontal man on top; JA: Jebel Akhdar, SG: Semail Gap

Profile FF' is located in the southern part of the study area, crossing the mostly undeformed Arabian plate, but is intercepted by the Hawasina formation (120 - 200 km) and the Wahiba sands (350 - 420 km). The Hawasina Formation shows slightly higher velocities in the uppermost 5 km of the subsurface compared to the surrounding areas of the profile, which are represented by undisturbed, young sedimentary formations. The radial anisotropy of the Hawasina Formation and its underlying crust is strongly differing as well. The upper 3 - 4 km are characterized by positive radial anisotropy, whereas only minor radial anisotropy is observable in the middle and lower crust. Positive anomalies are present further northwest and southeast at $10-20km$ depth. In addition, there is no radial anisotropy in the upper $\approx 5km$ of the Arabian platform. The Wahiba sands show higher velocities in the upper crust. Furthermore, strong negative radial anisotropy is observable in the entire crust beneath the Wahiba Sands. Again a shallowing Moho from northwest to southeast can be observed, ranging from 20 to 42 km. In addition, this profile features the clearest "stepwise" behaviour of the Moho which seems to delimit blocks of different geological properties.

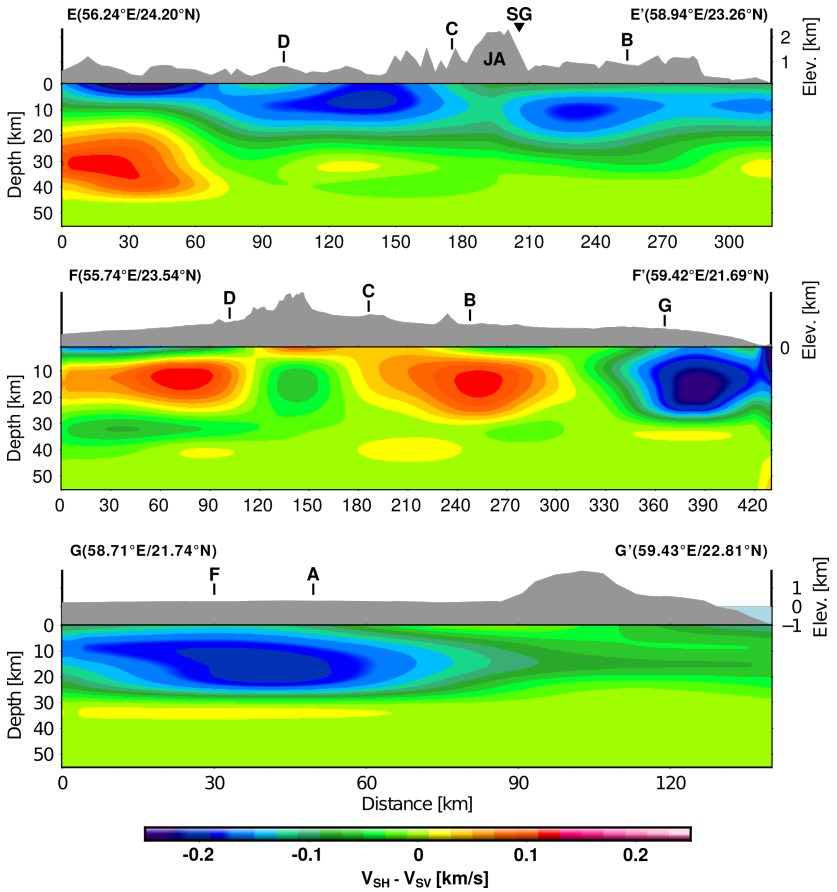

Figure 4.19: Vertical cross sections through the 3D model in northeastern Oman. Radial anisotropy is shown down to 55 km. The topography of each profile is plotted on top of each section; JA: Jebel Akhdar, SG: Semail Gap

The last cross section (GG') is located in the Wahiba Sands and extends northwards to the Eocene covered Salmah Plateau and Qalhat. The velocities in the entire crust are strongly differing and are higher in the Wahiba Sands. In general, the entire area features a shallow Moho compared to the rest of the study area. It is shallowing in northern direction and ranges overall from 20 to 28 km. Only minor radial anisotropy is observable beneath the Eocene Mountain range of the Salmah Plateau, whereas the crust below the Wahiba Sands is characterized by strongly negative radial anisotropy.

4.2.2 Moho map and receiver functions

Since the 1D depth inversion is parametrized to invert for the Moho as well, the results contain an expected Moho depth and a corresponding uncertainty. They can be used to construct a Moho map for the entire region (Fig.4.20). The Moho map on the left side show the behavior that was already observed in previous figures. The Moho is shallowing from northwest to southeast with a local crustal thickening beneath Jebel Akhdar ($\approx 43km$). In the easternmost part, the Moho is shallowing to $\approx 20km$. Here, we observe the smallest uncertainties of partly $< \pm 1km$, whereas they range from $\pm 2 - 3.5km$ in the central and western part of the study area. This seems reasonable, because the resolution of the 1D inversion decreases with depth. A shallower Moho might be better resolved than a deeper one.

In addition, we are able to compare the Moho map from the PSO inversion with the results from our receiver functions. Figure 4.20(left) shows the estimated Moho depth from P-receiver functions (triangles), calculated with Eq.(3.2). Despite some local variations, the results are consistent in the western and central part of the study area. However, east of the Semail Gap, the results are starting to differ. P- receiver functions also show an overall shallowing of the Moho to $\approx 32km$ towards eastern direction, but not in the same extent than the Moho map from the PSO inversion. The maximum difference between both methods is $\approx 12km$.

Figure 4.21 shows a comparison of the results between both methods in the Wahiba Sands. The 1D inversion (left) is performed for one local dispersion curve south of Jebel Ja'alan and features a well defined Moho at $\approx 19km$ with small uncertainties of $\pm 0.4km$, whereas the P-receiver functions (right) show a clear Ps- conversion from the Moho at $\approx 4.3s$. This corresponds to a Moho depth of $\approx 34km$. However, the P- receiver functions feature a different peak at $\approx 2.1s$. It is not as consistent as the later peak. The conversion would correspond to a depth of 16.6 km which would rather fit the Moho depth from the 1D inversion. Unfortunately, this is the only station at which we can observe this "earlier" conversion in such clarity. This needs to be further discussed.

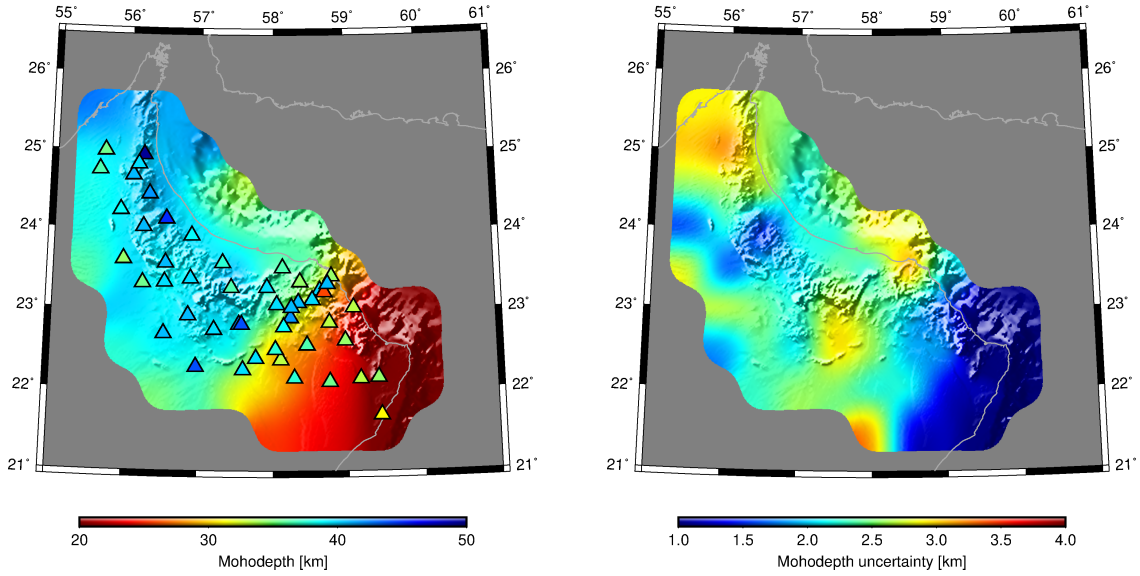

Figure 4.20: Results for the Moho depth. Left: expected Moho depth from 1D inversions and results from P- receiver functions (triangles). Right: uncertainties of the expected Moho depth from the 1D inversion

As mentioned before in section 3.2.4, the approach which we used to estimate the Moho depth has to deal with a strong trade-off between the depth and v_p/v_s ratio. A change of 0.1 in the v_p/v_s ratio can lead to a difference of 4 km in the crustal thickness [Zhu and Kanamori, 2000]. By combining the information from the 1D inversions and P- receiver functions, the calculation of a common Moho depth and a corresponding v_p/v_s ratio, which fits both data sets might be possible. We use the Ps- conversion from P- receiver functions and shear wave velocities from the 1D inversion. A weighted and averaged v_s over the entire crust and the six closest grid points around each station is calculated. This allows to estimate v_p for which the Ps- conversion time fits the Moho from the 1D inversion, together with a corresponding v_p/v_s ratio (Fig.4.22). The left part shows again the Moho map from the 1D inversion in comparison to the fitted Moho depths. They are very similar which confirms that a fit for each station was detected. The corresponding v_p/v_s ratio for each station is shown on the right side of figure 4.22. West of the Semail Gap, the v_p/v_s ratios range between 1.7 an 1.95 in the Al-Hajar Mountains and Jebel Akhdar, whereas they are smaller further south on the Arabian platform (1.6 - 1.7) which coincides with the v_p/v_s ratios from Al-Hashmi et al. (2011). East of the Semail Gap, v_p/v_s ratios are strongly increasing to 2.4 which is difficult to explain. A next step might include a joint inversion between receiver functions and our surface wave dispersion measurements to possibly obtain a common solution which fits both data sets. Anyway, the partly high inconsistency between the results in the eastern part of the study area needs to be further discussed.

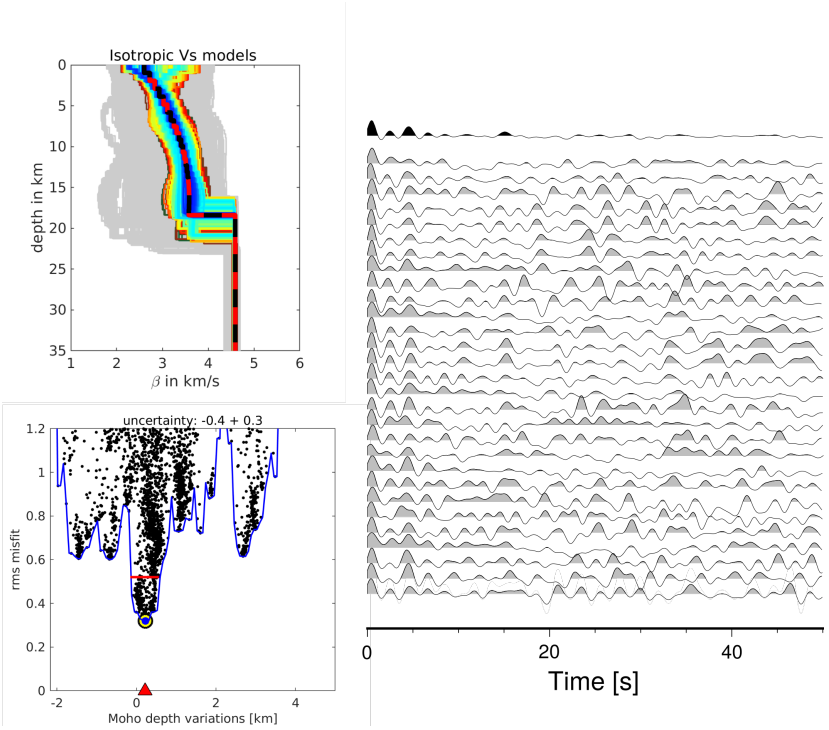

Figure 4.21: Comparison of the results of one 1D PSO inversion (left) and P- receiver functions (right) in the Wahiba Sands.

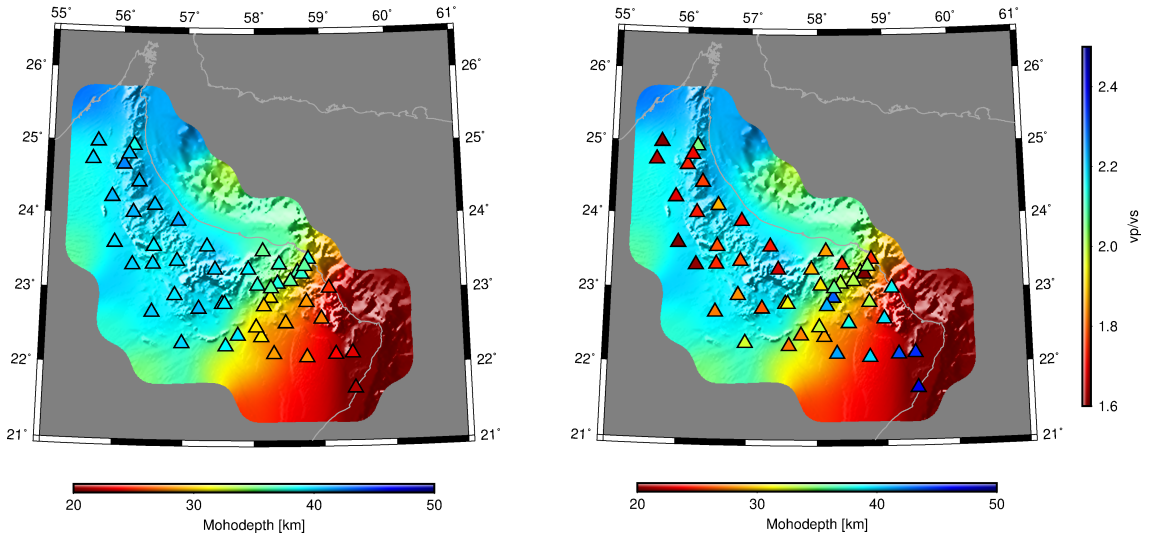

Figure 4.22: Results for the Moho depth. Left: expected Moho depth from 1D inversions and fitted Moho depth by using a weighted shear wave velocity from the 1D inversion and Ps-conversion time from receiver functions. Right: expected Moho depth from 1D inversions and the calculated v_p/v_s ratio at each station to fit the Moho from the 1D inversion

4.3 Discussion

The results, either from the 1D inversion for shear wave velocity over depth or receiver functions are suitable to image prominent geological features of the crust in northern Oman. The 3D model of anisotropic shear wave velocity over depth provides information on the 3D geometry of the ophiolite and will certainly contribute to the understanding of the tectonic setting and evolution of the Al-Hajar Mountains. Results from Ambient noise surface wave tomography provide additional information on azimuthal anisotropy. In the following we combine the obtained infomation on isotropic shear wave velocity, radial and azimuthal anisotropy and receiver functions to discuss certain geological features. Figure 4.23 combines all obtained information, exemplary for four of the seven shown vertical cross sections. Geological formations of the crust are drawn after the isotropic shear wave velocity perturbations from our 3D depth model. In addition, the sections show the most striking features of radial- and azimuthal anisotropy. Radial anisotropy is marked as vertical or horizontal blue dashed lines, depending on whether V_{SH} is larger than V_{SV} or vice versa. The azimuthal anisotropy is shown either as a dashed line or a circle, indicating that the azimuthal anisotropy is on average parallel or perpendicular to the direction of the vertical cross section. At last, the sections show the different Moho estimations, obtained from the 3D model and receiver functions.

From the beginning of this work, we were aiming for the 3D geometry of the Oman ophiolite. The results from surface wave tomography already provided information in terms of distinct higher velocities across the Al-Hajar Mountains at lowest periods, compared to the ones on southern Arabian platform. However, these anomalies were still observable up to intermediate periods of 12 s which coincides to $\approx 16-20km$ depth. Previous studies claimed that the thickness of the ophiolite is not larger than 12 km [Coleman, 1981; Shelton, 1990; Ravaut et al., 1997; Al-Lazki et al., 2002; Dewey and Casey, 2011]. This leads to two implications, first: the high velocity anomalies are just partially coming from the ophiolite, but from additional tectonic processes as well, which resulted in the appearance of high velocity anomalies in the upper and middle crust down to $\approx 20km$ beneath the Al-Hajar Mountains. Second: It will be difficult to obtain information regarding the lateral variations or thickness of the ophiolite directly from our phase velocity maps. However, the 3D model of isotropic shear wave velocity over depth allows for estimations on the thickness of the ophiolite. They are mostly consistent to previous geophysical studies based on 1D or 2D modelling of gravity data. We observe an ophiolite thickness of $4-5km$ in the Wadi Abiyyad area north of Jebel Akhdar which fits to the results from Al-Lazki et al. (2002). Shelton et al. (1990) proposed a comparable ophiolite thickness of $\approx 4km$ and $\approx 3.5km$ in the Haylayn- and Sarami region northwest of Jebel Akhdar and north of the Hawasina window, respectively. However, Ravaut et al. (1997) obtained with $9-10km$ a distinct higher thickness of the ophiolite

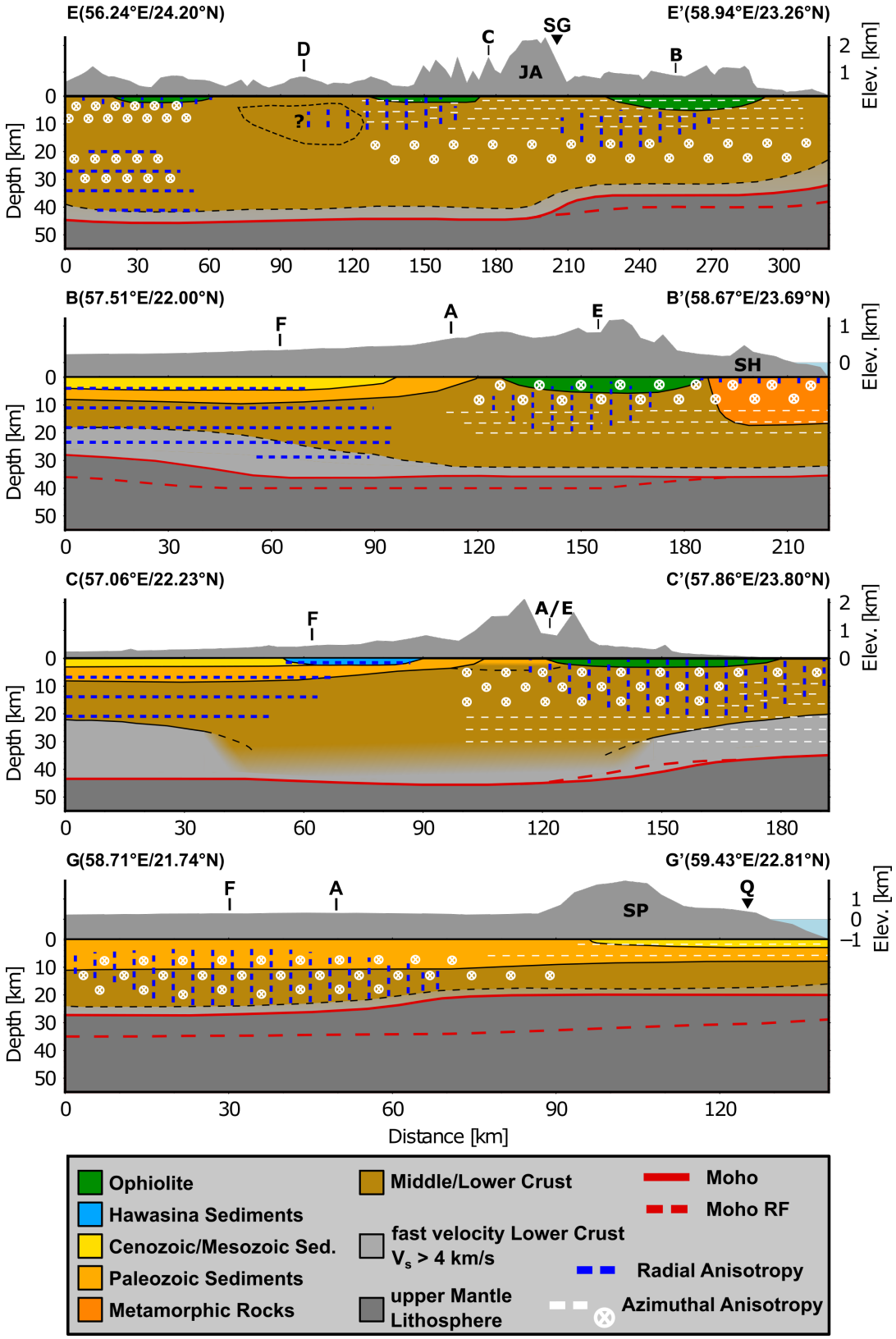

Figure 4.23: Summary of all obtained results including isotropic shear wave velocities and radial anisotropy from the 3D model, isotropic and azimuthal anisotropic phase velocities from ambient noise surface wave tomography and receiver functions for the vertical cross sections EE', BB', CC', GG'; JA: Jebel Akhdar; SH: Saih Hatat; SG: Semail Gap; SP: Salmah Plateau; Q: Qalhat

in the Haylayn region. Further east in Wadi Andam, east of the Semail Gap, a distinct larger thickness of the ophiolite is observable in our model ($\approx 8km$, see Fig.4.23 profile EE'). Manghnani and Coleman (1981) and Coleman (1981) confirm that the Oman ophiolite features its maximum thickness of $\approx 10-12km$ in that area which is more than our model provides.

Besides the ophiolite, there are different regions, like Jebel Akhdar and Saih Hatat which are of high geological interest. They represent probably the two most prominent tectonic windows in northern Oman. Here, the ophiolite got eroded and once subducted, old continental sediments were exhumed back on top of the surface. For that reason, there should be indications for lower velocities in the subsurface, compared to the high velocities of the surrounding ophiolite covered regions. The velocities in the uppermost $4-5km$ beneath Jebel Akhdar and Saih Hatat are indeed lower, whereas the ones beneath Saih Hatat are slightly higher than beneath Jebel Akhdar. In addition, the 3D model shows high velocities beneath Saih Hatat down to $\approx 20km$ which might be referred to high pressure metamorphic rocks (see Fig.4.23 profile BB'). This would coincide with previous works on the formation of Saih Hatat and the exhumation of sediments of the Arabian continental margin which were once subducted to depths of more than 60 km [Michard et al., 1991; Michard et al., 1994; Searle et al., 2004]. The pressure conditions in these depths led to a transformation to high pressure metamorphic rocks like blueschist or eclogite which are partly exhumed on the surface of Saih Hatat. Michard et al. (1994) and Fournier et al. (2006) claimed that the exhumation in Saih Hatat took place in late Maastrichtian to early Paleocene, during a post- obductional extension phase. This corresponds to the SW- NE directed azimuthal anisotropy from our phase velocity maps in that area at intermediate periods which corresponds roughly to depths of 20 km. In contrast, the velocities beneath Jebel Akhdar down to 20 km are distinct lower. This leads to the fact that the old sediments remained mostly unmetamorphosed during the subduction. Following previous works, the exhumation in Jebel Akhdar occured at the same time as in the Saih Hatat area [Glennie et al., 1974; Searle et al., 2004; Al-Wardi, 2006], featuring the same extensional regime. We observe a SW- NE directed azimuthal anisotropy beneath Jebel Akhdar which is comparable to the azimuthal anisotropy beneath Saih Hatat in the same depth range and might be an indication for the same extensional regime which resulted in the exhumation of old continental rocks.

The formation of todays topography of the Al-Hajar Mountains is of high interest and still not completely solved. Our 3D model shows higher velocities in the upper and middle crust beneath the Al-Hajar Mountains, compared to the mostly undeformed Arabian continental crust further southwest. In addition, we observe NW-SE directed azimuthal anisotropy in the Al- Hajar Mountains at lower periods in our phase velocity maps which is mostly parallel to the coast and almost perpendicular to the azimuthal anisotropy of the Arabian platform at the same period. East of the Semail Gap, the direction is slightly turning towards eastern direc-

tion. This would substantiate many previous works proposing compressional deformation as the main reason for the uplift which may have started in early Oligocene around 25 - 30 Ma. This is documented by apatite fission track data [Mount et al., 1998] and fault-slip data, especially strike-slip- and reverse faults [Fournier et al., 2006] which can be associated with a ≈E-W direction of compression. Hansman et al. (2017) proposed an uplift of the Al-Hajar Mountains in the late Eocene based on their thermal modelling. The cause of the compression in the central Oman Mountains is not very clear and might be of different reasons. Fournier et al. (2006) allocates the cause towards the Zagros collision like it is proposed for the Musandam area in the northermost Oman Mountains [Ricateau and Riche, 1980; Searle et al., 1983; Searle, 1988; Regard et al., 2005], while Hansman et al. (2017) claimed that the uplift of the Al-Hajar Mountains is caused by a slowdown of the Makran subduction. It could also be related to the rifting of the Gulf of Aden which has been initiated approximately at the same time [Leroy et al., 2013] or to the upwelling of the Afar hotspot which overall led to a net push effect on the Arabian continent. Interestingly, azimuthal anisotropy at higher periods ($> 12s$) points into SW-NE direction which provide indications for a rather extensional regime in the past (see also Fig.4.23 profiles EE',BB',CC'). It could be related to slab pull at the Makran subduction zone. The uplift of the Oman Mountains might than caused by an increase of subduction and thus comparable to the formation of rift shoulders, like the ones along the Red sea rift system [Bosworth, 2015]. Despite that the timing of this extensional phase has still to be identified, it would be incompatible with previous models and a reinvestigation of the question about the formation of the Oman Mountains seems to be required. Moreover, lateral and vertical variations of radial and azimuthal anisotropy might provide indications on local differences in cause and effect of the formation of the Al-Hajar Mountains. In the Salahi area (vertical cross section AA', 90 - 120 km), we observe negative radial anisotropy only down to $\approx 6km$ which includes mostly the ophiolite strata. This is distinct shallower compared to the vertical extent of negative radial anisotropy further southeast in the central and eastern part of the Al-Hajar Mountains. In addition, we observe low velocities and positive radial anisotropy in the middle and lower crust beneath Salahi. The crustal structure of the Salahi area seems to behave more like the Arabian continental crust further south than the central and eastern part of the Al-Hajar Mountains. This might be an indications that the crustal structure in the Salahi area was less affected by compressional or extensional events during and after the obduction than the Oman Mountains further north in Musandam or further southwest at the Jebel Akhdar or Wadi Andam.

Extent and dynamics of the obduction process depend strongly on the internal structure of the continental lithosphere beneath the Al-Hajar Mountains [Duretz et al., 2016]. For that reason, information on the present state of the continental lithposphere leads to a better understanding of the obduction process. Lateral variations in our isotropic and anisotropy 3D model clearly divide the upper crust of the study area in roughly two parts, a strongly deformed, obduction related area of the Al-Hajar Mountains with high isotropic shear wave

velocity and negative radial anisotropy and the mostly undisturbed continental crust of the Arabian platform with low velocities and horizontal layering (positive radial anisotropy). Interestingly, there is no radial anisotropy in the upper $\approx 5km$ of the Arabian platform where mostly Mesozoic and Cenozoic sediments are located. This can be associated with a change of conditions for sedimentation like minor consolidation and less shape- preferred orientation in the past. The transition between positive radial anisotropy beneath the Arabian platform and mostly negative radial anisotropy beneath the Al-Hajar Mountains collocates with the Hawasina Frontal Thrust, which marks the lateral extent of the obduction onto the Arabian continent (see Fig.4.15, $15km$). Especially in the central part of the Al-Hajar Mountains and east of the Semail Gap, this resemblance is observable to a depth of $\approx 26km$ and indicate that the obduction affected the crustal structure down to approximately this depth. In addition, differences in the lateral extent of the obduction is observed west of the Semail Gap, compared to the Wadi Andam area east of the Semail Gap. For simplification, we assume two geological crustal sections, a western and eastern block, separated by the Semail Gap which feature different properties in their tectonic setting. The western block features a crustal thickness of $\approx 43km$, whereas it is $\approx 35-38km$ in the eastern block. Higher shear wave velocities down to 20 km beneath Saih Hatat and exhumed high pressure metamorphic rocks on the surface indicate a stronger and steeper subduction in the eastern block compared to the western one. The western block features stronger negative radial anisotropy down to $\approx 20km$ compared to the eastern one which might indicate a higher deformability of the western block. Therefore, it seems that the properties of the western block, namely a larger crustal thickness, a flatter subduction and relative strong deformability are more beneficial for obduction. This is however partly in contrast to the numerical modelling of Duretz et al. (2016). They proposed that a strong continental crust in terms of rheology and thus a low deformability is a condition for ophiolite emplacement.

Apart of the Oman Mountains and the ophiolite, there is a different interesting feature in the easternmost part of the study area in the Wahiba Sands. Besides the shallow Moho, we observe relatively high velocities in the upper $10-12km$ compared to the northern situated Salmah Plateau (Profile GG') and the Oman Interior Basin westwards. In addition, our 3D model shows negative radial anisotropy beneath the Wahiba Sands (see also Fig.4.23 profile GG'). This area is part of a NNE- trending paleohigh which extents from the easternmost part of Arabia (Ra's Al Hadd) to Salalah in Dhofar. The most striking feature of this paleohigh would be the Haushi-Huqf area, southwards of our study area at the southeastern margin of the Arabian continent (see Fig.1.1 for location). It features once uplifted old Paleozoic sediments [Ries and Shackleton, 1990; Dubreuilh et al., 1992]. During Permian and Triassic times, the eastern part of Oman was involved in various episodes of faulting [Montenat et al., 2003]. They can be related to the breakup of Gondwana and the following Tethyan rifting which resulted in extensional deformation along the northeastern margin of the Arabian platform [Béchennec et al., 1993; Pratt and Smewing, 1993]. This also coincides

with the direction of azimuthal anisotropy in the eastern part of our study area at intermediate periods. In addition, the Haushi-Huqf area shows WNW-ESE directed compression which is documented by normal fault directions [Montenat et al., 2003] and interpretations of joints [Bertotti et al., 2005] and can be ascribed to Aptian times in lower Cretaceous. During that time, the major uplift of the Haushi-Huqf area occured [Ries and Shackleton, 1990]. This could be adapted to the Wahiba Sands in our study area. Higher velocities in the upper crust with negative radial anisotropy might be interpreted as the existence of relatively thick Paleozoic sediments which experienced the same kind of deformation in the past as observed in the Haushi-Huqf area. Since it is obvious that this part of the paleohigh shows no topography anymore, it might be either affected by stronger subsidence or experienced no or only minor uplift. Azimuthal anisotropy from our phase velocity maps does not provide indications for the WNW-ESE directed compression in that area which was observed in the Haushi-Huqf area. This would support the latter assumption that this area was not uplifted, at least not by compression.

Our 3D model provides a Moho map of the entire study region. It is mostly consistent to previous studies on the crustal thickness in northern Oman which were mostly based on gravity data [Shelton, 1990], a combination of gravity data with different geophysical methods [Ravaut et al., 1997; Al-Lazki et al., 2002] or by using a joint inversion of receiver functions and Rayleigh wave group velocities [Al-Hashmi et al., 2011] in one or two dimensions over certain locations across the Al-Hajar Mountains. The Moho map from our 3D model is pointwise mostly consistent with our P- and S- receiver functions in the northwestern and central part, west of the Semail Gap. It features a localized thickening of the crust and thus a deeper Moho in the Al-Hajar Mountains. We observe a maximum Moho depth of $\approx 43km$. Northwards to Wadi Abiyyad, north of Jebel Akhdar or southwards to Nizwa, south of Jebel Akhdar, the Moho is shallowing to 38 and 40 km, respectively (Fig.4.11). The overall trend of the Moho in theses areas is consistent with the 2D profil of Al-Lazki et al. (2002). They only observed slightly deeper Moho depths which are still within our uncertainties. By following the Al-Hajar Mountains further northwest, the thickening of the crust is still visible but only on minor scale. This is comparable with two 2D profiles by Ravaut et al. (1997) in the Salahi- and Haylayn area. Despite the fact that they observe slightly larger Moho depths, they showed a crustal thickening beneath the Al- Hajar Mountains in these areas as well. In addition, our results are consistent with the results of Al-Hashmi et al. (2011) west of the Semail Gap. Further east, we observe a shallower Moho of $\approx 35-38km$ beneath Wadi Andam, east of the Semail Gap, taking the results from the 3D Model and receiver functions into account. This coincides with the work of Manghnani and Coleman (1981) who also proposed a Moho depth of $< 40km$ in this area. Further east, the Moho is shallowing in our 3D Model and receiver functions. While the 3D model reveals a shallowing of the Moho up to a depth of $\approx 20km$, it is only about 32 km in the receiver functions. Al-Hashmi et al. (2011) even obtained crustal thicknesses of 42 and $46km$ at the stations Jabal Madar (JMD) and

Wadi Bani Khalid (WBK). However, their inversion results also showed an overall velocity increase from west to east in depths of 20 to 35 km with partly more than $4.2km/s$ in the east. This is consistent with our 3D model and let us assume that different interpretations of the crustal thickness in the eastern part of the study area and variations of more than 10 km are possible which needs to be further investigated. Especially, the obtained results from our 3D model and receiver functions seem to be reliable individually. Attempts to combine the information from the 3D model and receiver functions to estimate a common Moho depth, by taking v_p/v_s ratios into account, were only partly successful. While we obtain reliable v_p/v_s ratios in the western and central part of the study area, which are mostly consistent to the ones proposed by Al-Hashmi et al. (2011), v_p/v_s ratios in the eastern part are ≈ 2.4 for which it is difficult to find a reasonable explanation. Therefore, it might even be that both methods show different discontinuities in the lithospheric structure beneath the eastern part of our study area which leads to two options. First, the 3D model shows the shallow Moho at $\approx 20-25km$ and the receiver functions reveal a discontinuity in the mantle lithosphere which corresponds to a depth of $\approx 32km$. Since the parametrization of the 1D inversion is limited to the crust and allows for just one discontinuity, we obtain no information in the depth range in which the Moho from the receiver functions is located. For that reason, a second possibility might be that the 1D inversion reveals a discontinuity within the crust, e.g. towards a high- velocity lower crust and the crustal thickness is characterized by receiver functions with $\approx 32km$.

However, we find an overall agreement of a shallowing Moho in the eastern part of our study area. Together with observed NW- SE directed azimuthal anisotropy from our phase velocity maps at larger periods, this might be related to the extensional regime during the Gondwana breakup and Tethyan rifting in Triassic periods [Béchennec et al., 1993; Pratt and Smewing, 1993]. Marquer et al. (1998) provide information for a NW- SE directed stretching of the oceanic lithosphere of the Masirah basin which was formed during the time of the Gondwana breakup and obducted onto the Arabian continent in southern Oman. This coincides with the direction of the azimuthal anisotropy from our phase velocity maps. In addition, the thinning crust from west to east exhibit several stepwise decreases of more than 5 km over a short lateral distance (e.g. Fig.4.19, profile FF'). Since it is known that the Arabian plate is an accretion of terranes which occured in Precambrium [Stoeser and Camp, 1985; Husseini, 1988; Allen, 2007], the steps in the Moho depth might be a result of different deformational behaviour during the extensional regime of the Gondwana breakup and reveal the boundaries of individual Precambrian terranes.

Overall, the 3D model over depth for isotropic shear wave velocity and radial anisotropy cornfirms many common ideas and facts on the structure of the eastern Arabian continental margin. It provides additional information on the geometry of the lithosphere, especially for the Oman ophiolite and the crustal thickness. Moreover, in combination with azimuthal

anisotropy, it even yields new insights on the structural evolution of the entire region by providing additional information on deformational processes in the past. While NW-SE directed azimuthal anisotropy in the upper crust tends to the often stated compressional regime causative for the uplift of the Al-Hajar Mountains, SW-NE directed azimuthal anisotropy at larger depths rather indicates an importance of an extensional phase in the past. However, the timing of this extensional phase has still to be identified, but it would be incompatible with previous models which proposed a compressional phase causative for an uplift. High velocities beneath Saih Hatat and a corresponding direction of azimuthal anisotropy at intermediate periods support the idea of post- obductional extension, which is associated with the exhumation of high pressure metamorphic rocks. Lower velocities beneath Jebel Akhdar correlate with the fact of an exhumation of minor subducted and mostly unmetamorphosed continental sediments. In addition, radial anisotropy reveals that the Arabian continental plate was affected by the obduction process to a depth of $\approx 26km$. The results reveal distinct differences in the crustal structure west- and eastwards of the Semail Gap. In combination with differences in the lateral extend of the ophiolite, this allows for assumptions on geological properties which are more suitable for an obduction, namely a large deformability and crustal thickness and a rather flat subduction, like it is observable west of the Semail Gap. High velocities and negative radial anisotropy in the crust beneath the Wahiba Sands are comparable to the southern located Haushi-Huqf area, which is characterized by strongly deformed Paleozoic sediments. The 3D Model provides a Moho map which is mostly consistent with the results of our receiver functions. Minor variations in the central and western part of the study area are neglectable, whereas differences of partly more than 10 km in the east need to be further discussed. The overall shallowing of the Moho can be referred to the Tethyan rifting in Triassic times which is supported by azimuthal anisotropy from our phase velocity maps at higher periods.

Chapter 5

Conclusion and outlook

The main goal of this thesis was to calculate a 3D model of the lithospheric structure beneath the eastern Arabian continental margin which will contribute to the overall understanding of the obduction process and the formation of the today's topography of the Oman Mountains. For that reason, we used a long-term dataset of passively recorded continuous data and estimated azimuthal anisotropic surface wave phase velocity maps, based on ambient seismic noise cross correlations. By using a probabilistic 1D inversion method (Particle Swarm Optimization), phase velocity measurements were inverted for shear wave velocity over depth. In the end we were able to construct a 3D model of isotropic shear wave velocity and radial anisotropy over depth for the eastern Arabian continental margin. In combination with azimuthal anisotropy and receiver functions, it yields new insights in the lithospheric structure of the Oman Mountains and provides information, which is suitable for investigating its geodynamic evolution in the past.

Besides of geodynamic questions, this thesis dealed with partly new methodical approaches to calculate the 3D model. Surface wave phase velocities from ambient seismic noise are well suited for imaging the crust in the eastern Arabian continental margin. The newly developed grid search approach allows for estimations of Rayleigh and Love wave phase velocitiy dispersion curves in a period range of 2 - 40 s. In fact, this approach is more suitable than the more common zero crossing method in our case. Several tests have shown that the grid search approach provides more robust results at higher frequencies. Surface wave tomography was performed to construct 2D isotropic and azimuthal anisotropic phase velocity maps for Rayleigh and Love waves as a function of period. The obtained lateral resolution is overall $\approx 30km$. From the phase velocity maps, local Rayleigh and Love wave dispersion curves are constructed in a dense grid of $10km$ and a period range of $2-20s$. Each local dispersion curve is inverted individually for 1D shear wave velocity over depth using the Particle Swarm Optimization. By inverting Rayleigh and Love wave dispersion curves simultaneously, information on radial anisotropy was obtained. Inversion results of selected 1D grid points revealed that distinct structural differences in the upper crust can be resolved.

Receiver function studies enabled us to investigate lithospheric discontinuities beneath the eastern Arabian continental margin. A semblance based approach was used to estimate the crustal thickness beneath our array. Unfortunately, due to a poor data quality and inconsistencies between the different approaches for S- receiver functions, almost no information regarding the lithosphere- asthenosphere boundary were obtained. Locally, indications for a depth of $\approx 100km$ were observed in P- receiver functions which are however not consistent. At last, we were able to investigate the mantle transition zone beneath the eastern Arabian continental margin. The differential time between the 410 km and 660km discontinuity is only slightly differing from the IASP91 model and thus provide information of a mostly stable mantle transition zone. Overall, the introduced and performed procedures are suitable to be applied in different regions for investigating the Earth's crust. Especially, the grid search approach for calculating Rayleigh and Love wave phase velocity dispersion curves down to 2 s period by using ambient seismic noise data was already successfully utilized in the Pannonian Basin and in the Eifel region.

In the end, we were able to construct a high resolution 3D model over depth for isotropic shear wave velocity and radial anisotropy for the crust. It provides information on lateral and vertical variations beneath the Oman Mountains and confirm previous works on 1D and 2D modelling of the ophiolite structure. Moreover, the 3D model features a clear contrast between the highly deformed crustal structure of the Oman Mountains and the mostly undeformed Arabian platform. In combination with azimuthal anisotropy, lateral variations of the 3D model contribute to the ongoing debate about the cause and effect of the formation of today's topography of the Al-Hajar Mountains. NW-SE directed azimuthal anisotropy in the upper crust tends to the often stated compressional regime causative for the uplift, whereas SW-NE directed azimuthal anisotropy at larger depths rather points to the influence of an extensional phase in the past. Despite that the timing of this extensional phase has still to be identified, it would be incompatible with previous models which proposed a compressional phase causative for an uplift. Therefore, a reinvastigating of the question about the formation of the Oman Mountains seems to be required. In addition, our results substantiate previous works on post- obductional extension leading to the exhumation of once subducted and partly metamorphosed rocks in the Saih Hatat and Jebel Akhdar window. Variations in radial anisotropy showed that the obduction process affected the continental crust to a depth of $\approx 26km$. By evaluating the results on the structure of the continental lithosphere, distinct differences between the areas west- and eastwards of the Semail Gap were observable. In combination with differences in the lateral extent of the ophiolite, this might yield new insights in the required conditions for obduction to occur. It seems that the continental structure west of the Semail Gap is more beneficial for obduction. It shows a relatively large deformability and crustal thickness, in combination with a rather flat subduction of the continental plate during the obduction. At last, we present a map for crustal thickness across the entire eastern Arabian continental margin by combining the obtained information

from the 3D model and receiver functions. An overall thinning of the crust from west to east and NW-SE directed azimuthal anisotropy at higher periods can be related to the extensional regime during the Gondwana breakup and Tethyan rifting. In addition, it features a localized crustal thickening beneath the Oman Mountains with a maximum vertical extent beneath Jebel Akhdar. Differences between the 3D model and receiver functions of partly more than 10 km in the east need to be further discussed.

5.1 Outlook

Our 3D model of anisotropic shear wave velocity over depth, in combination with the results of receiver functions and azimuthal anisotropy from ambient noise surface wave tomography contributes significantly to the understanding of the tectonic setting and evolution of the Al-Hajar Mountains. It may lay the grounds for more detailed geodynamic modelling of the developement of the Oman Mountains and the ophiolite emplacement. However, a few question remained open. We clearly observed a localized thickening of the crust beneath the Oman Mountains. When did the thickening occur? Can it be related to the obduction process or to later deformational processes? In addition, we observed differences in the crustal structure beneath the Jebel Akhdar and Saih Hatat window compared to remaining Oman Mountains. Why are they so localized? Are there any relations to the Semail Gap? At last, a new question arises. The lithospheric structure beneath the Oman Mountains could provide indications for the cause of the overall northwards movement of the Arabian plate, either due to extension caused by slab pull of the Makran subduction zone or compression caused by push of upwelling of the Afar hotspot.

To solve these questions, even additional methodical approaches might be useful. A joint inversion between receiver functions and surface wave dispersion curves may provide a common solution for the crustal thickness in the eastern part of our study area. The resolution of dispersion curves from ambient seismic noise are mostly limited to the crust. By adding phase velocities from teleseismic measurements, the resolution at larger depths will be enhanced. This might lead to a more reliable crustal thickness over the entire area. In addition, we might obtain information on the depth of the lithosphere- asthenosphere boundary which would also contribute to the understanding of the geodynamic evolution of the Oman Mountains and the lithosphere of the eastern Arabien continental margin. In addidion, the 1D inversion over depth also allows to invert for azimuthal anisotropy. This would allow for more detailed discussions on lateral and vertical variations of deformational processes, but needs more detailed tests on the parametrization and regularization.

However, the presented results provide the first three-dimensional image of the lithosphere below the eastern Arabian passive continental margin.

Acknowledgments

I would like to express my gratitude to my supervisor Thomas Meier for his great support and the scientific discussions over the past years. He showed me how to work scientifically with a high standard and his constructive criticism helped my progress tremendously.

A special thank goes to Christian Weidle for all the support. He helped me a lot with endless discussions, encouragement and reading over and over the drafts of my thesis. This thesis could never been completed without his assistance.

I am really thankful to Frank Krüger from Potsdam university for his collaboration and support during my PhD, especially during the time when I was working in his working group for a couple of weeks. Since I never worked on receiver functions before, I am grateful for his patience, guidance and explanations to achieve good results.

Many thanks to Philippe Agard, from Sorbonne Université, Paris and Andreas Scharf, from Sultan Qabos University, Muskat, for the numerous discussions about our results and the geology of the Oman Mountains.

I also would like to thank the entire working group Seismologie for their support, ideas and discussions, especially during working group meetings and coffee breaks.

Lastly, I would like to thank my family for the support they gave me from the beginning of my studies.

Bibliography

[Aki, 1957] Aki, K. (1957). Space and time spectra of stationary stochastic waves, with special reference to microtremors. *Bull. Earthq. Res. Inst.*, 35:415–456.

[Aki and Richards, 2002] Aki, K. and Richards, P. G. (2002). *Quantitative seismology*. University Science Books Sausalito California.

[Al-Hashmi et al., 2011] Al-Hashmi, S., Gök, R., Al-Toubi, K., Al-Shijbi, Y., El-Hussain, I., and Rodgers, A. (2011). Seismic velocity structure at the southeastern margin of the arabian peninsula. *Geophysical Journal International*, 186(2):782–792.

[Al-Lazki et al., 2002] Al-Lazki, A. I., Seber, D., Sandvol, E., and Barazangi, M. (2002). A crustal transect across the oman mountains on the eastern margin of arabia. *GeoArabia*, 7(1):47–78.

[Al-Wardi, 2006] Al-Wardi, M. (2006). *Structural evolution of the Jebel Akhdar culmination and its implications for exhumation processes in the northern Oman Mountains*. PhD thesis, University of Leeds.

[Allen, 2007] Allen, P. A. (2007). The huqf supergroup of oman: basin development and context for neoproterozoic glaciation. *Earth-Science Reviews*, 84(3-4):139–185.

[Allen et al., 2004] Allen, P. A., Leather, J., and Brasier, M. D. (2004). The neoproterozoic fiq glaciation and its aftermath, huqf supergroup of oman. *Basin Research*, 16(4):507–534.

[Amthor et al., 2003] Amthor, J. E., Grotzinger, J. P., Schröder, S., Bowring, S. A., Ramezani, J., Martin, M. W., and Matter, A. (2003). Extinction of cloudina and namacalathus at the precambrian-cambrian boundary in oman. *Geology*, 31(5):431–434.

[Babuska and Cara, 1991] Babuska, V. and Cara, M. (1991). *Seismic anisotropy in the Earth*, volume 10. Springer Science & Business Media.

[Barmin et al., 2001] Barmin, M., Ritzwoller, M., and Levshin, A. (2001). A fast and reliable method for surface wave tomography. In *Monitoring the Comprehensive Nuclear-Test-Ban Treaty: Surface Waves*, pages 1351–1375. Springer.

[Bath and Stefánsson, 1966] Bath, M. and Stefánsson, R. (1966). Sp conversion at the base of the crust. *Annals of Geophysics*, 19(2):119–130.

[Béchennec et al., 1993] Béchennec, F., Le Métour, J., Platel, J., and Roger, J. (1993). Geological map of the sultanate of oman. scale 1: 1.000. 000, with explanatory notes. *Muscat, Directorate General of Minerals, Oman Ministry of Petroleum and Minerals*.

[Bensen et al., 2007] Bensen, G., Ritzwoller, M., Barmin, M., Levshin, A. L., Lin, F., Moschetti, M., Shapiro, N., and Yang, Y. (2007). Processing seismic ambient noise data to obtain reliable broad-band surface wave dispersion measurements. *Geophysical journal international*, 169(3):1239–1260.

[Bensen et al., 2008] Bensen, G., Ritzwoller, M., and Shapiro, N. M. (2008). Broadband ambient noise surface wave tomography across the United States. *Journal of Geophysical Research: Solid Earth*, 113(B5).

[Berkhout, 1977] Berkhout, A. (1977). Least-squares inverse filtering and wavelet deconvolution. *Geophysics*, 42(7):1369–1383.

[Bertotti et al., 2005] Bertotti, G., Immenhauser, A., and Taal-van Koppen, J. (2005). Stratigraphic and regional distribution of fractures in barremian–aptian carbonate rocks of eastern oman: outcrop data and their extrapolation to interior oman hydrocarbon reservoirs. *International Journal of Earth Sciences*, 94(3):447–461.

[Beucler and Montagner, 2006] Beucler, E. and Montagner, J.-P. (2006). Computation of large anisotropic seismic heterogeneities (CLASH). *Geophysical Journal International*, 165(2):447–468.

[Bina and Helffrich, 1994] Bina, C. R. and Helffrich, G. (1994). Phase transition clapeyron slopes and transition zone seismic discontinuity topography. *Journal of Geophysical Research: Solid Earth*, 99(B8):15853–15860.

[Bock, 1994] Bock, G. (1994). Synthetic seismogram images of upper mantle structure: No evidence for a 520-km discontinuity. *Journal of Geophysical Research: Solid Earth*, 99(B8):15843–15851.

[Bock and Kind, 1991] Bock, G. and Kind, R. (1991). A global study of s-to-p and p-to-s conversions from the upper mantle transition zone. *Geophysical journal international*, 107(1):117–129.

[Boschi and Ekström, 2002] Boschi, L. and Ekström, G. (2002). New images of the earth's upper mantle from measurements of surface wave phase velocity anomalies. *Journal of Geophysical Research: Solid Earth*, 107(B4):ESE–1.

[Boschi et al., 2012] Boschi, L., Weemstra, C., Verbeke, J., Ekström, G., Zunino, A., and Giardini, D. (2012). On measuring surface wave phase velocity from station–station cross-correlation of ambient signal. *Geophysical Journal International*, 192(1):346–358.

[Bostock, 1998] Bostock, M. (1998). Mantle stratigraphy and evolution of the slave province. *Journal of Geophysical Research: Solid Earth*, 103(B9):21183–21200.

[Bosworth, 2015] Bosworth, W. (2015). Geological evolution of the red sea: historical background, review, and synthesis. In *The Red Sea*, pages 45–78. Springer.

[Breton et al., 2004] Breton, J.-P., Béchennec, F., Le Métour, J., Moen-Maurel, L., and Razin, P. (2004). Eoalpine (cretaceous) evolution of the oman tethyan continental margin: insights from a structural field study in jabal akhdar (oman mountains). *GeoArabia*, 9(2):41–58.

[Burdick and Langston, 1977] Burdick, L. J. and Langston, C. A. (1977). Modeling crustal structure through the use of converted phases in teleseismic body-wave forms. *Bulletin of the Seismological Society of America*, 67(3):677–691.

[Chevrot and Zhao, 2007] Chevrot, S. and Zhao, L. (2007). Multiscale finite-frequency Rayleigh wave tomography of the Kaapvaal craton. *Geophysical Journal International*, 169(1):201–215.

[Christensen and Smewing, 1981] Christensen, N. I. and Smewing, J. D. (1981). Geology and seismic structure of the northern section of the oman ophiolite. *Journal of Geophysical Research: Solid Earth*, 86(B4):2545–2555.

[Coleman, 1971] Coleman, R. (1971). Plate tectonic emplacement of upper mantle peridotites along continental edges. *Journal of Geophysical Research*, 76(5):1212–1222.

[Coleman, 1981] Coleman, R. G. (1981). Tectonic setting for ophiolite obduction in oman. *Journal of Geophysical Research: Solid Earth*, 86(B4):2497–2508.

[Darbyshire and Lebedev, 2009] Darbyshire, F. A. and Lebedev, S. (2009). Rayleigh wave phase-velocity heterogeneity and multilayered azimuthal anisotropy of the Superior Craton, Ontario. *Geophysical Journal International*, 176(1):215–234.

[Debayle and Ricard, 2013] Debayle, E. and Ricard, Y. (2013). Seismic observations of large-scale deformation at the bottom of fast-moving plates. *Earth and Planetary Science Letters*, 376:165–177.

[Deschamps et al., 2008] Deschamps, F., Lebedev, S., Meier, T., and Trampert, J. (2008). Azimuthal anisotropy of Rayleigh-wave phase velocities in the east-central United States. *Geophysical Journal International*, 173(3):827–843.

[Deuss and Woodhouse, 2001] Deuss, A. and Woodhouse, J. (2001). Seismic observations of splitting of the mid-transition zone discontinuity in earth's mantle. *Science*, 294(5541):354–357.

[Dewey and Casey, 2011] Dewey, J. and Casey, J. (2011). The origin of obducted large-slab ophiolite complexes. In *Arc-Continent Collision*, pages 431–444. Springer.

[Dubreuilh et al., 1992] Dubreuilh, J., Platel, J., Le Métour, J., Roger, J., Wyns, R., Béchennec, F., and Berthiaux, A. (1992). Explanatory notes to the geological map of khaluf, sheet nf 40-15, scale 1: 250000. *Directorate General of minerals, Oman ministry of petroleum and minerals*.

[Dueker and Sheehan, 1997] Dueker, K. G. and Sheehan, A. F. (1997). Mantle discontinuity structure from midpoint stacks of converted p to s waves across the yellowstone hotspot track. *Journal of Geophysical Research: Solid Earth*, 102(B4):8313–8327.

[Duretz et al., 2016] Duretz, T., Agard, P., Yamato, P., Ducassou, C., Burov, E. B., and Gerya, T. V. (2016). Thermo-mechanical modeling of the obduction process based on the oman ophiolite case. *Gondwana Research*, 32:1–10.

[Dziewonski et al., 1969] Dziewonski, A., Bloch, S., and Landisman, M. (1969). A technique for the analysis of transient seismic signals. *Bulletin of the seismological Society of America*, 59(1):427–444.

[Dziewonski and Anderson, 1981] Dziewonski, A. M. and Anderson, D. L. (1981). Preliminary reference earth model. *Physics of the earth and planetary interiors*, 25(4):297–356.

[Eberhart and Kennedy, 1995] Eberhart, R. and Kennedy, J. (1995). A new optimizer using particle swarm theory. In *MHS'95. Proceedings of the Sixth International Symposium on Micro Machine and Human Science*, pages 39–43. Ieee.

[Egorkin, 1997] Egorkin, A. (1997). Evidence for 520-km discontinuity. In *Upper Mantle Heterogeneities from Active and Passive Seismology*, pages 51–61. Springer.

[Ekström, 2017] Ekström, G. (2017). Short-period surface-wave phase velocities across the conterminous United States. *Physics of the Earth and Planetary Interiors*, 270:168–175.

[Ekström et al., 2009] Ekström, G., Abers, G. A., and Webb, S. C. (2009). Determination of surface-wave phase velocities across USArray from noise and Aki's spectral formulation. *Geophysical Research Letters*, 36(18).

[Ekström and Dziewonski, 1998] Ekström, G. and Dziewonski, A. M. (1998). The unique anisotropy of the pacific upper mantle. *Nature*, 394(6689):168–172.

[El-Sharkawy, 2019] El-Sharkawy, A. M. M. E. (January 2019). *Surface wave tomography across Europe-Mediterranean and Middle East based on automated inter-station phase velocity measurements*. Christian-Abrechts-Universität zu Kiel, Kiel. xxvii, 178 Seiten, Illustrationen.

[Endrun et al., 2008] Endrun, B., Meier, T., Lebedev, S., Bohnhoff, M., Stavrakakis, G., and Harjes, H.-P. (2008). S velocity structure and radial anisotropy in the aegean region from surface wave dispersion. *Geophysical Journal International*, 174(2):593–616.

[Engelbrecht, 2005] Engelbrecht, A. P. (2005). Fundamentals of computational swarm intelligence. 2005. *Hoboken: John Wiley & Sons, Ltd*.

[Faber and Müller, 1980] Faber, S. and Müller, G. (1980). Sp phases from the transition zone between the upper and lower mantle. *Bulletin of the Seismological Society of America*, 70(2):487–508.

[Farra and Vinnik, 2000] Farra, V. and Vinnik, L. (2000). Upper mantle stratification by p and s receiver functions. *Geophysical Journal International*, 141(3):699–712.

[Fournier et al., 2006] Fournier, M., Lepvrier, C., Razin, P., and Jolivet, L. (2006). Late cretaceous to paleogene post-obduction extension and subsequent neogene compression in the oman mountains. *GeoArabia*, 11(4):17–40.

[Frederiksen and Bostock, 2000] Frederiksen, A. and Bostock, M. (2000). Modelling teleseismic waves in dipping anisotropic structures. *Geophysical Journal International*, 141(2):401–412.

[Gaherty and Jordan, 1995] Gaherty, J. B. and Jordan, T. H. (1995). Lehmann discontinuity as the base of an anisotropic layer beneath continents. *Science*, 268(5216):1468–1471.

[Glennie et al., 1974] Glennie, K. W., KW, G., MGA, B., MWH, C., et al. (1974). Geology of the oman mountains. *VERH. KKL. NEDERL. GEOL. MIJNBOUWKD. GENOOTSCH.*, 31.

[Gnos et al., 1997] Gnos, E., Immenhauser, A., and Peters, T. (1997). Late cretaceous/early tertiary convergence between the indian and arabian plates recorded in ophiolites and related sediments. *Tectonophysics*, 271(1-2):1–19.

[Gnos and Perrin, 1996] Gnos, E. and Perrin, M. (1996). Formation and evolution of the masirah ophiolite constrained by paleomagnetic study of volcanic rocks. *Tectonophysics*, 253(1-2):53–64.

[Godard et al., 2003] Godard, M., Dautria, J.-M., and Perrin, M. (2003). Geochemical variability of the oman ophiolite lavas: Relationship with spatial distribution and paleomagnetic directions. *Geochemistry, Geophysics, Geosystems*, 4(6).

[Gök et al., 2008] Gök, R., Mahdi, H., Al-Shukri, H., and Rodgers, A. J. (2008). Crustal structure of iraq from receiver functions and surface wave dispersion: implications for understanding the deformation history of the arabian–eurasian collision. *Geophysical Journal International*, 172(3):1179–1187.

[Gorin et al., 1982] Gorin, G., Racz, L., and Walter, M. (1982). Late precambrian-cambrian sediments of huqf group, sultanate of oman. *AAPG Bulletin*, 66(12):2609–2627.

[Hacker and Gnos, 1997] Hacker, B. R. and Gnos, E. (1997). The conundrum of samail: explaining the metamorphic history. *Tectonophysics*, 279(1-4):215–226.

[Haney et al., 2012] Haney, M. M., Mikesell, T. D., van Wijk, K., and Nakahara, H. (2012). Extension of the spatial autocorrelation (SPAC) method to mixed-component correlations of surface waves. *Geophysical Journal International*, 191(1):189–206.

[Hanna, 1990] Hanna, S. S. (1990). The alpine deformation of the central oman mountains. *Geological Society, London, Special Publications*, 49(1):341–359.

[Hansen et al., 2007] Hansen, S. E., Rodgers, A. J., Schwartz, S. Y., and Al-Amri, A. M. (2007). Imaging ruptured lithosphere beneath the red sea and arabian peninsula. *Earth and Planetary Science Letters*, 259(3-4):256–265.

[Hansman et al., 2017] Hansman, R. J., Ring, U., Thomson, S. N., den Brok, B., and Stübner, K. (2017). Late eocene uplift of the al hajar mountains, oman, supported by stratigraphy and low-temperature thermochronology. *Tectonics*, 36(12):3081–3109.

[Hess, 1964] Hess, H. (1964). Seismic anisotropy of the uppermost mantle under oceans. *Nature*, 203(4945):629–631.

[Husseini, 1988] Husseini, M. (1988). The arabian infracambrian extensional system. *Tectonophysics*, 148(1-2):93–103.

[Jiménez-Munt et al., 2012] Jiménez-Munt, I., Fernàndez, M., Saura, E., Vergés, J., and Garcia-Castellanos, D. (2012). 3-d lithospheric structure and regional/residual bouguer anomalies in the arabia—eurasia collision (iran). *Geophysical Journal International*, 190(3):1311–1324.

[Julià et al., 2000] Julià, J., Ammon, C. J., Herrmann, R., and Correig, A. M. (2000). Joint inversion of receiver function and surface wave dispersion observations. *Geophysical Journal International*, 143(1):99–112.

[Julià et al., 2003] Julià, J., Ammon, C. J., and Herrmann, R. B. (2003). Lithospheric structure of the arabian shield from the joint inversion of receiver functions and surface-wave group velocities. *Tectonophysics*, 371(1-4):1–21.

[Kästle et al., 2016] Kästle, E. D., Soomro, R., Weemstra, C., Boschi, L., and Meier, T. (2016). Two-receiver measurements of phase velocity: cross-validation of ambient-noise and earthquake-based observations. *Geophysical Journal International*, 207(3):1493–1512.

[Kennett, 1976] Kennett, B. (1976). The inversion of surface wave data. *pure and applied geophysics*, 114(5):747–751.

[Kennett, 1991] Kennett, B. (1991). The removal of free surface interactions from three-component seismograms. *Geophysical Journal International*, 104(1):153–163.

[Kind et al., 2017] Kind, R., Handy, M. R., Yuan, X., Meier, T., Kämpf, H., and Soomro, R. (2017). Detection of a new sub-lithospheric discontinuity in central europe with s-receiver functions. *Tectonophysics*, 700:19–31.

[Kind et al., 1995] Kind, R., Kosarev, G., and Petersen, N. (1995). Receiver functions at the stations of the german regional seismic network (grsn). *Geophysical Journal International*, 121(1):191–202.

[Kind et al., 2002] Kind, R., Yuan, X., Saul, J., Nelson, D., Sobolev, S., Mechie, J., Zhao, W., Kosarev, G., Ni, J., Achauer, U., et al. (2002). Seismic images of crust and upper mantle beneath tibet: evidence for eurasian plate subduction. *science*, 298(5596):1219–1221.

[Knapmeyer-Endrun et al., 2013] Knapmeyer-Endrun, B., Krüger, F., Legendre, C. P., Geissler, W. H., Group, P. W., et al. (2013). Tracing the influence of the trans-european suture zone into the mantle transition zone. *Earth and Planetary Science Letters*, 363:73–87.

[Knopoff, 1964] Knopoff, L. (1964). A matrix method for elastic wave problems. *Bulletin of the Seismological Society of America*, 54(1):431–438.

[Langston, 1977] Langston, C. A. (1977). Corvallis, oregon, crustal and upper mantle receiver structure from teleseismic p and s waves. *Bulletin of the Seismological Society of America*, 67(3):713–724.

[Laske et al., 2013] Laske, G., Masters, G., Ma, Z., and Pasyanos, M. (2013). Update on CRUST1. 0—A 1-degree global model of Earth's crust. In *Geophys. Res. Abstr*, volume 15, page 2658. EGU General Assembly Vienna, Austria.

[Lay and Wallace, 1995] Lay, T. and Wallace, T. C. (1995). *Modern global seismology*, volume 58. Academic Press San Diego.

[Lebedev et al., 2006] Lebedev, S., Meier, T., and van der Hilst, R. D. (2006). Asthenospheric flow and origin of volcanism in the baikal rift area. *Earth and Planetary Science Letters*, 249(3-4):415–424.

[Lebedev and Van Der Hilst, 2008] Lebedev, S. and Van Der Hilst, R. D. (2008). Global upper-mantle tomography with the automated multimode inversion of surface and S-wave forms. *Geophysical Journal International*, 173(2):505–518.

[Leroy et al., 2013] Leroy, S., Razin, P., Autin, J., Bache, F., d'Acremont, E., Watremez, L., Robinet, J., Baurion, C., Denèle, Y., Bellahsen, N., et al. (2013). From rifting to oceanic spreading in the gulf of aden: a synthesis. In *Lithosphere dynamics and sedimentary basins: The Arabian plate and analogues*, pages 385–427. Springer.

[Levshin et al., 2001] Levshin, A., Ritzwoller, M., Barmin, M., Villasenor, A., and Padgett, C. (2001). New constraints on the Arctic crust and uppermost mantle: Surface wave group velocities, Pn, and Sn. *Physics of the Earth and Planetary Interiors*, 123(2-4):185–204.

[Li et al., 2003] Li, X., Kind, R., and Yuan, X. (2003). Seismic study of upper mantle and transition zone beneath hotspots. *Physics of the Earth and Planetary Interiors*, 136(1-2):79–92.

[Li and Romanowicz, 1995] Li, X.-D. and Romanowicz, B. (1995). Comparison of global waveform inversions with and without considering cross-branch modal coupling. *Geophysical Journal International*, 121(3):695–709.

[Lin et al., 2008] Lin, F.-C., Moschetti, M. P., and Ritzwoller, M. H. (2008). Surface wave tomography of the western United States from ambient seismic noise: Rayleigh and Love wave phase velocity maps. *Geophysical Journal International*, 173(1):281–298.

[Lin et al., 2011] Lin, F.-C., Ritzwoller, M. H., Yang, Y., Moschetti, M. P., and Fouch, M. J. (2011). Complex and variable crustal and uppermost mantle seismic anisotropy in the western united states. *Nature Geoscience*, 4(1):55.

[Lowrie and Fichtner, 2007] Lowrie, W. and Fichtner, A. (2007). *Fundamentals of geophysics*. Cambridge university press.

[Manghnani and Coleman, 1981] Manghnani, M. H. and Coleman, R. G. (1981). Gravity profiles across the samail ophiolite, oman. *Journal of Geophysical Research: Solid Earth*, 86(B4):2509–2525.

[Marquer et al., 1998] Marquer, D., Mercolli, I., and Peters, T. (1998). Early cretaceous intra-oceanic rifting in the proto-indian ocean recorded in the masirah ophiolite, sultanate of oman. *Tectonophysics*, 292(1-2):1–16.

[Marquering et al., 1996] Marquering, H., Snieder, R., and Nolet, G. (1996). Waveform inversions and the significance of surface-wave mode coupling. *Geophysical Journal International*, 124(1):258–278.

[McEvilly, 1964] McEvilly, T. (1964). Central us crust—upper mantle structure from love and rayleigh wave phase velocity inversion. *Bulletin of the Seismological Society of America*, 54(6A):1997–2015.

[Meier et al., 2004] Meier, T., Dietrich, K., Stöckhert, B., and Harjes, H.-P. (2004). One-dimensional models of shear wave velocity for the eastern Mediterranean obtained from the inversion of Rayleigh wave phase velocities and tectonic implications. *Geophysical Journal International*, 156(1):45–58.

[Meier et al., 1997] Meier, T., Lebedev, S., Nolet, G., and Dahlen, F. (1997). Diffraction tomography using multimode surface waves. *Journal of Geophysical Research: Solid Earth*, 102(B4):8255–8267.

[Michard et al., 1991] Michard, A., Boudier, F., and Goffé, B. (1991). Obduction versus subduction and collision in the oman case and other tethyan settings. In *Ophiolite Genesis and Evolution of the Oceanic Lithosphere*, pages 447–467. Springer.

[Michard et al., 1994] Michard, A., Goffé, B., Saddiqi, O., Oberhänsli, R., and Wendt, A. (1994). Late cretaceous exhumation of the oman blueschists and eclogites: A two-stage extensional mechanism. *Terra nova*, 6(4):404–413.

[Montagner and Jobert, 1988] Montagner, J.-P. and Jobert, N. (1988). Vectorial tomography—ii. application to the indian ocean. *Geophysical Journal International*, 94(2):309–344.

[Montagner and Nataf, 1986] Montagner, J.-P. and Nataf, H.-C. (1986). A simple method for inverting the azimuthal anisotropy of surface waves. *Journal of Geophysical Research: Solid Earth*, 91(B1):511–520.

[Montagner and Tanimoto, 1991] Montagner, J.-P. and Tanimoto, T. (1991). Global upper mantle tomography of seismic velocities and anisotropies. *Journal of Geophysical Research: Solid Earth*, 96(B12):20337–20351.

[Montenat et al., 2003] Montenat, C., Barrier, P., and Soudet, H. J. (2003). Aptian faulting in the haushi-huqf (oman) and the tectonic evolution of the southeast arabian platform-margin. *GeoArabia*, 8(4):643–662.

[Mount et al., 1998] Mount, V. S., Crawford, R. I., and Bergman, S. C. (1998). Regional structural style of the central and southern oman mountains: Jebel akhdar, saih hatat, and the northern ghaba basin. *GeoArabia*, 3(4):475–490.

[Naville et al., 2013] Naville, C., Ancel, M., Andriessen, P., Ricarte, P., and Roure, F. (2013). New constrains on the thickness of the semail ophiolite in the northern emirates. In *Lithosphere Dynamics and Sedimentary Basins: The Arabian Plate and Analogues*, pages 43–59. Springer.

[Nicolas and Boudier, 2011] Nicolas, A. and Boudier, F. (2011). Structure and dynamics of ridge axial melt lenses in the oman ophiolite. *Journal of Geophysical Research: Solid Earth*, 116(B3).

[Nicolas et al., 2000] Nicolas, A., Boudier, F., Ildefonse, B., and Ball, E. (2000). Accretion of oman and united arab emirates ophiolite–discussion of a new structural map. *Marine Geophysical Researches*, 21(3-4):147–180.

[Nolet, 1987] Nolet, G. (1987). Seismic wave propagation and seismic tomography. In *Seismic tomography*, pages 1–23. Springer.

[Nolet, 1990] Nolet, G. (1990). Partitioned waveform inversion and two-dimensional structure under the network of autonomously recording seismographs. *Journal of Geophysical Research: Solid Earth*, 95(B6):8499–8512.

[Parkinson, 1998] Parkinson, C. (1998). Emplacement of the east sulawesi ophiolite: evidence from subophiolite metamorphic rocks. *Journal of Asian Earth Sciences*, 16(1):13–28.

[Pasyanos et al., 2007] Pasyanos, M. E., Tkalčić, H., Gök, R., Al-Enezi, A., and Rodgers, A. J. (2007). Seismic structure of kuwait. *Geophysical Journal International*, 170(1):299–312.

[Phinney, 1964] Phinney, R. A. (1964). Structure of the earth's crust from spectral behavior of long-period body waves. *Journal of Geophysical Research*, 69(14):2997–3017.

[Plesinger et al., 1986] Plesinger, A., Hellweg, M., and Seidl, D. (1986). Interactive high-resolution polarization analysis of broad-band seismograms. *Journal of Geophysics*, 59(2):129–139.

[Pratt and Smewing, 1993] Pratt, B. R. and Smewing, J. D. (1993). Early cretaceous platform-margin configuration and evolution in the central oman mountains, arabian peninsula. *AAPG bulletin*, 77(2):225–244.

[Qidwai et al., 1988] Qidwai, H., Khalifa, M., and Ba-mkhalif, K. A. (1988). Evidence of permo-carboniferos glaciation in the basal murbat sandstone formation, southern region, sultanate of oman. *Journal of Petroleum Geology*, 11(1):81–88.

[Rabu et al., 1993] Rabu, D., Nehlig, P., and Roger, J. (1993). Stratigraphy and structure of the oman mountains. *Documents- B. R. G. M.*

[Ravaut et al., 1997] Ravaut, P., Bayer, R., Hassani, R., Rousset, D., and Al Yahya'ey, A. (1997). Structure and evolution of the northern oman margin: gravity and seismic constraints over the zagros-makran-oman collision zone. *Tectonophysics*, 279(1-4):253–280.

[Rayleigh, 1885] Rayleigh, L. (1885). On waves propagated along the plane surface of an elastic solid. *Proceedings of the London Mathematical Society*, 1(1):4–11.

[Regard et al., 2005] Regard, V., Bellier, O., Thomas, J.-C., Bourlès, D., Bonnet, S., Abbassi, M., Braucher, R., Mercier, J., Shabanian, E., Soleymani, S., et al. (2005). Cumulative right-lateral fault slip rate across the zagros—makran transfer zone: role of the minab—zendan fault system in accommodating arabia—eurasia convergence in southeast iran. *Geophysical Journal International*, 162(1):177–203.

[Ricateau and Riche, 1980] Ricateau, R. and Riche, P. (1980). Geology of the musandam penninsula (sultanate of oman) and its surroundings. *Journal of petroleum geology*, 3(2):139–152.

[Ricou, 1971] Ricou, L. (1971). Le croissant ophiolitique péri-arabe, une ceinture de nappes mises en place au cretacé supérieur: Revue de géographie physique et géologie dynamique, v. 18.

[Ries and Shackleton, 1990] Ries, A. and Shackleton, R. (1990). Structures in the huqf-haushi uplift, east central oman. *Geological Society, London, Special Publications*, 49(1):653–663.

[Rieu and Allen, 2008] Rieu, R. and Allen, P. A. (2008). Siliciclastic sedimentation in the interlude between two neoproterozoic glaciations, mirbat area, southern oman: A missing link in the huqf supergroup? *GeoArabia*, 13(4):45–72.

[Rieu et al., 2007] Rieu, R., Allen, P. A., Cozzi, A., Kosler, J., and Bussy, F. (2007). A composite stratigraphy for the neoproterozoic huqf supergroup of oman: integrating new litho-, chemo-and chronostratigraphic data of the mirbat area, southern oman. *Journal of the Geological Society*, 164(5):997–1009.

[Sabra et al., 2005] Sabra, K. G., Gerstoft, P., Roux, P., Kuperman, W., and Fehler, M. C. (2005). Surface wave tomography from microseisms in Southern California. *Geophysical Research Letters*, 32(14).

[Sacks and Snoke, 1977] Sacks, I. and Snoke, J. (1977). The use of converted phases to infer the depth of the lithosphere-asthenosphere boundary beneath south america. *Journal of Geophysical Research*, 82(14):2011–2017.

[Scharf et al., 2019] Scharf, A., Mattern, F., Moraetis, D., Callegari, I., and Weidle, C. (2019). Postobductional kinematic evolution and geomorphology of a major regional structure—the semail gap fault zone (oman mountains). *Tectonics*, 38(8):2756–2778.

[Schreurs and Immenhauser, 1999] Schreurs, G. and Immenhauser, A. (1999). West-northwest directed obduction of the batain group on the eastern oman continental margin at the cretaceous-tertiary boundary. *Tectonics*, 18(1):148–160.

[Schwab and Knopoff, 1972] Schwab, F. and Knopoff, L. (1972). Fast surface wave and free mode computations. In *Methods in Computational Physics: Advances in Research and Applications*, volume 11, pages 87–180. Elsevier.

[Searle, 1988] Searle, M. (1988). Thrust tectonics of the dibba zone and the structural evolution of the arabian continental margin along the musandam mountains (oman and united arab emirates). *Journal of the Geological Society*, 145(1):43–53.

[Searle and Cox, 1999] Searle, M. and Cox, J. (1999). Tectonic setting, origin, and obduction of the oman ophiolite. *Geological Society of America Bulletin*, 111(1):104–122.

[Searle et al., 1983] Searle, M., James, N., Calon, T., and Smewing, J. (1983). Sedimentological and structural evolution of the arabian continental margin in the musandam mountains and dibba zone, united arab emirates. *Geological Society of America Bulletin*, 94(12):1381–1400.

[Searle et al., 2004] Searle, M., Warren, C., Waters, D., and Parrish, R. (2004). Structural evolution, metamorphism and restoration of the arabian continental margin, saih hatat region, oman mountains. *Journal of Structural Geology*, 26(3):451–473.

[Shackleton and Ries, 1990] Shackleton, R. and Ries, A. (1990). Tectonics of the masirah fault zone and eastern oman. *Geological Society, London, Special Publications*, 49(1):715–724.

[Shapiro and Ritzwoller, 2002] Shapiro, N. and Ritzwoller, M. (2002). Monte-carlo inversion for a global shear-velocity model of the crust and upper mantle. *Geophysical Journal International*, 151(1):88–105.

[Shapiro and Campillo, 2004] Shapiro, N. M. and Campillo, M. (2004). Emergence of broadband Rayleigh waves from correlations of the ambient seismic noise. *Geophysical Research Letters*, 31(7).

[Shapiro et al., 2005] Shapiro, N. M., Campillo, M., Stehly, L., and Ritzwoller, M. H. (2005). High-resolution surface-wave tomography from ambient seismic noise. *Science*, 307(5715):1615–1618.

[Shearer, 2009] Shearer, P. M. (2009). *Introduction to seismology*. Cambridge university press.

[Shelton, 1990] Shelton, A. (1990). The interpretation of gravity data in oman: constraints on the ophiolite emplacement mechanism. *Geological Society, London, Special Publications*, 49(1):459–471.

[Sheriff and Geldart, 1995] Sheriff, R. E. and Geldart, L. P. (1995). *Exploration seismology*. Cambridge university press.

[Smewing et al., 1991] Smewing, J., Abbotts, I., Dunne, L., and Rex, D. (1991). Formation and emplacement ages of the masirah ophiolite, sultanate of oman. *Geology*, 19(5):453–456.

[Smith and Dahlen, 1973] Smith, M. L. and Dahlen, F. (1973). The azimuthal dependence of Love and Rayleigh wave propagation in a slightly anisotropic medium. *Journal of Geophysical Research*, 78(17):3321–3333.

[Smith, 1970] Smith, W. D. (1970). S to p conversion as an aid to crustal studies. *Geophysical Journal International*, 19(5):513–519.

[Snieder, 1988] Snieder, R. (1988). Large-Scale waveform inversions of surface waves for lateral heterogeneity: 2. Application to surface waves in Europe and the Mediterranean. *Journal of Geophysical Research: Solid Earth*, 93(B10):12067–12080.

[Soomro et al., 2016] Soomro, R., Weidle, C., Cristiano, L., Lebedev, S., Meier, T., and Group, P. W. (2016). Phase velocities of Rayleigh and Love waves in central and northern Europe from automated, broad-band, interstation measurements. *Geophysical Journal International*, 204(1):517–534.

[Spakman and Nolet, 1988] Spakman, W. and Nolet, G. (1988). Imaging algorithms, accuracy and resolution in delay time tomography. In *Mathematical geophysics*, pages 155–187. Springer.

[Stehly et al., 2006] Stehly, L., Campillo, M., and Shapiro, N. (2006). A study of the seismic noise from its long-range correlation properties. *Journal of Geophysical Research: Solid Earth*, 111(B10).

[Stehly et al., 2009] Stehly, L., Fry, B., Campillo, M., Shapiro, N., Guilbert, J., Boschi, L., and Giardini, D. (2009). Tomography of the Alpine region from observations of seismic ambient noise. *Geophysical Journal International*, 178(1):338–350.

[Stern and Johnson, 2010] Stern, R. J. and Johnson, P. (2010). Continental lithosphere of the arabian plate: a geologic, petrologic, and geophysical synthesis. *Earth-Science Reviews*, 101(1-2):29–67.

[Stoeser and Camp, 1985] Stoeser, D. B. and Camp, V. E. (1985). Pan-african microplate accretion of the arabian shield. *Geological Society of America Bulletin*, 96(7):817–826.

[Tanimoto and Anderson, 1984] Tanimoto, T. and Anderson, D. L. (1984). Mapping convection in the mantle. *Geophysical Research Letters*, 11(4):287–290.

[Trampert and Woodhouse, 2003] Trampert, J. and Woodhouse, J. H. (2003). Global anisotropic phase velocity maps for fundamental mode surface waves between 40 and 150 s. *Geophysical Journal International*, 154(1):154–165.

[Tromp et al., 2010] Tromp, J., Luo, Y., Hanasoge, S., and Peter, D. (2010). Noise cross-correlation sensitivity kernels. *Geophysical Journal International*, 183(2):791–819.

[Tsai and Moschetti, 2010] Tsai, V. C. and Moschetti, M. P. (2010). An explicit relationship between time-domain noise correlation and spatial autocorrelation (SPAC) results. *Geophysical Journal International*, 182(1):454–460.

[Villasenor et al., 2001] Villasenor, A., Ritzwoller, M., Levshin, A., Barmin, M., Engdahl, E., Spakman, W., and Trampert, J. (2001). Shear velocity structure of central eurasia from inversion of surface wave velocities. *Physics of the Earth and Planetary Interiors*, 123(2-4):169–184.

[Vinnik and Farra, 2002] Vinnik, L. and Farra, V. (2002). Subcratonic low-velocity layer and flood basalts. *Geophysical Research Letters*, 29(4):8–1.

[Vinnik et al., 2004] Vinnik, L., Farra, V., and Kind, R. (2004). Deep structure of the afro-arabian hotspot by s receiver functions. *Geophysical research letters*, 31(11).

[Wang and Dahlen, 1995] Wang, Z. and Dahlen, F. (1995). Validity of surface-wave ray theory on a laterally heterogeneous earth. *Geophysical Journal International*, 123(3):757–773.

[Wilken and Rabbel, 2012] Wilken, D. and Rabbel, W. (2012). On the application of particle swarm optimization strategies on scholte-wave inversion. *Geophysical Journal International*, 190(1):580–594.

[Wyns et al., 1992] Wyns, R., Béchennec, F., Le Métour, J., Roger, J., and CHERVEL, S. (1992). Explanatory notes to the geological map of sur, sheet nf 40-08, scale 1: 250,000. *Sultanate of Oman, Minist. of Petrol. and Miner., Muscat*, pages 1–103.

[Yang et al., 2007] Yang, Y., Ritzwoller, M. H., Levshin, A. L., and Shapiro, N. M. (2007). Ambient noise Rayleigh wave tomography across Europe. *Geophysical Journal International*, 168(1):259–274.

[Yao et al., 2006] Yao, H., van Der Hilst, R. D., and De Hoop, M. V. (2006). Surface-wave array tomography in SE Tibet from ambient seismic noise and two-station analysis—I. Phase velocity maps. *Geophysical Journal International*, 166(2):732–744.

[Yoshizawa and Kennett, 2002] Yoshizawa, K. and Kennett, B. (2002). Determination of the influence zone for surface wave paths. *Geophysical Journal International*, 149(2):440–453.

[Yuan et al., 2006] Yuan, X., Kind, R., Li, X., and Wang, R. (2006). The s receiver functions: synthetics and data example. *Geophysical Journal International*, 165(2):555–564.

[Zhu and Kanamori, 2000] Zhu, L. and Kanamori, H. (2000). Moho depth variation in southern california from teleseismic receiver functions. *Journal of Geophysical Research: Solid Earth*, 105(B2):2969–2980.

Appendix A

Ambient noise surface wave tomography

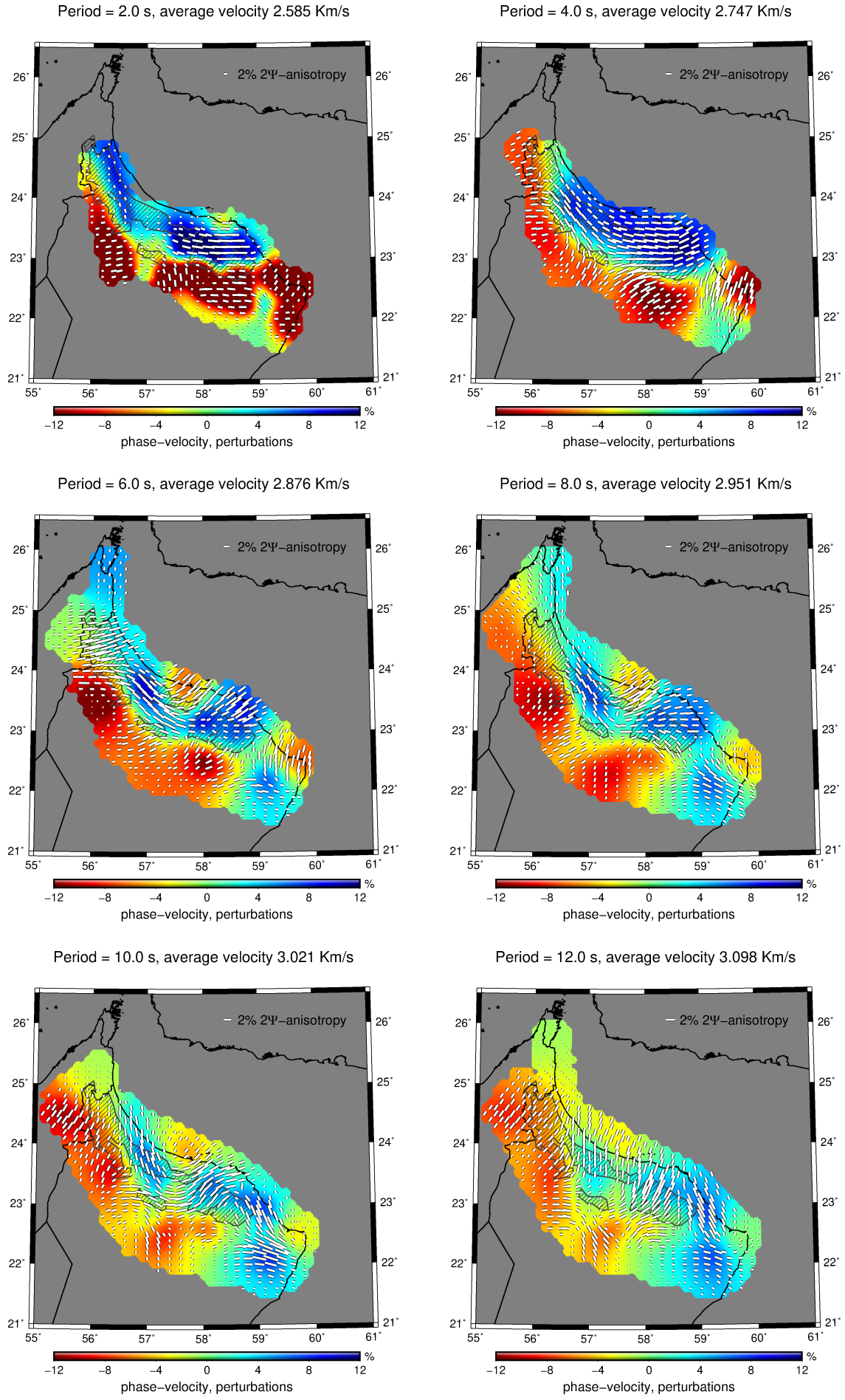

Figure A.1: Isotropic and Anisotropic Rayleigh wave phase velocity maps for 2, 4, 6, 8, 10 and 12 s

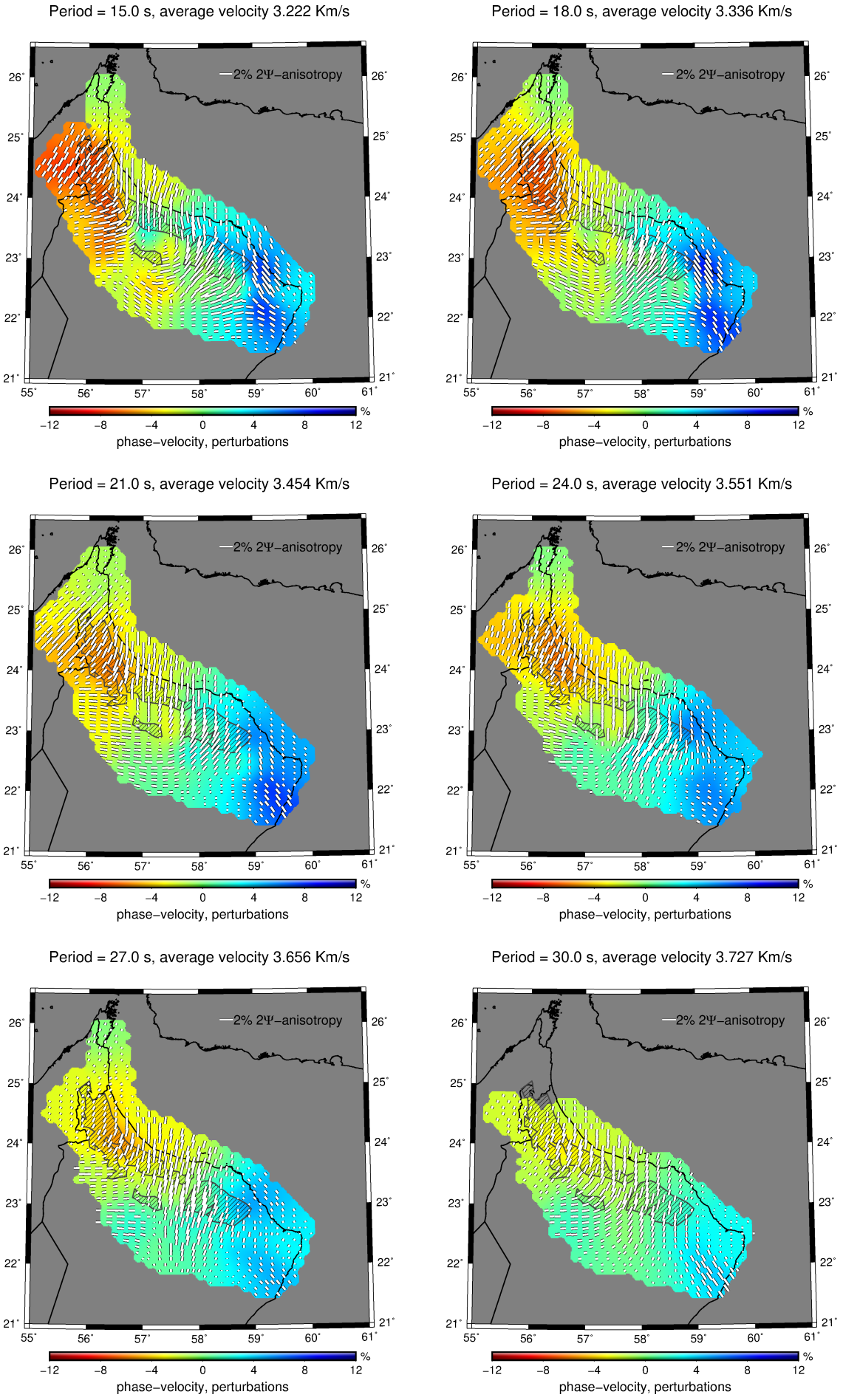

Figure A.2: Isotropic and Anisotropic Rayleigh wave phase velocity maps for 15, 18, 21, 24, 27 and 30 s

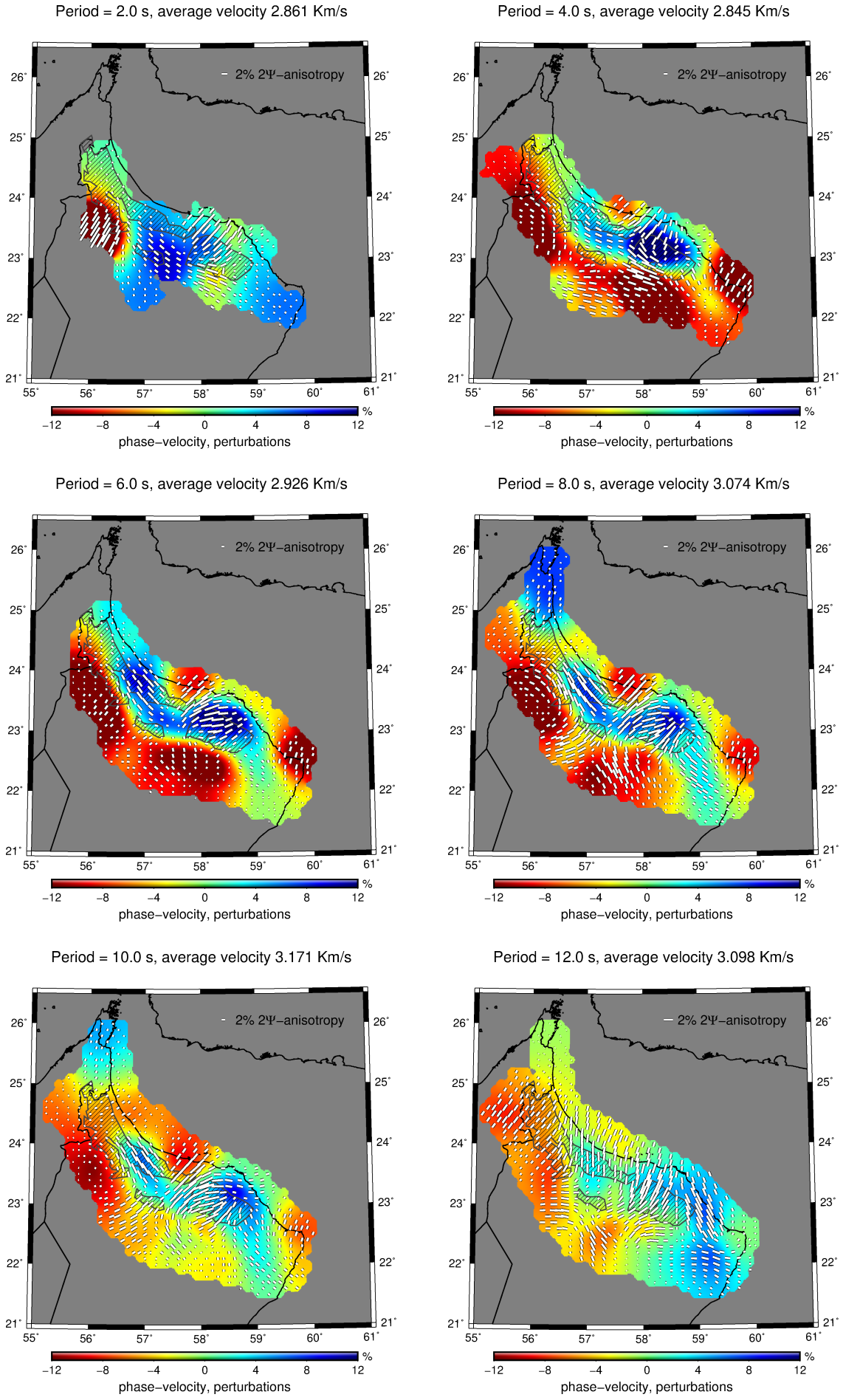

Figure A.3: Isotropic and Anisotropic Love wave phase velocity maps for 2, 4, 6, 8, 10 and 12 s

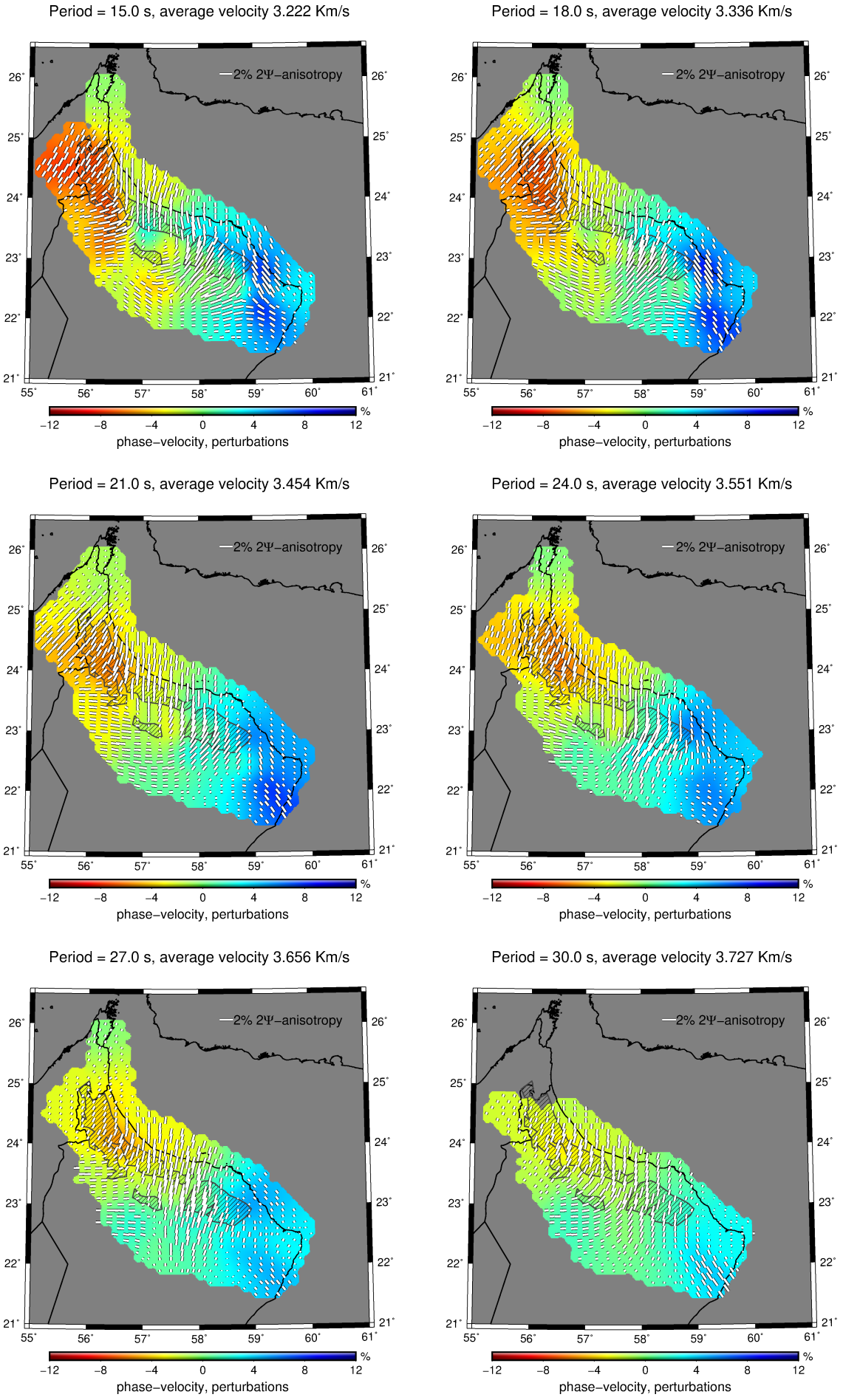

Figure A.4: Isotropic and Anisotropic Love wave phase velocity maps for 15, 18, 21, 24, 27 and 30 s

Appendix B

Receiver functions

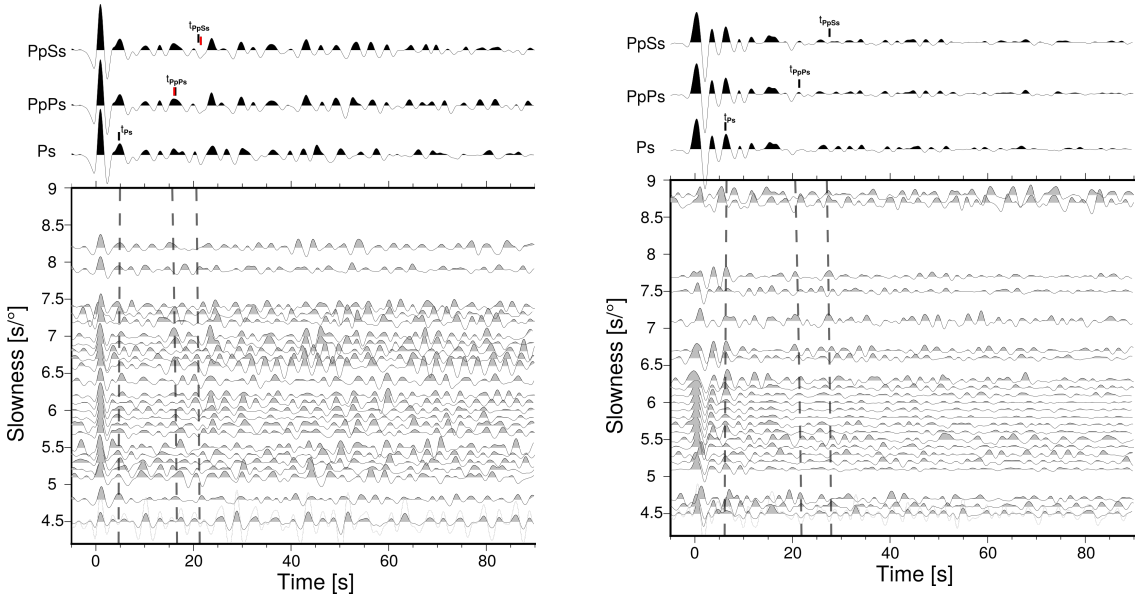

Figure B.1: Detection of different P- phases for station COO42 (left) and UOSS (right). centre: single receiver functions, sorted by slowness. Dashed lines: theoretical arrival times for Ps, PpPs and PpSs based on velocities from IASP91 as a function of slowness; top: stacked receiver functions, moveout corrected for the different phases Ps, PpPs and PpSs. Black line: theoretical arrival times of the respective phase; Red line: observed arrival time of the respective phase.

Table B.1: Summary of the observable P- phases for each station; x indicates that the certain P phase is observable in the stacked and moveout corrected receiver function nearby its corresponding theoretical arrival time

Station	Ps	PpPs	PpSs
ARQ	x	x	x
ASH	x	x	x
ASU			
BAN			
BID	x		
BSY	x	x	
FAQ	x		x
HAT	x		
HOQ	x		x
JLN	x	x	
JMD	x		
MDH			
NAZ	x		
SMD	x		
SOH	x		
WBK	x	x	
WSAR	x		
UOSS	x		
COO01	x		
COO02	x	x	x
COO03	x		
COO04	x		
COO05	x	x	x
COO06	x	x	
COO07			
COO08	x		
COO09	x		
COO10	x		
COO11			
COO12	x		
COO13	x		
COO14			
COO15			
COO16	x	x	x
COO17	x		
COO18			
COO19			
COO20	x		
COO21			
COO22	x	x	x
COO23	x		
COO24	x		
COO25			
COO26	x		x
COO27	x		
COO28	x	x	
COO29	x		
COO30	x		
COO31	x		
COO32	x		x
COO33	x		
COO34			
COO35			
COO36	x		x
COO37	x	x	
COO38			
COO39			
COO40	x		
COO41			
COO42	x	x	x
COO43	x		
COO44	x		
COO45	x		
COO46			
COO47			
COO51	x		x
COO53	x		x

Appendix C

3D Structure of the lithosphere of the eastern Arabian continental margin

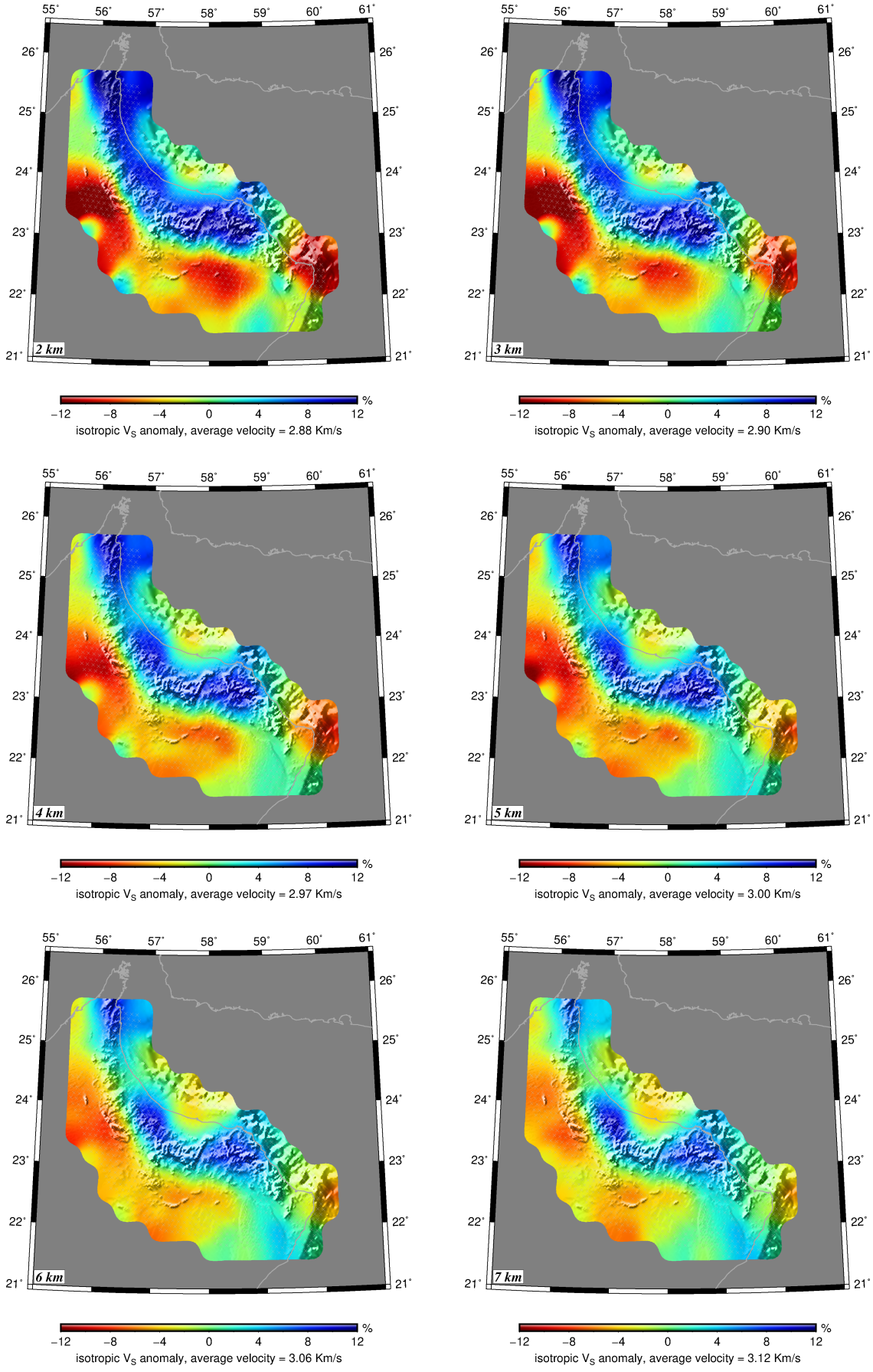

Figure C.1: Horizontal maps of the 3D shear wave velocity model at depths of 2, 3, 4, 5, 6 and 7 km. The isotropic shear wave velocity is shown as perturbations with respect to the average value of each respective depth.

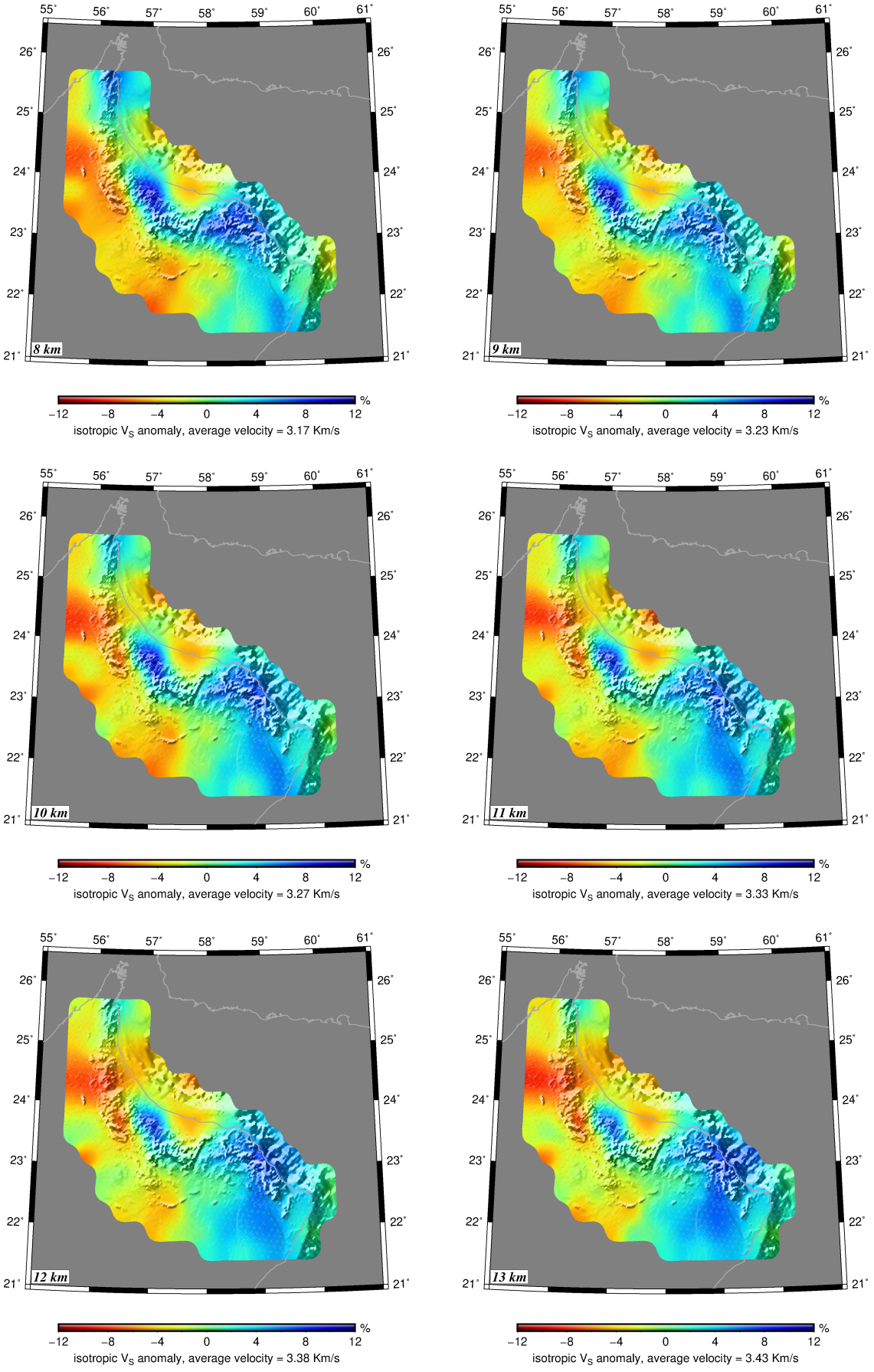

Figure C.2: Horizontal maps of the 3D shear wave velocity model at depths of 8, 9, 10, 11, 12 and 13 km. The isotropic shear wave velocity is shown as perturbations with respect to the average value of each respective depth.

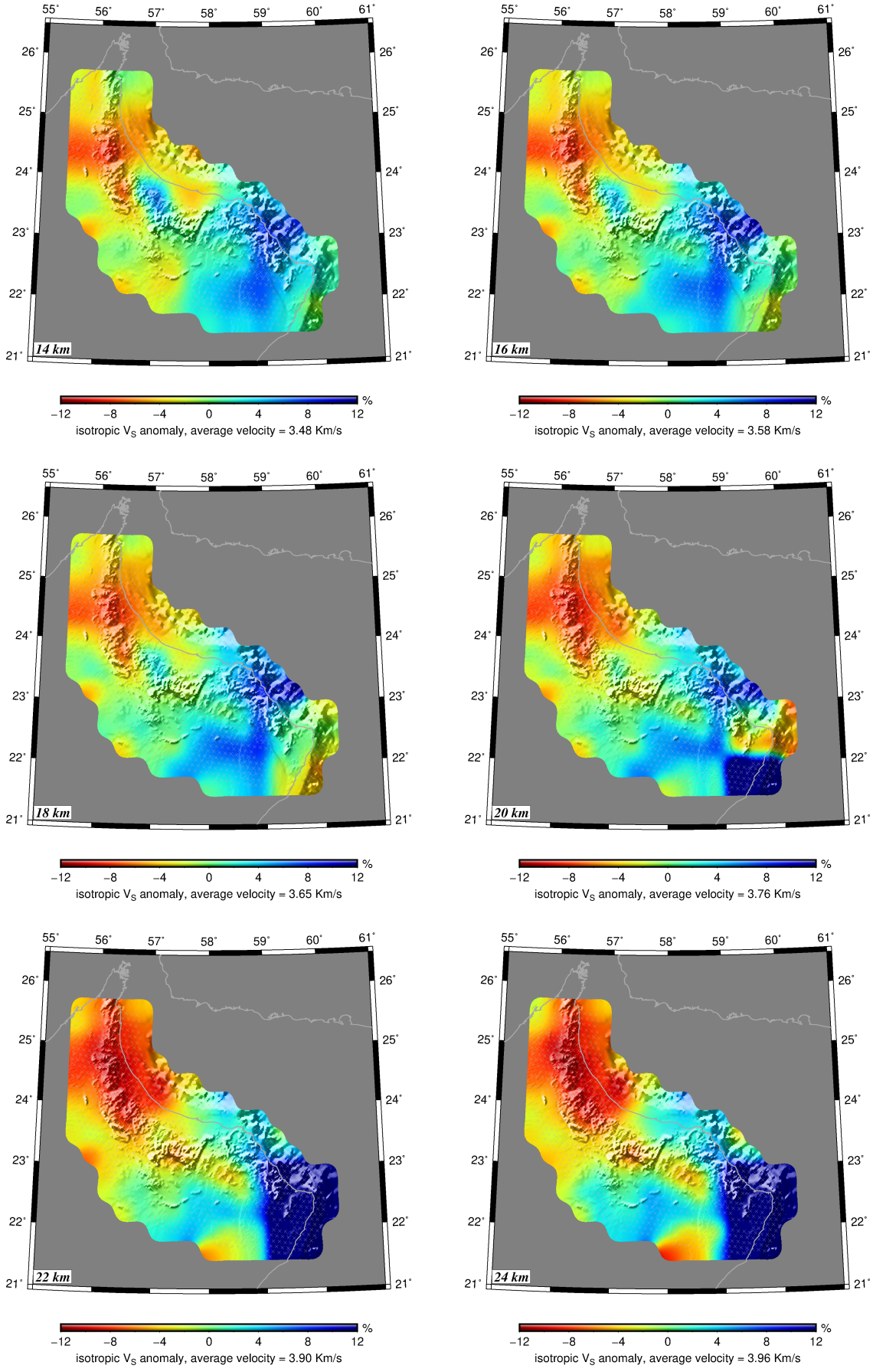

Figure C.3: Horizontal maps of the 3D shear wave velocity model at depths of 14, 16, 18, 20, 22 and 24 km. The isotropic shear wave velocity is shown as perturbations with respect to the average value of each respective depth.

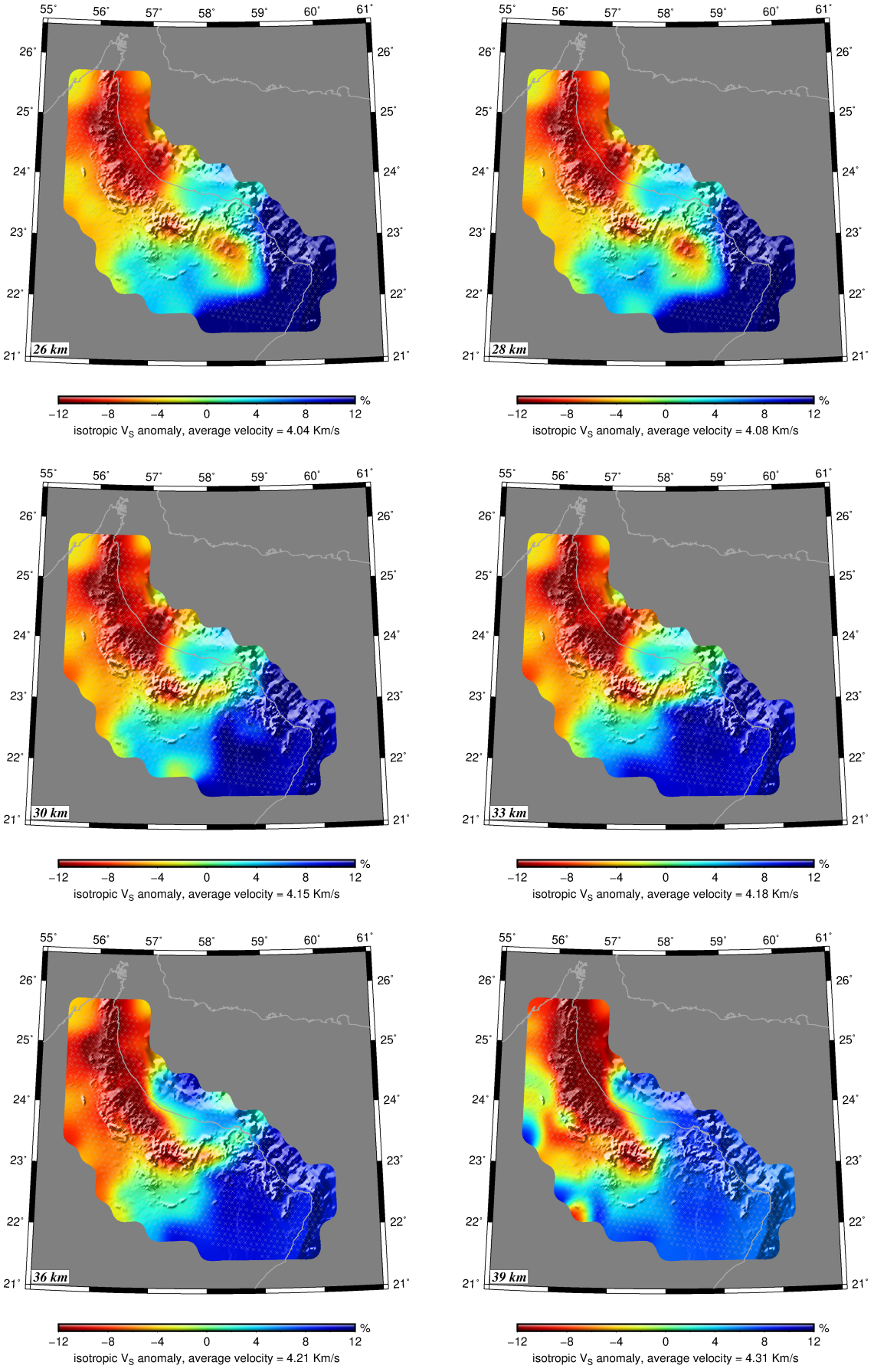

Figure C.4: Horizontal maps of the 3D shear wave velocity model at depths of 26, 28, 30, 33, 36 and 39 km. The isotropic shear wave velocity is shown as perturbations with respect to the average value of each respective depth.

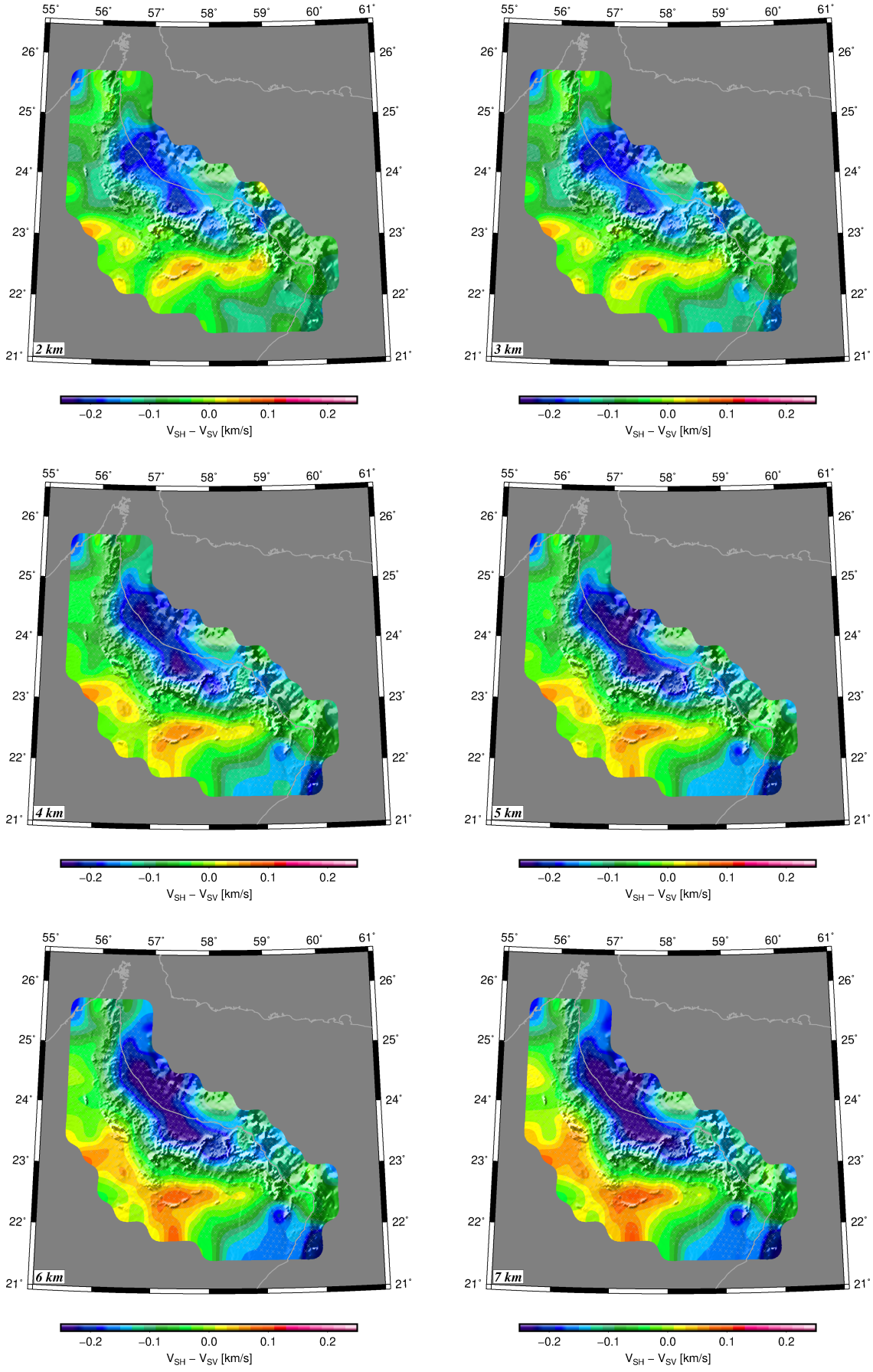

Figure C.5: Horizontal maps of the radial anisotropy at depths of 2, 3, 4, 5, 6 and 7 km. The radial anisotropy is shown as absolute difference between V_{SH} and V_{SV}.

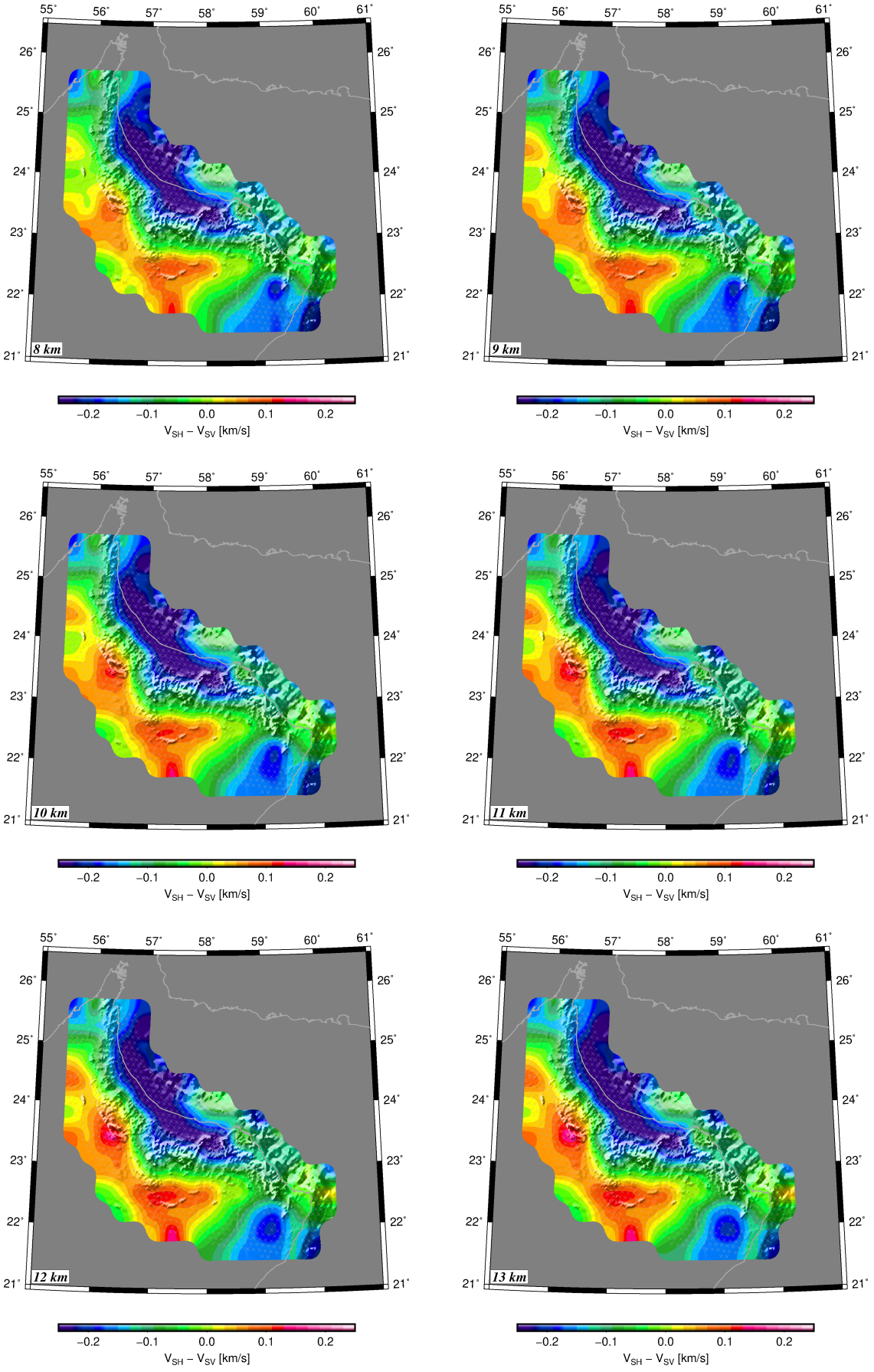

Figure C.6: Horizontal maps of the radial anisotropy at depths of 8, 9, 10, 11, 12 and 13 km. The radial anisotropy is shown as absolute difference between V_{SH} and V_{SV}.

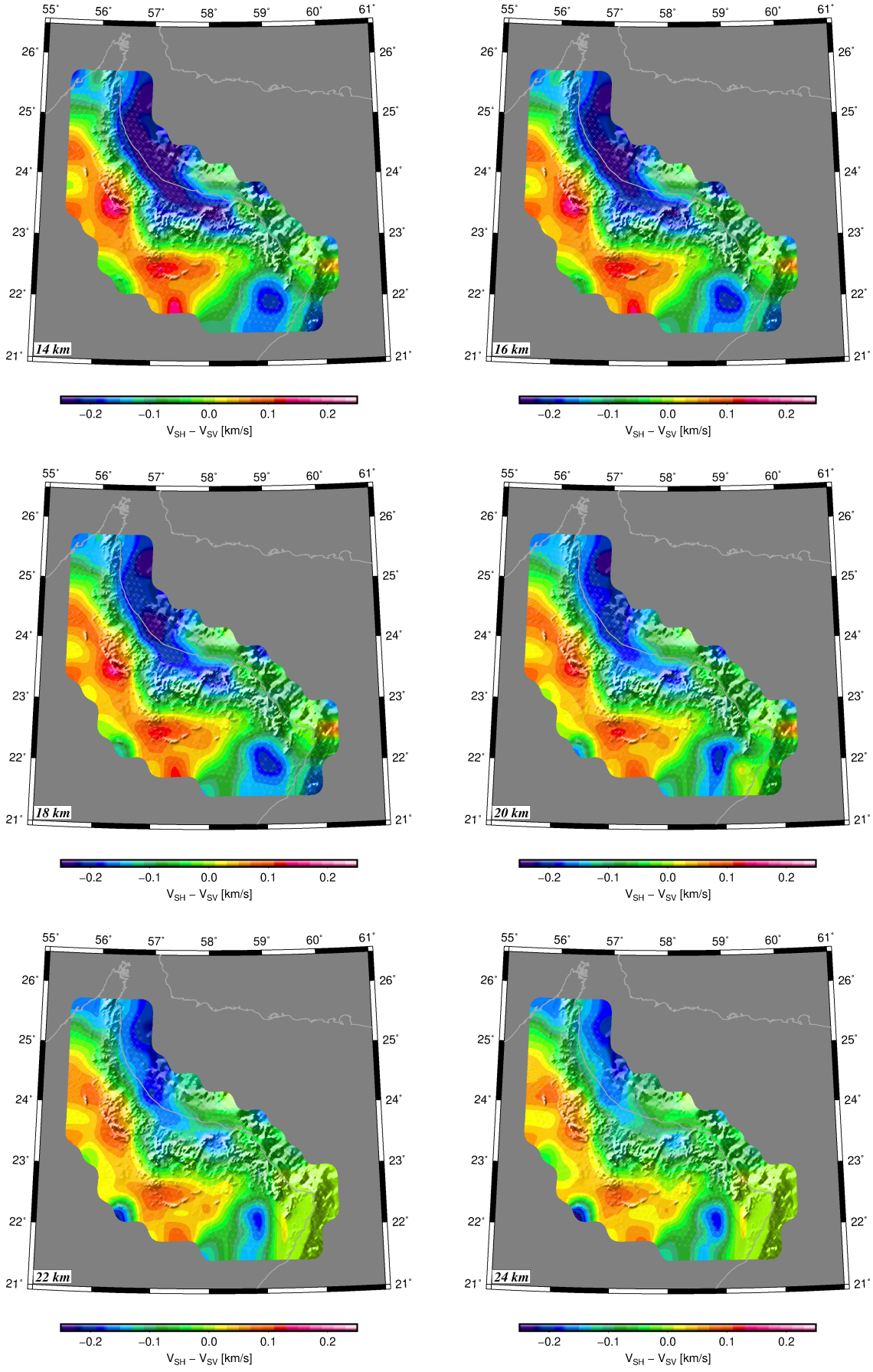

Figure C.7: Horizontal maps of the radial anisotropy at depths of 14, 16, 18, 20, 22 and 24 km. The radial anisotropy is shown as absolute difference between V_{SH} and V_{SV}.

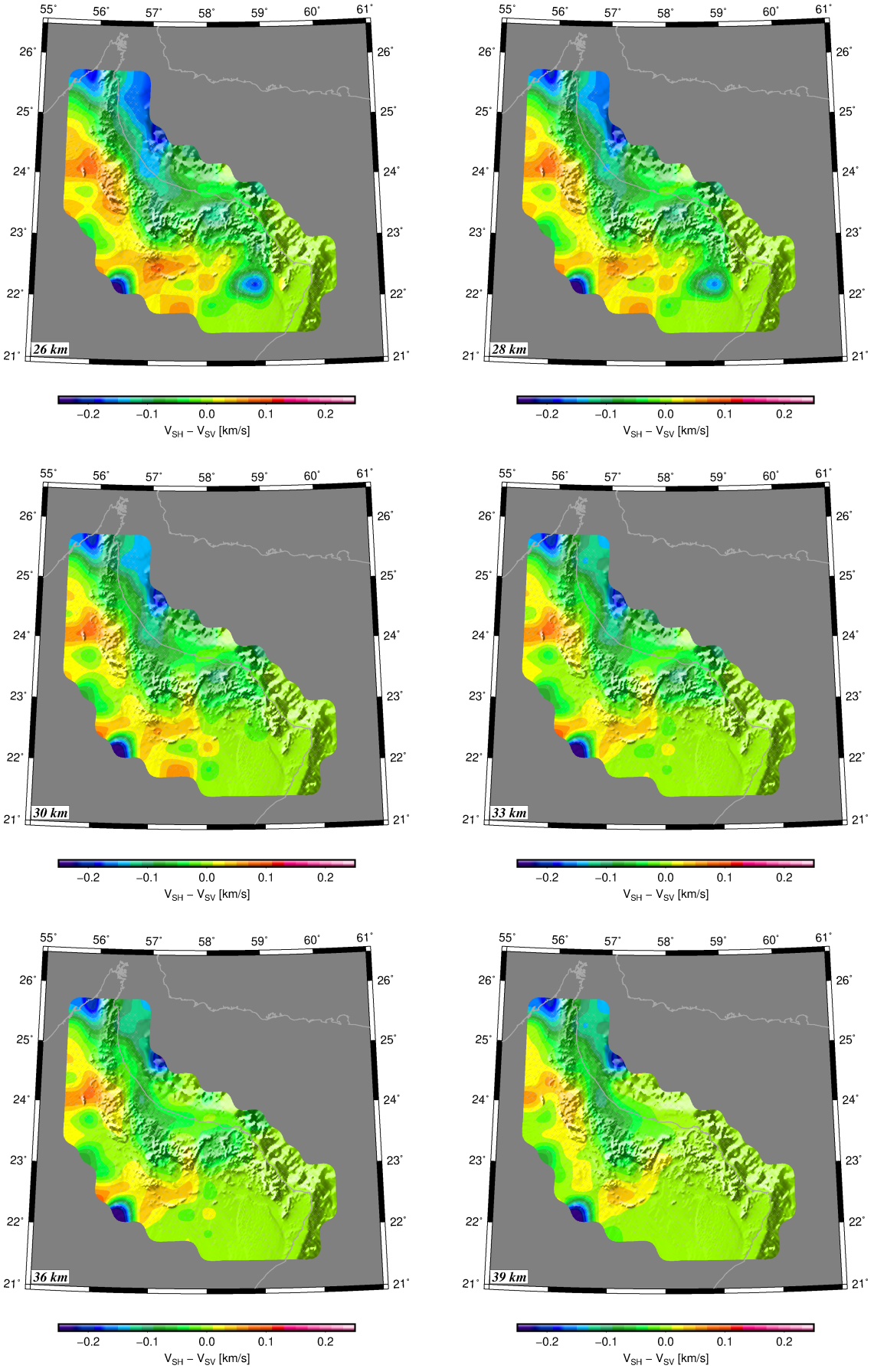

Figure C.8: Horizontal maps of the radial anisotropy at depths of 26, 28, 30, 33, 36 and 39 km. The radial anisotropy is shown as absolute difference between V_{SH} and V_{SV}.